A Three – tier bio-implantable sensor monitoring and communications platform

by

Ayodele A. Sanni

A thesis submitted for the degree of Doctor of Philosophy of
Imperial College London

Department of Electrical and Electronic Engineering,
Imperial College London

2013

ABSTRACT

One major hindrance to the advent of novel bio-implantable sensor technologies is the need for a reliable power source and data communications platform capable of continuously, remotely, and wirelessly monitoring deeply implantable biomedical devices.

This research proposes the feasibility and potential of combining well established, ‘human-friendly' inductive and ultrasonic technologies to produce a proof-of-concept, generic, multi-tier power transfer and data communication platform suitable for low-power, periodically-activated implantable analogue bio-sensors.

In the inductive sub-system presented, 5 W of power is transferred across a 10 mm gap between a single pair of 39 mm (primary) and 33 mm (secondary) circular printed spiral coils (PSCs). These are printed using an 8000 dpi resolution photoplotter and fabricated on PCB by wet-etching, to the maximum permissible density.

Our ultrasonic sub-system, consisting of a single pair of Pz21 (transmitter) and Pz26 (receiver) piezoelectric PZT ceramic discs driven by low-frequency, radial/planar excitation (-31 mode), without acoustic matching layers, is also reported here for the first time. The discs are characterised by propagation tank test and directly driven by the inductively coupled power to deliver 29 µW to a receiver (implant) employing a low voltage start-up IC positioned 70 mm deep within a homogeneous liquid phantom. No batteries are used.

The deep implant is thus intermittently powered every 800 ms to charge a capacitor which enables its microcontroller, operating with a 500 kHz clock, to transmit a single nibble (4 bits) of digitized sensed data over a period of ~18 ms from deep within the phantom, to the outside world.

A power transfer efficiency of 83% using our prototype CMOS logic-gate IC driver is reported for the inductively coupled part of the system. Overall prototype system power consumption is 2.3 W with a total power transfer efficiency of 1% achieved across the tiers.

DECLARATION OF ORIGINALITY

The research work presented in this thesis is the original work of the author conducted between September 2008 and August 2012. Parts researched externally have been duly referenced.

Ayodele A. Sanni

Copyright Declaration

ACKNOWLEDGMENTS

I would like to appreciate my supervisor, Prof. Chris Toumazou, for providing the conducive research and learning environment for the successful completion of this research work.

I would also like to express my gratitude to Dr. Antonio Vilches, now at Brunel University, for his support throughout the duration of this research work. Dr. Vilches was the author of the research idea and also the research Co-investigator of the EPSRC grant for this work.

I extend my appreciation to the staff, research students and management of the Centre for bio-inspired Technology where this research work was conducted.

Appreciation is due to the Engineering and Physical Sciences Research Council (EPSRC) for their grant (EPSRC/EP/F04612X/1) which funded this research work.

Mention should also be made of the Management of Shield Guarding for approving my study leave to attend this research program.

To my parents, Prof. & Mrs. Sanni, Prof. Onojobi, and my sisters: Mrs. Bola Onobanjo, Mrs. Toyin Esho, Dr. (Mrs). Bukky Alebiosu, and Mrs. Lolade Iheanacho for all their continued support and unending encouragements which has seen me to the completion of this research work.

Special thanks to Nicole, Imperial Central Library for the usual prompt and concise responses to my numerous research and literature enquiries. Many thanks to Ellen, Registry, Imperial College London for sorting out admission/access issues during write-up. My sincere appreciation also goes to Iza and Wiesia for sorting and ironing out administrative issues that arose during my stay at Imperial. To my colleagues, Kwok and Santos (now at Brunel), I wish to express thanks for the brain-storming periods in the lab – 'stewing' over a circuit challenge.

Despite her busy schedule, I will also like to appreciate the support of Leila, DNA Electronics.

To my friends: the Akande family, the Odetoyinbo family, the Alebiosu family, the Onojobi family, and the Iheanacho family for their invaluable support throughout this work. You are all appreciated!

And, above everything else, glory to Him whose grace and mercy saw me through to successful completion.

TABLE OF CONTENTS

LIST OF FIGURES

LIST OF TABLES

1 INTRODUCTION

A major hindrance to the advent of novel bio-implantable sensor technologies is the urgent need for reliable power source and data communications platform. The interface platform is capable of continuously, remotely, and wirelessly monitoring deeply implantable biomedical devices. This research work focuses on a proof-of-concept, generic and reliable bio-implantable, multi-tier interface platform. This multi-tier interface is capable of remotely and wirelessly monitoring deeply implantable analog sensors without the use of batteries. The proposed solution outlined in this thesis employs a multi-tier approach using a combination of inductive coupling and ultrasonics. Sufficient amounts of power are transferred wirelessly to the implant device immersed in liquid and captured sensed data transmitted from the powered implant to the outside.

1.1 Motivation

Global economies, including those of the United States, China, India, Japan, and Europe, are all burdened with crippling health costs accruing from increases in global population, especially the aging population; resulting in a push and clamor for the development of an alternative to the costly existing traditional health care delivery [1-10].

As of October 31, 2011, according to the United Nations (U.N.) Population Fund, there are now 7 billion people sharing the Earth’s land and resources and growing at an annual rate of 5% [11-12]. The U.N. estimates world/global population will reach 8 billion by 2025 and 10 billion by 2083 [4, 13]. Of the 7 billion global population, the World

Health Organization (WHO) states those aged 60 and over is projected to grow from its 760 million today to 1 billion by 2020 and almost 2 billion by 2050 (representing 22% of the world's population) when there will be more people aged over 60 than children under the age of 15. Likewise, the global population of people aged 80 and over is projected to rise from 11 million today to near 400 million by 2050 [2, 4, 14-16].

In the United Kingdom (UK), there were 12.1 million people aged over 60 in 2001, of which 4.4 million were over 75. In 2011, it is projected that the UK will have 13.9 million people over 60 of which 4.4 million will be over 75. By 2021, the UK is estimated to have 15.9 million people aged over 60 of which 5.3 million will be over 75 [17]. It is interesting to note that in 2007, in the UK, those aged over 65 outnumbered those aged under 16 for the first time ever [18].

The graying population is significant for the medical device industry because the elderly use a disproportionate share of health care resources. Therefore an increase in the elderly segment of the population can be expected to increase health care spending [2, 4, 5, 19-22]. Conversely, the graying population accounts in part for the prevalence of chronic diseases as they are more susceptible/vulnerable to them; where about 80% of the elderly have one chronic disease and 50% have at least two [4,23]. According to the WHO, the global aging population resulted in a global expenditure for health per person per year of US$4.1 trillion in 2007 representing an average of US$639 spent on health per person per year globally [2, 24]. In 2009, healthcare spending in China was approximately 4.5% of GDP amounting to

US$220 billion [3] while in the US, healthcare spending in 2010 was US$2.5 trillion representing 18% of GDP [2]. In 2011, global annual health expenditure will be US$5.3 trillion [25]. These exorbitant health care costs are expected to put pressure on the price and demand for health care products encouraging the development of innovative emerging and future technologies which will shape the overall medical device industry [4]. To alleviate this increasing burden of taking care of the global aging population, there is a growing clamor for better health care delivery systems – particularly, home – based/outpatient healthcare solutions (evolving from hospital/clinic – based treatment to home-based, remote and personalized telecare which focuses on prevention and proactive approaches to health) [26-28]. Results of experimental research carried out on the benefits of personalized tele-healthcare show the following:

- OwnHealth Telehealth monitoring programme, UK [29], shows reduced hospital admissions and a 95% patient satisfaction

- The world's first large-scale, randomized prospective telemonitoring trail, sponsored by the European Commission, TEN-HMS [26], shows cost savings of 10%, 26% reduced number of days spent in hospital, and 15% improved survival rate compared with traditional care

- The 2008 U.S. Department of Veterans Affairs' (VA), Health Buddy [27] shows a 19% hospital admissions reduction, a 25% reduction in days spent in hospital/health care facility and costs just US$1600 per patient per year compared with US$13,121 for visiting nurses or US$77,745 for nursing home care (saving up to US$6.4 billion annually through reduced hospital admissions).

This global aging population, rising global healthcare costs due to the prevalence of chronic diseases in the elderly, and the urgent need for access to medical diagnosis and treatment in remote and emerging regions and in our homes coupled with the continuing technological innovations in diagnostic and therapeutic medical devices are driving the global market for medical devices [2, 4, 10, 30-31]. Estimates show that worldwide medical device companies bring in over US$200 billion in annual revenues with the United States being the largest consumer and producer of medical devices in the world [32]. The 2011 Freedonia market report forecasts an 8.3% annual increase in global market for IMDs rising from US$33 billion in 2009 through to US$49 billion by 2014 [30]. Against the backdrop of a rapidly aging world population – which is driving demand for IMDs – the world Microelectromechanical systems (MEMS) devices market is forecast to reach US$9.2 billion by 2015 [33]. In the U.S., this is expected to result in MEMS demand in the biomedical sector advancing 13.3% annually from 2004 to reach US$420 million in 2009 with a projected expansion of 12.3% annually through to 2014. In the UK, the medical device market is valued at US$9 billion in 2011 (per capital expenditure of US$144) and predicted to increase 3.6% annually to US$10.8 billion by 2016 [34]. These gains will also be propelled by the development of next generation devices that are based on new technologies and improved materials [30, 34]. Device segments within medical devices, expected to experience high growth, include implantable devices (IMDs), diagnostic testing devices (which generated sales of US$34 billion in 2007, representing 10% of the total worldwide medical device market), and home healthcare products and electronic monitoring devices (forecast to grow close to

70% annually over the next couple of years) [21]. Furthermore, the shortcomings in existing drug therapies will promote a surge in the use of IMDs in the treatment and management of neurological, orthopaedic, cardiovascular, ophthalmic, and various other chronic disorders [30]. An important trend in the medical electronics device market over the coming decades will be the rapid development of devices with functionalities of portability, wireless connectivity and data security; sustaining the shift from the hospital environment to the home [4, 10]. These devices will give patients a lower-cost and hassle-free option for continuous monitoring of vital signs and in some cases treatment of their health conditions right from their homes [2]. There will be less need to have them travel to a hospital, medical clinic, or doctor’s office. Medical checkups would no longer be an annual event; it will happen every day as we go about our daily lives. Eventually, health care will occur not during scheduled, intervaled, and occasional visits to the doctors’ offices, clinics, or hospitals but continuously, during ordinary activities in people’s homes, cars and workplaces [27]. The avoidance of hospitalization is good for both patients and for the health care system. For instance, in the U.S., the cost of a hospital stay for heart failure averages US$10,000 with nearly 30% of those hospitalized ending up back in hospital within 30 days. So, provided the cost of the implant is reasonable, potential savings from using it could be significant if it can avert even a single hospitalization [27].

The technologies or product groups expected to become widespread and fuel emerging and future trends in IMDs and also support new product research and development, the following are pertinent for mention [4]:

- Improvement in diagnostic capabilities are expected to drive the development of new predictive, diagnostic, and prognostic products and improved surgical techniques

- Escalating health costs are expected to increase the emphasis on outpatient care. Enabling technologies such as home telemetry systems, wireless device communication technologies, and remote monitoring technologies are expected to make telemedicine increasingly popular. Integration of these technologies with implantable medical devices or patient home monitoring devices has the potential to make health care more affordable and reduce hospitalization costs

- Advances in power supply technologies are expected to increase durability and reliability of devices and lead to innovative technologies such as wireless transfer of power.

1.2 Bioelectronics

One of the great impacts of bioelectronics – the intersection of bio/medicine and semiconductor/electronics – is the development of innovative, multi-functional Implantable medical devices (IMDs) that will have the potential of ushering in affordable healthcare. The system design requirements as well as design constraints of these implantable devices include the following:

- ultra-low overall system power consumption
- miniature device size for placement within a human body
- low off-state operating current (nanoamperes)
- low dynamic power consumption
- low transistor leakages in the off-state;

making commercially available solutions inadequate [35]. Consequently, Silicon-based CMOS technology is the basic building block of IMDs because of its inherent ultra-low power as well as its ability to integrate multi-functionality without increase in overall power consumption and size factor.

Advances in sub-micron electronics, nanotechnology, as well as MEMS are also now being used to build miniature, multi-functional and highly intelligent implantable devices that will have a profound effect on medicine [36]. The integrated mechanical sensing and computational multi-functions of lab-on-a-chip, System-on-Chip (SoC), and System-in-Package (SiP) with accompanying low manufacturing costs is now a reality through MEMS technology. MEMS technology enables the development of ultra-low power miniature transceivers for wireless medical applications [37]. It also meets the requirement for the continuous introduction of complex, intelligent, multi-functional, and modular implantable devices for instance SiP (which is currently the fastest growing packaging technology) [38].

Given the profound impact electronics has had on medicine and biology from the 1940's, it is easy to imagine that integrating modern electronics (i.e. semiconductor technology) with biology and medicine will result in equally profound quantum leaps; for example [39]:

- Ongoing miniaturization of semiconductor devices is leading to new opportunities in biomedical research and commercial medical applications – with healthcare costs drastically reduced and some untreatable diseases now curable

- Nanoscale bioelectronics is enabling the development of molecular-based personalized medicine

- Nanoscale electrical measurements will be important in genomics and proteomics for identifying the function of proteins and their reaction pathways inside cells and membranes

- Advances in integration and packaging produce circuitry integrated with sensors, actuators, and computers, enabling the creation of devices and systems that can intelligently probe biological systems from molecule to cell to whole organism levels

In summary, the principal advantage of miniature (micro-scale) implantable devices include: achievable extreme levels of miniaturization; the integration of multiple functions including sensing, delivery, and closed loop control; as well as precision micro-scale and nano-scale features [40].

Key landmarks and trends in medical devices development are listed below [41]:

1800 – 1850s	First “modern” stethoscopes, laryngoscopes, and ophthalmoscopes
1895	X-Rays discovered
1903	First electrocardiograph developed
1927 – 1928	First respirator developed and first cardiac catheterization performed
1940	First metallic hip replacement surgery performed
1945	First kidney dialysis machine
1950	First artificial hip replacement performed
1951	First commercially available artificial heart valve

1952	First successful external cardiac pacemaker
1960	First totally internal pacemaker
1970	First Computerized Tomography (CT) scanner
1972	First Laparoscopic procedure performed
1976	First regulatory system for medical devices and first Positron Emission Tomography (PET) scanning performed
1977	First Magnetic Resonance Imaging (MRI) device
1978	First multi-channel cochlear implant
1982	First permanent artificial heart
1985	First implantable Cardioverter Defibrillator and first robot-assisted surgical procedure performed
1993	First European Union regulatory system for medical devices

Bioelectronics will support the development of IMDs and the advent of bio-implantable solutions; making impacts through the following:

1) **Measurement and analysis** - The shift from hospital-based care to home-based care using biotelemetry. Biotelemetry (aka Remote Monitoring) is the transmission of biological or physiological data from a remote, inaccessible location to a remote monitoring site capable of interpreting the data and effecting timely decision making. As measurement of physiological variables is carried out in conscious, unrestrained humans (and animals) natural physiological data is produced. Biomedical

telemetry therefore offers wireless, restraint-free, simultaneous, and long-term data gathering, making the cornerstones of modern biotelemetry miniaturization, micro-power, and wireless communication [42].

Biotelemetry requires wireless communication for the transfer of information between sensors and the device and between the device and the telemedicine server. Available medical telemetry transmission frequency bands for the transfer of physiological data and information include [43] – [44]:

- Medical Implant Communication Service (MICS) = 402 – 405 MHz. Maximum transfer power = 25 µW, maximum bandwidth used at any one time = 300 kHz i.e. low bit rate system compared with WiFi and Bluetooth. Range is a couple of meters
- VHF = 174 – 206 MHz
- UHF = 450 – 470 MHz
- Industrial, Scientific and Medical band (ISM) = 902923 MHz, 2.4 – 483 GHz
- Wireless Medical Telemetry Service bands (WMTS) = 608 – 614 MHz, 1395 – 1400 MHz, and 1427 – 1432 MHz
- MedRadio = 401 – 406 MHz.

Figure 1 shows available wireless communication technology (protocol) in biotelemetry [45] for Implantables, Body Area Network (BAN), Personal Area Network (PAN), short mobility distance (WLAN), and global mobility distance [Wireless WAN (WWAN)]. These include:

- Bluetooth – 2.4 GHz; data rates of between 750 Kbps and 3 Mbps; transmission range of between 10m and 100m

- ZigBee – 2.4 GHz, 868 MHz (Europe) and 902 MHz (USA); data rates of 250 Kbps; transmission range of 10 – 30m indoors and 200 – 1000m outdoors; it can incorporate advanced encryption and authentication

- RFID – up to UHF frequency range (868 – 956 MHz); transmission range of a few meters; usually passive

- Ultra Wideband (UWB) – data rates of 500 Mbps at 2m and 110 Mbps for upto 10m

- IEEE 802.11 – Wireless LAN (WLAN), 900 MHz, 2.4 GHz, and 5 GHz; data rates up to 54 Mbps; transmission range up to 100m

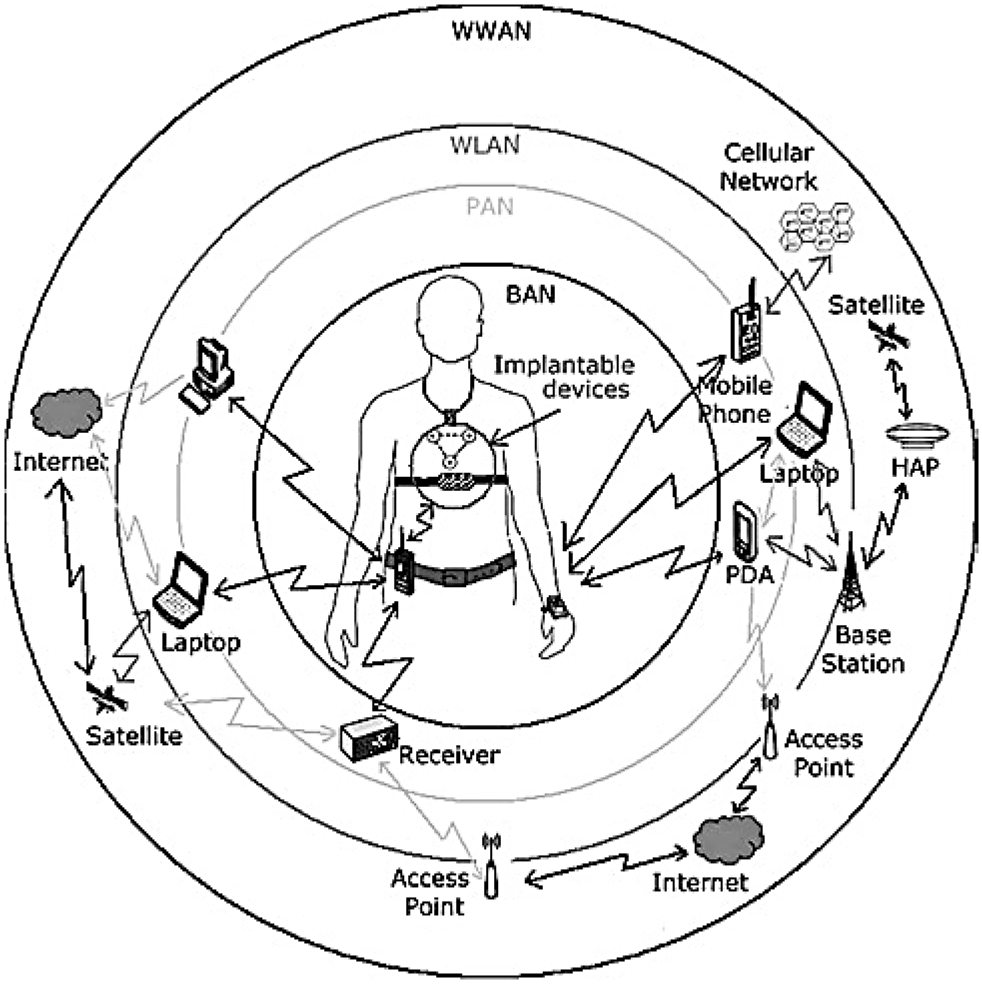

Figure 1: Biotelemetry wireless communication protocols for Implantables [45]

2) **Manufacturing/Fabrication/Packaging** – The emergence of BioMicroElectroMechanical Systems (BioMEMS) fabrication technologies such as soft lithography, micromolding, 3D structure assembly, and microfluidics. The precision and scalability offered by these fabrication technologies promise dramatic improvements in device performance and consequently patient outcomes. BioMEMS fabrication techniques are known to produce well-controlled feature sizes ranging from millimeters to submicrometers. Requirements for feature sizes below 100 nm

has required new nano-fabrication methods including extreme ultraviolet (EUV), X-Ray lithography, micro-contact printing, soft molding, and molding in capillaries (MMIC). It is no wonder that BioMEMS: is the platform upon which the human genome was sequenced in record time; the platform for performing print-of-service diagnostic testing; the basis for research of protein expression in health and disease; and eventually, monitoring the evolution of diseases in an individual, and delivering customized nano-medicine therapy [40], [46], [47]. Examples include: SoC [48] – [49], SiP [50] – [51], microfluidics [52] – [53], Microelectrode array [54], Camera pill [55] – [58], and down-sizing of implantable defibrillators from 209cc to 36cc [59]. There has also been a corresponding evolution of different packaging technologies since the 1950s including Surface Mount Devices (SMD), chip-on-board, chip-on-chip, and now 3D chip scale packaging. We are now in the era of "disposable electronics". BioMEMS have driven the implantable medical devices to higher integration, lower volumes with smaller sizes, and increased durability.

A smaller size usually denotes low power consumption, evidenced in the total power consumption requirements of available implantable systems listed below [60] – [61]:

- Pacemakers: 30 – 100 µW
- Cardiac Defibrillator: 30 – 100 µW
- Neurological stimulator: 30 µW to several mW

- Drug pump: 100 µW – 2 mW
- Cochlear implants: 10 mW
- Retinal stimulator: 250 mW
- Body area monitoring: 140 µW
- Neural recording: 10 mW
- Analog Cochlear processor: 1 – 10 mW
- Hearing aid: 100 – 2000 µW
- Telemedicine: 300 mW

3) **Device and material biocompatibility** – Biocompatibility concerns the safety of devices that are in contact with humans, either directly by surface contact or implantation, or indirectly through external communicating devices (catheters etc). The ISO 10993 International Standards pertain to the biological evaluation (and certification) of medical devices so as to protect humans while serving as a framework for selecting tests which will evaluate biological responses [46]. The biomaterials used should be able to resist degradation within the body as well as generate beneficial cellular or tissue response in specific situations thereby optimizing the performance of the devices. Available biomaterials include stainless steel, polymers, Platinum Iridium, Titanium, and Polytheretherketone polymer. Materials for electrical interconnects are also considered and include brass, Beryllium Copper, and stainless steel [62].

4) **Power sources** – The wireless power transfer capabilities of some available interface platform are listed below [63] – [64]:

- Implantable rechargeable batteries with high energy densities include Lithium Carbon Monofluoride (Li/CFx) – used in many neurostimulation devices and drug pump applications - and Lithium Silver Vanadium Oxide (Li/SVO) used in defibrillators [65]
- Radio Frequency (RF) using antennas – up to 135 mW at a range of 1m
- Inductive Coupling – up to 150 mW over a couple of centimeters range
- Ultrasonics – up to 1 W at a range of 10 cm.
- Energy harvesting – Kinetic (80 µW), Thermoelectric (30 µW), Vibration (335 µW)
- Infra Red – 4 mW
- Photovoltaic – 5 mW
- Magnetic resonance – 3 W over distances up to 1 m

The future trends of medical devices will include: the development of small and less expensive robotic systems for high-precision surgery notable for orthopedics and neurological procedures; synergy and miniaturization for future innovations in medical device design; nanotechnology and genomics in personalized care; and tissue-engineered products [41], [66] – [69].

Of the impacts of bioelectronics that will boost the development of IMDs highlighted above, this thesis will be focusing on power sources i.e. IMD power transfer and data transmission interfaces. The following chapters will discuss the development of a novel, multi-tier wireless power transfer and data communication interface for low-power, periodically-activated implantable analogue bio-sensors combining inductive coupling and ultrasonics.

1.3 Research contributions

On the basis of our focus on alternative (communication) interfaces for IMDs particularly combining transcutaneous inductive coupling and ultrasonics to wirelessly transfer power and transmit sensed data with periodically-activated deeply implantable analogue bio-sensors, the research contributions – results of which are already published in [70] – [72] - include:

- Design planar, circular printed spiral coils (PSCs) using our proprietary ‘coil calculator’ Visual Basic application with Advanced Design System (ADS)

- Evaluate PSCs fabricated on FR4 substrate for maximum permissible density using wet-etching by investigating the quality of the template mask produced as well as the etching process

- Design, simulate and evaluate the prototype CMOS logic-gate coil driver

- Characterise PZT ceramic discs using a propagation tank test containing a ‘home-made’ homogeneous liquid phantom

- Verify for the first time, by the development of an application, the feasibility of PZT transducer discs, driven in their low-frequency, radial/planar excitation (-31) mode, for wireless power and data transmission deep inside a homogenous liquid phantom

- Verify and evaluate a prototype ultrasonic power and data transfer interface system based on measurements from the propagation tank test

- Evaluate a novel multi-tier, low-power, wireless, non-invasive interface system for deeply implantable medical devices (IMDs) based on the combination of both inductive coupling and ultrasonics

1.4 Structure of thesis

This thesis is structured as follows: in chapter Two, current and relevant literature review of IMD interfaces for power and data communication are discussed, with emphasis on Transcutaneous Inductive coupling interfaces as well as Ultrasonic interfaces. A discussion of experimental methodologies for the Inductive coupling sub-system and ultrasonic sub-system of the novel multi-tier interface system is highlighted in Chapter Three. While Chapter Four discusses laboratory experimental results from the designed and developed multi-tier interface system. Chapter Five summarizes and concludes with suggestions for future work.

2. IMPLANTABLE MEDICAL DEVICES (IMDs) INTERFACES

In the preceding chapter, global healthcare systems are undergoing a crucial and radical change from the traditional/conventional hospital-centred system to an individual/home-centred system. This transformation is being driven by the aging global population and the spread of chronic diseases; both culminating in increasing global healthcare spending. Current and emerging developments in wearable medical systems (including on-body and implantable medical devices) are effecting this shift by providing accessible and affordable healthcare while encouraging early detection and timely response through continuous monitoring of human physiological conditions [73] – [80].

To achieve continuous monitoring of diverse human physiological conditions, durable, efficient, intelligent, and practical power transfer interfaces (that is communications link) are essential. In this chapter, applications of IMDs are briefly discussed with a listing of available practical power transfer and data communication interfaces for IMDs. Current published designs of inductive coupling and Ultrasonics interfaces are further listed and their short-comings discussed.

2.1. Implantable Medical Devices (IMDs)

From the first battery-operated Cardiac Pacemaker in the 50's, IMDs have been evolving. This evolution has been characterised by smaller footprints having multi-functional capabilities for diagnosis, telemetry, sensing, and therapeutics. This evolution is facilitated by advancements in technology such as microelectronics, smart textiles, wireless communication, miniature bio-sensors, and ubiquitous computing. It is therefore no wonder that IMD’s have a crucial role in modern medicine with great potential for pervasive healthcare [81] – [92].

IMD’s combined with remote patient monitoring (telemedicine) enables improved healthcare delivery by encouraging continuous monitoring combined with patient mobility; endearing patients’ compliance for frequent and better quality measurements [93] – [99]. This wireless biomedical sensor network will provide meaningful sampled physiological data for medical personnel by establishing a real-time link between patients and service providers [100] – [103]. With this advent of smaller, safer, intelligent, efficient, maintenance-free, longer-lasting, and multi-functional IMDs, patient identification, continuous real-time monitoring, and automated delivery of precise medications can now be achieved [104] – [106].

2.1.1. Definitions

Active Implantable Medical Device

An active implantable medical device, according to the International Organization for Standardization (ISO), is a medical device that is totally or partially inserted into the human body by surgical procedure and is powered by electricity or other form of energy. It is expected to remain after completion of the medical procedure [107].

Telemedicine

The American Telemedicine Association [95] defines telemedicine as the transmission of patient's medical information between sites for the primary purpose of improving health.

Telemetry

Telemetry is the process whereby data/measurements are collected at a remote/inaccessible point and transmitted (preferably wirelessly) to another point having receiving equipments for monitoring, display, and/or recording [108].

2.1.2. History of IMD telemetry

As early as the 1950's, wireless telemetry has been demonstrated for fetal heart rate, pH, temperature, electrocardiogram (ECG), and gastrointestinal parameters. In the 70's, wireless bio-monitoring was first used in humans for monitoring fetal heart rate. Recently, we are now witnessing the development and deployment of inexpensive, practical, and portable devices for wireless telemetry systems [109]. A timeline of IMD telemetry is as below:

1980s – Inductive Telemetry: Near field (sub MHz) at data rates <50 kHz; low power (<1 mA); pick up in implant using small coil; very short range (10 cm max) requiring close skin contact

1999s – RF Telemetry: Medical Implant Communication Service (MICS) Band; 402-405 MHz frequency allocation; FCC was petitioned in mid–1990s, spectrum allocated in 1999; 2003 - Biotronik release

MICS device (non-compliant); 2004 - Medtronic release MICS device; 2005 - Guidant release ISM band (915 MHz) device; ISM bands (13.56, 433, 868, 915 MHz) are sometimes used

2002 - Ultrasonic Telemetry

2.1.3. Classifications of IMDs

There are three categories of medical devices: implanted, in-vitro, and external; with implanted medical devices the most challenging in terms of power consumption [110]. Furthermore, wireless implantable devices can be classified according to their application: Identification, Monitoring, and Control (Actuation/Stimulation) [109], [111]. Implantable identification devices (IIDs) principally provide personal information i.e. sending a patient's identifier to an external reader e.g. RFID. Implantable monitoring devices on the other hand measure physiological characteristics of a patient and transmit these data to an external device e.g. blood glucose sensors and electrocardiogram monitors. Finally, Implantable Control Devices (ICDs) alter the physiological characteristics of a patient. Commands from an external device are received which enable the adjustment of settings on the implanted device. If integrated with monitoring capabilities, they relay back information of their current status as well as the sensed data to an external device. Examples include pacemakers, implantable Cardioverter defibrillators, neurostimulators, and cochlea implants.

2.1.4. IMD applications

As illustrated in Figure 2 [60], the concept of Implantable Medical Devices (IMDs) is in fact diverse, covering the entire human body.

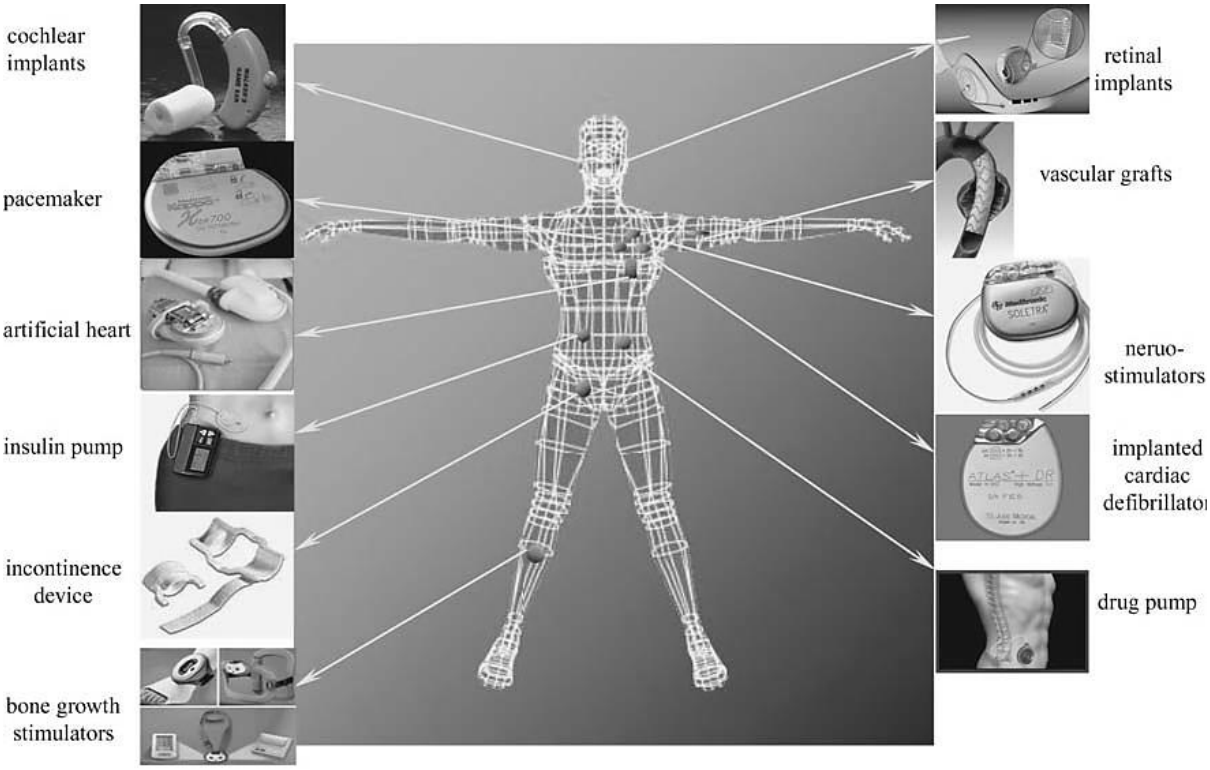

Figure 2: IMD applications [60]

Many long-term IMDs – in one or more of the application fields in Figure 2 - have already been tested, certified, and are already on the market from the following manufacturers: Remon; Zarlink (ZL70101); Avaak; RF micro devices; ULP Medical Transmitter; Given Imaging (Camera Pill); Cambridge Consultants; Toumaz (Sensium) etc. A current list of global medical device companies is highlighted in [112], [113]; while [114] lists the top eleven most implanted medical devices in the USA in 2011.

In order to satisfy the applications shown in Figure 2, the future development of implantable devices is expected to concentrate on smaller footprints, efficient power management, reliability by the inclusion of energy harvesting from the surrounding environment, and in-built wireless (communication) telemetry [115].

2.2. Characteristics of IMD interface

IMDs, once implanted, are not accessible except by costly, life-threatening surgery and must therefore be self-sustaining i.e. be able to survive the harsh conditions inside the human body to foreign objects, be able to continuously communicate wirelessly (bi-directional data transmission) with external instrumentation, have sufficient power for the duration of the intended operation, allow adjustment, resetting or reprogramming of operational settings, and be able to adequately control data acquisition, processing and wireless transmission, all on a miniature footprint [116]. This implies that for long-term, maintenance-free operations, IMDs will of a necessity have an efficient power management system in order to avoid the costs that are associated with periodic replacement of traditional batteries. For real-time monitoring applications on the other hand, the IMDs will also need to transmit sensed vital information to outside of the human body for further diagnostics and processing i.e. remote (wireless) monitoring [117]. According to Farahi et al [116], the functions of an IMD include (but are not limited to): efficient power management for all components in the system; sense and condition analog signals from implanted bio-sensors; wirelessly transmit conditioned (digital) sensed data; store sensed data as well as operational parameters and settings, wireless communication with a base station for sensed data transmission as well as operation parameters resetting; and be capable of low-duty cycles operation to conserve power.

2.2.1. Interface design considerations and challenges

Despite the fact that design requirements for IMD interfaces are application-specific, hardware design implementations share a common set of constraints in: power (and its efficient management), size, and functionality. It is interesting to note that the combination of these constraints, among others, determines the life time of the device in the case of battery-powered implants, places restrictions on the available communication range and bandwidth of the wireless communication link, as well as determining the available processing bandwidth for the front-end electronics. As restriction of the device size invariably impacts system power efficiency, computational capacity, as well as overall system functionality, hardware design considerations are usually trade-offs between required functionality, power consumption requirements, and size; with ultra-low power, multi-functional, miniature *in vivo* devices the most challenging [78].

The unique combination of ultra-low power with high reliability and wireless (bi-directional) communications differentiates IMD electronics from other electronic systems [35]. From a key requirement such as ultra-low power integrated circuits used in personal healthcare devices [92], it can be deduced that the ultra-low power and ‘fine-fabrication’ of CMOS technology is conducive for the development of implantable devices used for biomedical applications [104].

According to Oesterle et al [59], the design of an IMD requires attention to a minimum of three balanced key design requirements namely: how to interface with the implant; sensing, processing, and transmission of sensed information/data; and a power source with an efficient power management facility. Hence, their common terminology as Smart Medical Devices (SMD), Implantable Medical Devices (IMD), System-on-Chip (SoC), System-in-Package (SiP), and Laboratory-on-a-chip [116].

Because of limited power supply, a common feature of many portable/wearable medical devices is that they are operated in low-duty cycles i.e. they are periodically used. Their active duty cycle and therefore active current consumption is low due to intermittent usage. Additionally, biomedical data signals have a low frequency spectrum, for example, heart beat rate is susceptible to interferences (and therefore leakages) [92], [93].

Limited battery life impacts the lifespan of the implant and is a significant obstacle to future implantable interventions. To alleviate this impact, developments for alternative powering methods have become imperative – this is supported by the assertions of Xiao-Fei et al [73] and Loughlin [118] that a crucial issue for developing wearable/implantable medical devices is the critical need for alternative power sources.

Once the power source is selected, it becomes important to efficiently manage it by reducing overall system power consumption through novel signal processing/conditioning techniques as well as efficient analog sub-systems. Furthermore, sensed data transmission is often power intensive, preferring to process the sensed data signals by extracting the salient features before transmission [82].

Most IMDs now communicate wirelessly with an external reader, raising security and privacy-intrusion concerns because unauthenticated entry can gain access to a patient’s IMD causing direct harm to the patient [119] – [124]. In short, IMDs must be miniaturized, integrated, networked, digitalized, smart, and standardized (MINDSS) [102].

In summary, according to Schuylenbergh et al [125], IMD design challenges include:

- Low power consumption. Typically, TX/RX current of < 6 mA with low sleep/listen current of ideally < 0.1 mA

- minimal external components. Fewer components ensures lower manufacturing cost, smaller footprint, and higher reliability

- selection of ‘reasonable’ data transmission rates. Data transmission volume, speed, and range requirements dictate the wireless protocol. Bluetooth offers data rates of 3 Mbps; ZigBee offers data rates up to 250 kbps; Ultra Wideband (UWB) offers data rates between 110 – 500 Mbps; while WLAN offers data rates up to 54 Mbps

- Selection of effective operating (wireless) coverage range. For short distances of several millimeters inductive coupling is used. In the middle range of several meters, ultrasonic and electromagnetic resonance induction is used. For long distances, microwave and laser transmissions is used

- Reliability i.e data and link integrity, selectivity and interference rejection

While IMD design considerations include:

- Use of multi-tier interface platform for low operating voltages, equating to low overall system power consumption

- Implementation of ‘periodic’ duty cycle operation to conserve power through ‘sniffing’ for wake-up and turning-off sub-systems in chip not required (non-essentials)

- Use of reasonable data rate for high sensitivity; ensuring data is transmitted in short intermittent bursts

- Use of CMOS sub-micron technology

2.2.2. Interfacing IMDs – communication and power

Implanted devices communicate with the external world for power, telemetry (data transmission) and control. They operate either as sensors or stimulators. Sensors measure physiological signals inside the body and transmit this information (wirelessly) to an external device. These measured signals include body temperature, blood pressure, glucose concentration, detection of contraction/dilation of blood vessels, cardiac and arterial wall movements, respiratory, as well as cardiac pressure disorders. The continuous monitoring of these bio-signals will enable early diagnosis and the prevention of critical medical conditions. IMDs operating as stimulators on the other hand receive and relay specific control information/data and stimulate specific nerves for healing, reconstruction and/or therapeutic purposes. From the above, it is essential that implanted devices are provided adequate power in order to sense and stimulate and this cannot cease [126].

Table 1: Characteristics of primary and secondary communication nodes [126]

	Wireless Communication	**Active Telemetry**	**Passive Telemetry**
Power Source	Both nodes have their own separate power source	Located only in the primary (external) node.	The implanted node is powered from the primary node.
Transmitted signal	Only data is transmitted	Both power (from primary to implanted) and bi-directional data	Both power (from primary to implant) and data transmission. The secondary passively loads the primary correlating to the measurement of the implant device.
Device size	Bulky – to accommodate implanted power source and associated circuitry	The implanted node is smaller as it is remotely powered by the primary node and requires no power system	Minimized secondary size
Longevity	Finite. Battery requires frequent recharging	Long lifetime	Extended lifetime
Transmission bandwidth	High	Limited	Smallest bandwidth
Wireless range	Btw 20 – 1000cm	5 – 30cm	0.5 – 20cm

From Table 1, based on the characteristics of the primary (external) and secondary (implanted) communication nodes, wireless communication systems can be grouped into three categories – Wireless Communication, Active Telemetry, and Passive Telemetry [126].

The following wireless data communication and power transfer interfaces for IMDs have been considered practical [126 - 132]:

- Equipping the implanted device with Lithium ion primary batteries whose lifetime is 5 – 10 years [133] – [143]. Battery development spans from the Ruben Malloy Zinc/Mercury cells powering the early implantable pacemakers of the 1940's to the Lithium Iodine (Li-Ion) battery of the early 70s. Lithium/Silver Vanadium Oxide batteries are now used to power the high current pulse demand of Implantable Cardioverter defibrillators (ICDs).

- Radio frequency (RF) transmission [144] – [163]. RF transmission overcomes the range limitations of inductive systems. It consists of a minimum of a pair of antennas used for power transfer and data transmission over a range up to 2 m. Operating frequency is selected from the Medical Implant Communication Service (MICS) frequency band. Antennas can be on-body i.e. wearable (incorporating flexible textile substrates) or in-body i.e. subcutaneous. Design considerations include small antenna footprint, SAR levels of power radiated, directivity of the transmitter, and interference from other EM sources.

- Transcutaneous electromagnetic inductive coupling [70-72, 164 - 200]. These are used for applications where the operating range is small (millimeters). A minimum of a pair of coils is used for both power transfer and data transmission. Design considerations include fabrication of high quality coils, proper alignment of a pair of coils, and an efficient drive circuit to achieve high transfer efficiencies. It is also MRI non-compliant.

- Optics i.e light/infrared rays [201] – [209]. This system involves harvesting the energy of ambient light passing through tissues using an array of Photovoltaic (PV) cells embedded under the skin. Though power transfer is low, it is MRI compliant.

- Ultrasonics [70, 210 - 234]. This system is based on the ability of piezoelectric PZT transducers to convert ultrasonic (mechanical) waves to voltage and vice versa. Power is transferred and data transmitted via ultrasound. Design considerations for high transfer efficiency include acoustic impedance matching and an efficient drive circuitry.

- Permanent Magnet [235] – [237]. The core of a permanent magnet system is a linear generator consisting of multiple layers of permanent magnet (PM) and coils. The relative movement of the coils (due to multidirectional body movements) versus the PMs creates a varying flux in the windings. This change in flux produces voltage.

- Magnetic Resonance [238] – [244]. Strongly coupled magnetic resonance (SCMR) employs resonators to transmit power wirelessly and efficiently over mid-range distance. The adverse effects of low coupling coefficient in inductive coupling are compensated by a high quality factor 4-element system. A standard SCMR system consists of four elements – typically multiple loops and spiral coils.

- Volume Conduction (VC) [245] – [248]. This system utilizes the natural volume conducting properties of the body to facilitate power transfer. The capability of ionic fluids within biological tissues to conduct current is used for power transfer and data transmission.

- Witricity [249] – [256] – Wireless electricity – is based on using coupled resonant objects. The two electromagnetic resonators are coupled through magnetic fields. The powered sending unit fills the space around it with a non-radiative magnetic field which causes the receiving unit to resonate with it.

- Bone conduction [257] – [258]. In contrast to hearing aids, bone conduction devices convert a received sound into mechanical vibrations. These vibrations, transferred through the skull, can then converted to useable power.

- Microbial Fuel Cells [259] are devices that use bacteria as the catalyst to oxidise organic and inorganic matter and generate current.

- Energy harvesting [260] – [261]; generally from thermoelectric power generation [262] – [267], radio frequency power conversion [268] – [271], solar/photovoltaic energy conversion [272] – [274], and vibration-to-electrical energy conversion [275] – [277]. Vibration-to-electrical energy conversion is further classified by the mechanism of transduction thus: piezoelectric [278] – [281], electromagnetic [282] – [283], and electrostatic [284].

Energy received in any of the above-mentioned ways is used at once or stored in an implant's own power source using a super capacitor or rechargeable battery.

Traditional power transfer relied on wire transmission using electrical wire or cable. This method was characterized by poor safety, poor reliability and patients' inconvenience. On the other hand, with wireless power transfer, electrical power is transferred from an external source to the load without using interconnecting wires.

Based on the effective operating range, wireless transmission can be divided into three categories [285]: short distance, middle distance, and long distance. Short distance mode of transmission indicates a transmission distance of several millimeters and is typically implemented using electromagnetic inductive coupling technology. In the middle distance mode, operating range is several meters and is divided into two categories: ultrasonic and electromagnetic resonance induction. Ultrasound is a mechanical wave consisting of sound wave above 20 kHz. Power transmission via ultrasonics is based on the piezoelectric effect and converse piezoelectric effect of piezoelectric materials i.e. the conversion of mechanical vibration to electrical voltage and vice versa. Electromagnetic waves possess strong radiation property, but over long distances received power is low. This has been resolved by resonance induction technology. For long distances, the main categories are: microwave transmission and laser transmission. Microwave transmission is characterized by wavelengths from as low as 1 mm and frequency between 300 MHz to 300 GHz. The large wavelengths of microwave transmissions make them susceptible to scattering. Laser, on the other, is characterized with better directional properties and the capability to transmit larger power. In summary, the selection of an interface will be determined by the required operating range, the expected lifetime of the device, the implant size (implant location), and the data bandwidth (transmitted sensed data rate).

On the basis of how a connection is established, wireless data transmission and/or powering methods are classified into three groups [125]:

- Wireless links/interface based on wave propagation. These include radio frequency (R.F.) links (30 kHz – 300 GHz), optical links (infrared (10^{12} Hz) to Ultraviolet (10^{17} Hz), and ultrasound links (10 kHz – 10 MHz). A general requirement for all wave-based links for efficient wave generation or reception is that transducer dimensions are comparable to the wavelength

- Wireless links/interface based on electrical conduction. The wireless transmission of alternating current through the earth with an equivalent displacement through the air above it. This displacement is by electrostatic induction

- Wireless links/interface based on an alternating, but non-radiating quasi-stationary field. These include inductive links (typically 1 kHz – 100 MHz) and capacitive links (via an electrostatic field)

The most appropriate interface is determined, according to Puers et al [286], from the dimensions of the transducer, the interactions between the link and its surroundings, and the effects of the implant's environment on the performance of the interface. From published literature, inductive coupling and ultrasonics are the dominant interface for IMDs and examples of published designs for each will now be described below.

2.2.3. Inductive coupling interface design

IMDs are foreign objects placed inside the human body. Their shape and overall size is confined by the anatomical region in which they are to reside. For traditional battery-operated IMDs, implant life is restricted by the lifespan of the battery. For long term implantable devices including cochlear implants, retinal implants, pacemakers, orthopaedic implants, defibrillators, and neuro-muscular stimulation and recording devices, inductive powering is becoming the preferred link [287]. For short range links of between 1 cm and 10 cm, low-frequency inductive coupling links provide a simple interface for both power transfer and data telemetry

[78]. A generalised schematic overview of a transcutaneous inductive power and data link is shown in Figure 3.

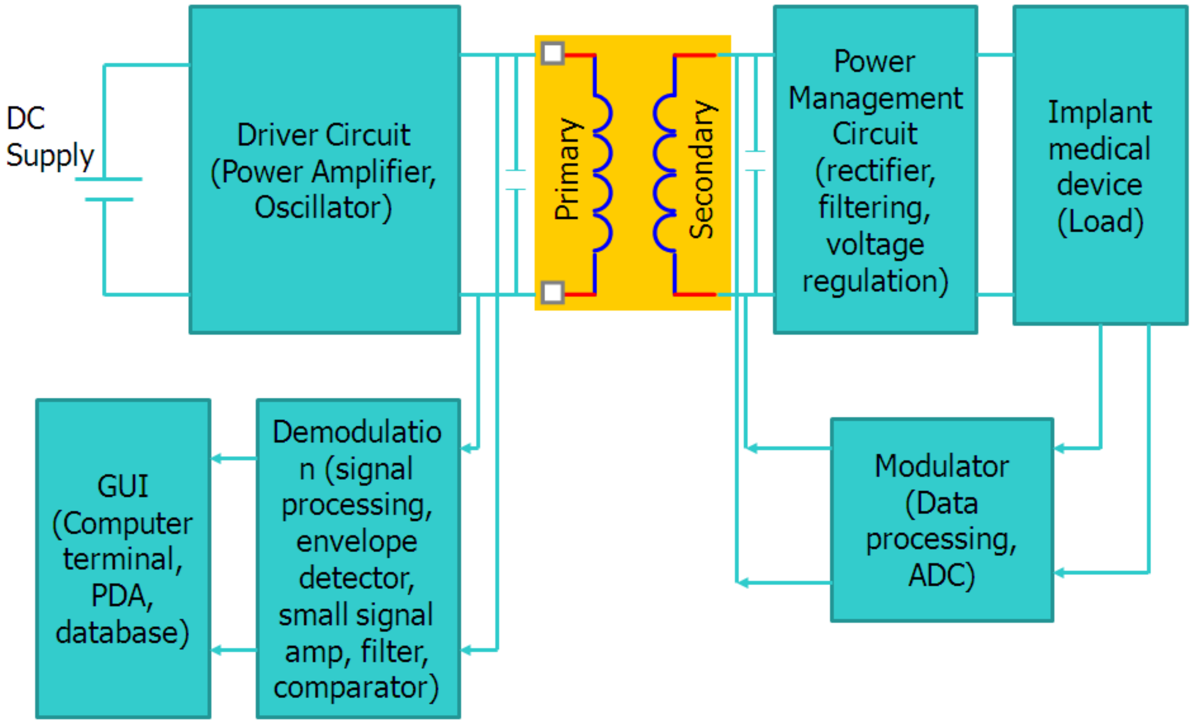

Figure 3: Generalized inductive coupling link block diagram

According to Figure 3, a generalized inductive coupling link comprises of: a small-signal master oscillator followed by a power amplifier driver; minimally, a pair of coils (the primary, external coil and the secondary, implant coil); rectifier; and regulator. The pair of coils forms a loosely-coupled transformer for wirelessly transferring energy/power to remote electronics placed within the reach of the near-field of the coils. A dedicated power amplifier is used to drive high current into the primary coil in order to generate the magnetic fields required for power transfer. Class E power amplifiers are characterised with a double-tuned circuit with a series-tuned coil and a parallel-connected capacitor. This configuration offers an elegant solution because it combines the benefits of low-current operation of a parallel resonance with the low-voltage operation of a series resonance. For small loads, high efficiency series-resonant links are appropriate while a parallel-resonance secondary is required for a voltage-source type output application [286] – [287].

Powering the primary coil generates an alternating magnetic field at the carrier resonance frequency. By an inductive coupling mechanism via mutual inductance, part of the generated magnetic field is picked up by the secondary (implant) coil. The output sinusoidal signal at the secondary coil is rectified (and regulated) to the desired supply voltage for the implant. The effectiveness of the coupling between the primary and secondary coils depends on the following: the primary coil operating drive frequency, the geometry of both coils, the gap (separation) between the coils, axial alignment between the coils, the load experienced by the primary coil, and angular alignment [78]. Transfer efficiency is a function of and increases with coil coupling, *k* between the coils and the quality factor, *Q* of each coil. To minimize misalignment, the primary coil has a larger diameter than the secondary i.e. the primary coil diameter is selected to be approximately three times the diameter of the secondary (implant) coil [287].

Inductive coupling links transfer power and have integrated data transmission – uplink for recording/monitoring devices and downlink for stimulation devices. To transmit “intelligent” data, some form of modulation is required. An inductive link, comprising the coupling of power between a primary source and a secondary LC tank, is conducive for short-distance passive data telemetry based on Amplitude Shift

Keying (ASK) and Phase Shift Keying (PSK) modulation. Amplitude modulation is characterised by simple encoding and decoding circuits and is therefore preferred to frequency and phase modulation. The decoding (demodulation) circuit comprises an envelope detector, band-pass filter, and a comparator [286 - 288]. Examples of Inductive interface circuits are given below:

1. Figure 4 is the inductive wireless power transfer system for implantable sensor applications by Adeeb et al [289].

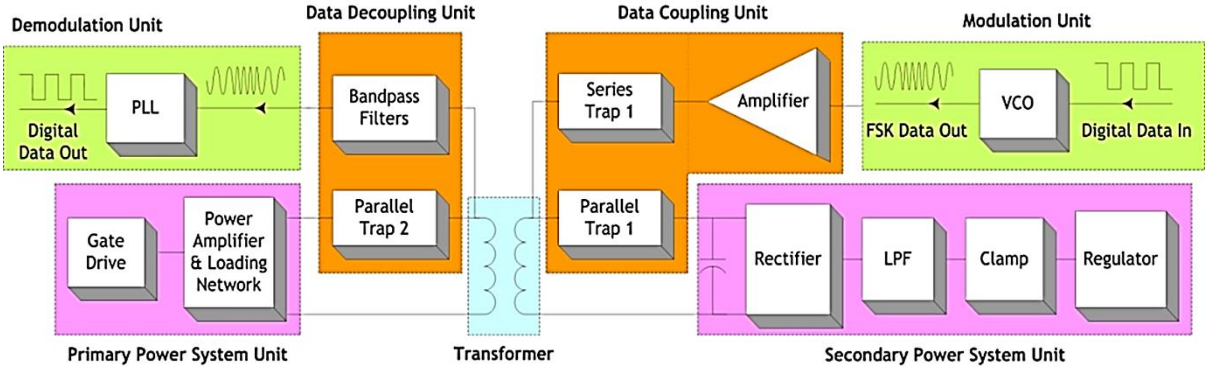

(a)

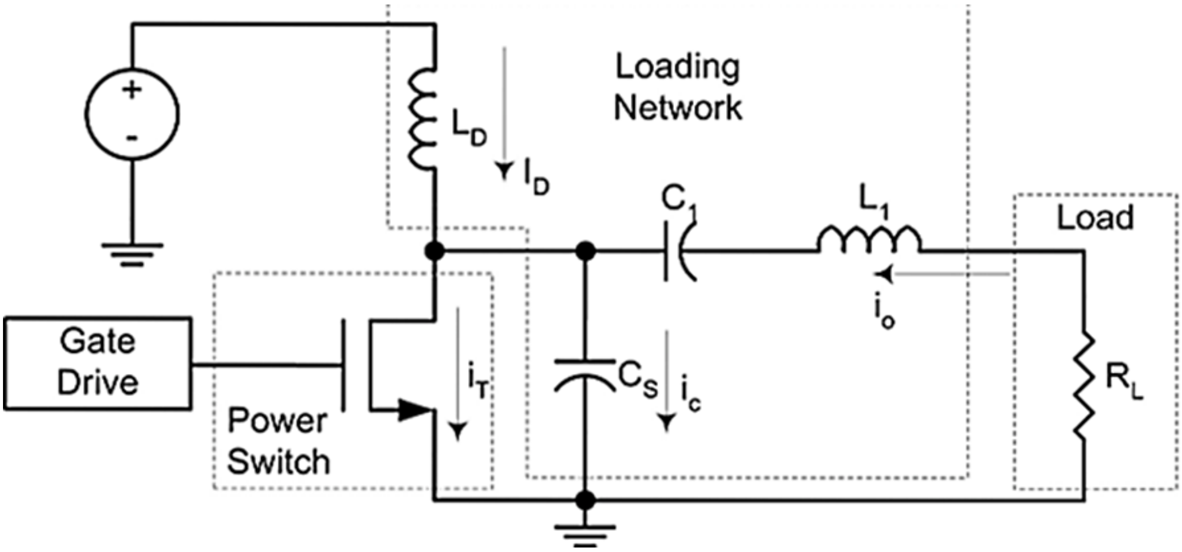

(b)

Figure 4: Inductive link wireless power transfer system for implantable sensors: (a) System block diagram (b) Class-E power amplifier driver schematic [289]

The system in Figure 4a makes use of a single pair of coils driven at a resonance frequency of 206 kHz using a Class-E power amplifier. A power of 125 mW is transferred with a power link transmission efficiency of 12.5% over an operating range of 10 mm. Frequency Shift Key (FSK) modulation scheme is used to transmit 10 Kbps of sensed data.

2. In their optical wireless USB 2.0 system, Yakasi et al [290] wirelessly transfer data and power between a portable music/video player and a PC as shown in Figure 5.

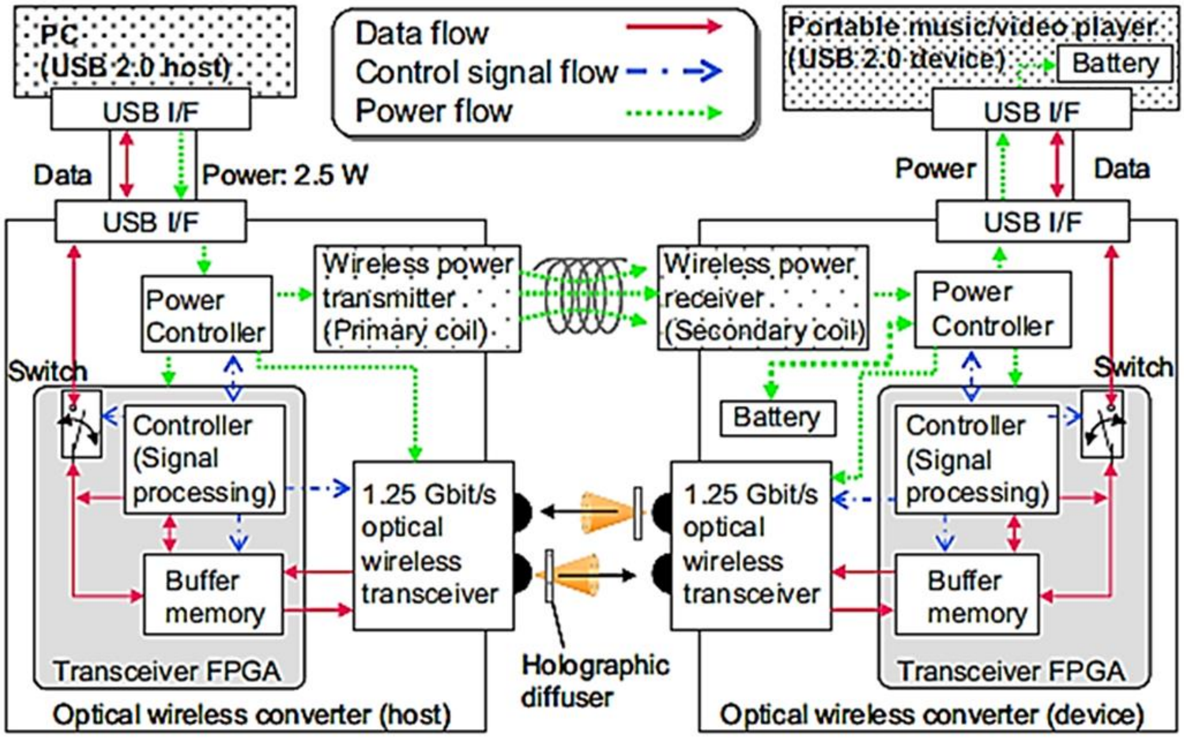

Figure 5: Optical wireless USB 2.0 system incorporating inductive coupling [290]

The system consists of a single pair of coils transferring > 1.5 W of power over an operating range of 7 mm (max) with a maximum power transfer efficiency of 70%. The radiation angle of the optical wireless transceiver is optimized using a holographic diffuser with a diffusion angle of 20 degrees. The optical data link transmits sensed data at 1 Gbps.

3. A high-efficiency inductive power link with backward telemetry for biomedical applications by Ma et al [179] is shown in Figure 6.

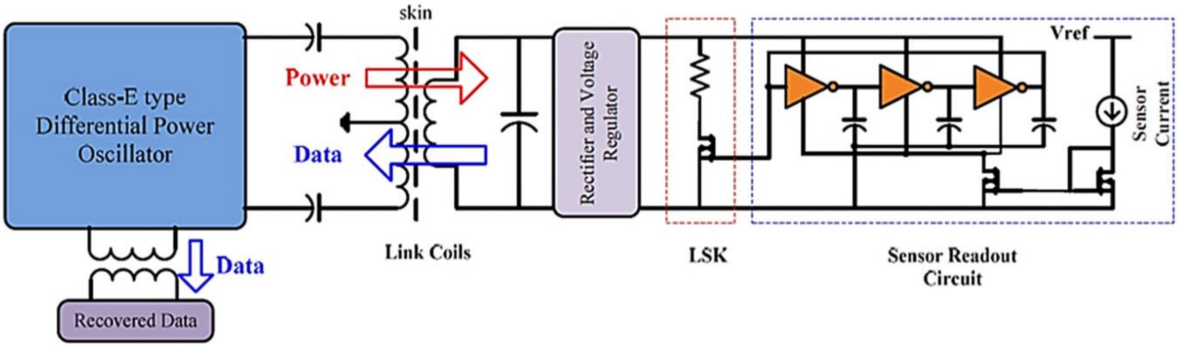
skin
Class-E type Differential Power Oscillator
Power
Data
Rectifier and Voltage Regulator
Vref
Sensor Current
Data
Recovered Data
Link Coils
LSK
Sensor Readout Circuit

(a)

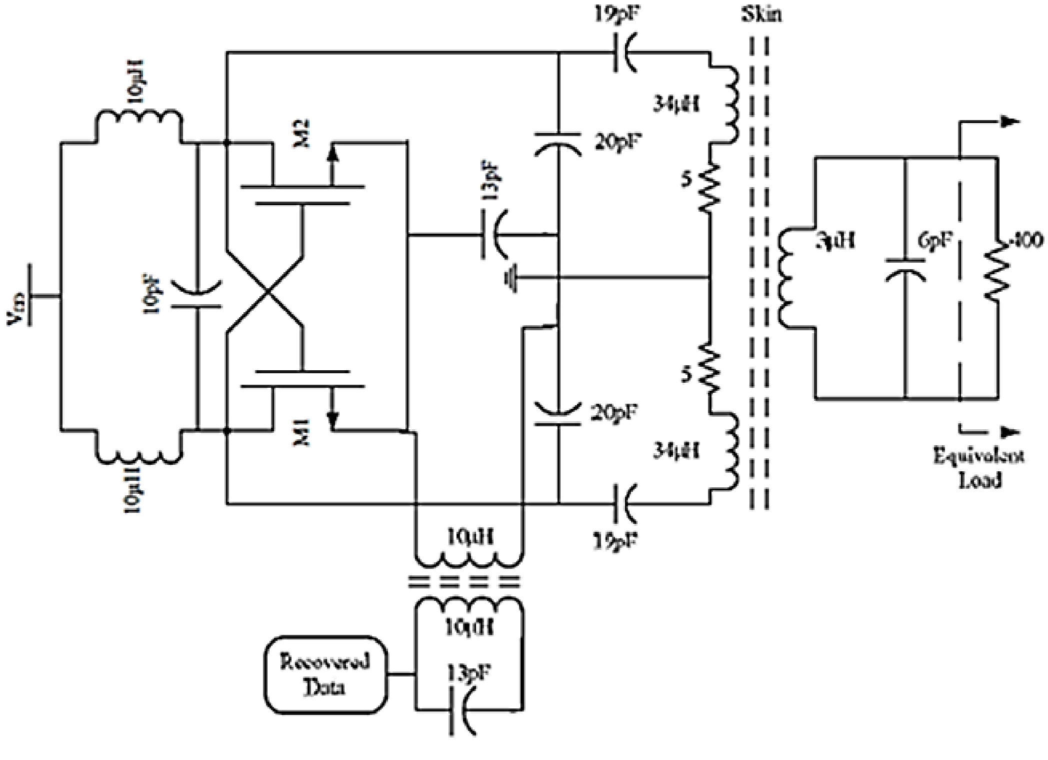
19pF
Skin
10μH
M2
34μH
20pF
5
13pF
V_DD
10pF
3μH
6pF
400
5
20pF
M1
34μH
Equivalent Load
10μH
19pF
10μH
10μH
Recovered Data
13pF

(b)

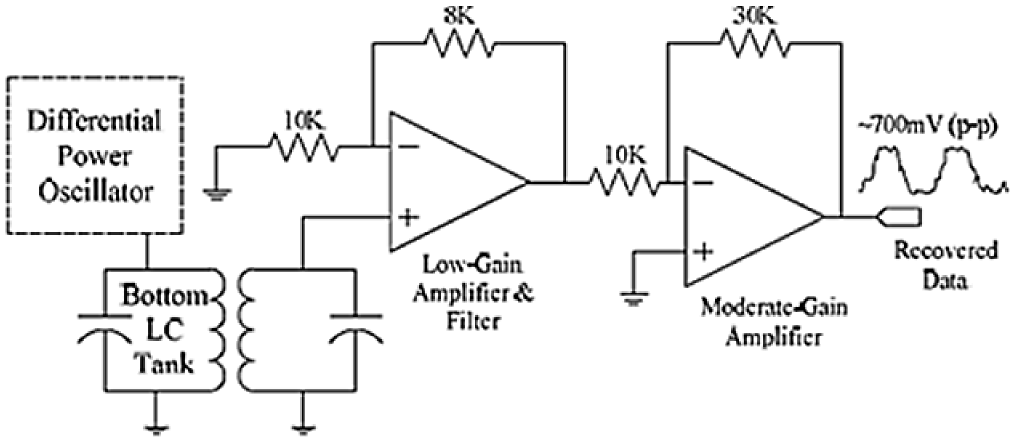

(c)

Figure 6: Inductive power link with backward telemetry for biomedical applications. (a) System block diagram (b) Differential Class-E power oscillator with data recovery (c) Power recovery unit schematic [179]

The system comprises two primary coils and a single secondary coil driven at a resonance frequency of 7 MHz. One of the primary coils is for power transfer while the other is for data transmission. The power primary coil is driven by a cross-coupled, MOSFET-based differential Class-E power oscillator. The system delivers ~ 11 mW over an operating range of 10 mm with a system efficiency of 74%. Load Shift Keying (LSK) is used to back- transmit sensed data to the external.

4. The design by Hmida et al [291] in Figure 7 is a wireless power and data transmission circuit for implantable microsystems.

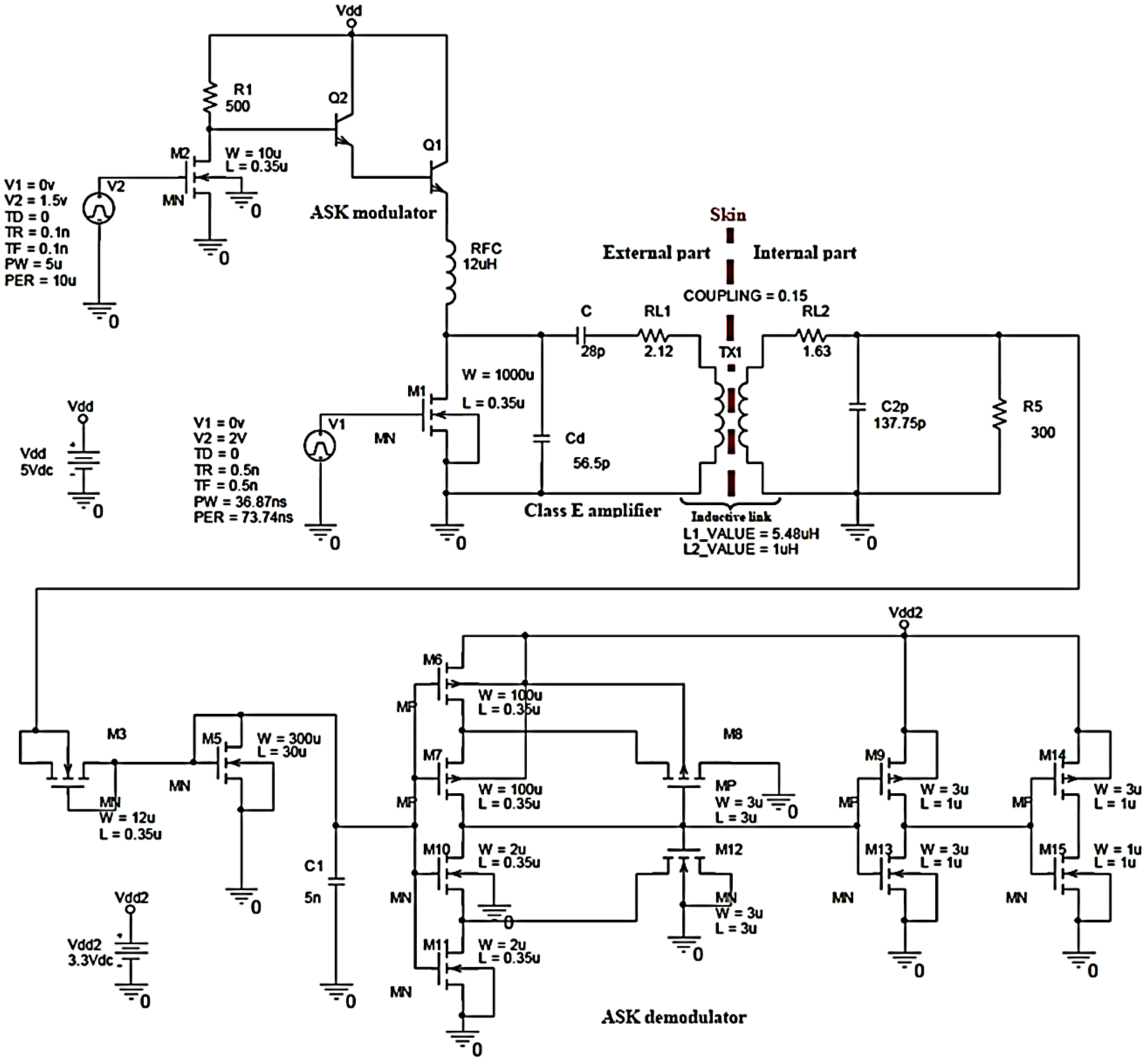

Figure 7: Wireless power and data transmission circuit for implantable bio-microsystem [291]

The system in Figure 7 makes use of an inductive coupling link comprising a single pair of coils driven at a resonance frequency of 13.56 MHz via a Class-E power amplifier. About 136 mW of power is transferred over an operating range of 15 mm with an efficiency of 50%. A data rate of 1 Mbps is achieved using an Amplitude Shift Keying (ASK) modulation scheme.

5. A microcontroller-based implantable neuromuscular stimulation system with wireless controller for data and power transmission by Liang et al [292] is shown in Figure 8.

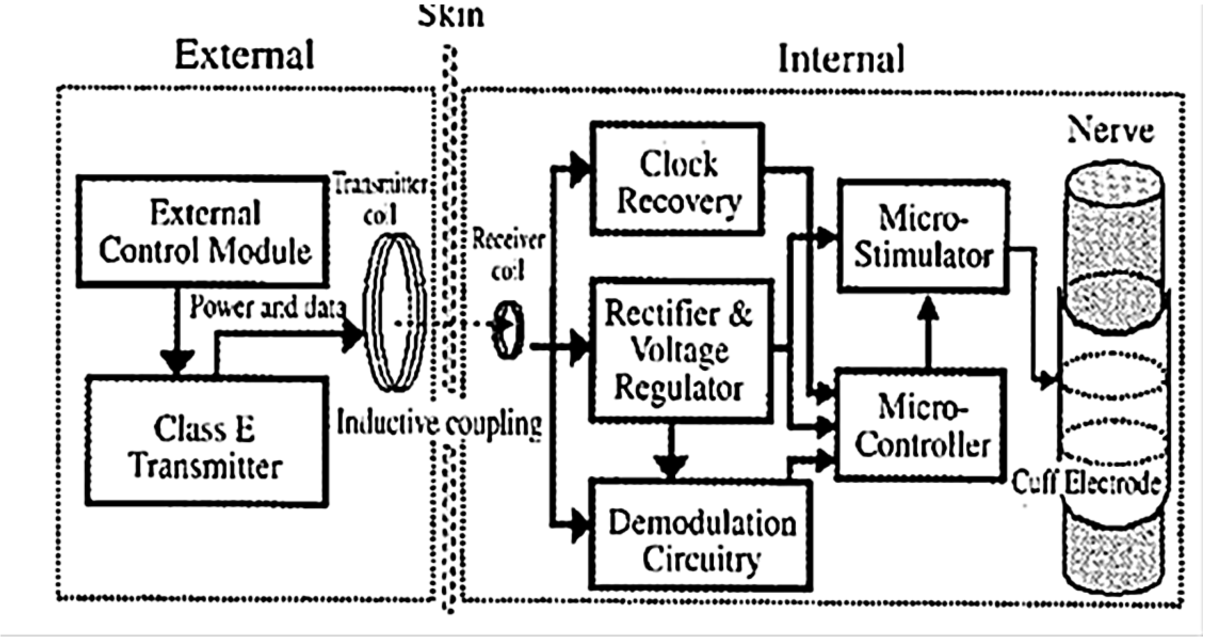

(a)

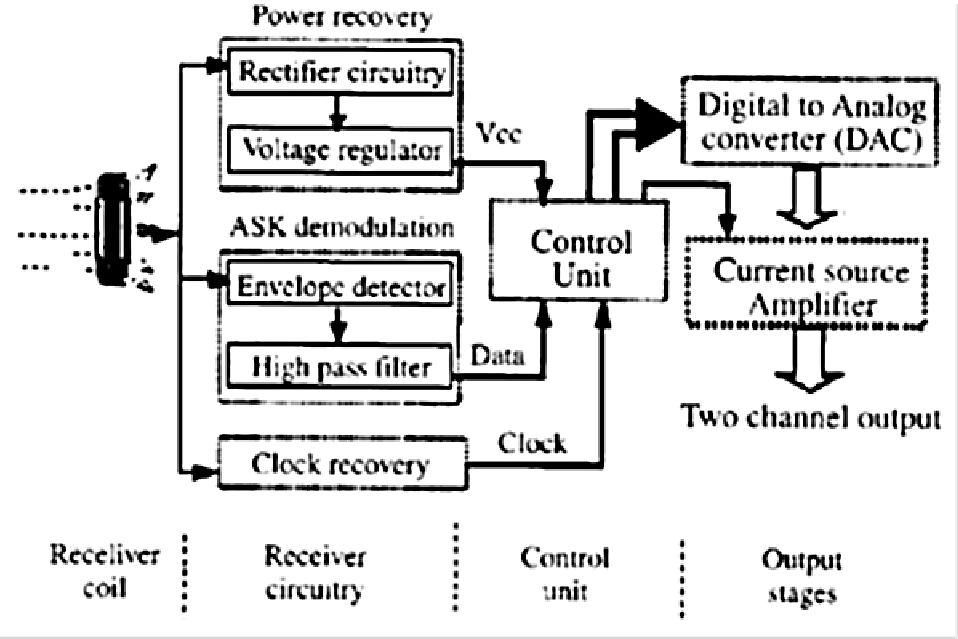

(b)

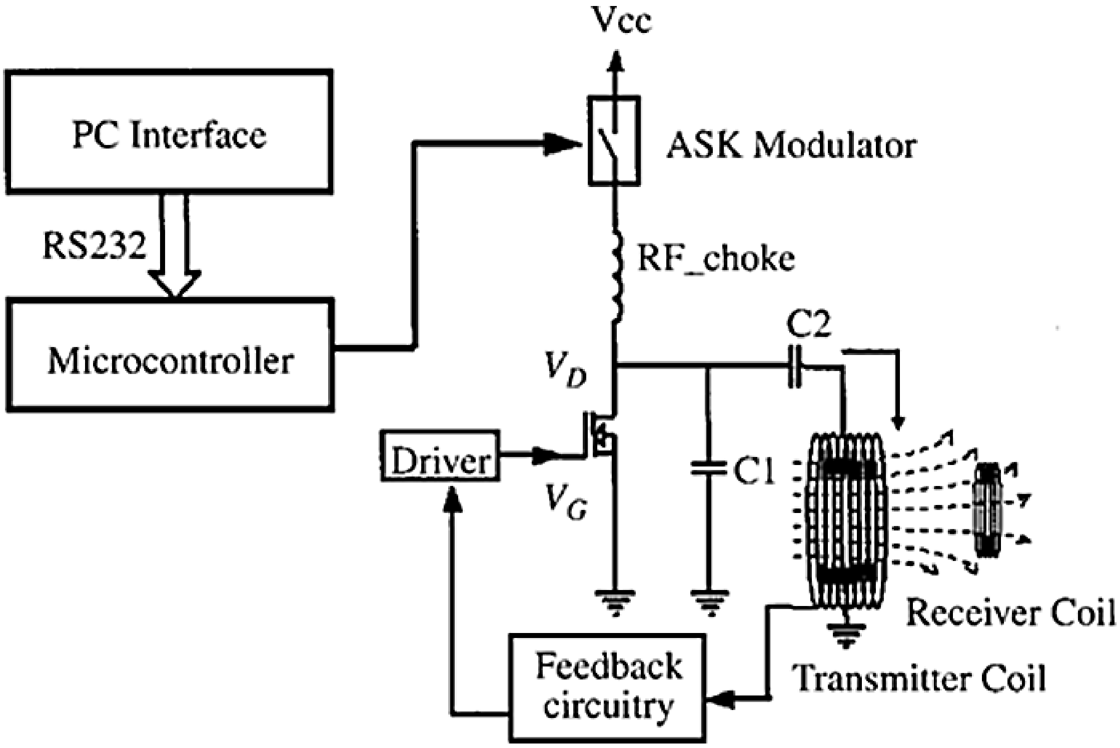

(c)

Figure 8: Microcontroller-based implantable neuromuscular stimulation system with wireless power and data transmission. (a) System block diagram (b) Implantable Microstimulator block diagram (c) External/transmitting coil schematic [292]

The system comprises a single pair of coils driven at a resonance frequency of 2 MHz via a self-oscillating Class-E power amplifier delivering about 30 mW over an operating range of 30 mm with a system efficiency of about 25%. Sensed data is transmitted using ASK modulation scheme (with 50% modulation index).

Table 2: Comparison of Inductive Coupling interface systems

Ref.	**System Specifications**	**Transmitter drive scheme**	**Data transmission scheme**	**Operating range (mm)**	**Efficiency (%)**	**Power transmitted**
289	Single pair of coils at resonance frequency of 206 kHz	Class – E power amplifier	Frequency Shift Key (FSK) modulation @ data rate of 10 Kbps	10	12.5	125 mW
293	Multi-receiving coils system comprising a single transmitting coil and three orthogonal receiving coils at resonance frequency of 1 MHz	Class – E power amplifier	Amplitude modulation @ data rate of 9.6 Kbps	N/A	N/A	> 300 mW
290	Single coil pair	N/A	Optical data link @ 1Gbps	7	70	> 1.5 W
186	Multiple planar primary coils transmitting to a single secondary coil	N/A	2.2 KHz sampling rate	N/A	N/A	~ 20 mW
294	Single coil pair fabricated using Litz wire	Class – E power amplifier	Amplitude Modulation through an RF link for bi-directional data transmission	10	N/A	Delivers 70 mA DC to implant rechargeable battery
179	Single pair of coils at resonance frequency of 7 MHz	Cross-coupled MOSFET-based differential Class-E power oscillator	Load Shift Keying (LSK)	10	74	~ 11 mW
295	Single pair of coils at	Class – E driver	N/A	10	~ 35	N/A

	resonance frequency of 10 MHz					
291	Single coil pair at resonance frequency of 13.56 MHz	Class – E power amplifier	Amplitude Shift Keying (ASK) modulation @ 1 Mbps data rate	10	50	136 mW
181	Single coil pair	Class – E power amplifier	LSK @ 3.3 Kbps data rate	15	~ 35 (with adaptive control)	~ 250 mW
292	Single pair of coils at resonance frequency of 2 MHz	Class – E power amplifier	ASK modulation (50% modulation index)	30	~ 25	~ 30 mW
296	Single coil pair at resonance frequency of 600 kHz	N/A	N/A	N/A	94	20 W

A summary of some recent inductively coupled interface designs is tabulated in Table 2. It can be noted from Table 2 that the power transferred is between 11 mW and 20 W over an operating range of between 7 mm and 30 mm with achieved transfer efficiency between 12.5% and 74%. Class-E power amplifier is the preferred transmitter drive scheme while operating resonance frequency is between 206 kHz and 13.56 MHz.

2.2.4. Ultrasonic interface design

From the 1950s, ultrasound has been applied to medicine – primarily for medical imaging. The inherent properties of ultrasound compared with RF include: it penetrates deeper inside the human body with minimal attenuation; it is free from Electromagnetic interference (EMI); minimal tissue heat dissipation; and lower operating frequency hence smaller wavelengths. This has made ultrasound a primary candidate for wireless electric power transfer for future ultra-low power implantable medical devices [201] - [203], [297] - [302]. The radiated energy from ultrasound is well suited for implants because of its low power consumption and the fact that it is safe and has no ill-effects on the human body when maintained below the FDA stipulated limits [303].

With distances between the implant microsensor and the external unit now extending beyond a few centimetres, new powering and telemetry alternatives are needed to inductive coupling power transfer because:

- It becomes impractical at operating ranges greater than several centimetres
- transfer efficiency diminishes with angular misalignment
- characteristic low coupling factor
- susceptibility to electromagnetic interference (EMI)
- selection of operating resonance frequency is limited to frequency band for medical applications
- poor efficiency [88], [304].

For implantable devices requiring low power, penetration of energy through the skin i.e. transcutaneous energy transfer by inductive coupling is enough. For power transfer in the range of tens of milli-Watts (for smart IMDs such as bio-MEMS devices) and for powering deep implantation IMDs, ultrasonic energy transfer is a preferable interface due to its compactness, electromagnetic coupling immunity and relatively high power transfer efficiency [88], [203]. The transfer of electrical energy by ultrasound pressure waves has so far been promising on account of its suitability to the predominantly liquid environment within the human body, its inherent design simplicity, and its capability to reach the penetration depths required for interfacing with deeply implantable medical devices [203]. Even though ultrasound has the above characteristics, it is lossy i.e. susceptible to attenuation when moving from one transmission medium to another. Electromagnetic energy and ultrasound have been applied in medicine, but the focus is now on the application of ultrasound for therapeutic, monitoring, powering, and communication purposes [298], [305] - [306]. Additionally, according to Yadav et al [307], ultrasonic interface systems are characterised by an order of magnitude reduction in power consumption over RF-based interface systems. It is worth mentioning that for an inductive coupling system, Bhuyan et al [308] claims that the effective operating range cannot be greater than the size of the transducer.

In an ultrasonic energy transfer interface, power is transferred by acoustic pressure waves. The external power source energizes the transmitting ultrasonic piezoelectric transducer, converting electrical energy to acoustic pressure waves which are propagated through the liquid transmission medium to the implanted piezoelectric transducer receiver. The receiver, positioned within the radiation lobe of the transmitting piezoelectric transducer, converts acoustic energy back to electrical energy for use in the implantable medical device.

Ultrasound pressure waves impinging upon a piezoelectric transducer generates an AC electrical output which can be rectified to provide DC for powering the electronic circuits of the implant or charging the implant’s rechargeable battery. The size of the piezoelectric transducer is limited to half the wavelength of the generated sound pressure wave propagating through the liquid medium [309].

The three mechanisms by which mechanical vibrations are converted to electrical energy are electromagnetic, electrostatic, and piezoelectric [310]. Lead Zirconate Titanate (PZT) devices, whether used as single crystals, ceramics or composites [311], are particularly suited for electrical power generation because their mechanical to electrical conversion efficiency is high. This high mechanical to electrical conversion is governed by: their inherent high Electromechanical coupling factor, *k*; high Piezoelectric Charge Constant, *d*; high Piezoelectric Voltage Constant, *g*; and high quality factor [312]. The Electromechanical coupling factor, *k*, indicates the effectiveness with which a piezoelectric material converts electrical energy into mechanical energy and vice versa. The Piezoelectric Charge constant, *d*, on the other hand, is the polarization generated per unit of mechanical stress (T) applied to a piezoelectric material or alternatively, is the mechanical strain (S) experienced by a piezoelectric material per unit of electric field applied. Large *d* constants relate to large mechanical displacements which are sought in motional transducer devices. The Piezoelectric Voltage constant, *g*, is the electric field generated by a piezoelectric material per unit of mechanical stress applied or alternatively, is the mechanical strain experienced by a piezoelectric material per unit of electrical displacement applied.

Generally, each piezoelectric constant has two subscripts indicating the directions of two related quantities e.g. stress (force on the ceramic element) and strain (change in the length of the element) for elasticity.

The Z-axis coincides with the direction of positive polarisation. The axes X, Y, Z are represented by the subscripts 1, 2, 3 respectively. Shear about these axes is represented by the subscripts 4, 5, 6 respectively.

PZT piezoelectric materials convert mechanical vibration into useful electrical energy via the 'piezoelectric effect' [312], [313] – [317]. The piezoelectric effect exists in two domains direct piezoelectric effect and indirect piezoelectric effect. Direct piezoelectric effect describes the property of the material to transform applied mechanical strain into electrical charge and is therefore responsible for its ability to function as a sensor. The indirect/reverse piezoelectric effect describes its property to convert an applied electrical potential into mechanical strain – accounting for its ability to function as an actuator. When a piezoelectric element is exposed to an alternating electric field its size changes in accordance to the (resonant) frequency of the driving field. In other words, it oscillates. These 'energy-carrying' pressure oscillations propagate through a (homogeneous) liquid transmission media. Piezoelectric transducers can therefore be used as a motor – where it undergoes changes in dimensions when electrically driven, or as a generator – where it produces an electrical charge when mechanically loaded.

Published literatures show PZT ceramics applied as electrical power generators when excited in their thickness/longitudinal (-33) mode (polarization and change in size is in the Z-axis). Though the planar/radial (-31) mode (polarization is in the Z-axis while change in size is lateral in the X-axis) is hardly mentioned in literature, it has been shown to exhibit the following worthwhile characteristics: it is driven at a lower resonant frequency than the 33-mode implying low power consumption; it is common in thin elements where the thickness is much smaller than the radius; it has a lower electrical/mechanical coupling than the 33-mode; it produces larger mechanical vibration output (strains) with minimum input; and has an improved radiating area ensuring maximum receiver output voltage [200], [298], [302], [310], [312], [315] – [319]. Examples of ultrasonic interface designs are described below:

1. The transfer of energy using ultrasound through the skin by Ozeri et al [203] is shown in Figure 9.

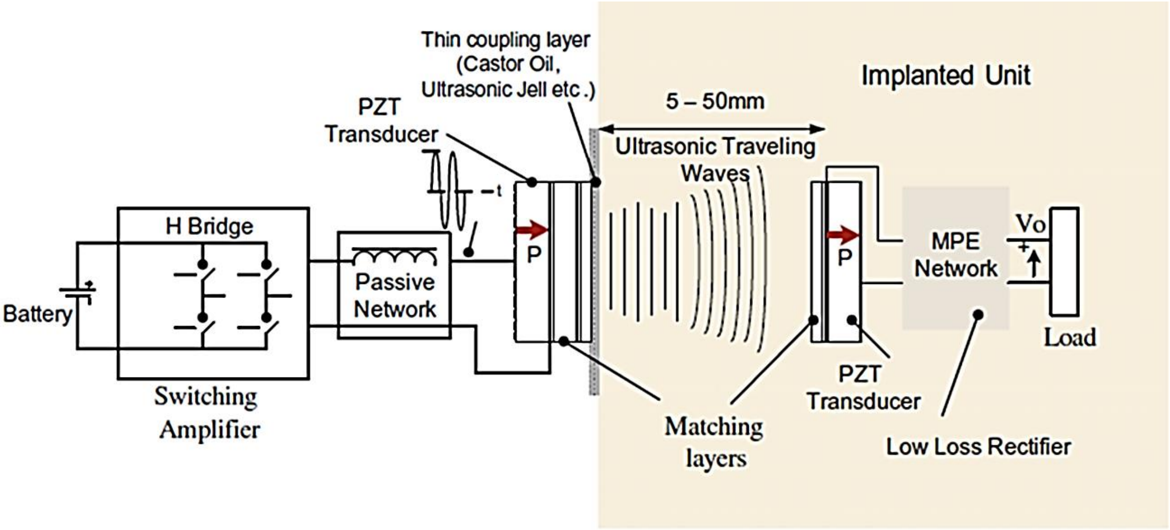

(a)

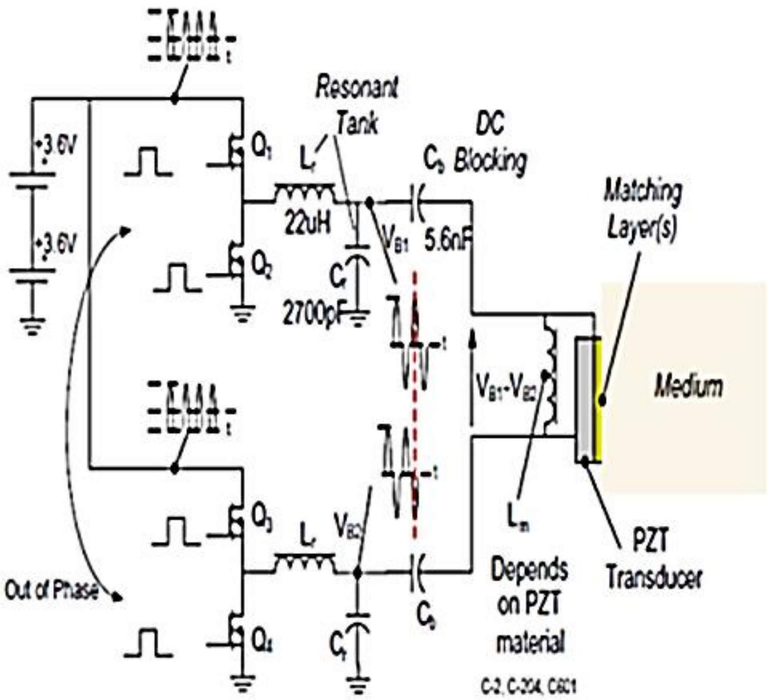

(b)

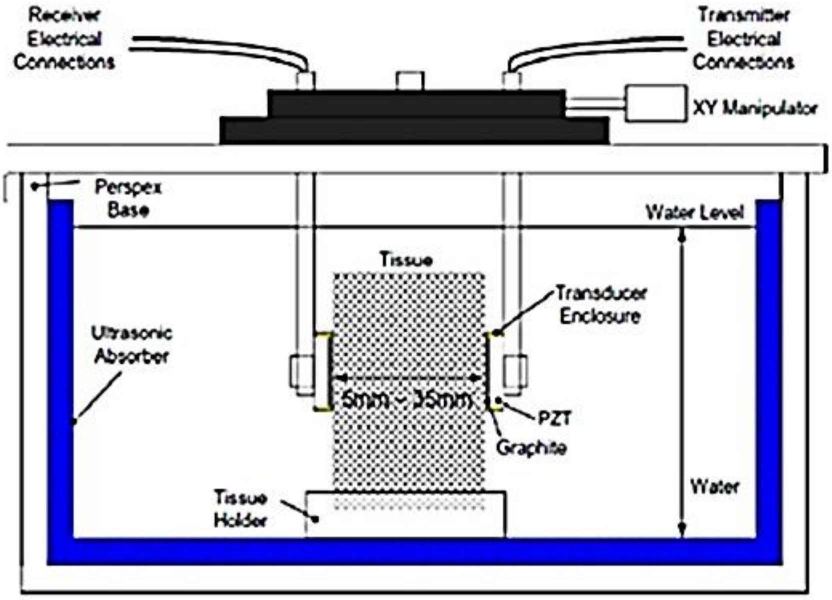

(c)

Figure 9: Ultrasonic transcutaneous energy transfer for powering implanted devices (a) UTET system (b) drive excitation circuit (c) test tank [203]

The ultrasonic transcutaneous energy transfer (UTET) interface in Figure 9a consists of a pair of disc-shaped PZT transducers immersed in a liquid media. The discs are excited in their thickness vibration mode at a resonant frequency of 673 kHz and incorporate a graphite acoustic matching layer. An output power of 70 mW is achieved for a power transfer efficiency of 27% over an operating range of 40 mm.

2. An ultrasonic power transfer system by Shigeta, Y. et al [202] is shown in Figure 10.

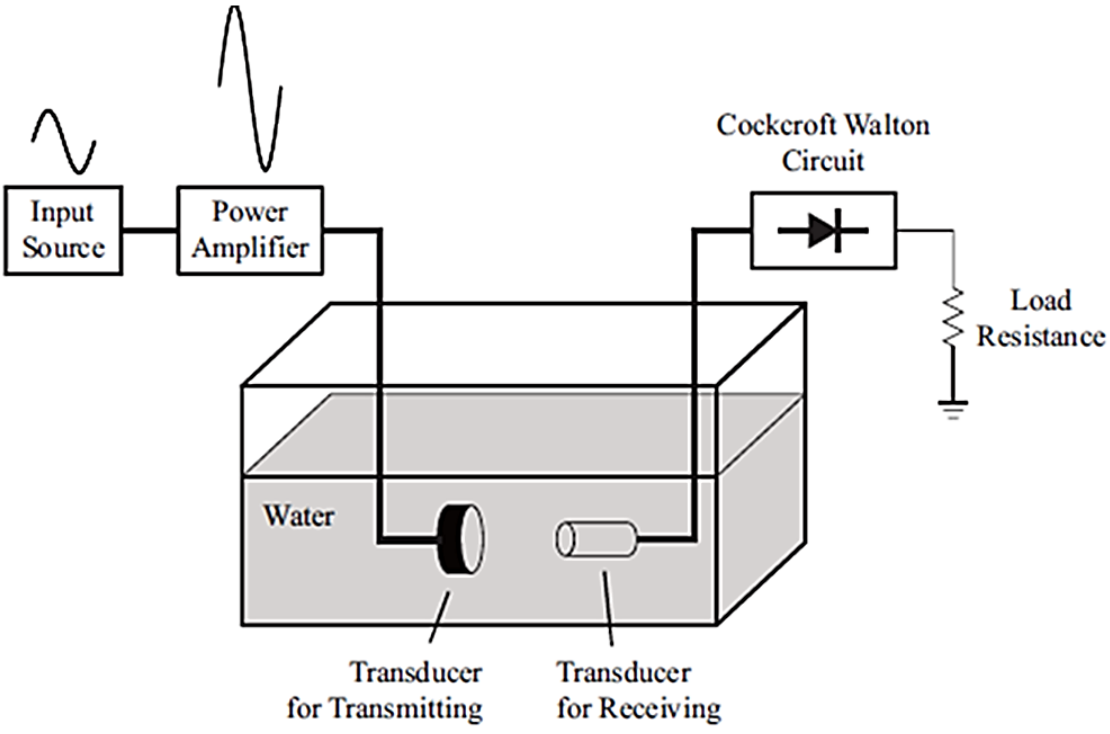

Figure 10: Ultrasonic wireless power transmission system incorporating a Cockcroft-Walton voltage rectifier and booster circuit [202]

In Figure 10, a single pair of PZT transducers, both immersed, excited at a resonant frequency of 4.2 MHz, transfer 800 µW with an efficiency of 0.39% (max) over a range of 7 cm to an implantable electronic device.

3. The power and interactive information transmission system for implanted medical devices using ultrasonics by Suzuki, S. et al [221] is shown in Figure 11.

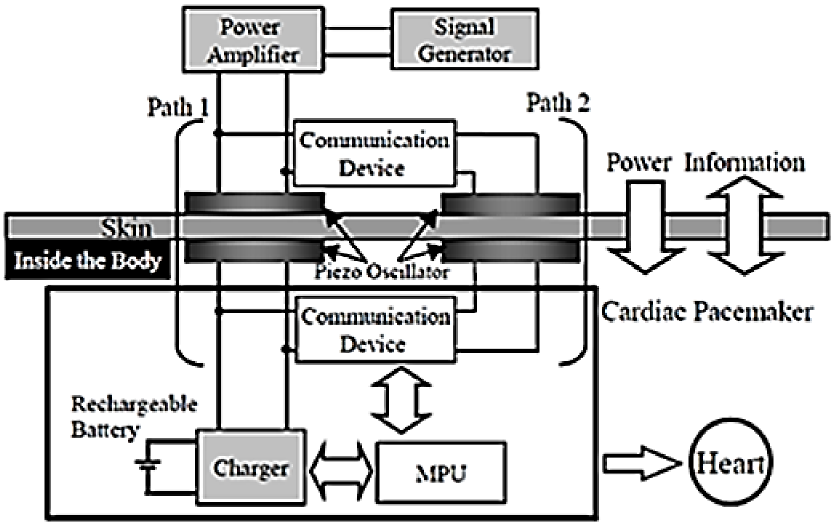

(a)

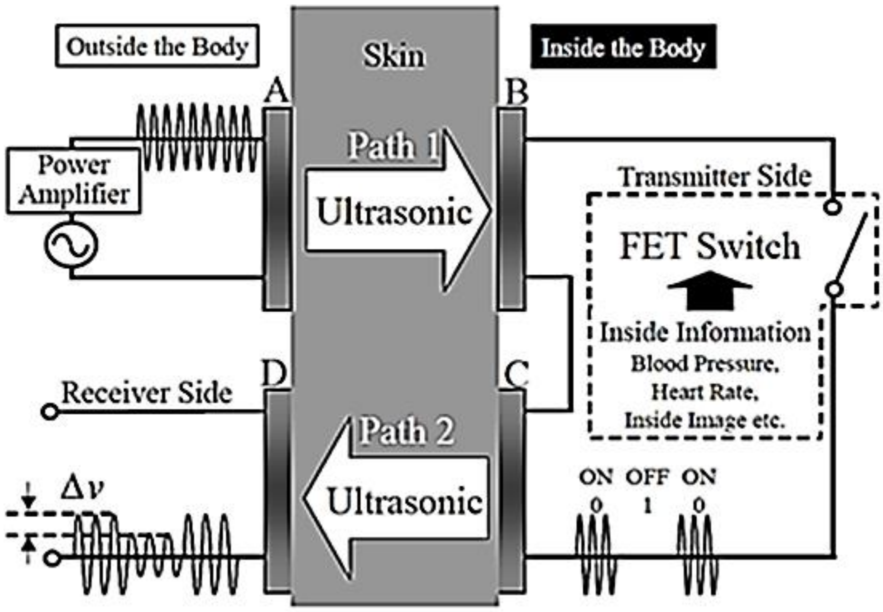

(b)

Figure 11: Ultrasonic power and interactive information transmission system (a) schematic (b) signal path [221]

The ultrasonic system in Figure 11 comprises two pairs of PZT transducers excited at a resonance frequency of 1 MHz. A pair of the transducers is situated outside while the second pair is immersed in the liquid media. A combination pair (one outside and one immersed) is used for power transfer while the other combination pair is used for data transmission. A power transfer of 2.1 W is achieved over a range of 4 cm for an efficiency of 20%. Image data is transmitted at upto 9.6 Kbps.

Table 3: Comparison of Ultrasonic interface systems

Ref.	System Specifications	Drive mode	Operating range (cm)	Efficiency (%)	Power transmitted
320	Single pair of PZT transducers at resonance frequency of 2.3 MHz	N/A	4	N/A	N/A
307	Single pair of PZT transducers in free air	N/A	86	N/A	4 µW
308	Resonant coupling system driving an ultrasonic plate at a resonant frequency of 772 KHz	Thickness vibration mode	4	48	1.26 W
309	Single pair of PZT transducers with the transmitter external. Both excited at a resonant frequency of 1 MHz	Thickness vibration mode	12	N/A	223 mW
203	Single pair of disc-shaped PZT transducers at resonance frequency of 673 KHz	Thickness vibration mode	0.4	27	70 mW
200	Single pair of PZT transducers at resonant frequency of 1.7 MHz ; incorporating matching layers	N/A	N/A	0.95	84 mW (@ 15V DC supply)
297	Two pairs of transducers; a pair for power transfer and the second for data transmission at resonant frequency of 1 MHz	N/A	50	N/A	~ 3 mW
202	Single pair of PZT	N/A	7	0.35	800 µW

	transducers both immersed @ resonant frequency of 4.2 MHz				
219	Hybrid power supply system comprising a pair of magnetostriction devices and a receiver implant PZT transducer at resonant frequency of 100 KHz	N/A	4	36	5.4 W
221	Two pairs of PZT transducers with a pair outside the skin at resonant frequency of 1 MHz and image data rate of 9.6 Kbps	N/A	4	20	2.1 W

A summary of some published ultrasonic interface designs is tabulated in Table 3. It can be noted from Table 3 that the power transferred is from 4 µW to 5.4 W over an operating range from 0.4 cm to 86 cm with achieved transfer efficiency from 0.35 % to 45 %. The preferred drive mode is thickness vibration with operating resonance frequency from 100 kHz to 4.2 MHz.

2.2.5. Discussion

Considering Tables 2 and 3 as well as the power consumption figures of ‘single-tier’ interface systems in [70], the following can be surmised:

- High overall system power consumption for single-tier systems. Typically, > 30 W for ‘single-tier’ inductive systems and between 230 mW – 1 W for ‘single-tier’ ultrasonic systems

- Average Power transfer efficiency using a Class E power amplifier drive scheme is 50% for ‘single-tier’ inductive systems

- Relatively high power transfer efficiency for ‘single-tier’ ultrasonic systems thickness mode excitation but at the expense of high power consumption

- Average effective operating range of ‘single-tier’ ultrasonic systems is 10 cm with thickness mode excitation

The implementation of a multi-tier interface system (combining inductive coupling and ultrasonics) should ensure low voltages across the tiers, consequently guarantying low total power consumption when compared to ‘single-tier’ interface systems. Additionally, this multi-tier system should provide the platform for achieving the operation range required to communicate effectively (through wireless power transfer and data transmission) with deeply implantable devices while still maintaining low total power consumption as well as comparable power transfer efficiencies across the tiers.

In summary, this chapter has covered the classifications and applications of Implantable Medical Devices (IMDs). Available interfaces for IMDs have been elaborated and their design considerations and challenges highlighted. As a result of their dominance in published literature, some ‘single-tier’ inductive coupling and ultrasonics interface designs are listed and their short-comings discussed.

3. THE 2-TIER WIRELESS INTERFACE

In the previous chapter, practical wireless power transfer and data transmission interfaces for IMDs are highlighted with emphasis on inductive coupling and ultrasonics. The shortcomings of single-tier inductive coupling and ultrasonic interfaces were discussed and the potential of a multi-tier interface were enumerated to ensure low voltages across the tiers and consequently, low system power consumption while achieving the operation range with comparable transfer efficiency.

To overcome the high power consumption of single-tier interfaces and achieve the operational range (with comparable transfer efficiency) required to interface/communicate with deeply implantable medical devices, a multi-tier interface is proposed. In this chapter, the design methodology for a multi-tier interface combining inductive coupling and ultrasonics is described. It details a proof-of-concept, novel, multi-tier power and communication interface prototype system for low-power, periodically-activated deeply implantable analog bio-sensors by combining both transcutaneous inductive coupling and ultrasonics.

Results detailed in this chapter have been published in [70 – 72].

The overall prototype interface system block diagram is shown in Figure 12.

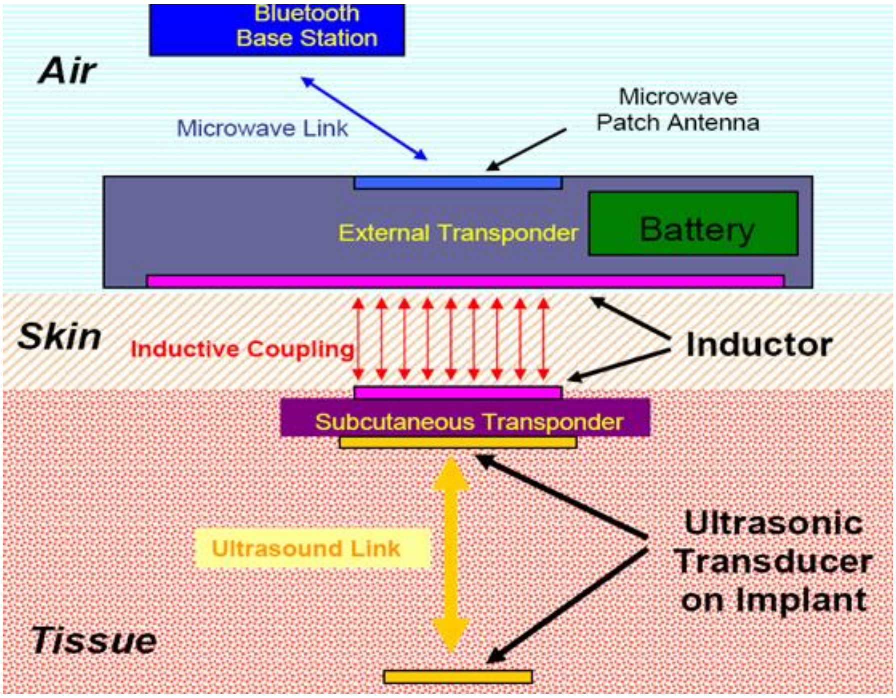

Figure 12: Prototype interface system block diagram

In Figure 12, energy from an externally worn battery is wirelessly transferred through the skin (intermittently) by a single pair of inductor coils via the well-established inductive coupling. The liquid medium in a living bio-system (humans: 60 – 70% volume) presents an effective transmission medium for ultrasonic signals.

From Figure 12, Tier 1 is the external transponder situated outside the body. It comprises the rechargeable battery pack; some form of communication unit (this is a microwave patch antenna in Figure 12); the primary inductive coil and its associated driver circuitry; and a microcontroller CPU. It can be noted in Figure 12 that the external, primary coil is rightly depicted as bigger in size than the subcutaneous, secondary coil (which is constrained by space restrictions under the skin). The communication unit has not been discussed in this report as any one of the available options – RF, infrared, optical, Bluetooth, USB 2.0 etc. - can be implemented depending on the intended application.

Energy from the external (transmitting) primary coil is transferred via Inductive coupling through the skin to Tier 2, the subcutaneous transponder. The subcutaneous transponder comprises: the secondary (receiving) coil, the envelope detection and amplifier circuit, a subcutaneous microcontroller CPU, and the primary (transmitting) piezo disc and its associated driver circuitry. The radially excited subcutaneous transmitting piezo disc propagates sound waves through the liquid medium (phantom) which is received by the deep implant (receiving) piezo disc in Tier 3. Tier 3 comprises the secondary (receiving) piezo disc, the implant microcontroller CPU, and the analog sensor. The alternating voltage output from the implant piezo disc is then rectified to power the implant CPU which in turn powers the analog sensor. The functional block diagram of the multi-tier prototype interface system is illustrated in Figure 13.

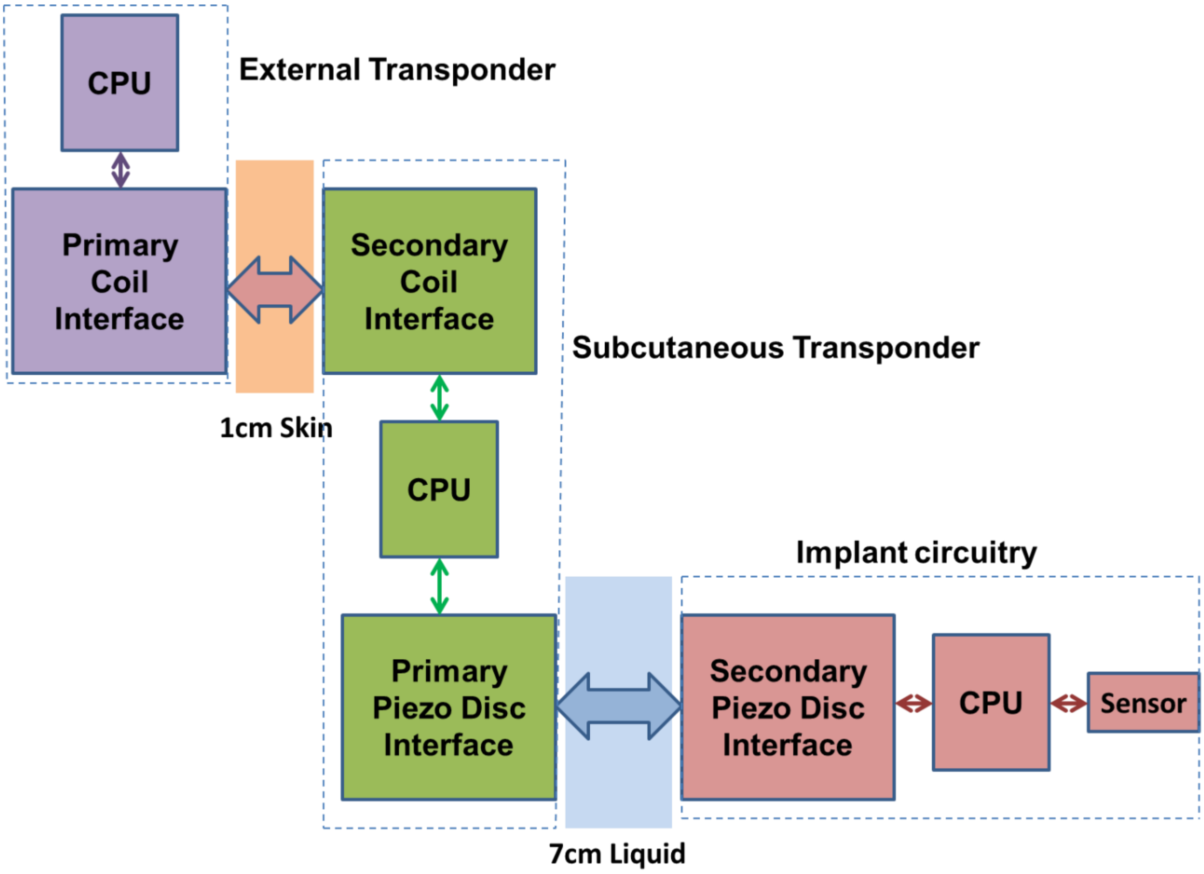

Figure 13: Prototype interface system functional block diagram

From Figure 13, during the ‘power transfer phase’, power from the external DC source (battery) is transmitted via the Primary Coil interface through the skin by inductive coupling (via mutual inductance) to the subcutaneous transponder. The subcutaneous transponder transfers this power by ultrasound energy to the implant circuitry placed 70 mm deep inside a homogeneous liquid medium (phantom). During the ‘data transmission phase’, digitized sensed data is transmitted from the (energized) implant as a burst of ultrasonic pulses via the liquid phantom and is recovered in the subcutaneous transponder. By amplitude modulation (ASK), the subcutaneous transponder transmits the reconstructed sensed data bit stream via the coil pair to the external transponder; from where, through any of the available communication's options (microwave, RF, Bluetooth etc.), it can be read or displayed.

3.1. The Ultrasonic sub-system

The block diagram of the prototype Ultrasonic sub-system is as shown in Figure 14.

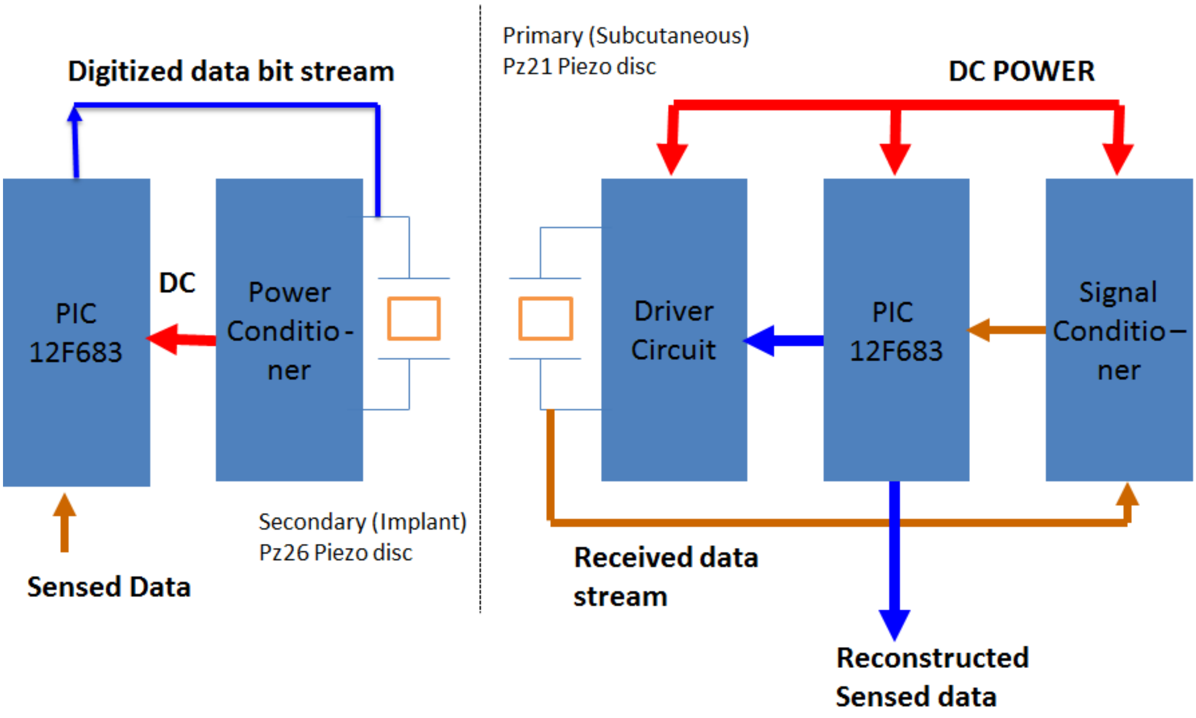

Figure 14: Prototype Ultrasonic sub-system block diagram

In Figure 14, Pz21 is the primary piezoelectric transducer while Pz26 is the secondary transducer. Red arrows in Figure 14 denote power signals; blue denotes digital data signals while brown denotes analog data signals.

The driver circuit excites the primary (subcutaneous) Pz21 disc and generates ultrasonic pressure waves by the indirect piezoelectric effect which is propagated through the liquid medium. Ultrasonic pressure waves sensed by the secondary (receiving) Pz26 disc on the implant are converted (by the direct piezoelectric effect) providing electrical power to the implant microcontroller (µC) through the power conditioner circuit. The ultrasonic pressure waves generated by the radially-excited Pz21 disc are propagated radially through the homogenous liquid phantom. The powered implant Microchip PIC 12F683 µC powers the sensor, captures its sensed analog data, digitizes it using its built-in Analog-to-Digital Converter (ADC), and then transmits the digitized bit stream as a burst of ultrasonic pulses via the same pair of piezo discs. The transmitted sensed data is reconstructed using the signal conditioning circuit.

3.1.1. Piezoelectric transducer material selection

There are several piezoelectric materials used for transducer applications as shown in Table 4 [321], but Lead Zirconate Titanate (PZT) is the more attractive material because of its inherent excellent electromechanical characteristics [322] – [325].

Table 4: Characteristics of piezoelectric materials [321]

Physical property	**Lead Zirkonate Titanate**	**Lead Titanate**	**Lead Metaniobate**	**PVDF**	**I-3 Composite**
Acoustic Impedance Z [10e^6 kg/m^{2}s]	33.7	33	20.5	3.9	9
Resonant Frequency f [MHz]	< 25	< 20	< 30	160	< 10
Coupling Coefficient (thickness mode) k_t	0.45	0.51	0.3	0.2	0.6
Coupling Coefficient (radial mode) k_p	0.58	< 0.01	< 0.1	0.12 (k_{31})	~ 0.1
Dielectric constant	1700	215	300	10	450
Maximum temperature [^{o}C]	365	350	570	80	100

PZT ceramic devices used in this research work have been supplied by Ferroperm Piezoceramics A/S, Kvistgaard, Denmark [326]. A typical material data sheet for PZT devices manufactured by Ferroperm is shown in Table 5.

Table 5: Ferroperm material data sheet for PZT devices [326]

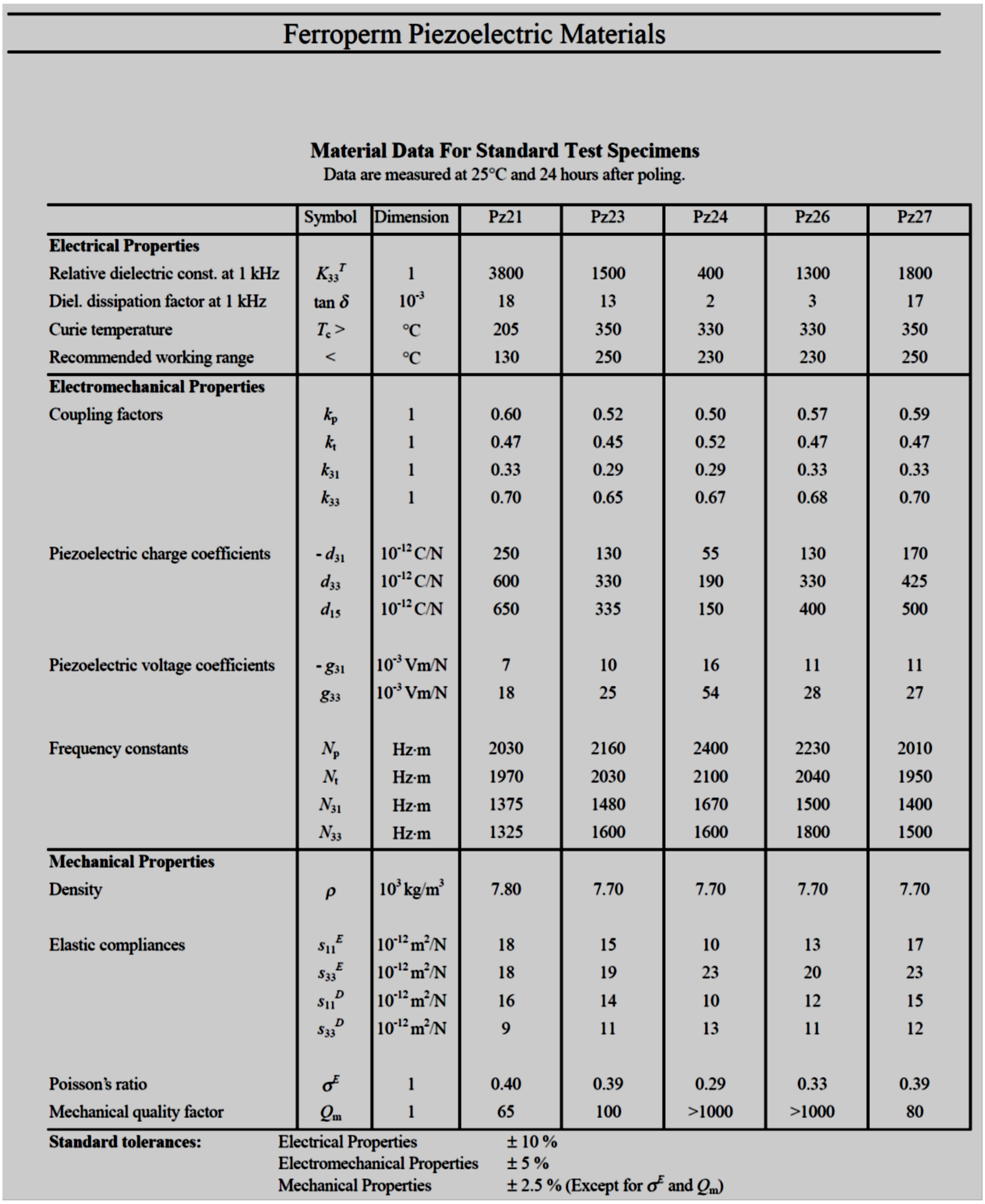

Ferroperm Piezoelectric Materials

Material Data For Standard Test Specimens

Data are measured at 25°C and 24 hours after poling.

	Symbol	Dimension	Pz21	Pz23	Pz24	Pz26	Pz27
Electrical Properties							
Relative dielectric const. at 1 kHz	K_{33}^T	1	3800	1500	400	1300	1800
Diel. dissipation factor at 1 kHz	tan δ	10^{-3}	18	13	2	3	17
Curie temperature	$T_c >$	°C	205	350	330	330	350
Recommended working range	<	°C	130	250	230	230	250
Electromechanical Properties							
Coupling factors	k_p	1	0.60	0.52	0.50	0.57	0.59
	k_t	1	0.47	0.45	0.52	0.47	0.47
	k_{31}	1	0.33	0.29	0.29	0.33	0.33
	k_{33}	1	0.70	0.65	0.67	0.68	0.70
Piezoelectric charge coefficients	$-d_{31}$	10^{-12} C/N	250	130	55	130	170
	d_{33}	10^{-12} C/N	600	330	190	330	425
	d_{15}	10^{-12} C/N	650	335	150	400	500
Piezoelectric voltage coefficients	$-g_{31}$	10^{-3} Vm/N	7	10	16	11	11
	g_{33}	10^{-3} Vm/N	18	25	54	28	27
Frequency constants	N_p	Hz·m	2030	2160	2400	2230	2010
	N_t	Hz·m	1970	2030	2100	2040	1950
	N_{31}	Hz·m	1375	1480	1670	1500	1400
	N_{33}	Hz·m	1325	1600	1600	1800	1500
Mechanical Properties							
Density	ρ	10^3 kg/m^3	7.80	7.70	7.70	7.70	7.70
Elastic compliances	s_{11}^E	10^{-12} m^2/N	18	15	10	13	17
	s_{33}^E	10^{-12} m^2/N	18	19	23	20	23
	s_{11}^D	10^{-12} m^2/N	16	14	10	12	15
	s_{33}^D	10^{-12} m^2/N	9	11	13	11	12
Poisson's ratio	σ^E	1	0.40	0.39	0.29	0.33	0.39
Mechanical quality factor	Q_m	1	65	100	>1000	>1000	80

Standard tolerances:		
	Electrical Properties	± 10 %
	Electromechanical Properties	± 5 %
	Mechanical Properties	± 2.5 % (Except for σ^E and Q_m)

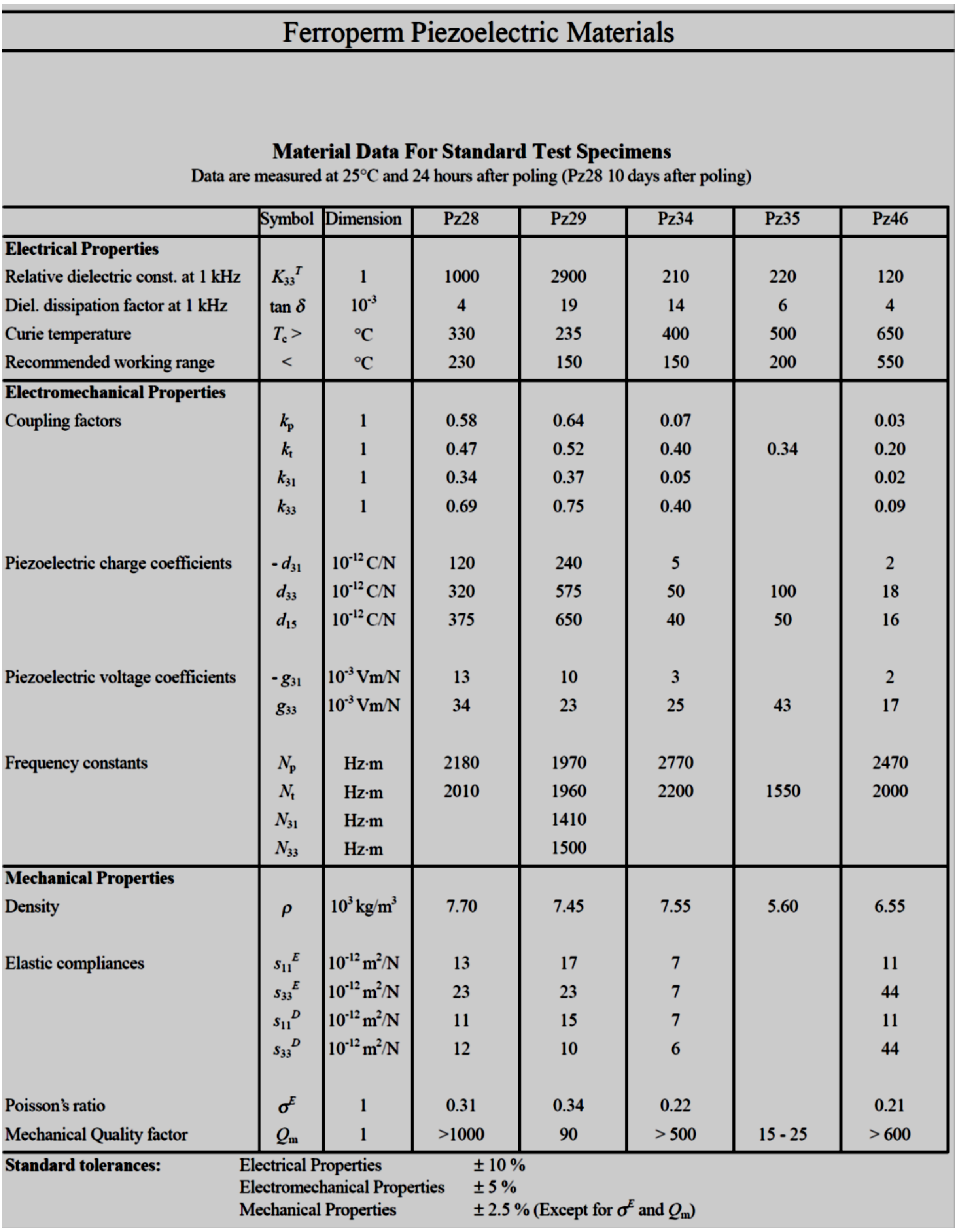

Ferroperm Piezoelectric Materials

Material Data For Standard Test Specimens

Data are measured at 25°C and 24 hours after poling (Pz28 10 days after poling)

	Symbol	Dimension	Pz28	Pz29	Pz34	Pz35	Pz46
Electrical Properties							
Relative dielectric const. at 1 kHz	K_{33}^{T}	1	1000	2900	210	220	120
Diel. dissipation factor at 1 kHz	tan δ	10^{-3}	4	19	14	6	4
Curie temperature	$T_c >$	°C	330	235	400	500	650
Recommended working range	<	°C	230	150	150	200	550
Electromechanical Properties							
Coupling factors	k_p	1	0.58	0.64	0.07		0.03
	k_t	1	0.47	0.52	0.40	0.34	0.20
	k_{31}	1	0.34	0.37	0.05		0.02
	k_{33}	1	0.69	0.75	0.40		0.09
Piezoelectric charge coefficients	$-d_{31}$	10^{-12} C/N	120	240	5		2
	d_{33}	10^{-12} C/N	320	575	50	100	18
	d_{15}	10^{-12} C/N	375	650	40	50	16
Piezoelectric voltage coefficients	$-g_{31}$	10^{-3} Vm/N	13	10	3		2
	g_{33}	10^{-3} Vm/N	34	23	25	43	17
Frequency constants	N_p	Hz·m	2180	1970	2770		2470
	N_t	Hz·m	2010	1960	2200	1550	2000
	N_{31}	Hz·m		1410			
	N_{33}	Hz·m		1500			
Mechanical Properties							
Density	ρ	10^3 kg/m^3	7.70	7.45	7.55	5.60	6.55
Elastic compliances	s_{11}^{E}	10^{-12} m^2/N	13	17	7		11
	s_{33}^{E}	10^{-12} m^2/N	23	23	7		44
	s_{11}^{D}	10^{-12} m^2/N	11	15	7		11
	s_{33}^{D}	10^{-12} m^2/N	12	10	6		44
Poisson's ratio	σ^E	1	0.31	0.34	0.22		0.21
Mechanical Quality factor	Q_m	1	>1000	90	> 500	15 - 25	> 600

Standard tolerances:

	Electrical Properties	± 10 %
	Electromechanical Properties	± 5 %
	Mechanical Properties	± 2.5 % (Except for σ^E and Q_m)

Table 5 is a typical Ferroperm material data sheet for a range of manufactured PZT transducer devices. Of the properties listed in Table 5, the following are worth mentioning:

i. Electromechanical coupling factor, *k* – an indicator of the effectiveness (not efficiency) with which a piezoelectric material converts electrical energy into mechanical energy or vice versa
ii. Piezoelectric charge constant, *d* – a measure of the electric charge induced in response to a mechanical stress or the achievable mechanical strain when an electric field is applied. It indicates a materials suitability for actuator applications
iii. Piezoelectric voltage constant, *g* – defines the ratio of electric field strength to effective mechanical. It is important for assessing a materials suitability for sensing (sensor) applications
iv. Permittivity or dielectric constant, ε - dielectric displacement per unit electric field. It is a measure of the polarizability of the material. The relative dielectric constant, K is the ratio of ε relative to the absolute dielectric constant, ε_0 (= 8.85 x 10^{-12} Farad/m)
v. Elastic compliance, *s* – the strain/deformation produced in a piezoelectric material per unit of stress applied
vi. Mechanical Quality factor, Q_m – characterizes the “sharpness of the resonance” of a piezoelectric resonator

3.1.2. Immersible PZT transducer probe configuration

The prototype Ultrasonic sub-system is built around a single pair of completely immersed Ferroperm-supplied [326] piezoelectric PZT transducer ceramic discs. The technical specifications of the Pz21, Pz24, Pz26, Pz27, and Pz54 transducers used in this research work are listed in Table 6.

Table 6: Piezoelectric transducer discs technical specifications

Type	**Pz21**	**Pz24**	**Pz26**	**Pz27**	**Pz54**
Diameter (mm)	10	10	10	10	15
Thickness (mm)	1	1	1	1	1
Hardness	Soft relaxor	Hard	Hard	Soft	-
Relative Dielectric Constant K_{33}^{T}	3800	400	1300	1800	2800
Coupling Coefficient, k_p	0.6	0.5	0.57	0.59	0.59
Coupling Coefficient, k_{31}	0.33	0.29	0.33	0.33	-
Piezoelectric Charge Coefficient, -d_{31}	260 pC/N	58 pC/N	130 pC/N	170 pC/N	180 pC/N
Mechanical Quality Factor, $Q_{m,p}$	65	> 1000	> 1000	80	1500
Density, ρ	7.8 g/cm^3	7.7 g/cm^3	7.7 g/cm^3	7.7 g/cm^3	7.8 g/cm^3
Piezoelectric Voltage Coefficient, -g_{31}	0.0074 Vm/N	0.0154 Vm/N	0.0109 Vm/N	0.017 Vm/N	-
Measured Capacitance	2.43 nF	584 pF	850 pF	350 pF	3.3 nF
Measured Impedance	1 KΩ	650 Ω	800 Ω	500 Ω	170 Ω

Measured and manufacturer-supplied technical specifications for the transducers used are listed in Table 6. A Fluke PM6303A Auto RCL meter is used to measure the capacitance and impedance of prepared immersible transducer disc probes.

From Table 6, the following can be inferred:

- A high planar electromechanical coupling factor, k_p of 0.6 coupled with a high Relative dielectric constant, K of 3800 makes the Pz21 transducer suitable for use as a transmitter compared with the other transducers

- Though the Pz24 and Pz26 transducers both have a mechanical quality factor, Q_m of >1000, its higher Piezoelectric charge coefficient, d_{31} of 130, makes the Pz26 a better receiver. Additionally, the electromechanical coupling factor, k_p of 0.57 of the Pz26 makes it a compatible pair with the Pz21 transducer having a k_p of 0.6.

A piezoelectric transducer disc consists, in its simplest form, of a disc of PZT material coated with thin (< 1 mm) silver electrode layers. One of the prepared immersible PZT transducer probes used in this work is shown in Figure 15.

Figure 15: Immersible PZT transducer disc probe

From Figure 15 it can be noted that the probe consists of semi-rigid RG75, 50 Ω screened coaxial cable soldered on one end to the PZT disc and an SMA connector on the other end.

Immersed PZT discs are characterised by Frequency response, Transfer function, and Transient response [327]. The following sections will outline the measured characteristics of the prepared immersible probes under these headings.

3.1.3. Immersible PZT probe Frequency response characteristics

Connecting, one at a time, each of the prepared immersible probes (as shown in Figure 15) to a Rhode & Schwarz ZVL Vector Network Analyzer (VNA) produced plots of impedance magnitudes over a range relevant to the discs’ two prominent resonant modes – radial/planar @ 200 kHz and thickness @ 1 MHz. The VNA impedance magnitude plots for the Pz27 and Pz21 immersible disc probes are shown in Figures 16 and 17 respectively.

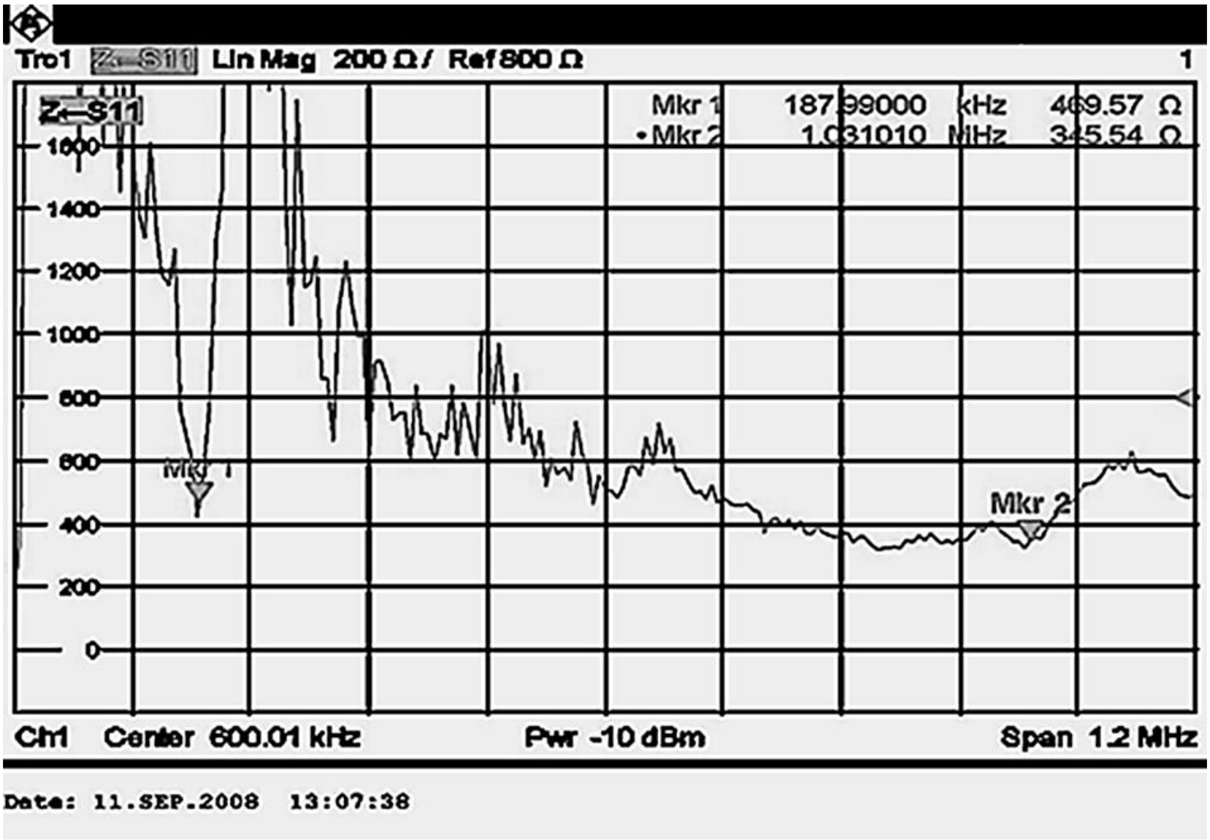

Figure 16: VNA impedance magnitude plot of Pz27 disc probe

Figure 17: VNA Impedance magnitude of Pz21 disc probe

It can be noted from Figures 16 and 17 that the two prominent resonant frequencies, designated by markers Mk 1 and Mk 2, are 200 kHz and 1 MHz. The VNA traces shown in both Figures 16 and 17 have horizontal axes denoting frequency in MHz while the vertical axes denote impedance in Ohms. Additionally, from Figure 16, the impedance magnitude of the Pz27 disc probe at 188 kHz is 470Ω and 350 Ω at 1.1 MHz; while from Figure 17, the impedance magnitude of the Pz21 disc probe at 188 kHz is 300 Ω and 170 Ω at 1 MHz - comparable to measured values in Table 6.

3.1.4. Transient response characteristics of immersible probes

To determine the transient response characteristics of the prepared immersible PZT disc probes, propagation tests involving a liquid phantom were carried out.

3.1.4.1. Propagation tank test

The propagation test setup shown in Figure 18 consists of a plastic tank measuring 60 cm in length, 40 cm in width, and 15 cm in depth with 5 cm holes drilled in its lid to accommodate the immersible probes (shown in Figure 16).

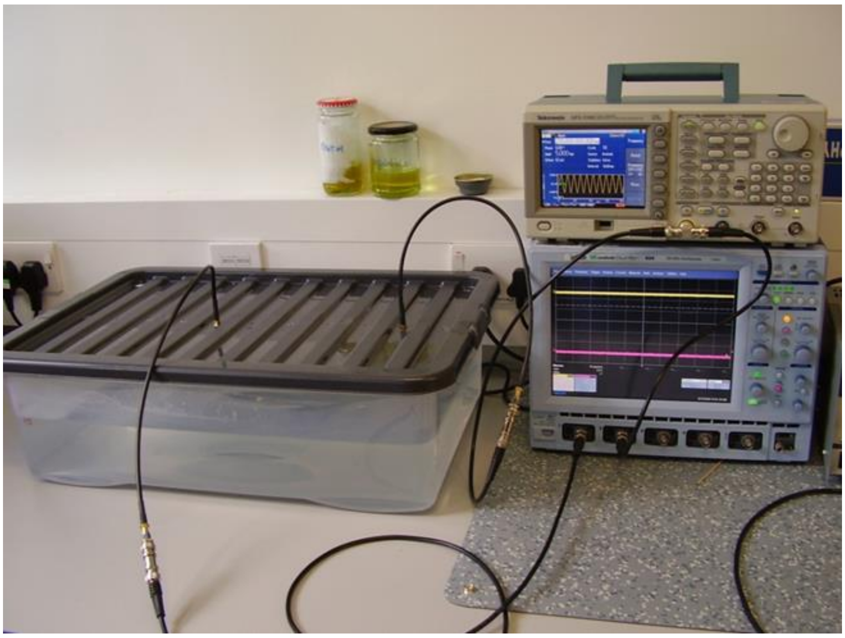

Figure 18: Initial propagation tank experimental setup

The tank is filled with a liquid (phantom) and tests carried out using different materials including water, De-Ionised (DI) water, olive oil, rapeseed oil, and polysaccharide gel (agar) at room temperature (23^{o}C).

Agar consists of 8.5% glycerol to water mix [328] – [331]. Experimental tests involved immersing a pair of disc probes directly facing each other in the phantom. The pair of disc probes was a combination from the list in Table 6.

Table 7: Measured phantom material characteristics

Phantom material	Transient signal time (µs/cm)	Received voltage (mV)
Water	15	69
Olive oil	16	76
Rapeseed oil	16	65

Results of transient signal time and received voltage for water, olive oil and rapeseed oil phantoms are tabulated in Table 7. Note that, compared to the average transit time in blood of 1576 m/s, the measured average transient signal time of 16 µs/cm = 625 m/s is low. Therefore, the phantom materials of water, olive oil and rapeseed oil were discarded.

The transmitting disc probe was powered directly from a Tektronix AFG 3102 dual-channel function generator set to output a burst of ten (10), 10 V_{p-p} sine-wave cycles every 10 ms. The 10 ms repeat rate was selected because it was observed that reverberations at the drive resonance frequency of 200 kHz took 4 ms to fade within the tank. Alternatively, the duty cycle can be numerically calculated using Equations (1) to (3) [332]:

$$V_{rms} = \frac{1}{2}\sqrt{2}V_{p-p} \quad (1)$$

$$\text{Duty cycle} = \frac{Z*P_{tot}}{(V_{rms})^2*Cos(phase\ angle)} \quad (2)$$

$$\text{Cycles per burst} = (Freq.) * (Duty\ cycle) * Rep\ rate \quad (3)$$

Where: $V_{p-p} =$ peak-to-peak voltage

Z = impedance of the transducer @ resonance frequency

Freq. = operating resonance frequency

P_{tot} = 0.125 W; which is the maximum recommended value for any transducer

Phase angle and Rep. rate are provided by the manufacturer

The drive frequencies are 200 kHz to drive the transmitter in its planar/radial mode and 1 MHz to drive the transmitter in its thickness mode. The receiver disc was oriented to face the transmitter and was connected directly to one of the 1 MΩ AC inputs of a Lecroy Wavesurfer 434 Oscilloscope. The signal generator was also connected to another input of the oscilloscope via a BNC T-junction. For driving purposes, high-voltage, short duration spikes across the PZT discs cause it to oscillate across its entire bandwidth. This is less efficient than a direct sinusoidal drive at one of its fundamental resonant frequencies (i.e. its lowest impedance point). In practice it was observed that burst continuous wave (CW) was the best way to drive the PZT discs in order to maximize received signals whilst not overloading our drive electronics. Figure 19 is the 'oscilloscope-captured' transient response trace for a pair of immersible disc probes placed 35 cm apart and driving the transmitter at a resonant frequency of 200 kHz.

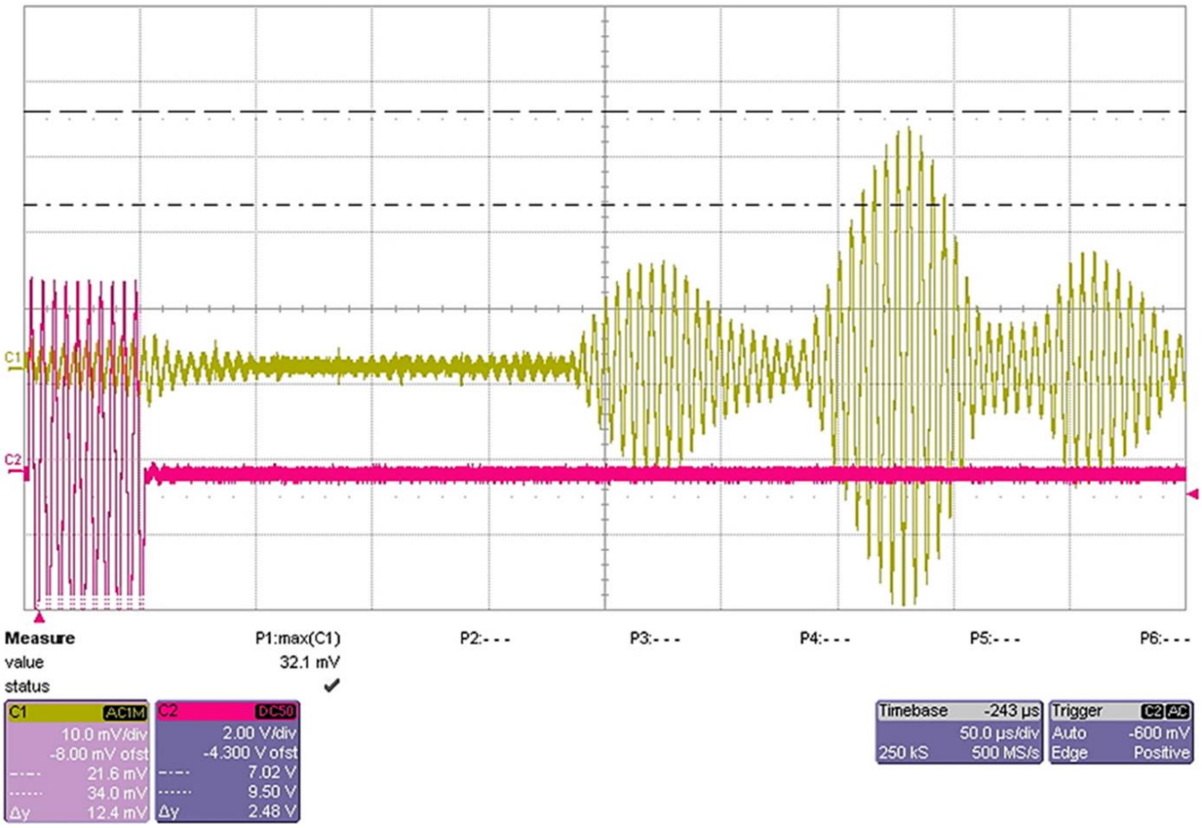

Figure 19: Oscilloscope trace of transient response

The ‘oscilloscope-captured’ trace in Figure 19 represents measurements for a 200 kHz – driven Pz21 transmitter disc probe directly aligned (face-to-face) with a Pz26 receiving disc probe placed 35 cm away from the transmitter. The horizontal axis of the trace in Figure 19 denotes propagation delay in µs while the vertical axis denotes voltage. Trace C2, the red signal, in Figure 19, is the signal recorded across the transmitting disc probe and corresponds to the ten sinewave 10 $V_{p\text{-}p}$ driving burst signal. Trace C1, the green signal, shows a peak output of 65 $mV_{p\text{-}p}$ at the receiver beginning 240 µs after the start of the burst driving signal. The 30 $mV_{p\text{-}p}$ signals on either side of the peak are as a result of reverberations and reflections within the tank.

3.1.4.2. Signal absorption (voltage attenuation) within DI Water phantom

Using the experimental setup described in section 3.1.4.1, signal absorption rates were tabulated for each resonant frequency over a range of distances between probes immersed in DI water as shown in Figure 20.

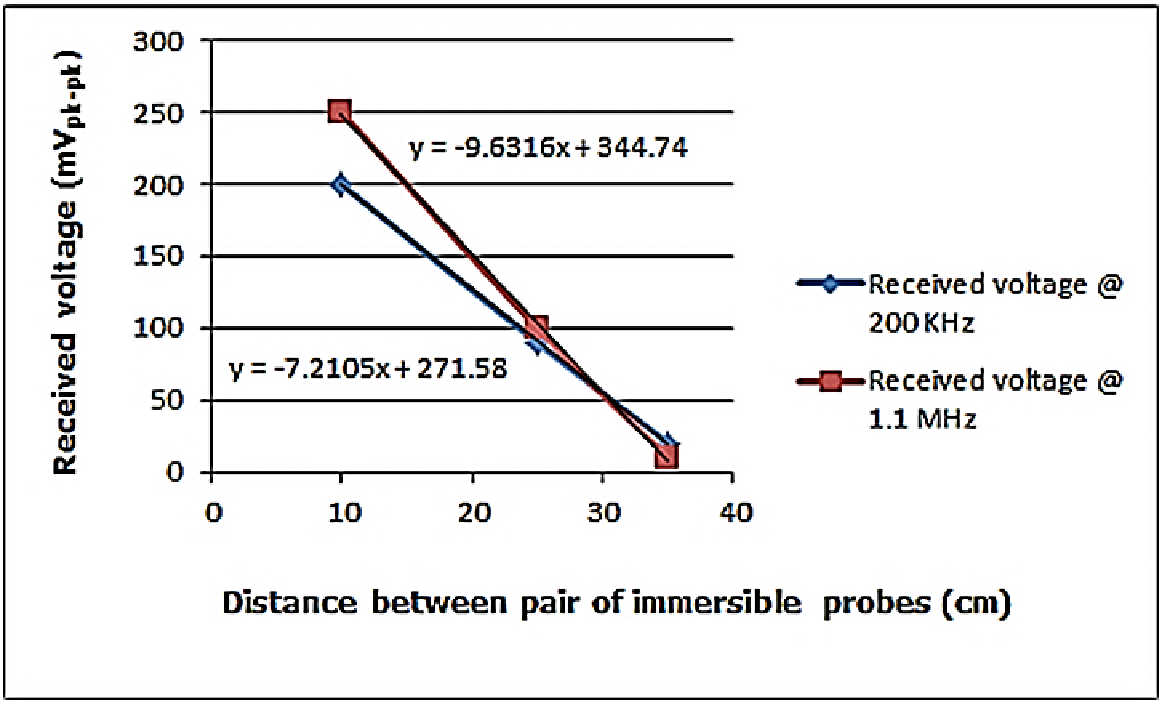

Figure 20: Voltage attenuation in phantom versus distance between disc probes

To minimize effects of reflections, measurements were taken for distances between the probes from 10 cm to 35 cm. The slopes from Figure 20 for the DI Water phantom are: 9.6 mV/cm @ 1.1 MHz and 7.21 mV/cm @ 200 kHz. With an impedance of 300 Ω @ 200 kHz and 180 Ω @ 1.1 MHz for the transmitting Pz21 immersible probe, the power loss between two points on the graph is calculated using P = V^2/X_r, where X_r is the impedance of the device.

From Figure 20, power received at 20 cm and 200 KHz = 0.1252/300 = 52.1 µW while power at 30 cm and 200 kHz = 0.052/300 = 8.4 µW. This gives a power loss over 10 cm of 10Log (8.4/52.1) = 7.9 dB or 0.79 dB/cm.

From Figure 20, power received at 20 cm and 1.1 MHz = 0.152/180 = 125 µW while power at 30 cm and 1.1 MHz = 0.0552/180 = 16.8 µW. This gives a power loss over 10 cm of 10Log (16.8/125) = 8.7 dB or 0.87 dB/cm.

3.1.4.3. Transit time within DI Water phantom

Using the experimental setup described in section 3.1.4.1, transit times within the DI Water phantom were tabulated for each resonant frequency over a range of distances between probes as shown in Figure 21.

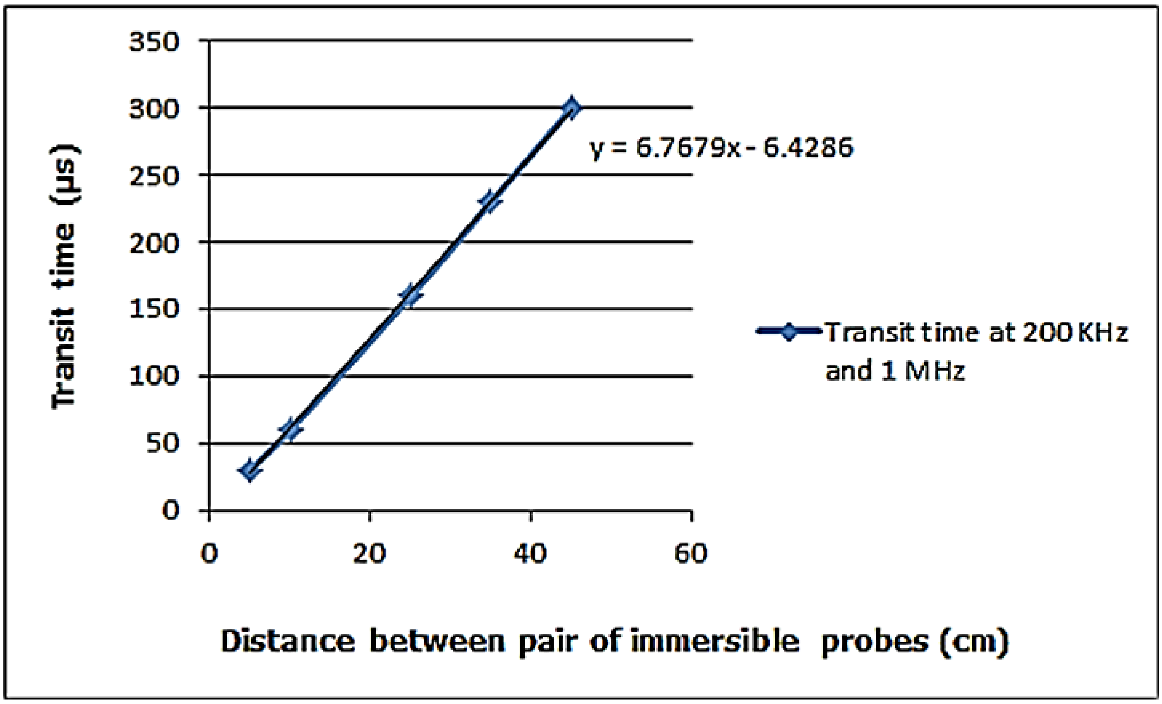

Figure 21: Transient time in phantom versus distance between probes

From Figure 21, the average transit time in DI Water is: (230-160)/10 = 7 µS/cm = 1429 m/s. A summary of the acoustic characteristics of the DI Water phantom compared with human blood are shown in Table 8.

Table 8: Measured DI water phantom characteristics compared with blood

	DI Water Phantom, 23°C	**Human blood, 37°C**
Propagation speed (m/s)	1429	1576
Attenuation (dB/cm)	0.8	0.09

Measurements using agar (with no dispersants) showed similar acoustic properties to that obtained for DI Water. The propagation tests show that DI Water and Agar have mean acoustic properties similar to those of liquid blood at frequencies of 200 kHz and 1 MHz as tabulated in Table 8. It can be noted from Table 8 that the propagation speed in DI water (and Agar) is 10% greater in blood [333] – [334]. Also, from Figure 20, an attenuation of 0.8 dB/cm for DI water (and Agar) is 10 times more than blood – making it safe to use DI water as a 'worst case' phantom. To improve the attenuation of DI Water and Agar, methods are detailed in [335] - [336].

3.1.4.4. Selection of operating resonance frequency

Using the propagation test set-up described in section 3.1.4.1 with a combination of Pz27* to Pz21, Pz27* to Pz27, Pz21 to Pz21, and Pz21 to Pz27 immersible disc probe pairs; measured output are shown in Figure 22 for resonance frequency of 200 kHz and 1.1 MHz. The * denotes that the transmitting immersible disc probe has been fitted with a 1/4λ Dural disc glued to its forward surface. Input transmitter drive is a burst of 10 V $_{p\text{-}p}$ every 10 ms.

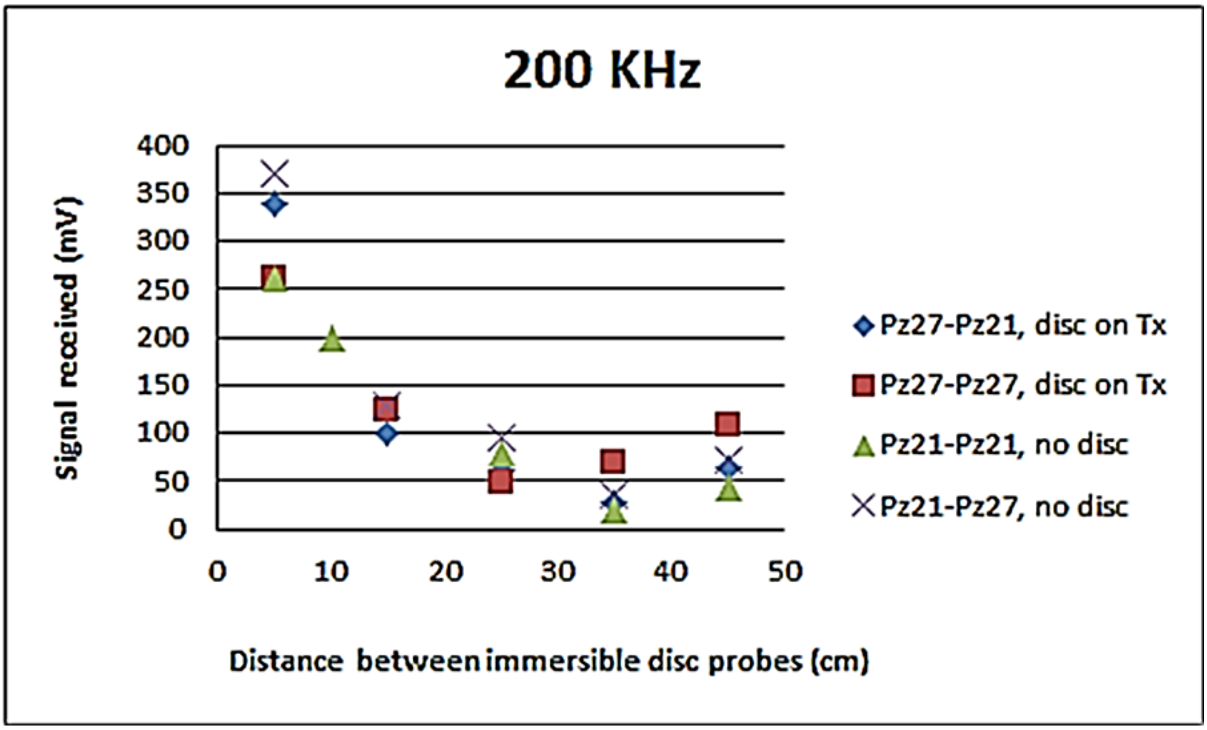

(a)

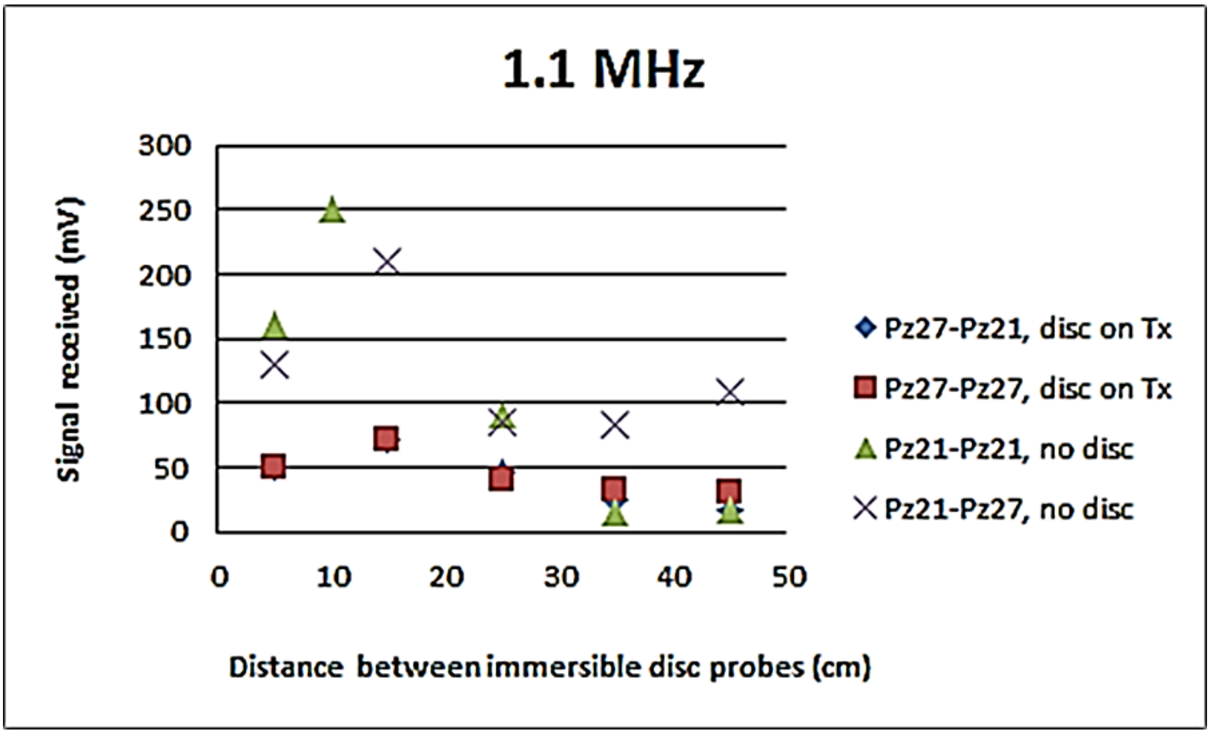

(b)

Figure 22: Received (incident) signal vs. distance between probes (a) at 200 kHz and (b) at 1.1 MHz

Figure 22 shows the voltage received for combination pairs of immersible disc probes at resonance frequency of 200 kHz and 1.1 MHz. It can be noted from the two graphs in Figure 22 that a peak voltage of 360 mV is received for a resonance frequency of 200 kHz compared to 250 mV for 1.1 MHz. This implies that the transducer discs tested exhibit better performance when excited in their radial/planar (-31) mode. Also, the peak voltages received are within short distances between the probes, implying that the effective operation range of the transmitting discs tested is between 1 cm and 10 cm. Additionally, it can be observed that a combination pair consisting of different devices offers better performance at 200 kHz; possibly due to the differences in operating impedance of each.

The presence of the impedance matching 1/4λ Dural disc hindered performance rather than enhancing it due to the lack of a backing medium for the transmitting device to resonate against.

There is also a noticeable peaking of output signal with respect to distance at 1.1 MHz varying between 10 cm and 15 cm depending on the immersible disc probe combination pair used. Such peaking is not evident at 200 kHz and it is suspected that this is due to an increase in focusing that takes place when the disc resonates in the thickness (1.1 MHz) mode.

The measurements furthest in distance between probes and nearest the tank edges can be seen from the graphs to still be affected by reverberations at lower frequency but less so at 1.1 MHz.

3.1.5. Transfer function characteristics of immersible PZT probes

Figure 23 represents plots of the output voltage across the receiving immersible disc probe placed 10 cm away from the transmitting immersible disc probe with varying transmitter input excitation voltage.

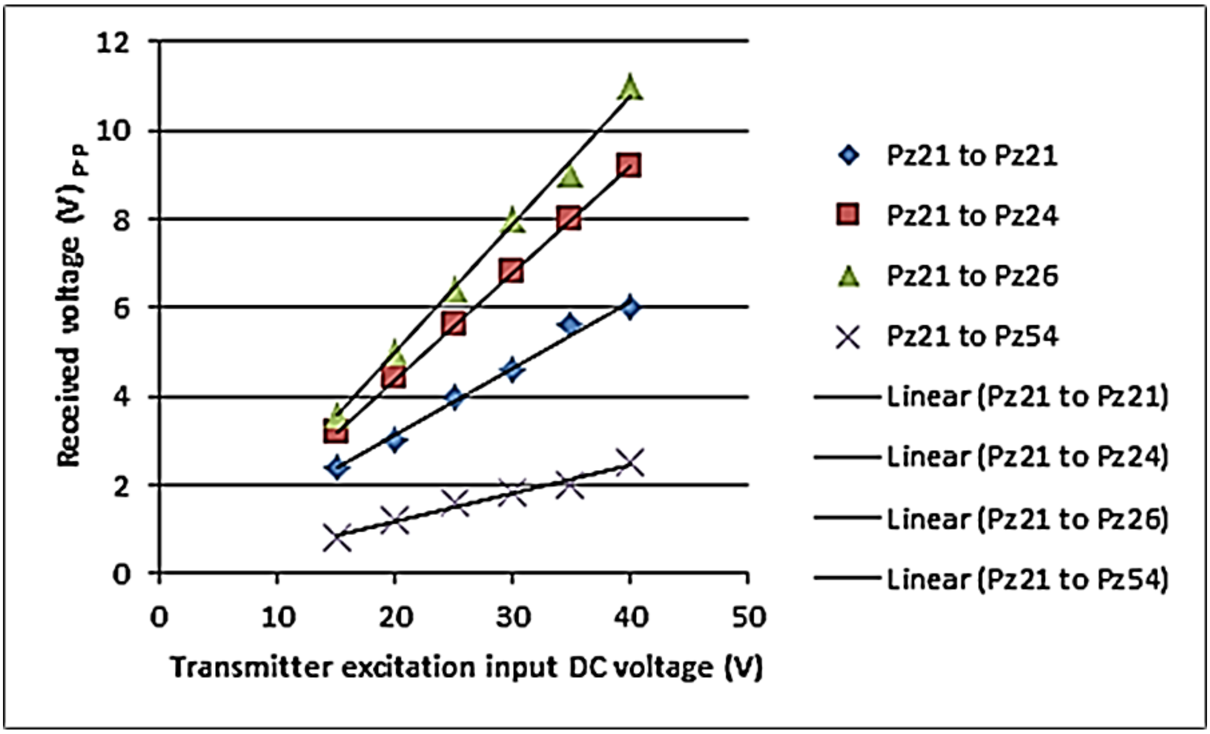

Figure 23: Transmitting immersible probe excitation drive input voltage vs. received output voltage i.e. transfer function characteristics

Figure 23 represents transfer function characteristics of immersible probes in single pair combinations. It can be noted that the Pz21 transducer is used as transmitting disc probe. This is based on the following: the high planar coupling coefficient, k_p of 0.6 and relative dielectric constant K_{33} of 3800 as seen in Table 6 and the peak outputs received transmitting with the Pz21 as shown in the graphs of Figure 22. A maximum output voltage of 11 V_{p-p} for an input excitation of 40 V, 200 kHz for probes 10 cm apart can be noted for the pair of Pz21 (transmitter) and Pz26 (receiver). This corroborates the compatibility of the Pz21 and Pz26 discs due to the similarity of their planar coupling coefficient, k_p; Piezoelectric voltage coefficient, g_{31} and measured impedance as shown in Table 6.

3.1.6. Immersible PZT probe sound pressure tests

Driving the immersible disc probes with a 40 V_{p-p}, 200 kHz input for maximum output as observed in Figure 23, ultrasonic pressure signals within the tank were recorded using a Reson TC4034 hydrophone [337] and is shown in Figure 24.

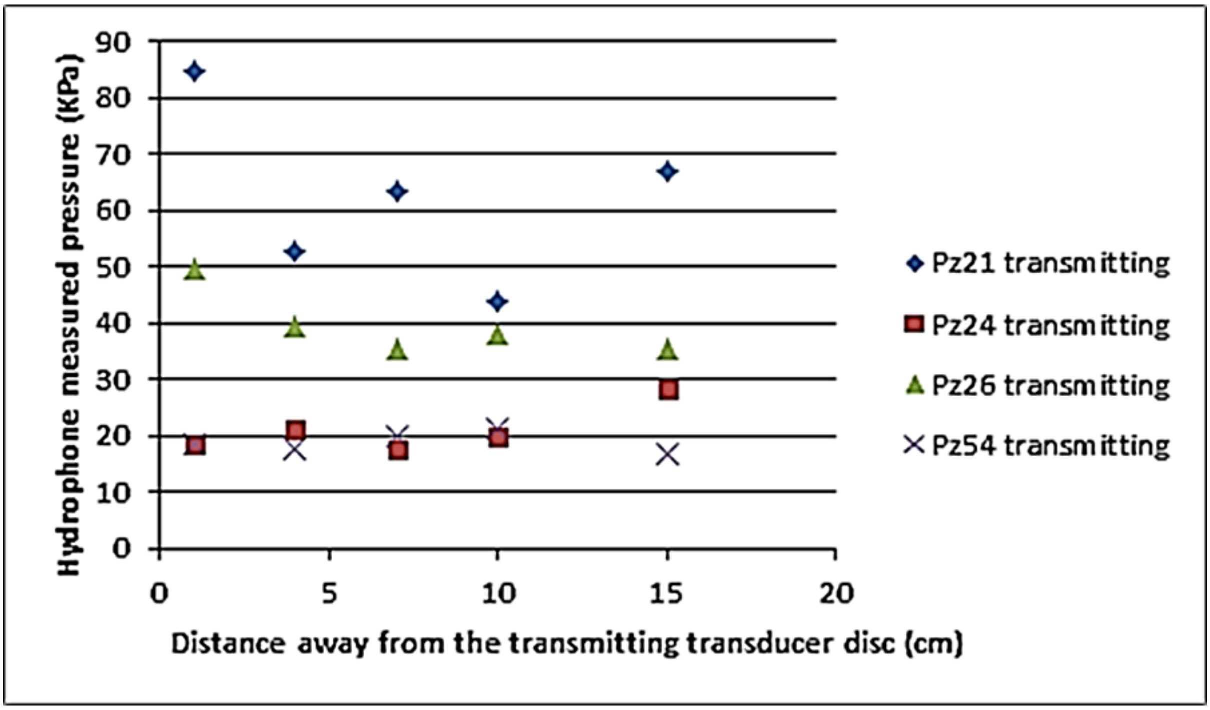

Figure 24: Hydrophone measured ultrasound pressure as a function of distance from the transmitting immersible probe

Driving all immersible disc probes with a 40 Vp-p, 200 kHz input excitation, it can be noted from Figure 24 that peak measured hydrophone pressure are obtained for the Pz21. Specifically, 7 cm away from the transmitting Pz21 immersible probe corresponds to a hydrophone output voltage of 1.8 V_{p-p}. This translates to a pressure of about 64 kPa using Equations 4 and 5 [338]. The results depicted in the graph of Figure 24 corroborates that the Pz21 immersible disc probe is the best choice as transmitter as it has the largest output pressure reading.

$$\text{SPL (dB (re 1µPa/V))} = 20 * \log(V_{rms}) - OCV \quad (4)$$

$$\text{P (kPa)} = \frac{10^{\frac{SPL}{20}}}{1000000000} \quad (5)$$

Where SPL = Sound Pressure Level in dB

OCV = Hydrophone receiving sensitivity

= - 220 (for the TC4034 @ 200 KHz) [337]

$V_{rms} = \frac{V_{p-p}}{2\sqrt{2}}$

3.1.7. High voltage propagation

In order to obtain transfer function characteristics for higher input excitation voltage (> 40 V), a bench variable power supply capable of supplying up to 120 V DC (Circuit Specialists Europe – Model CS12001X) was purchased. A simple driver circuit based on a BF258 transistor driving a 100 Ω, 100 W resistor was fabricated on printed circuit board (PCB) in order to switch the higher DC supply across the transmitting immersible disc probe under test. A 1% duty cycle drive signal was inputted into the base of the transistor. Figure 25 shows the high input voltage drive experimental set-up while Figure 26 shows the transfer function plots.

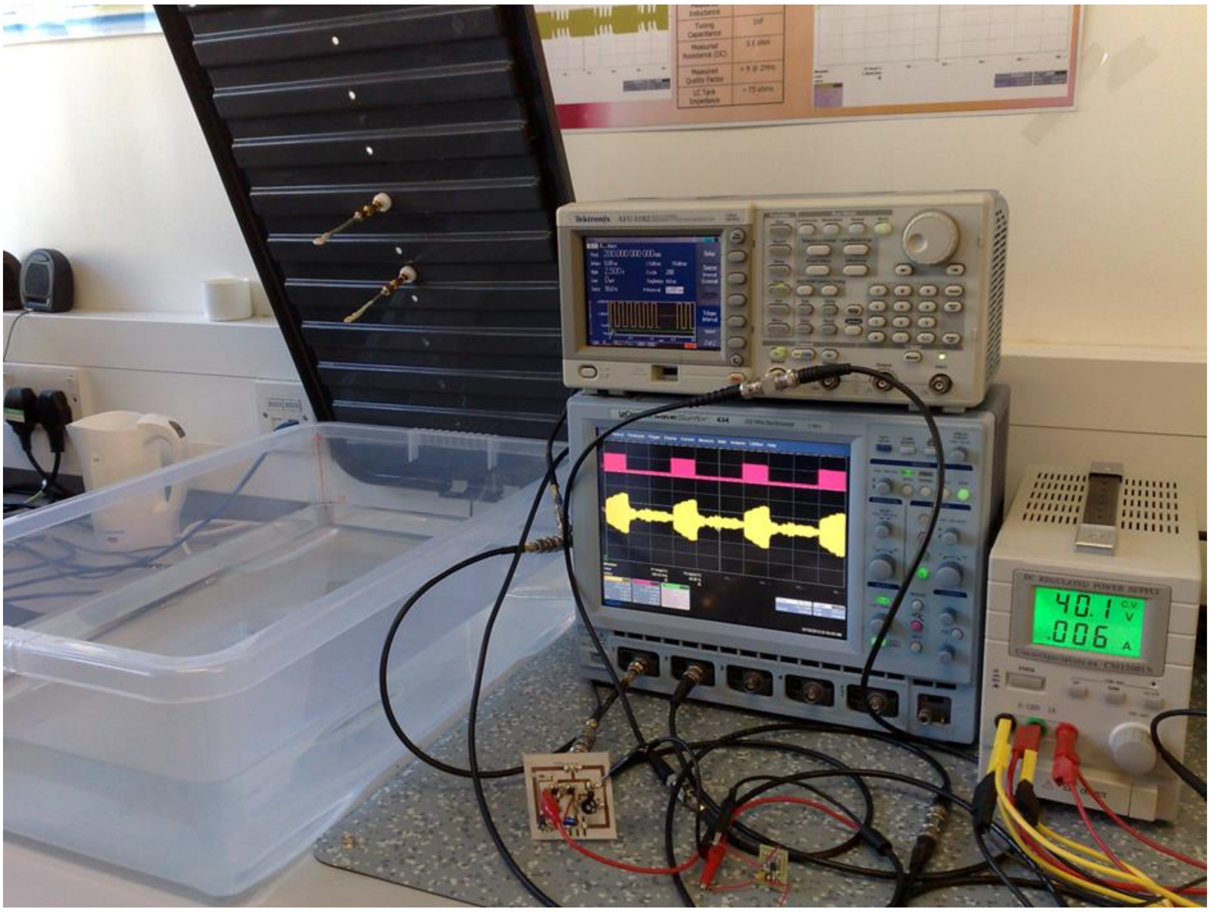

Figure 25: High input drive experimental set-up

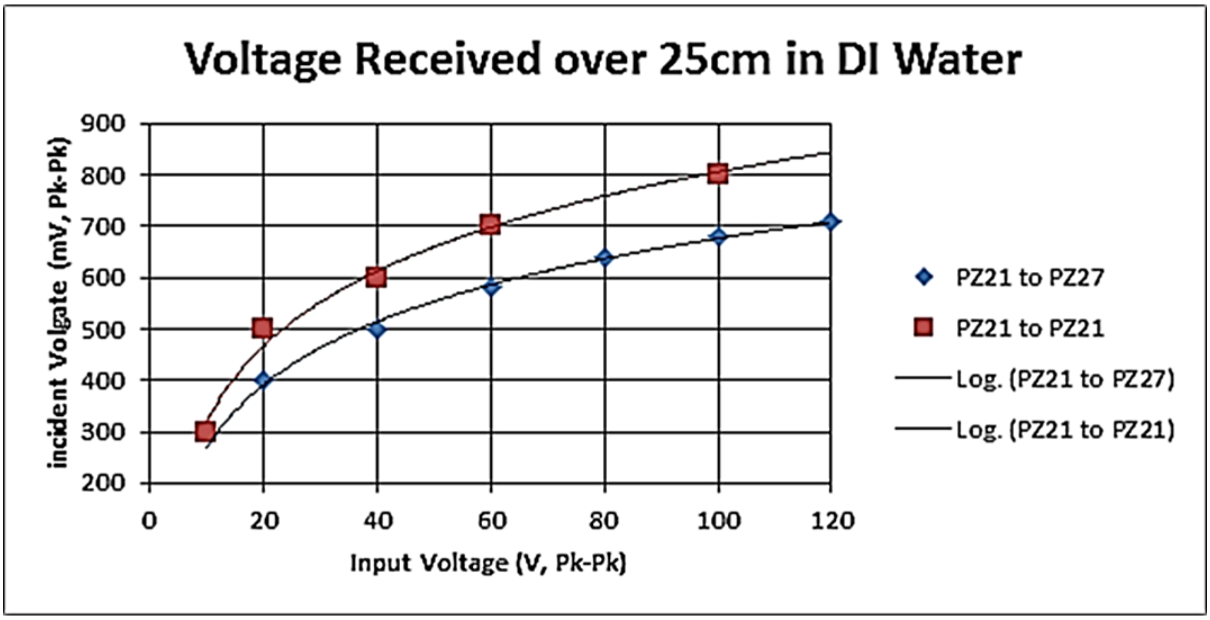

Figure 26: Transfer function plots for upto 120 V DC transmitter input drive

Figure 26 shows the transfer function logarithmic plots for input excitation voltage up to 120 V driving the Pz21 transmitting disc probe. It can be noted from Figure 26 that the efficient input excitation voltage is between 30 V and 40 V with an output voltage of between 500 mV and 600 mV respectively, for probes 25 cm apart. This is because subsequent increments higher than 40 V input voltage do not result in linear increments in output voltage. Additionally, a minimum input drive of around 20 V should be used whenever possible.

3.1.8. Primary (transmitting) PZT immersible disc probe excitation drive circuit

The results of the propagation tests discussed in the preceding sections include the following:

- the transmitting disc probe is Pz21 and the receiver is Pz26 (Figure 23)
- the operating resonance frequency is 200 kHz which drives the disc in its radial/planar (- 31) mode (Figure 22)
- the input excitation voltage is 40 V DC (Figure 26)
- the operating range is 7 cm (Figure 24).

Coupled with piezoelectric transducer driver characteristics highlighted in [218], [339] – [343], the transmitting PZT immersible disc probe excitation drive circuit is designed, simulated in OrCAD PSpice as shown in Figure 27, and implemented on a printed circuit board (PCB) as shown in Figure 28.

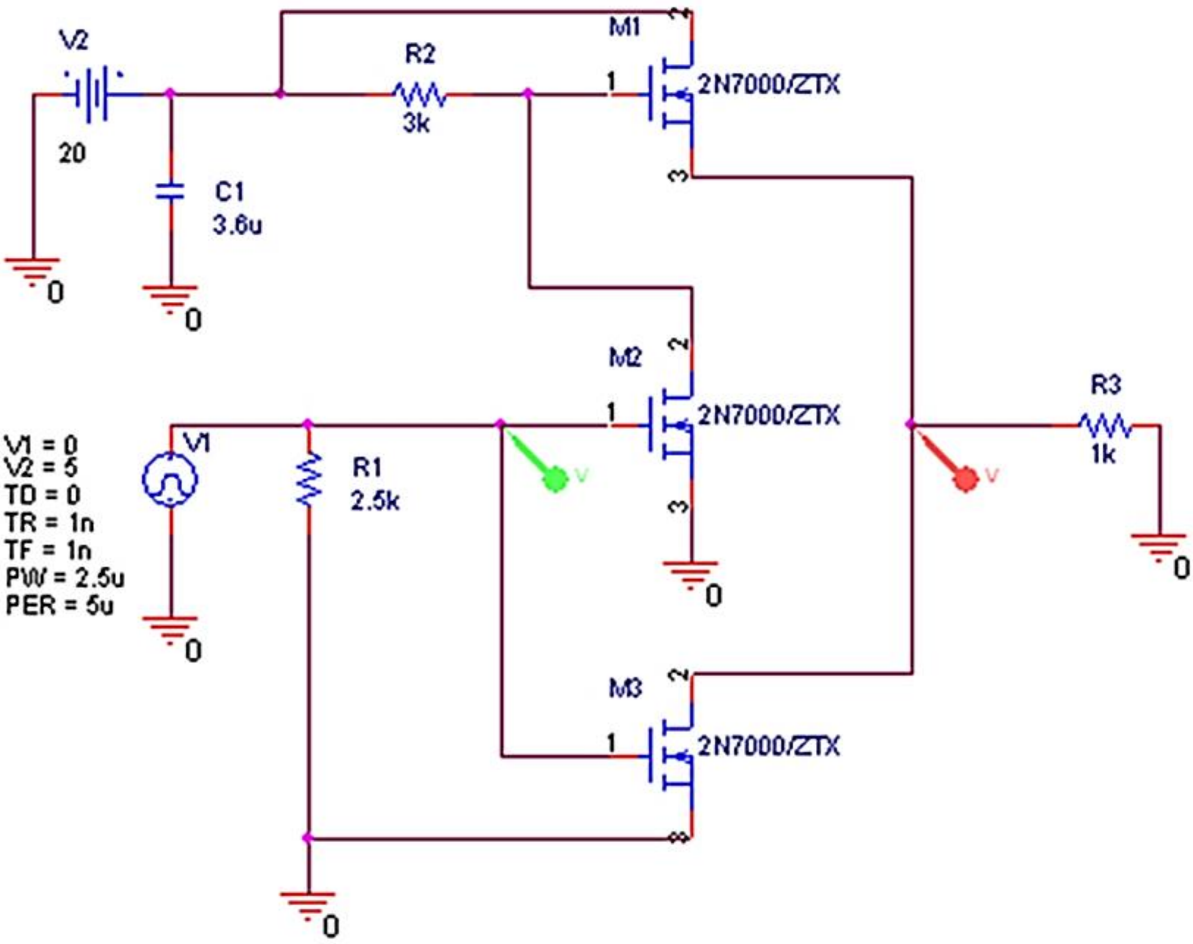
V2
20
C1
3.6u
R2
3k
M1
2N7000/ZTX
M2
2N7000/ZTX
M3
2N7000/ZTX
V1 = 0
V2 = 5
TD = 0
TR = 1n
TF = 1n
PW = 2.5u
PER = 5u
V1
R1
2.5k
R3
1k
0

(a)

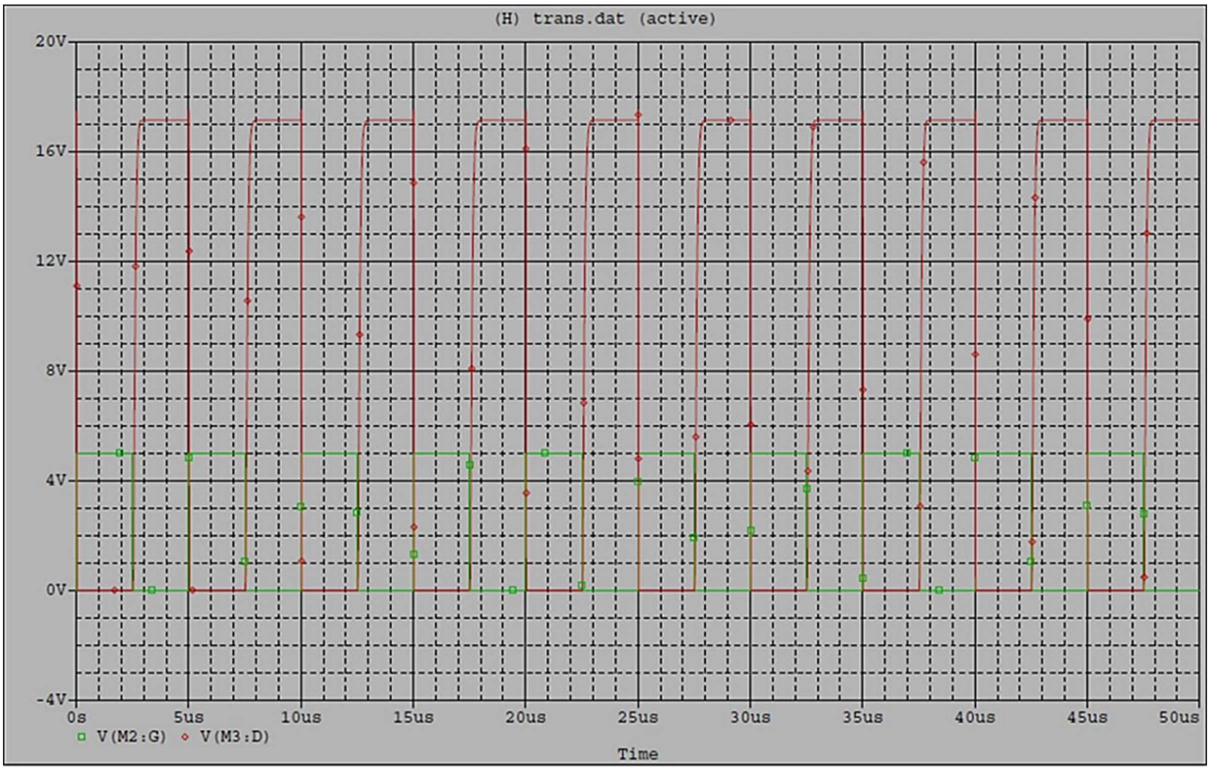

(b)

Figure 27: PSpice simulation (a) schematic (b) simulated output

In the PSpice simulation schematic in Figure 27a, voltage probes are placed to monitor Transistor M2 gate drive (green) and the output (red). These are highlighted in the simulation output in Figure 27b. In Figure 27b, the green trace represents the 5 V, 200 kHz square wave gate drive signal (from source V1 in Figure 27a) while the red trace represents the output voltage (across load resistor R3 in Figure 27a representing the transmitting immersible disc probe). Also, it can be noted that on start-up, the totem-pole configuration outputs 17.5 V across the transmitting disc for a 20 V DC input supply ensuring that the power supply is loaded only during switching.

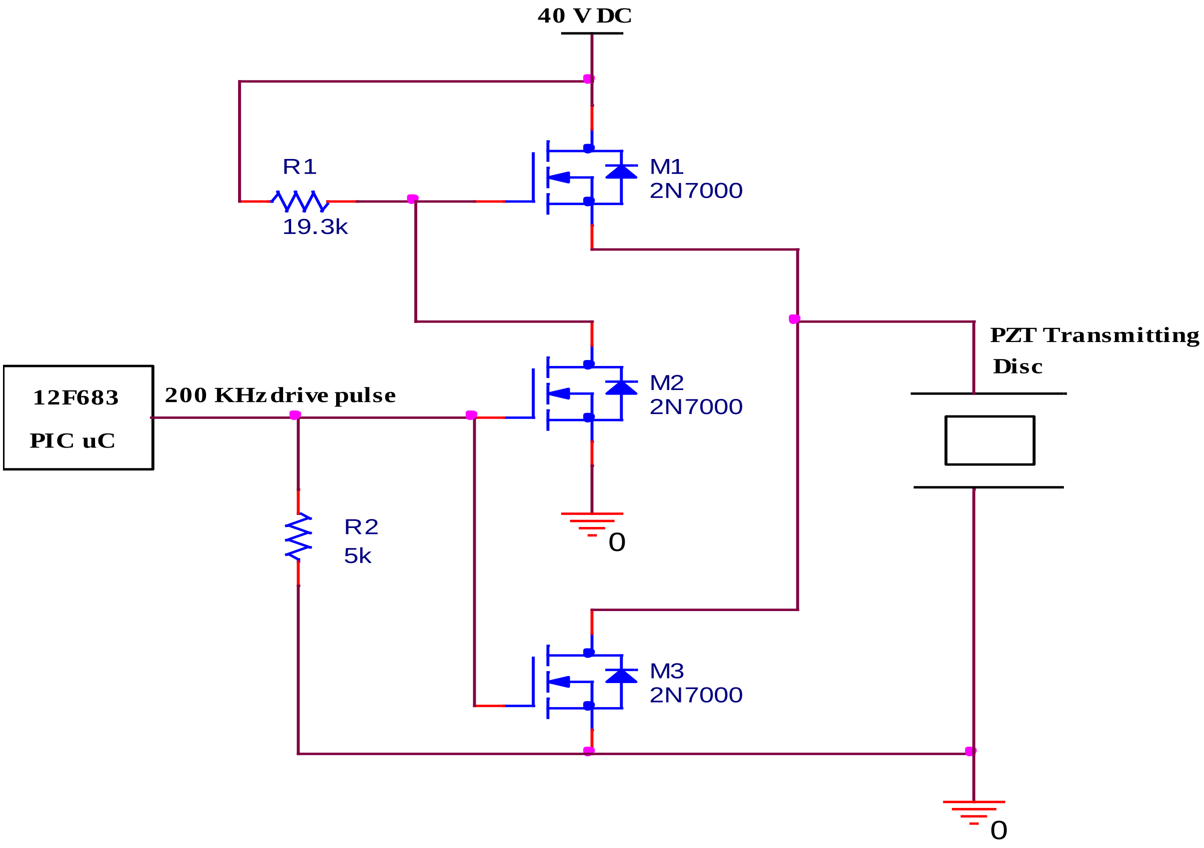

Figure 28: PCB layout of disc probe excitation drive circuit

In Figure 28, the primary transmitting PZT disc driver is assembled using discrete components built around the N-channel Enhancement mode Field Effect Transistor, 2N7000 [344]. The subcutaneous 12F683 Microchip PIC microcontroller (μC) [345], running at an internal software-preset operating frequency of 8 MHz is programmed to generate 200 kHz Pulse Width Modulated (PWM) pulses with a 43% duty cycle into the gate of two of the 2N7000 NMOS transistors used to switch voltage across the transmitting PZT disc probe using an input supply of 40 V (V_{DD}). The totem-pole configuration on start-up creates an initial potential equal to the supply voltage via Transistor M1, across the disc ensuring that the supply is only loaded during switching. With a positive pulse input from the μC, transistors M2 and M3 are ‘turned-on’ with M1 turned-off switching the output to the disc to low. The PCB fabricated driver circuit is as shown in Figure 29.

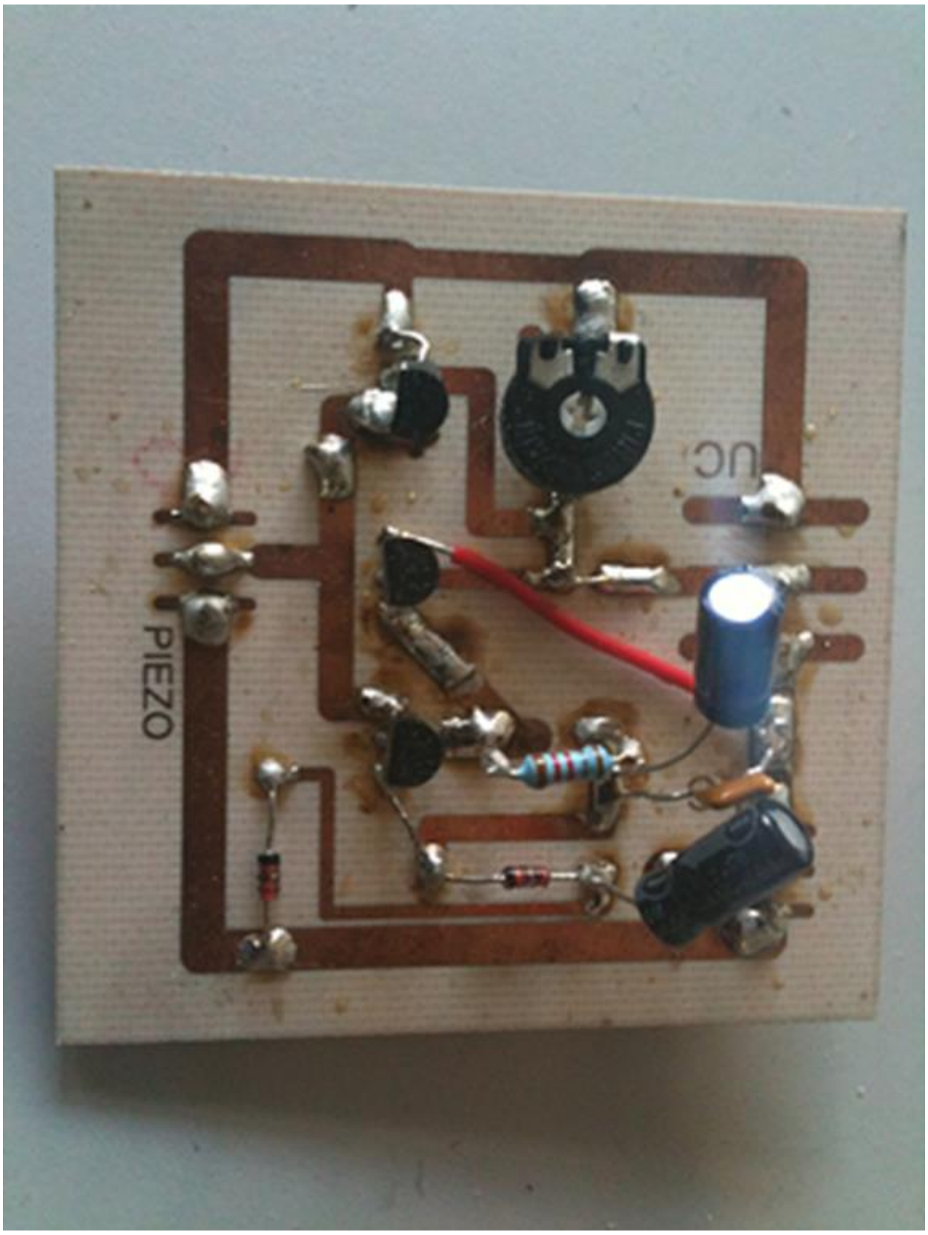

Figure 29: Actual PCB implemented transmitter PZT disc driver

3.1.9. Receiving PZT disc power conditioning circuit

By the direct piezoelectric effect, the receiving PZT disc on the implant circuit converts ultrasonic pressure waves generated by the transmitting PZT disc probe and propagated through the homogenous liquid medium (phantom) into low amplitude sinusoidal voltage signals. A power conditioning circuit is therefore required to provide the implant circuit with useable power. Figure 30 is the ultrasonic power conditioning circuit based around a tuned LC resonator circuit and the ultra-low voltage Seiko startup charge pump IC [346].

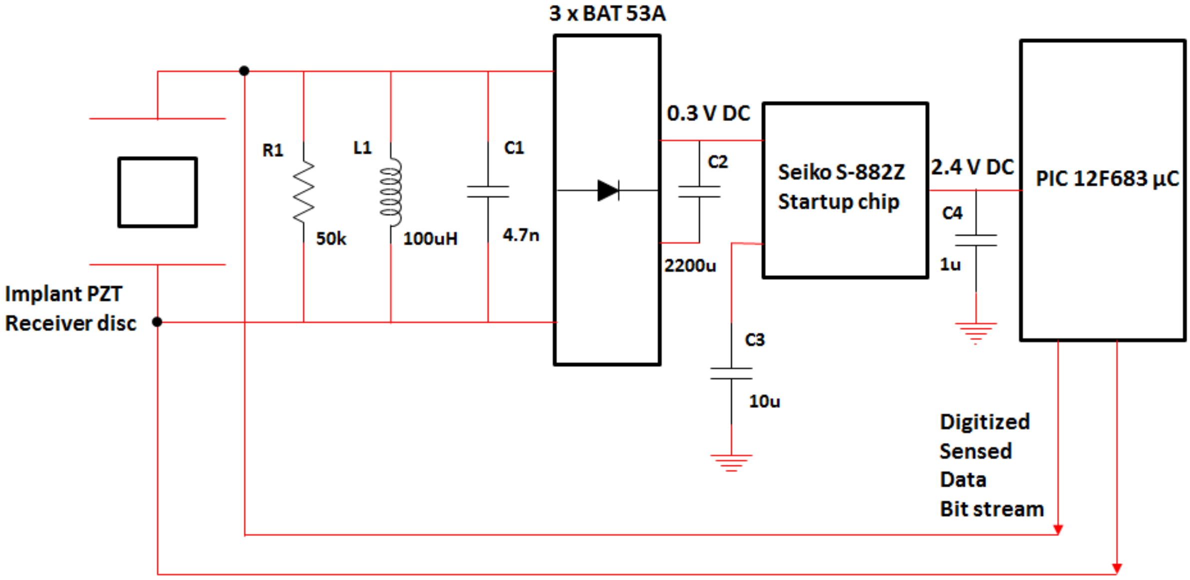

Figure 30: Ultrasonic sub system power conditioning circuit

The low amplitude output of the receiving PZT disc is passed through the tuned LC resonator circuit (L1 = 100 µH // C1 = 4.7nF) as shown in Figure 30. The tuned resonator circuit maximizes the sensitivity of the receiving PZT transducer disc and also multiplies its output AC voltage signal [340]. This multiplied output AC voltage is then passed through a full-wave rectifier consisting of three BAT 54A surface-mount Schottky diodes [347]. Capacitor C2, valued at 2200 µF, is selected to hold charge to power the Seiko charge pump long enough after the power carrier is interrupted for the implant to retrieve analog signals from the implant bio-sensor, convert to a digital bit stream using the built-in ADC of the implant µC, and then transmit it as a burst of ultrasonic pulses. The rectified and smoothened 0.3 V DC output is fed into the input of the Seiko charge pump which charges its load capacitor C3 (10 µF) to 2.4 V DC in order to power the implant µC which consequently powers the implant analog bio-sensor. The implant µC is software-preset for low power operation (consuming 8.5 µA @ 32 KHz @ 2 V DC).

3.1.10. Ultrasonic sub system signal conditioning circuit

The transmitted burst of ultrasonic pulses from the implant through the homogenous liquid medium (phantom) produces low amplitude sinusoidal voltage signals on the subcutaneous primary piezo disc via the direct effect. This low-amplitude output is passed through the signal conditioning circuit to reconstruct the transmitted data bit stream. The signal conditioning circuit, shown in Figure 31, is built around a two-stage, small signal amplifier consisting of two high-precision and high common-mode rejection OPA 277 operational amplifiers [348].

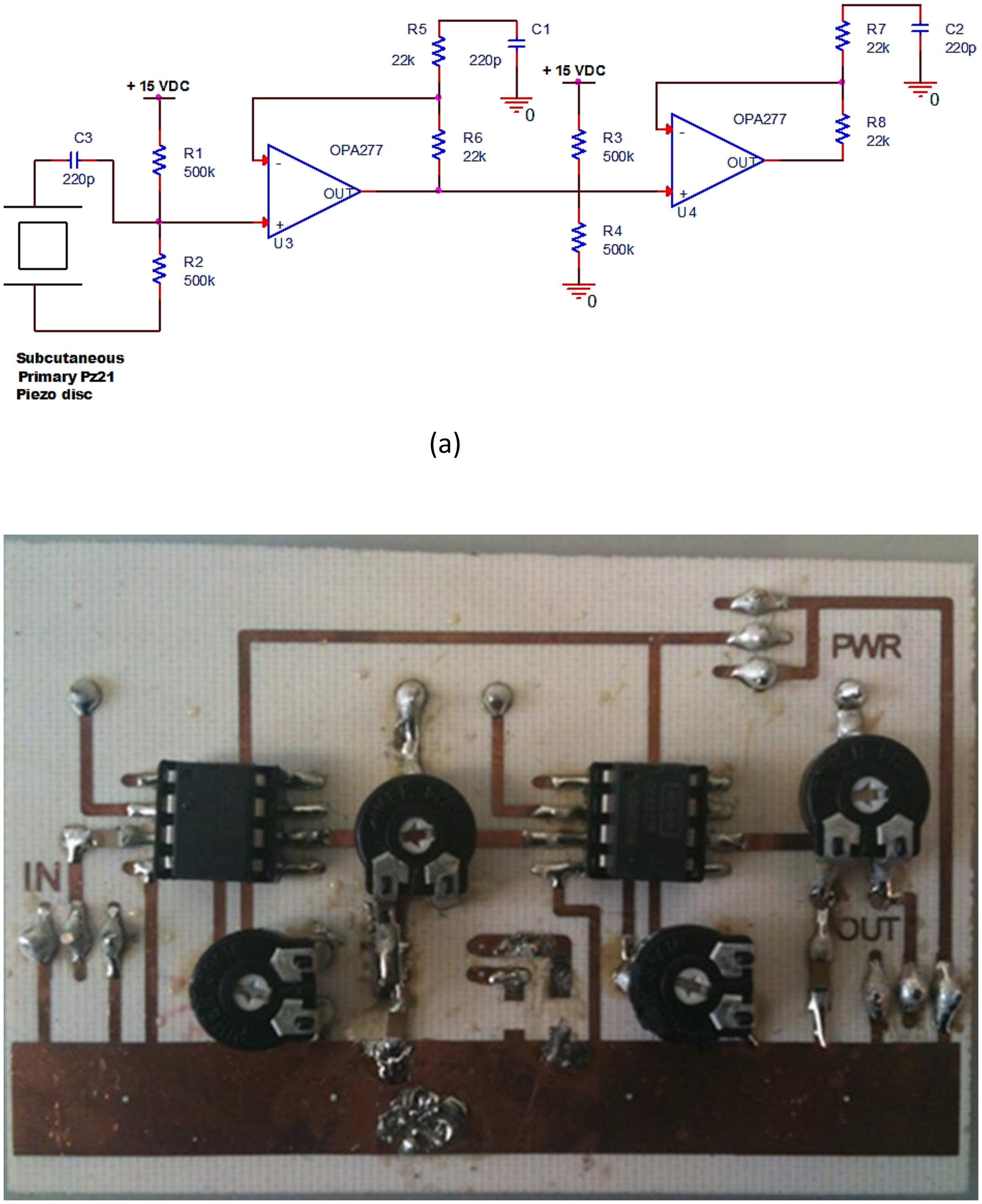

Figure 31: Ultrasonic sub system signal conditioning circuit (a) schematic (b) PCB fabrication

The ~ 4 $mV_{p\text{-}p}$ low amplitude data signal received on the primary piezo disc, as shown in Figure 32, are passed through the two stages of amplification of the signal conditioning circuit of Figure 31a.

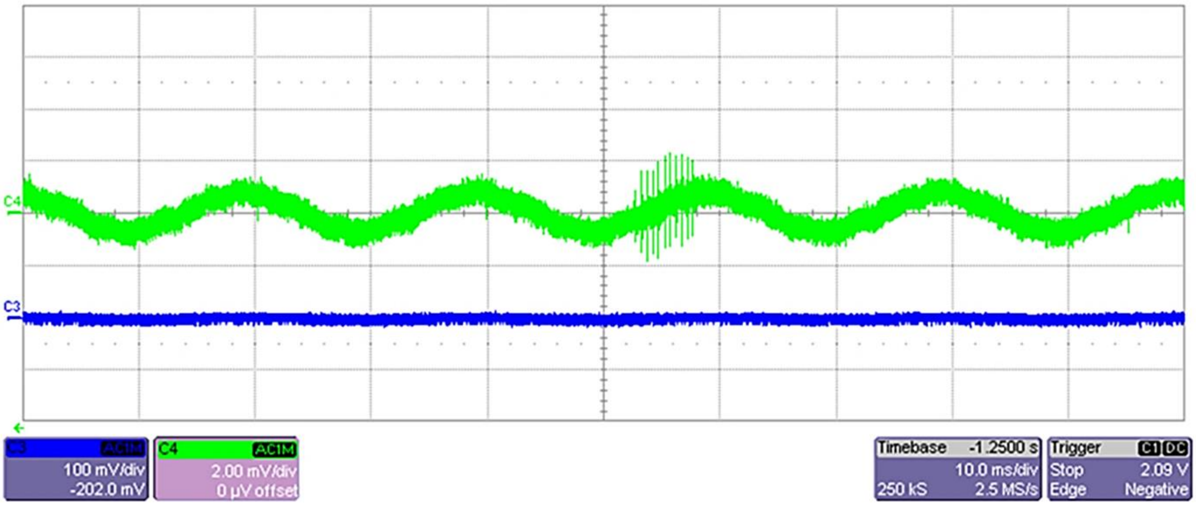

Figure 32: Oscilloscope trace of received transmitted data signal on primary piezo disc

In Figure 32, the horizontal axis is propagation delay while the vertical axis is voltage. It can be noted that the background sinusoidal signal (Trace C4) is 50 Hz mains picked up because of the high gain setting (2 mV/div). The ~ 2 $V_{p\text{-}p}$ output signal from the signal conditioning circuit is rectified and inputted into the in-built software-configured comparator circuit of the subcutaneous µC (see Figure 13). The reconstructed transmitted data bit stream is shown in Figure 33.

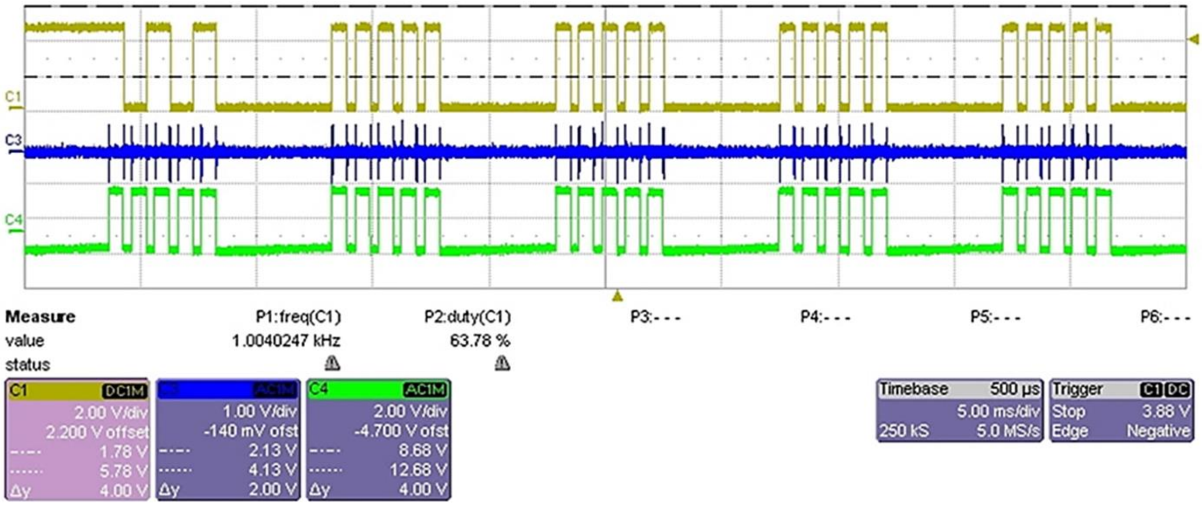

Measure	P1:freq(C1)	P2:duty(C1)	P3:- - -	P4:- - -	P5:- - -	P6:- - -
value	1.0040247 kHz	63.78 %				
status	⚠	⚠				

C1 DC1M
2.00 V/div
2.200 V offset
-·-·- 1.78 V
······ 5.78 V
Δy 4.00 V

AC1M
1.00 V/div
-140 mV ofst
-·-·- 2.13 V
······ 4.13 V
Δy 2.00 V

C4 AC1M
2.00 V/div
-4.700 V ofst
-·-·- 8.68 V
······ 12.68 V
Δy 4.00 V

Timebase 500 µs
5.00 ms/div
250 kS 5.0 MS/s

Trigger C1 DC
Stop 3.88 V
Edge Negative

Figure 33: Oscilloscope trace of reconstructed data bit stream

Figure 33 is the oscilloscope trace showing the output of the signal conditioning circuit, the reconstructed data bit stream output and the transmitted data bit stream. The horizontal axis in Figure 33 is propagation delay while the vertical axis is voltage.

From Figure 33, Trace C4 (green) is the transmitted data bit stream from the implant. Trace C3 (blue) is the output of the signal conditioning circuit while Trace C1 (brown) is the reconstructed data bit stream. Observe that the first data reconstructed in Trace C1 in Figure 33 doesn’t correspond with the transmitted data. This is due to the set-up profile of the comparator circuit of the subcutaneous µC which requires an initial time delay for setting up and initializing before outputting the data. Data transmission in Figure 33 corresponds to a Bit Error Rate (BER) of 20%.

3.2. Inductive sub-system

The block diagram of the inductive sub-system is shown in Figure 34.

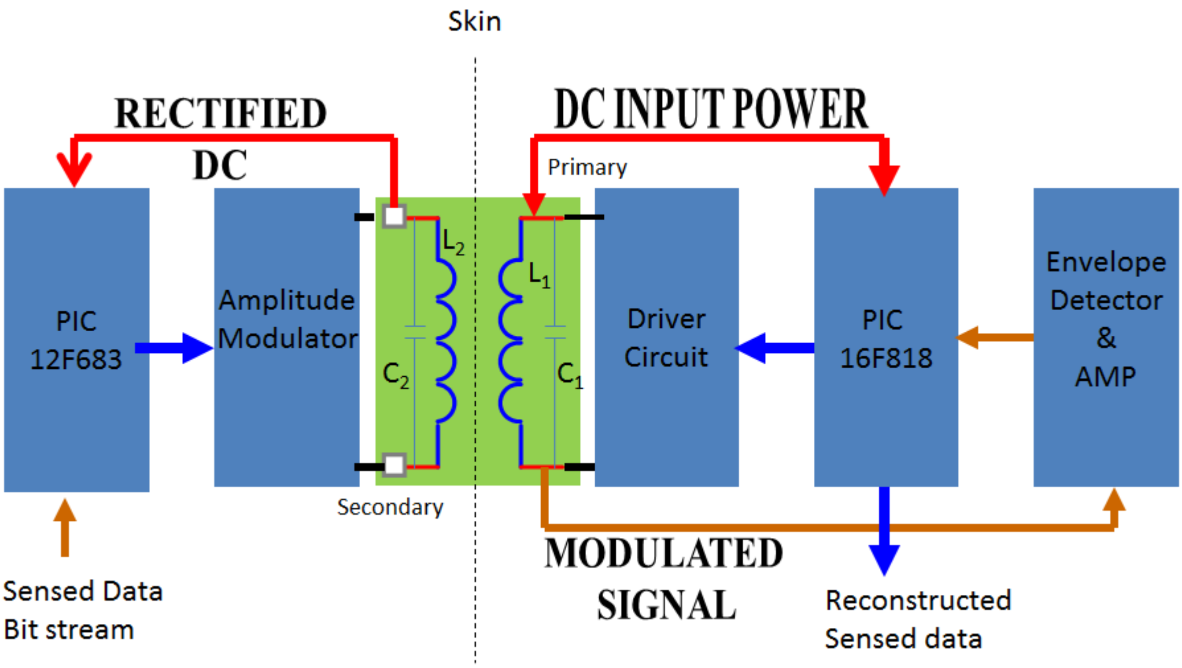

Figure 34: Inductive sub system block diagram

In Figure 34, red denotes power signals; blue denotes digital data signals, while brown denotes analog data signals. In Figure 34, the primary coil (with associated circuits) is external of the human body; while the secondary coil (and associated circuits) is implanted transcutaneously, under the skin. Therefore, L_1C_1 make up the external/primary LC-tank while L_2C_2 make up the implant/secondary/receiver LC-tank. AC energy transfer takes place across the skin gap between the coils by the mutual inductance coupling the two coils. The coils are tuned to a single carrier resonance frequency using parallel capacitors, C1 and C2. The transcutaneous Microchip PIC 12F683 reconstructs the transmitted data bit stream using its in built comparator and modulates it to the power carrier at the secondary coil. The envelope detection and amplifier circuit reconstructs the data bit stream from the power carrier coupled back to the primary coil. The Microchip PIC 16F818 performs a dual role: generating the gate pulse voltage signal for the driver circuit as well as converting the reconstructed data bit stream to analog using its built-in Digital-to-Analog Converter (DAC).

3.2.1. Coil design, characterisation, and fabrication

Design, theoretical analysis, and geometrical optimization of conventional multi-coil inductive links have been covered extensively in literature [167], [168], [174], [349] – [361]. Derived closed form expressions/equations from these literatures for Printed Spiral Coils (PSCs) are inputted into ‘Coil Calculator’; a Visual Basic application with window screenshot as shown in Figure 35.

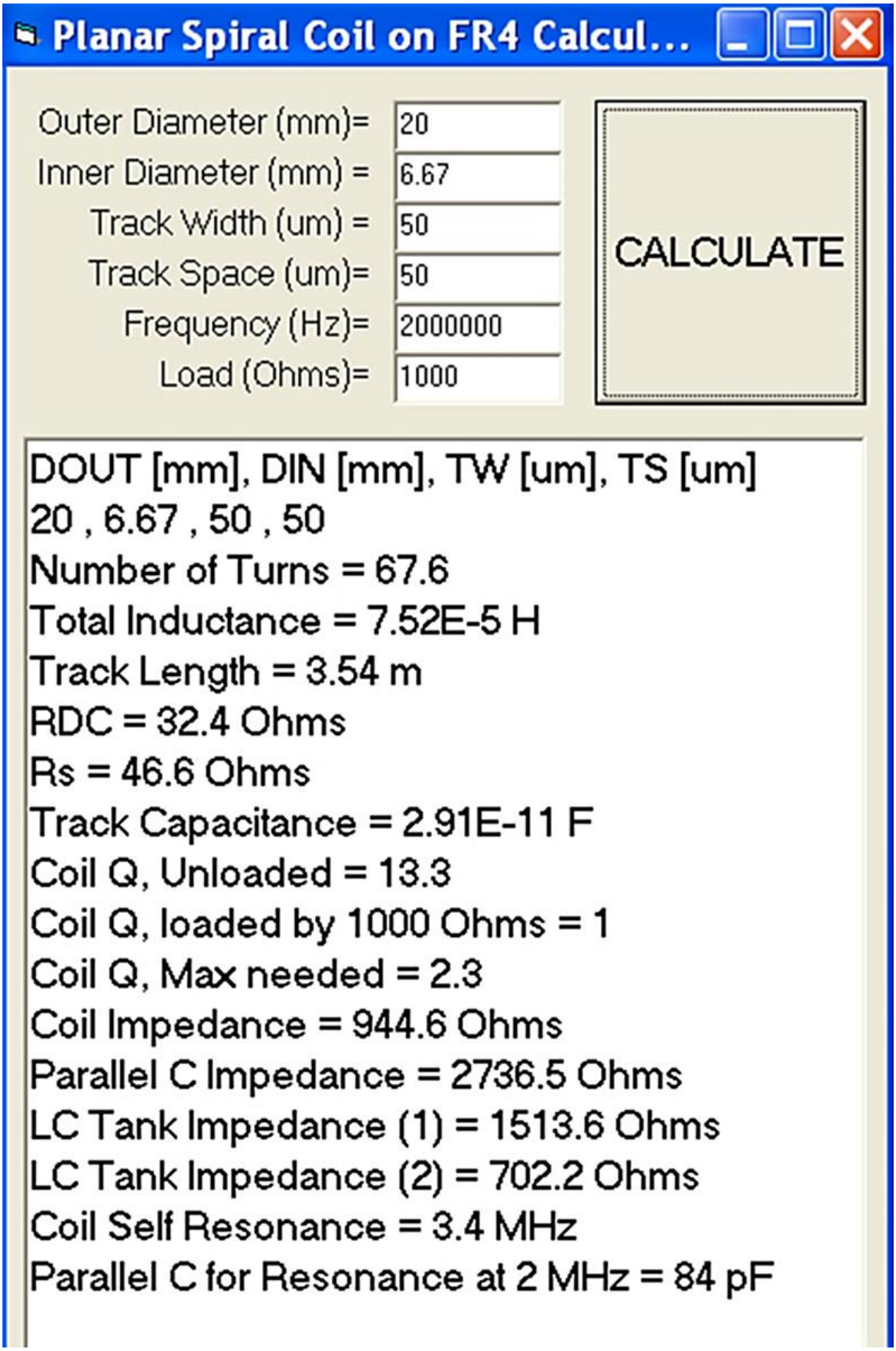

Outer Diameter (mm)= 20
Inner Diameter (mm) = 6.67
Track Width (um) = 50
Track Space (um)= 50
Frequency (Hz)= 2000000
Load (Ohms)= 1000

```
DOUT [mm], DIN [mm], TW [um], TS [um]
20 , 6.67 , 50 , 50
Number of Turns = 67.6
Total Inductance = 7.52E-5 H
Track Length = 3.54 m
RDC = 32.4 Ohms
Rs = 46.6 Ohms
Track Capacitance = 2.91E-11 F
Coil Q, Unloaded = 13.3
Coil Q, loaded by 1000 Ohms = 1
Coil Q, Max needed = 2.3
Coil Impedance = 944.6 Ohms
Parallel C Impedance = 2736.5 Ohms
LC Tank Impedance (1) = 1513.6 Ohms
LC Tank Impedance (2) = 702.2 Ohms
Coil Self Resonance = 3.4 MHz
Parallel C for Resonance at 2 MHz = 84 pF
```

Figure 35: Coil Calculator VBA window screenshot

Inputting values of the outer diameter, inner diameter, track width, track spacing, resonant frequency, and the expected load into the coil calculator produces computed characteristics of the designed PSC as listed in Figure 35. The computed characteristics listed in Figure 35 are for a 20 mm (outer) diameter circular planar spiral coil having a resonance frequency of 2 MHz with track width and track spacing of 50 µm. It can be noted that the inner diameter is a third of the outer diameter as stipulated by Ghovanloo [357]. The computed characteristics from the coil calculator are then inputted into the respective RF design software – in our case, the Advanced Design System (ADS) 2006A by Agilent Technologies [362].

The geometrical shape for PSCs used in the design of inductive links is circular shaped and square shaped. Chen [358] showed that the circular shaped inductor coil is more efficient and yields better performance. In support, Burghartz [363] showed that a circular structure allows for significant reduction in the complexity of the model compared to a square structure whose sharp corners induce excess capacitance.

Constrained by the design requirement for low PSC conductor losses, an operating resonance frequency of 2 MHz is selected. Additionally, at this frequency, the carrier wavelength is significantly larger than the cross-section of the human body being penetrated and therefore results in low attenuation as well as optimized power transfer.

Inputting the computed characteristics from the coil calculator (Figure 35) into ADS generates the schematic and outline diagrams as shown in Figures 36 and 37 respectively.

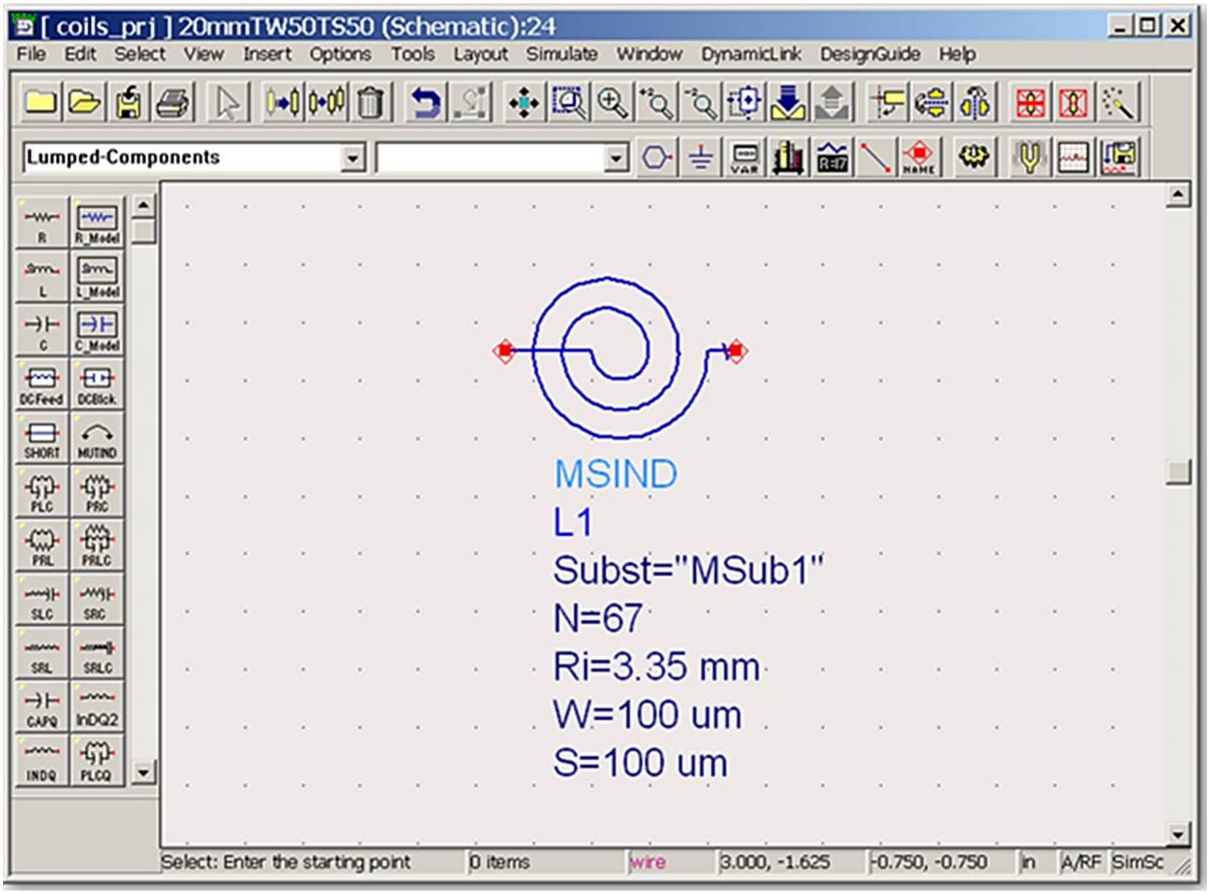

[coils_prj] 20mmTW50TS50 (Schematic):24

MSIND
L1
Subst="MSub1"
N=67
Ri=3.35 mm
W=100 um
S=100 um

Select: Enter the starting point | 0 items | wire | 3.000, -1.625 | -0.750, -0.750 | in | A/RF | SimSc

Figure 36: ADS-generated 20 mm PSC schematic

In Figure 36, the ADS-generated schematic is for a 20mm (outer diameter) circular spiral coil having an inner diameter of 6.67 mm, a track width of 50 µm (microns) and a track spacing of 50 microns with a total of 67 turns.

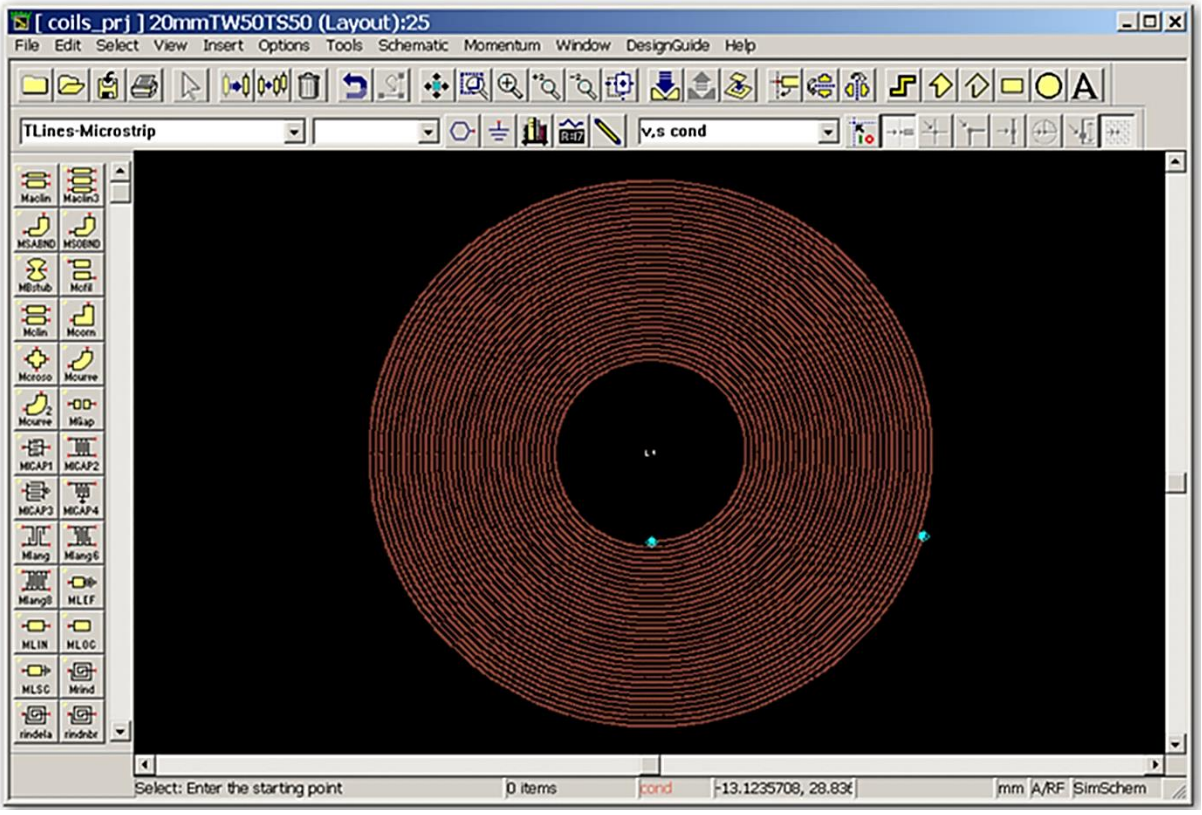

Select: Enter the starting point

-13.1235708, 28.83€

Figure 37: ADS-generated 20 mm PSC layout

Using the schematic of Figure 36, ADS generates a layout as shown in Figure 37. A template mask is then developed by printing the layout on transparency film [364] using a LaserJet printer. The template mask is first exposed unto the positive photoresist top layer of an FR4 (Flame Retardant, Class 4) printed circuit board (PCB) using an ultraviolet light exposure unit [365] and then fabricated using a bubble etch tank [366]. Figure 38 shows some of the fabricated PSCs.

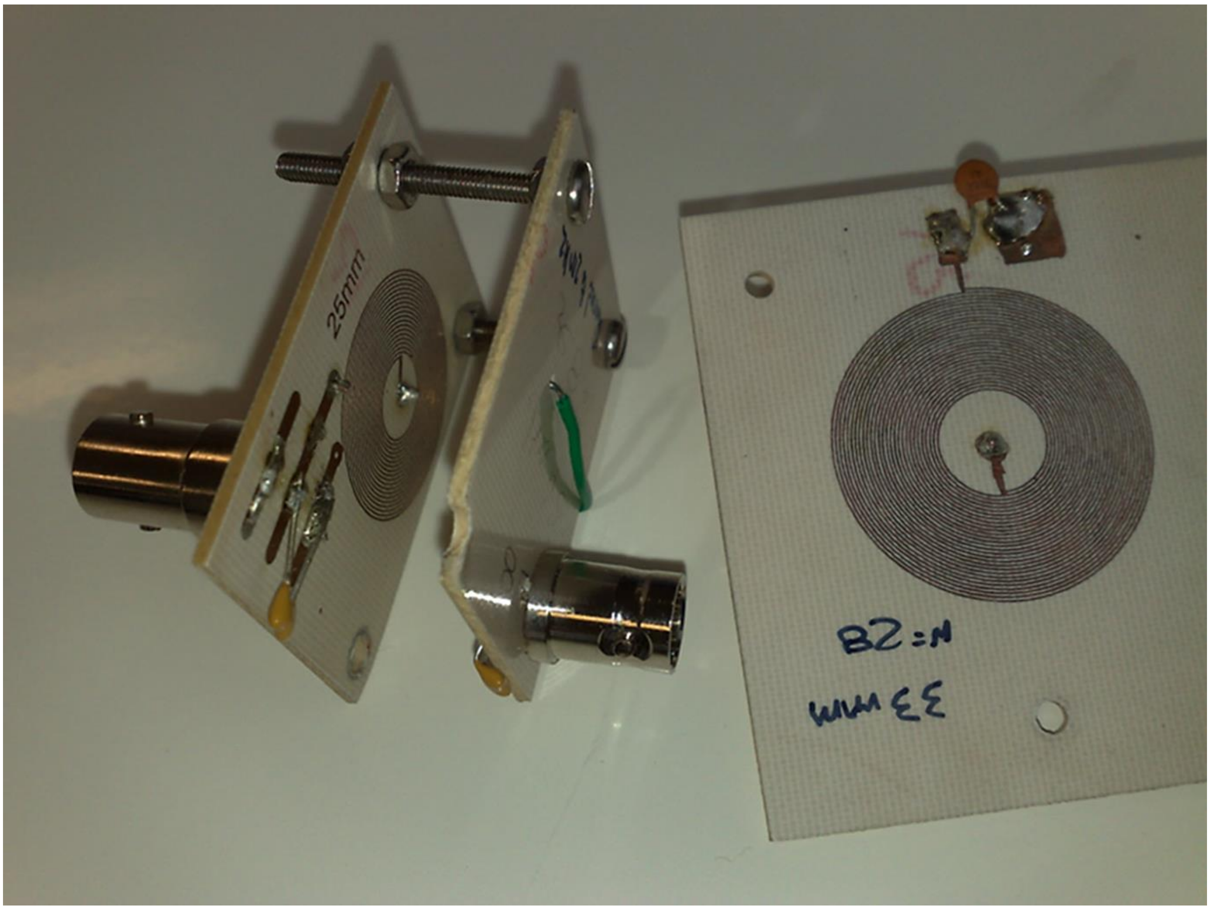

Figure 38: Fabricated printed spiral coils on PCB

Figure 38 shows fabricated 25 mm, 20 mm and 33 mm (outer diameter) PSCs. It can be noted that soldering pads have been included for ease of connecting BNC/SMA connectors as well as the appropriate parallel resonance capacitor. The left hand side unit in Figure 38 is a typical test configuration of a single pair of coils to maintain the coils in parallel alignment at a fixed distance apart.

Table 9: Comparison of theoretical and measured characteristics for fabricated 20 mm PSC

Characteristics	**Theoretical values**	**Measured values**
D_{outer} (mm)	20	
D_{inner} (mm)	6.67	
Track width, TW (µm)	50	
Track spacing, TS (µm)	50	
No. of turns, N	67.6	
Inductance, L (µH)	75	3.1
DC Resistance, R_{DC} (Ω)	32.4	4.6
Quality Factor, $Q_{unloaded}$	13.3	4

A comparison of theoretical (generated from the 'Coil Calculator' application) and measured (actual) characteristics for the 20 mm PSC shown in Figure 37 are tabulated in Table 9. The wide discrepancies between the measured (actual) and theoretical values shown in Table 9 were investigated under the quality of the template mask produced and the PCB etching process.

3.2.1.1. Template mask (transparency film) quality

The quality of the template mask affects the quality of the fabricated PCB. The layout of Figure 37 was initially printed on transparency film using the HP LaserJet 4250n [367]; having a maximum print resolution of 1200 x 1200 dpi.

On the basis of the listings below of equations for inductance and Quality factor for PSCs from [168], [174], [218], [340 - 349], [357], the following can be deduced:

$$L = \left[\frac{1.27 * \mu_0 * n^2 * d_{avg}}{2}\right] * \left[\ln\left(\frac{2.07}{\varphi}\right) + 0.18\varphi + 0.13\varphi^2\right] \tag{6}$$

$$\varphi = \frac{d_o - d_i}{d_o + d_i} \tag{7}$$

$$Q = \frac{\omega L - \omega\left(R_S{}^2 + \omega^2 L^2\right)C_P}{R_S} \sim \frac{\omega L}{R_S} \text{ (for small } C_P\text{)} \tag{8}$$

$$C_P = C_{pc} + C_{ps} \sim (\alpha\varepsilon_{rc} + \beta\varepsilon_{rs}) * \varepsilon_0 * \frac{t_c}{s} * l_g \tag{9}$$

$$l_g = 4(d_o - w * n)(n - 1) - 4s * n(n + 1) \tag{10}$$

$$R_S = R_{dc} * \frac{t_c}{\delta * \left(1 - e^{\frac{-t_c}{\delta}}\right)} \tag{11}$$

$$\delta = \sqrt{\frac{\rho_c}{\pi * \mu * f}} \tag{12}$$

$$\mu = \mu_r * \mu_0 \tag{13}$$

$$R_{dc} = \rho_c * \frac{l_c}{w * t_c} \tag{14}$$

$$l_c = 4 * n * d_0 - 4 * n * w - ((2n + 1)^2)(s + w) \tag{15}$$

Where: L = inductance (µH)

d_o = outer diameter (mm)

d_i = inner diameter (mm)

$d_{avg} = (d_o + d_i)/2$ (mm)

μ_o = permeability of free space

φ = fill factor

n = number of turns

Q = quality factor

C_P = parallel plate parasitic capacitance

ε_{rc} and ε_{rs} = relative dielectric constants of coating and substrate materials, respectively

R_S = series resistance

R_{dc} = DC resistance of the coil

l_g = length of the gap

l_c = length of conductive trace

δ = skin depth

μ_r = relative permeability of the conductor

w = track width

s = track spacing

ρ_c = resistivity of conductive material

t_c = thickness of conductive trace.

It can be noted from equations (6) and (7) that the inductance of a spiral coil is dependent on the physical dimensions of the coil; particularly the inner and outer diameter which are also dependent on the track width and track spacing. Additionally, the Quality Factor from equations (8) to (15) is influenced by the inductance of the spiral coil as well as the track series resistance and track parallel capacitance. This implies that uneven/non-uniform tracks on the mask will influence the measured inductance and Quality Factor of the fabricated PSCs. Consequently, to ascertain the quality of template masks produced, a clean room talistep was used to measure the average step height of the tracks as well as the track width. Additionally, the quality of the mask was observed under a clean room digital microscope as well as the Lumenera Infinity 2 scientific camera [368]. The following deductions were arrived at:

(a) . Data from the talistep showed that the track width and step height on the template mask are not uniform; this is further corroborated by the image of the mask under the digital microscope shown in Figure 39.

Figure 39: Image of transparency film under digital microscope

It can be noted from Figure 39 that the dark shade of copper tracks and lighter shade of track spacing are not uniform. The thin copper track has therefore resulted in a much lower inductance and Quality factor measured. The black spots seen are as a result of splattering of the printer ink during printing.

(b) . To rule out faulty transparency films, masks were produced using the same layout in Figure 37 printed on the same transparency film but using different ranges of printers with varying print resolutions. The results showed that as the print resolution of the printer increased, the quality of the mask improved. From tests carried out, it was discovered that to use the LaserJet HP p4515x or 4250n, both with a maximum print resolution of 1200 x 1200 dpi, the track width and track spacing should not be lower than 250 microns. While, to produce masks with track widths and track spacing as low as 50 microns, the Photoplotter FP-8000 [369], [370] is better suited. The Photoplotter has a ‘software-adjustable’ maximum print resolution of 8192 x 8000 dpi. Layout images saved as ‘.dns’ files in ADS are first converted to ‘.gds/.cfi/.dxf’ using CleWin layout Editor 4.0.0 by Wieweb, The Netherlands [371] and then finally converted to ‘.gerber’ files, required by the Photoplotter, using LayoutEditor [372]. Figure 40 is a Photoplotter-generated transparency film seen under the Infinity 2 camera for a mask containing a 10 mm PSC with track width and track spacing of 100 micron.

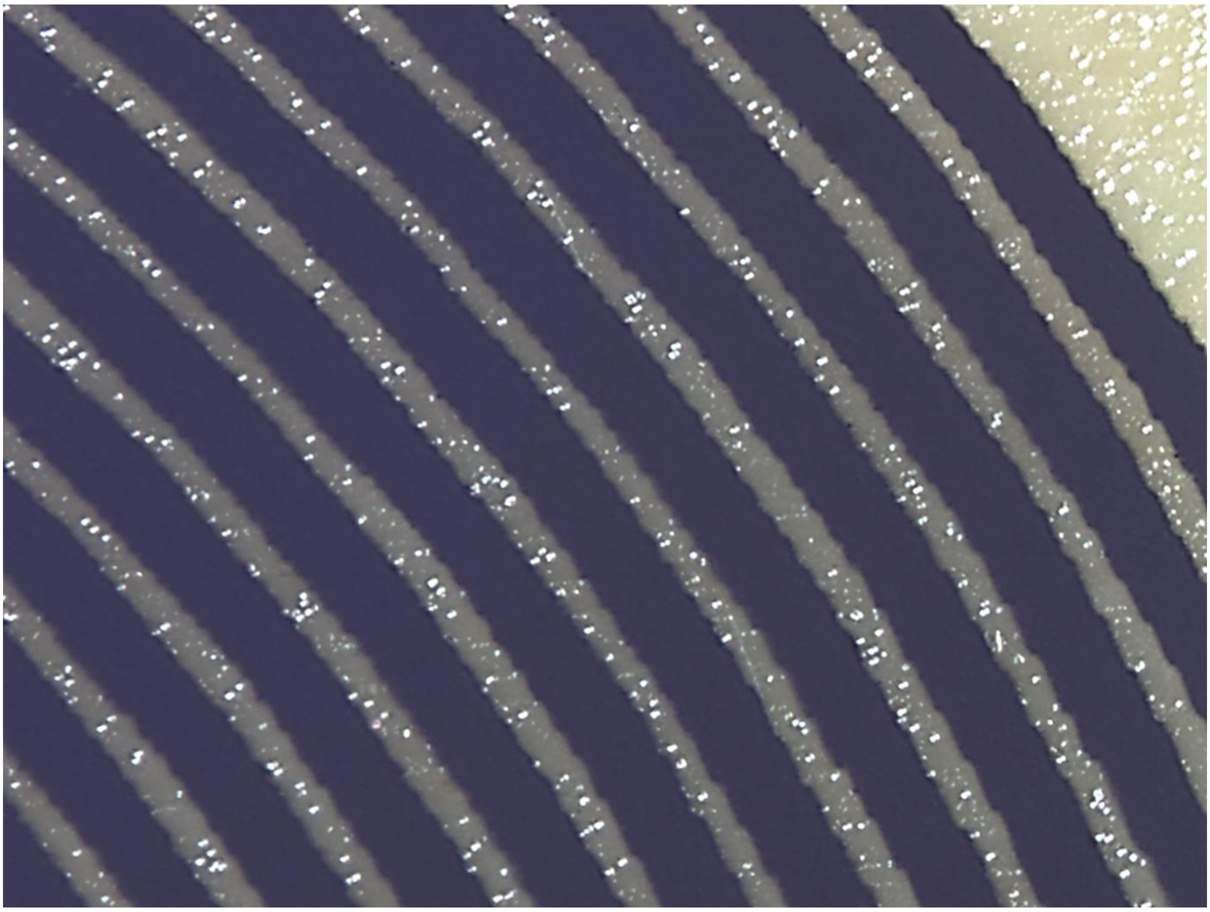

Figure 40: Photoplotter-generated transparency film for 10mm coil with 100 micron track width and spacing

Though the edges of the darker shade copper tracks appear jagged, the track width and spacing in Figure 40 are even and uniform – promising better correlation between measured and theoretical values.

3.2.1.2. FR4 PCB etching process

After ascertaining that a quality template mask has been produced in section 3.2.1.1, we now turn our attention to the quality of the PCB wet etching process.

A simplified block diagram of the cross-section of a single-sided FR4 printed circuit board (PCB) is as shown in Figure 41. It consists of 30 µm thickness of positive photoresistant top layer followed by 35 µm thickness of copper layer and finally 1.6 mm thickness of dielectric substrate.

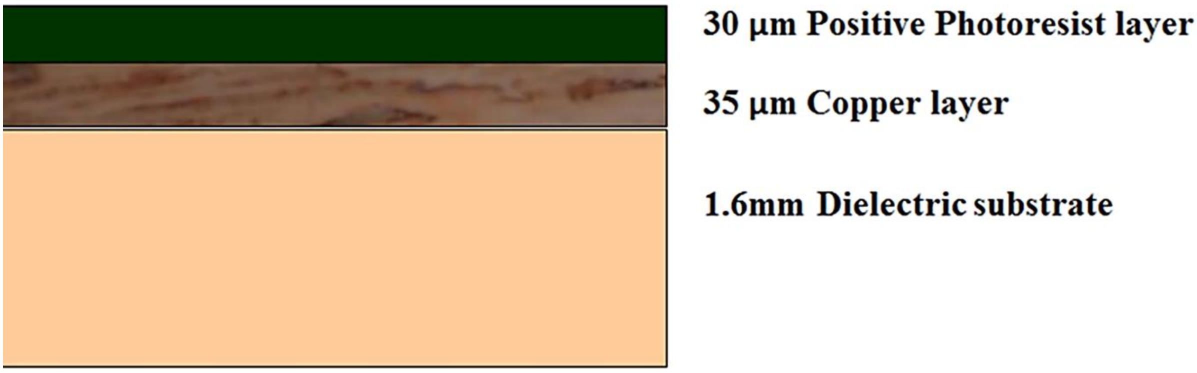

Figure 41: Block diagram of the cross-section of FR4 PCB

In Figure 41, it can be noted that because of the thin positive photoresist and the copper layers, over-exposure and over-etching is common. An efficient etching process developed from numerous tests involves warming-up the ultraviolet light exposure unit for 100 s before placing the PCB in the exposure unit and exposing it to the mask for another 100 s. Immerse the exposed PCB in a developer for between 20 and 40 sec. The developed PCB is then immersed in a bubble etch tank consisting of a Ferric Chloride etchant solution [373]. The final etched PCB is removed from the etch tank after periodic visual checks to ensure that all the copper tracks are fully resolved. It is then washed in acetone. The etch rate versus temperature for popular etchant solutions is shown in Figure 42.

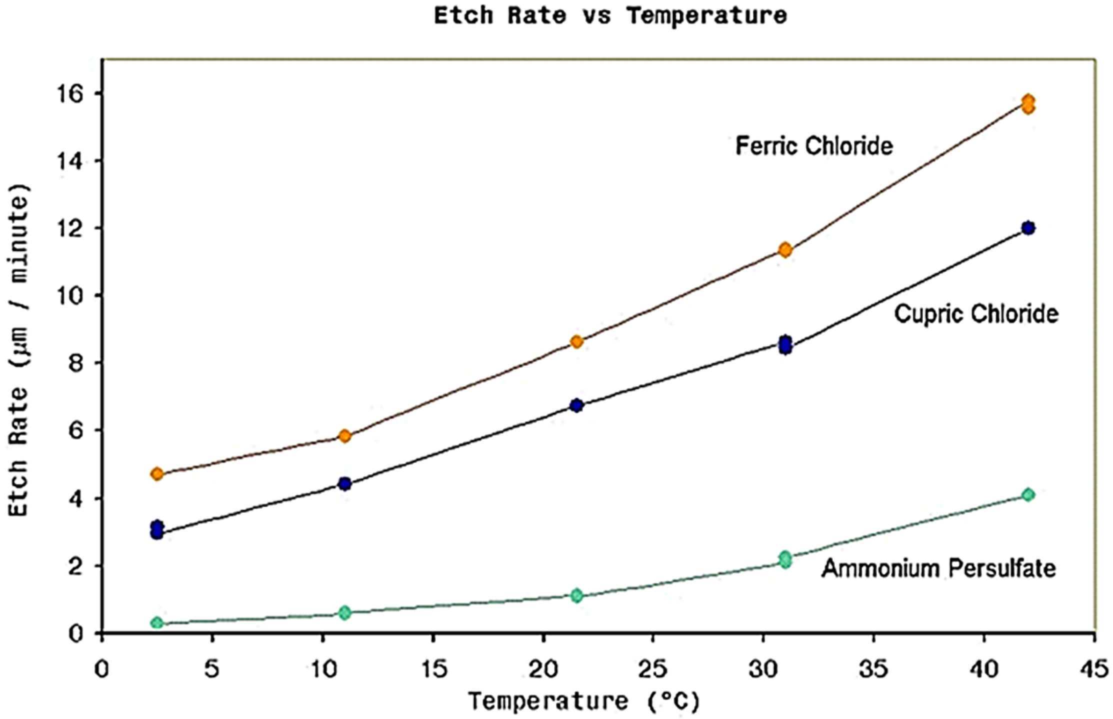

Figure 42: Etching rate versus temperature for different etchant solutions

From Figure 42, it can be noted that the ferric chloride etchant solution displays the highest etch rate over all measured temperatures followed by cupric chloride. Also, the etch rate of all etchant solutions shown in Figure 42 increases linearly as the temperature of the etchant solution increases.

Extensive tests carried out show that fabricated PCBs with well-defined copper tracks are only possible from template masks consisting of PSCs with track width and track spacing up to 200 µm. This work is therefore limited to the fabrication via wet-etching of PSCs with track width and track spacing of a minimum of 200 µm.

Using the Photoplotter, a mask for a Primary coil of 39 mm (outer diameter), track width of 250 µm, and track spacing of 200 µm was produced and etched on PCB. A secondary coil of 33 mm (outer diameter), track width of 250 µm, and track spacing of 200 µm was also fabricated on PCB by the same process.

Table 10: Comparison of characteristics for 39 mm primary coil

Characteristics	**Theoretical values**	**Measured values**
D_{outer} (mm)	39	
D_{inner} (mm)	13	
Track width, TW (µm)	250	
Track spacing, TS (µm)	200	
No. of turns, N	29.9	
Inductance, L (µH)	28.6	17.1
DC Resistance, R_{DC} (Ω)	5.4	7.8
Quality Factor, $Q_{unloaded}$	44.7	17

Table 11: Comparison of characteristics for 33 mm secondary coil

Characteristics	**Theoretical values**	**Measured values**
D_{outer} (mm)	33	
D_{inner} (mm)	11	
Track width, TW (µm)	250	
Track spacing, TS (µm)	200	
No. of turns, N	25.4	
Inductance, L (µH)	17.5	14.8
DC Resistance, R_{DC} (Ω)	3.9	3.5
Quality Factor, $Q_{unloaded}$	39	13

A comparison of measured and theoretical values for the primary 39 mm and secondary 33 mm coils is tabulated in Tables 10 and 11 respectively. It can be noted from Tables 10 and 11 that the measured values of inductance and DC resistance are comparable to the theoretical for both coils. The measured (unloaded) quality factor values are still a bit off from the theoretical pointing to the poor dielectric substrate of the PCB which influences the parasitic capacitance elements of the fabricated coil, which in turn lowers the measured Q. The coil pair configuration shown in Figure 43 - consisting of the fabricated primary 39 mm and secondary 33 mm coils - is used in this work to achieve the results that will be discussed in Chapter 4.

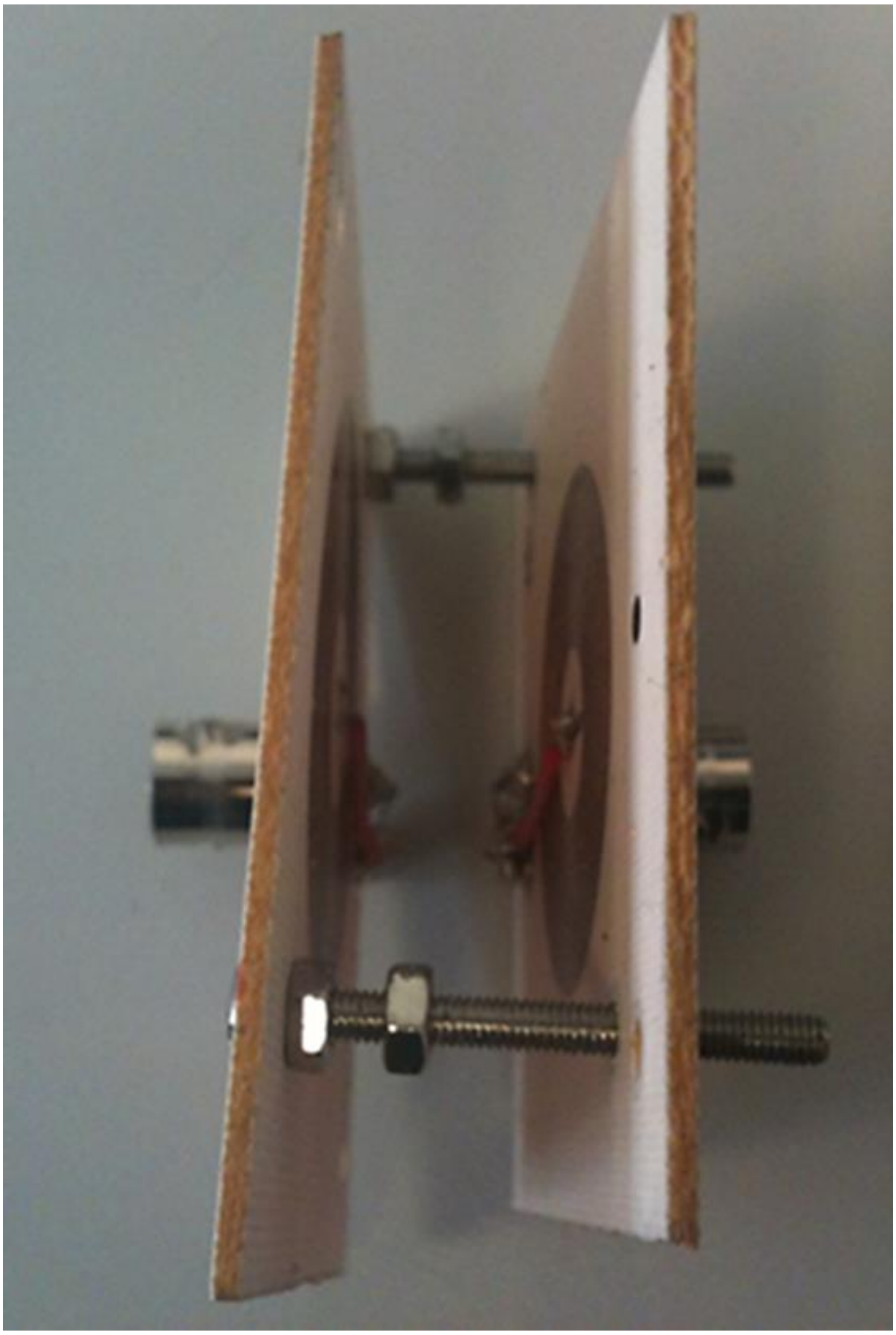

Figure 43: PCB fabrication of coil-pair configuration used in this work

3.2.1.3. Selection of parallel resonance capacitor

From [374], the resonance frequency of a parallel LC circuit is given by:

$$F = \frac{1}{2 * \pi * \sqrt{LC}} \qquad (16)$$

From equation (16), the parallel resonance capacitor required to tune the primary coil (L = 17.1 µH) to resonate at a frequency of 2 MHz is 370 pF (compared to the theoretical value of 221 pF). To tune the secondary coil (L = 14.8 µH) to resonate at a frequency of 2 MHz, the parallel resonance capacitor required is 428 pF (compared to the theoretical value of 361 pF).

3.2.2. Primary coil driver circuit

The design requirements for a coil driver, summarised by Gutmann [375], are as follows:

- A switch-mode amplifier having active elements operating as a switch should be used. This will ensure that only current is drawn without carrying voltage, thereby minimizing dissipation

- The driver output should be pure sinusoidal as only the fundamental component is received on the secondary coil

- The primary inductance is tuned with a resonance capacitor to the resonance frequency. This will cancel out the large primary leakage inductance

A dedicated amplifier (which can be Class – C, D, or E) drives the required high current into the primary coil in order to generate the magnetic fields required for power transfer. A common concept in using Class– C, D, or E amplifiers are that the primary tank freely resonates using the power supply and the drive transistor just to compensate for the tank losses. Additionally, primary coil drivers are not linear amplifiers since their output signal is not an amplified representation of their input signal. They merely act as a DC to AC power inverter taking up the DC energy from the supply source and converting it, as efficiently as possible, into AC energy to power the primary coil. The output is either a sinusoidal current into the coil or a sinusoidal voltage across the primary coil whereas the input signals are pulses [376]. To describe the design of the coil driver, two circuits will be discussed – a transceiver circuit using an NMOS driver and a CMOS logic gate IC driver circuit.

3.2.2.1. Transceiver circuit using NMOS driver

The circuit diagram of the transceiver shown in Figure 44 is reproduced from our paper [72]. The transceiver showcases the transcutaneous transfer of power as well as the transmission of data (in this case audio music) using a single pair of coils.

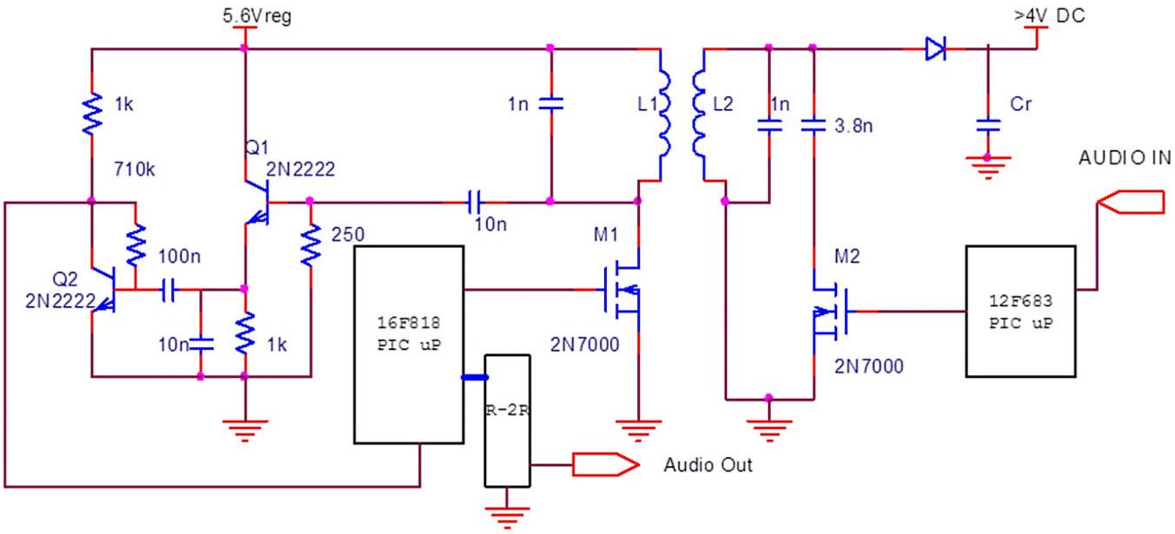

Figure 44: Transceiver circuit consisting of an NMOS driver

Using a regulated DC supply source of 5.6 V, power is transferred over a 5 mm air gap between a single pair of 25 mm (outer diameter) coils (see specification in [72]). About 4 V DC (rectified) is supplied to the secondary Microchip PIC 12F683 µC [345]. The energized secondary µC then samples audio music from an mp3 player connected to one of its analog inputs and converts it to a digital bit stream using its in-built ADC. The digital bit stream amplitude modulates (ASK) the incoming carrier signal using a 2N7000 NMOS transistor [344] situated at the secondary coil circuit. Using the 2N2222 BJT transistors [377] in Figure 44, the modulated signal appearing on the primary coil (via mutual inductance) is buffered, rectified and then amplified in order to reproduce the original bit stream which is inputted into the in-built 'software-configured' DAC of the primary Microchip PIC 16818 µC [378]. The DAC outputs a parallel 8 bit-word which is passed through an R2R resistor network to reconstruct the original transmitted analog music and outputted via a loudspeaker. Taking into consideration power consumption, the entire system draws 45 mA from the single 5.6

V DC supply (Total power consumed = 0.25 W) of which 25 mA is drawn by the coil drive circuitry. Signals at various points across the transceiver system as well as the system software flow-chart are shown in Figure 45.

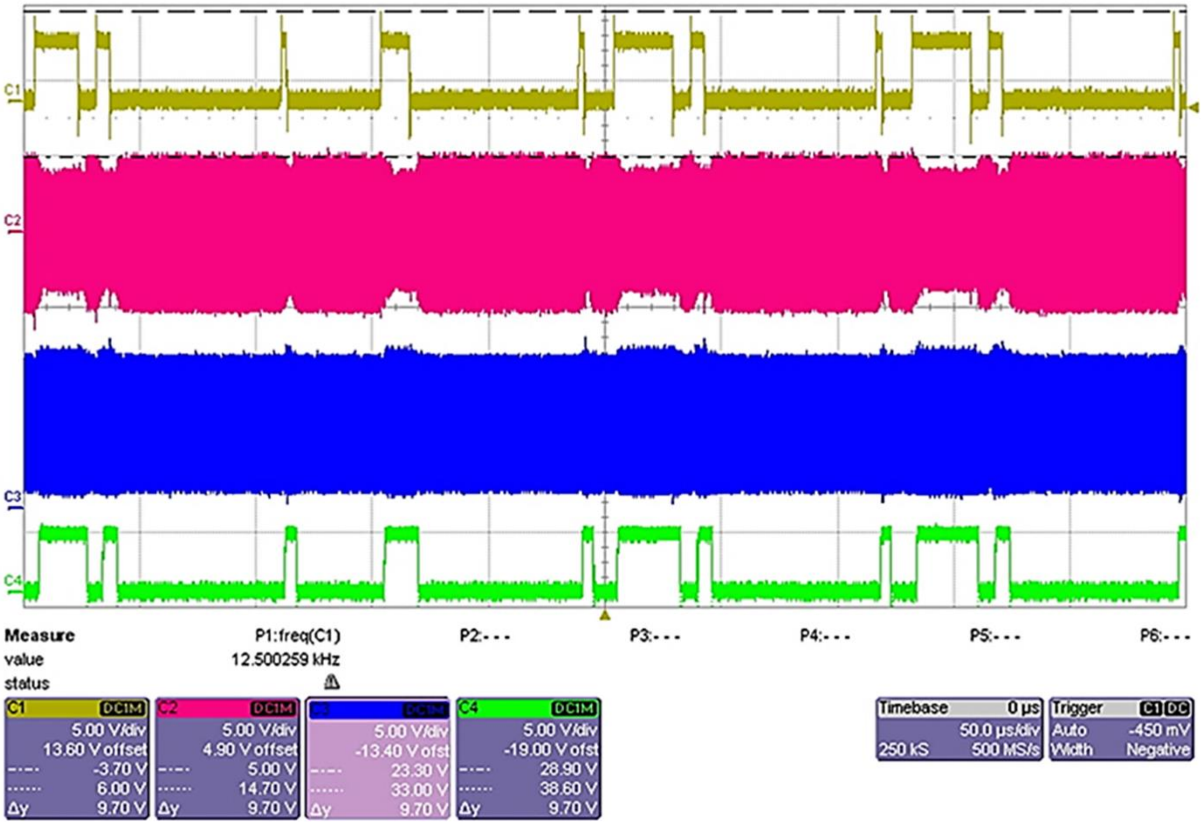

Measure	P1:freq(C1)	P2:- - -	P3:- - -	P4:- - -	P5:- - -	P6:- - -
value	12.500259 kHz					
status	⚠					

C1 DC1M	C2 DC1M	C3 DC1M	C4 DC1M
5.00 V/div	5.00 V/div	5.00 V/div	5.00 V/div
13.60 V offset	4.90 V offset	-13.40 V ofst	-19.00 V ofst
-·-·- -3.70 V	-·-·- 5.00 V	-·-·- 23.30 V	-·-·- 28.90 V
······ 6.00 V	······ 14.70 V	······ 33.00 V	······ 38.60 V
Δy 9.70 V	Δy 9.70 V	Δy 9.70 V	Δy 9.70 V

Timebase	0 µs	Trigger	C1 DC
	50.0 µs/div	Auto	-450 mV
250 kS	500 MS/s	Width	Negative

(a)

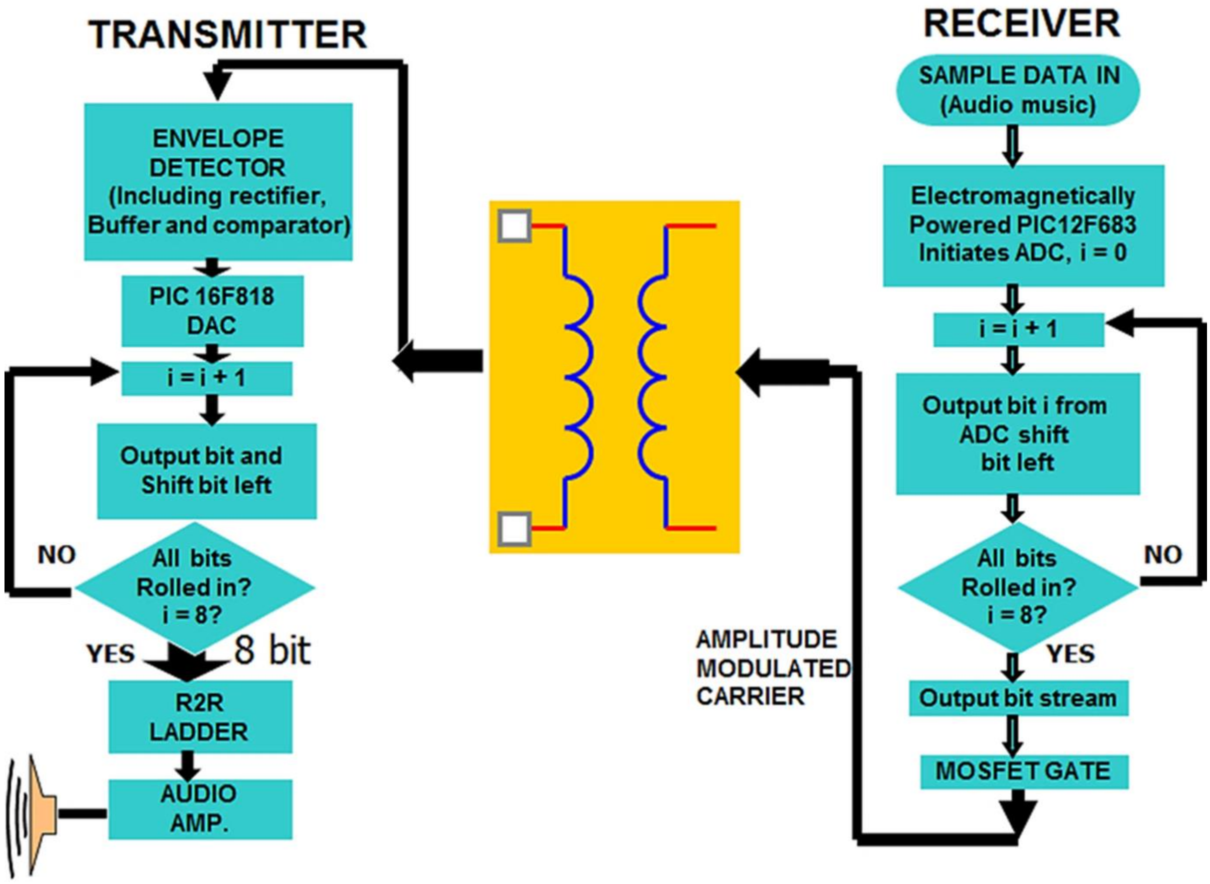

(b)

Figure 45: Transceiver outputs (a) captured signals across system (b) system software flowchart

Figure 45a is the oscilloscope trace of captured signals across the circuit in Figure 44. The horizontal axis in Figure 45a is propagation delay while the vertical axis is voltage. Trace C4 (green) in Figure 45a is the transmitted digital bit stream from the secondary µC. Trace C2 (pink) is the modulated signal at the secondary coil, L2. Trace C3 (blue) is the modulated signal mutually induced across the primary coil, L1. Trace C1 (brown) is the reconstructed digital bit stream fed into the primary µC. The following can be noted from Figure 45a:

- The reconstructed digital bit stream (Trace C1) is an exact replica of the transmitted data bit stream (Trace C4).

- The modulated signal on the secondary coil (Trace C3) shows the low amplitude of the data (the ‘humps’ above the carrier signal) compared to the carrier signal – hence the need for buffering (to prevent loading), filtering and rectification (to remove the negative half cycle of the carrier signal), and amplification (to raise the voltage level to that acceptable by the primary µC).

3.2.2.2. Prototype CMOS logic-gate IC driver

To lower the power consumed by the driver circuit (25 mA for a 5.6 V supply) a prototype, all-CMOS coil driver was designed, simulated (using OrCAD PSpice) and fabricated on PCB. The prototype all-CMOS logic gate coil driver consists of a combination of AND/XOR logic gate buffers driving an RC network. The AND gates are formed from a single quad dual-input CMOS 74HC08 IC chip [379] while the XOR gate is formed from a single quad dual-input CMOS 74HC86 IC chip [380]. The PSpice circuit simulation is shown in Figure 46.

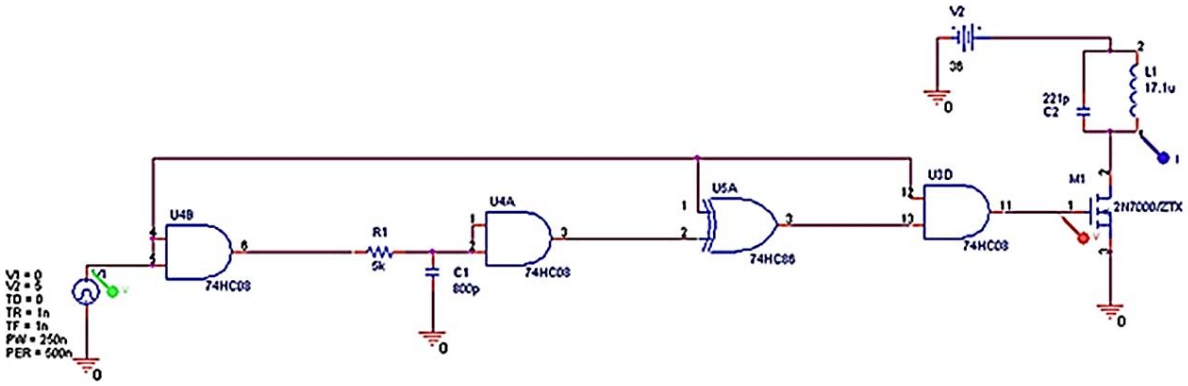

Figure 46: PSpice simulated prototype CMOS coil driver circuit

Clock pulses are generated at the resonant frequency of the primary coil, i.e. 2 MHz (PER = 500 ns). The time delay created by charging this network results in an increase in pulse transit time between AND gates. The delayed arrival of that pulse versus the applied input clock enables the XOR gate to produce a narrow output pulse equivalent to the difference at its inputs every time the clock changes state. The output of the XOR gate is then fed into another AND gate in order to clock its output so that only one of the two changes per clock cycle remains. The resulting narrow pulse is then fed to the gate of a 2N7000 MOSFET and used to switch the connected supply through the primary coil. In order to observe the circuit, voltage probes were placed at the output of the clock pulse generator (green trace) and at the gate of the 2N7000 (red trace). A current probe was also placed at the primary coil (blue trace). Changing the values of R1 and C1 changes the width of the drive pulse observed at the gate of the 2N7000 and therefore the current through the primary coil and consequently, the consumed power. The simulated output A/D waveform of Figure 46 is shown in Figure 47.

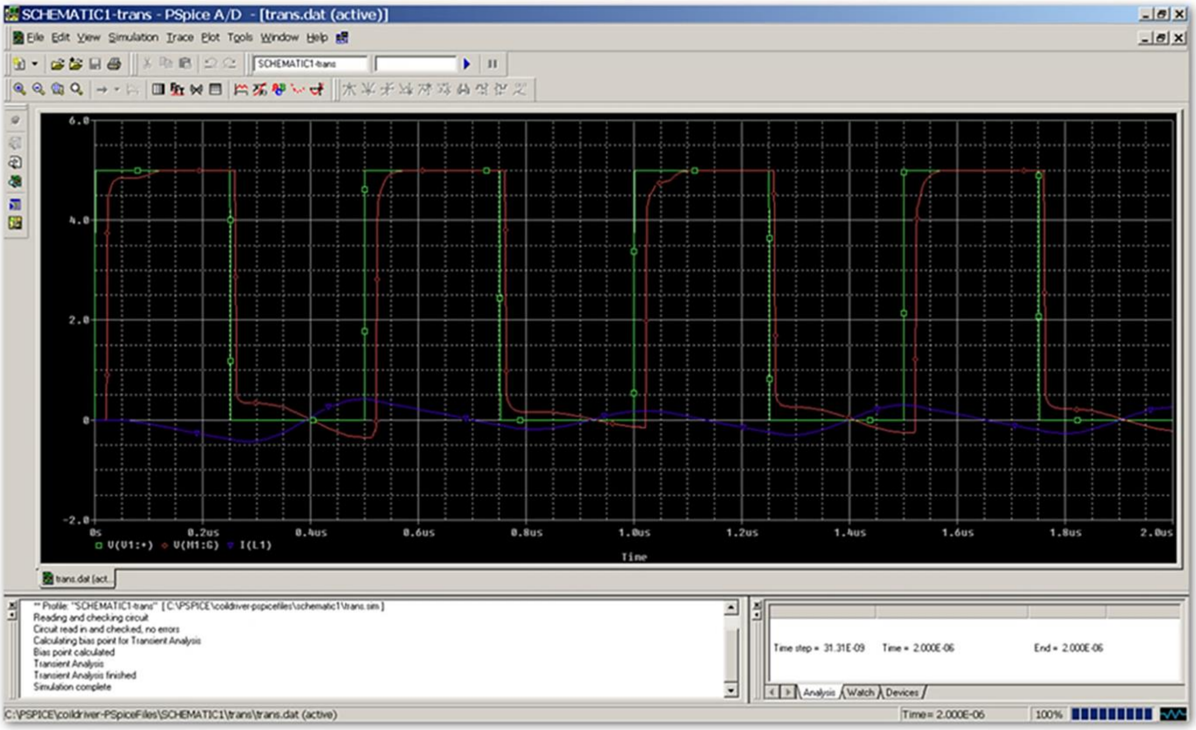

```
** Profile: "SCHEMATIC1-trans" [ C:\PSPICE\coildriver-pspicefiles\schematic1\trans.sim ]
Reading and checking circuit
Circuit read in and checked, no errors
Calculating bias point for Transient Analysis
Bias point calculated
Transient Analysis
Transient Analysis finished
Simulation complete
```

```
Time step = 31.31E-09     Time = 2.000E-06          End = 2.000E-06
```

```
C:\PSPICE\coildriver-PSpiceFiles\SCHEMATIC1\trans\trans.dat (active)     Time= 2.000E-06     100%
```

Figure 47: Simulated output A/D waveform for circuit in Figure 43.

The blue trace in Figure 47 represents the current through the primary coil L1. The red trace, on the other hand, represents the drive pulse into the gate of transistor M1, the 2N7000 while the green trace represents the input clock pulse. Setting R1 = 5 KΩ and C1 = 800 pF (in Figure 46) produces a 0.25 µs wide pulse which drives the gate of transistor M1 thereby switching close to 1 A_{p-p} AC current through the primary coil.

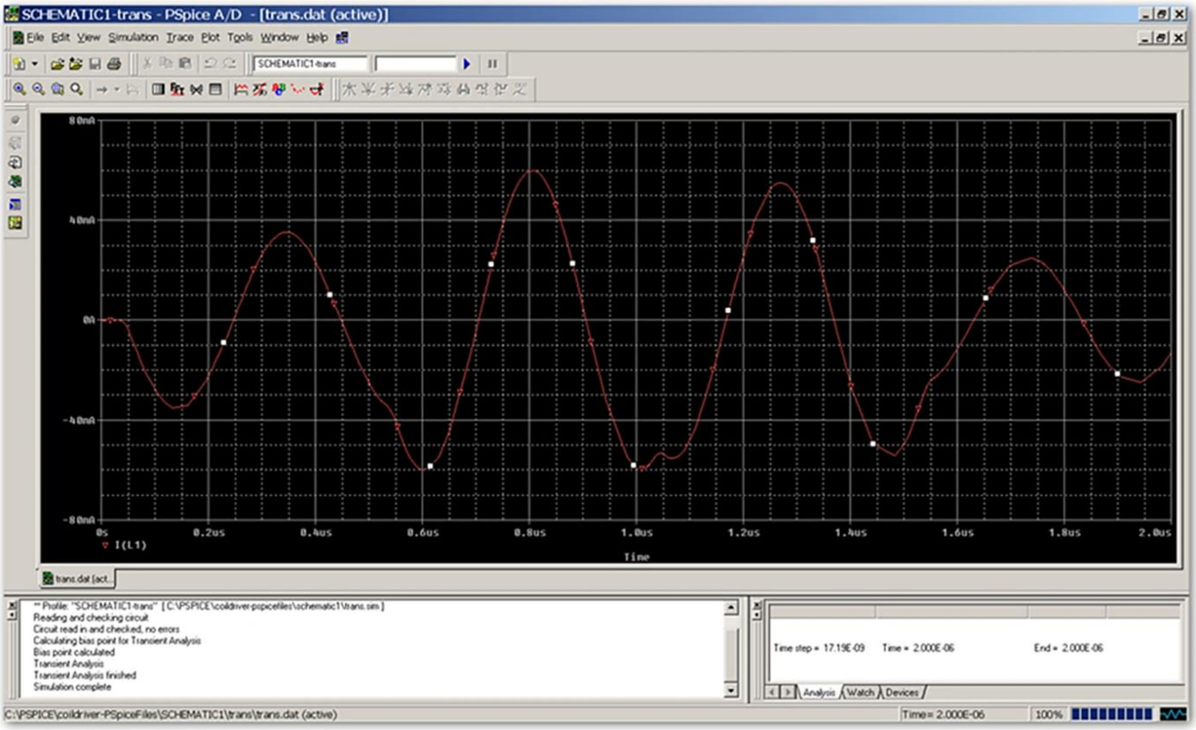

```
** Profile: "SCHEMATIC1-trans"  [ C:\PSPICE\coildriver-pspicefiles\schematic1\trans.sim ]
Reading and checking circuit
Circuit read in and checked, no errors
Calculating bias point for Transient Analysis
Bias point calculated
Transient Analysis
Transient Analysis finished
Simulation complete
```

```
Time step = 17.19E-09    Time = 2.000E-06    End = 2.000E-06
```

```
C:\PSPICE\coildriver-PSpiceFiles\SCHEMATIC1\trans\trans.dat (active)    Time= 2.000E-06
```

Figure 48: PSpice simulation of coil current with varied R1C1

On the other hand, changing R1 = 50 Ω and C1 = 100 pF (in Figure 46) switches about 100 mA through the primary coil as shown in Figure 48. The fabricated prototype CMOS logic gate primary coil driver circuit is shown in Figure 49.

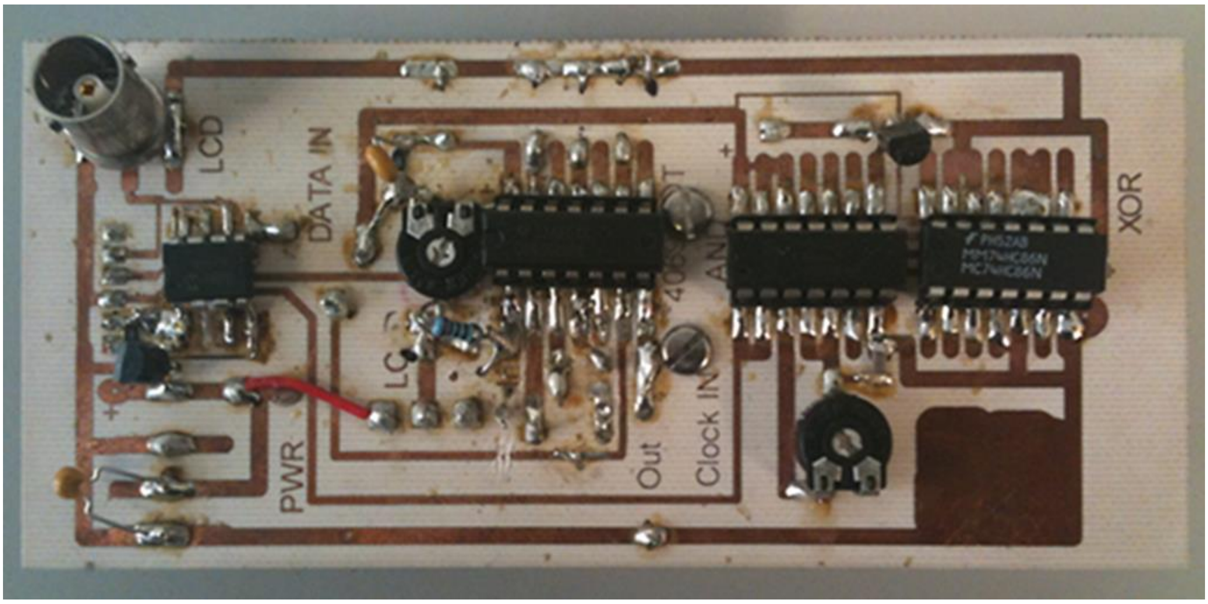

Figure 49: Fabricated prototype coil driver circuit

3.2.3. Inductive sub system envelope detection circuit

The amplitude modulated signal - mutually induced to the primary coil (Trace C3 in Figure 45a) – is passed through the envelope detection circuit in Figure 50 to reconstruct the transmitted data bit stream.

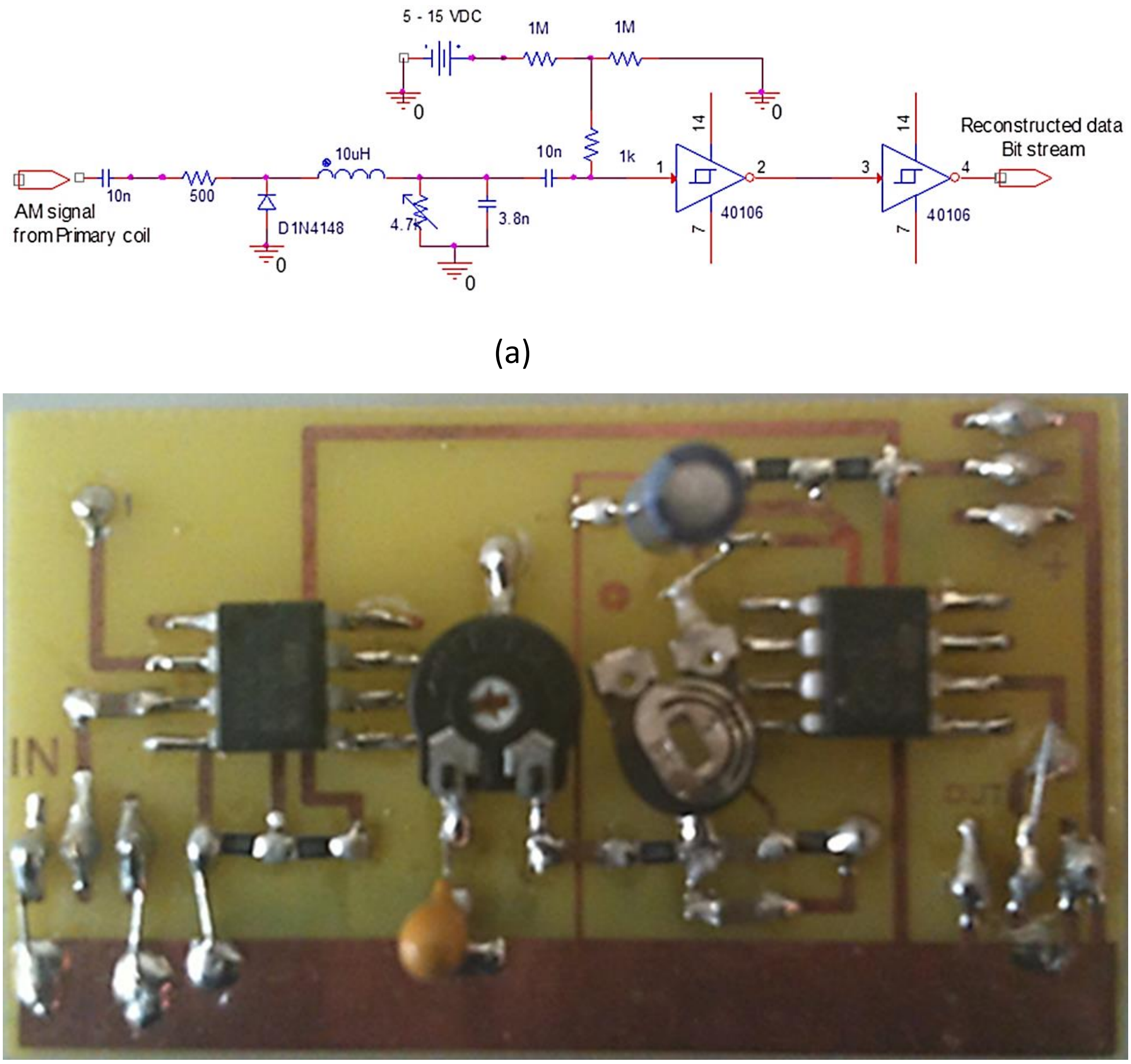

(a)

(b)

Figure 50: Envelope detection circuit (a) schematic (b) PCB fabrication

The envelope detection circuit in Figure 50a is built around the HEF 40106B Hex Inverting Schmitt Trigger IC [381]. The coupling devices in Figure 50a (series connected 10 nF capacitor and 500 Ω resistor) ensure that the primary coil is not unnecessarily loaded during the reconstruction of the data bit-stream. The D1N4148 high speed diode [382] ensures that the negative half cycle of the modulated signal is shorted to ground. Only the positive half cycle of the modulated signal containing the data bit stream passes through to the low-pass filter which attenuates and filters out the high frequency carrier signal. The two Schmitt trigger ICs reconstructs the data bit-stream. Figure 51 shows the reconstructed data bit stream.

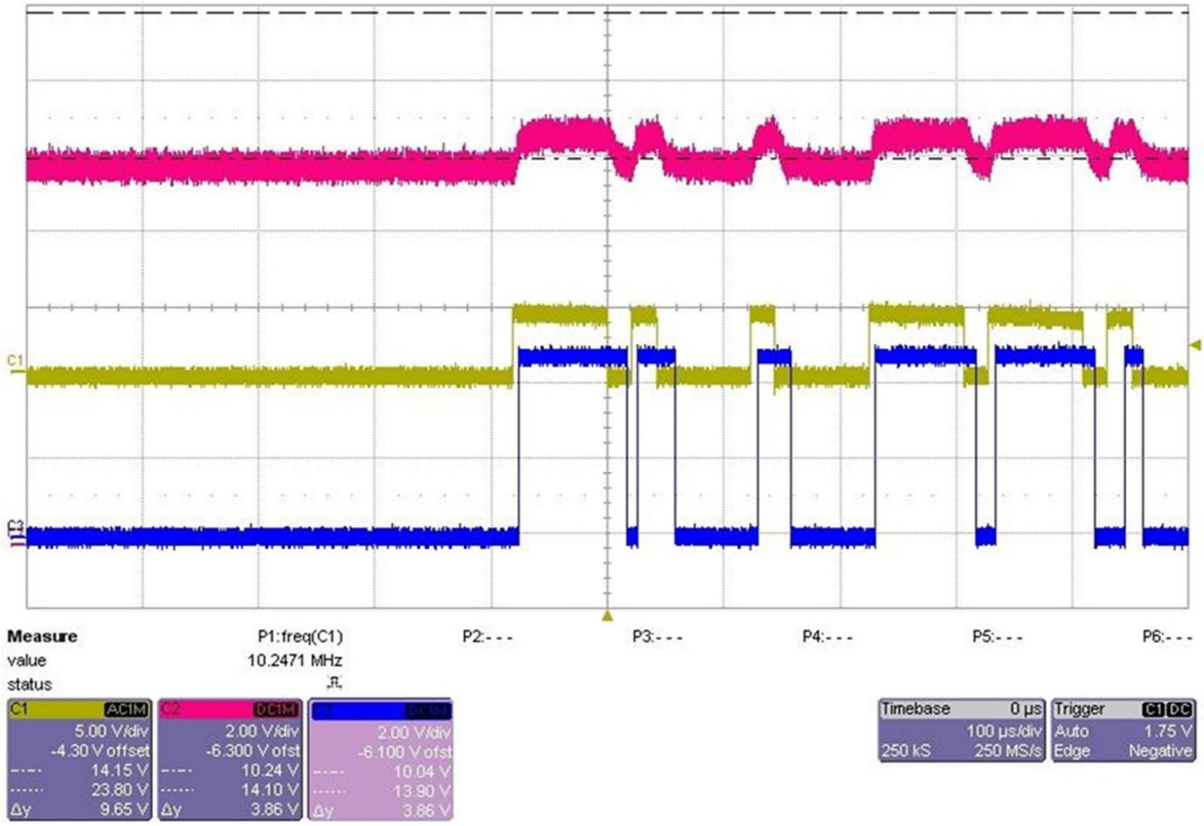

Measure P1:freq(C1) P2:- - - P3:- - - P4:- - - P5:- - - P6:- - -
value 10.2471 MHz
status

C1 AC1M: 5.00 V/div; -4.30 V offset; 14.15 V; 23.80 V; Δy 9.65 V
C2 DC1M: 2.00 V/div; -6.300 V ofst; 10.24 V; 14.10 V; Δy 3.86 V
C3 DC1M: 2.00 V/div; -6.100 V ofst; 10.04 V; 13.90 V; Δy 3.86 V
Timebase 0 µs; 100 µs/div; 250 kS 250 MS/s
Trigger C1 DC; Auto 1.75 V; Edge Negative

Figure 51: Reconstructed data bit-stream at output of envelope detection circuit

Figure 51 is the oscilloscope trace of the reconstructed data bit stream at the output of the envelope detection circuit. In Figure 51, the horizontal axis is propagation delay while the vertical axis is voltage. In Figure 51, Trace C1 (brown) in Figure 51 is the transmitted digital data bit-stream. Trace C2 (pink) is the signal seen at the input into the first Schmitt trigger IC (Figure 50a) but raised on a 10 V DC voltage level. Trace C3 (blue) is the output of the second Schmitt trigger IC i.e. the reconstructed data bit-stream which is the exact replica of the original transmitted data bit stream of Trace C1.

To conclude, masks of the fabricated circuits were produced on transparency film using PCB Wizard Professional Edition 3.50 from New Wave Concepts Ltd [383]. Devices/components used on PCBs were Surface-mount (SMD) ensuring that the finished footprint is as compact as possible. PIC µCs used in this work were programmed and configured using the MPLAB Integrated Development Environment (IDE) by Microchip [384] - [385], the CCS C-compiler by Custom Computer Services, Inc. [386], the PICkit 3 programming and debugging interface by Microchip [387] - [388], and the Logic 8 analyser by Saleae [389].

Propagation tank tests to determine the characteristics of the piezoelectric immersible disc probes have been described. The results of the propagation tests show that the optimum combination pair for the ultrasonic sub system is Pz21 (transmitter) and Pz26 (receiver) driven at a resonance frequency of 200 kHz and placed 7 cm apart.

In the inductive coupling sub system discussed, the PCB fabricated printed spiral coils (PSCs) were 39 mm (primary) and 33 mm (secondary).

4. EXPERIMENTAL RESULTS

In the preceding chapter, characteristics of immersible PZT disc probes used in this research work are obtained via propagation tank tests and discussed. Using the characteristics obtained, the ultrasonic sub system comprises the combination pair of Pz21 (transmitter) and Pz26 (receiver) both driven at 200 kHz, 40 V supply and placed 70 mm apart. The analysis of PCB fabricated printed spiral coils (PSCs) were also highlighted with the inductive coupling sub-system comprising the pair of 39 mm (primary) and 33 mm (secondary) PSCs.

In this chapter, a system test set up carried out under laboratory conditions is discussed. The experiments highlighted verify the performance of the combined inductive and ultrasonic sub-systems developed in Chapter 3. Results obtained will amplify and support the potential of this proof-of-concept, novel, and generic multi-tier power transfer and data communication interface system for low-power, deeply implantable analog bio-sensors.

Results detailed in this chapter have been published in [70 – 72].

The block diagram of the combined inductive and ultrasonic multi-tier interface prototype system is shown in Figure 52.

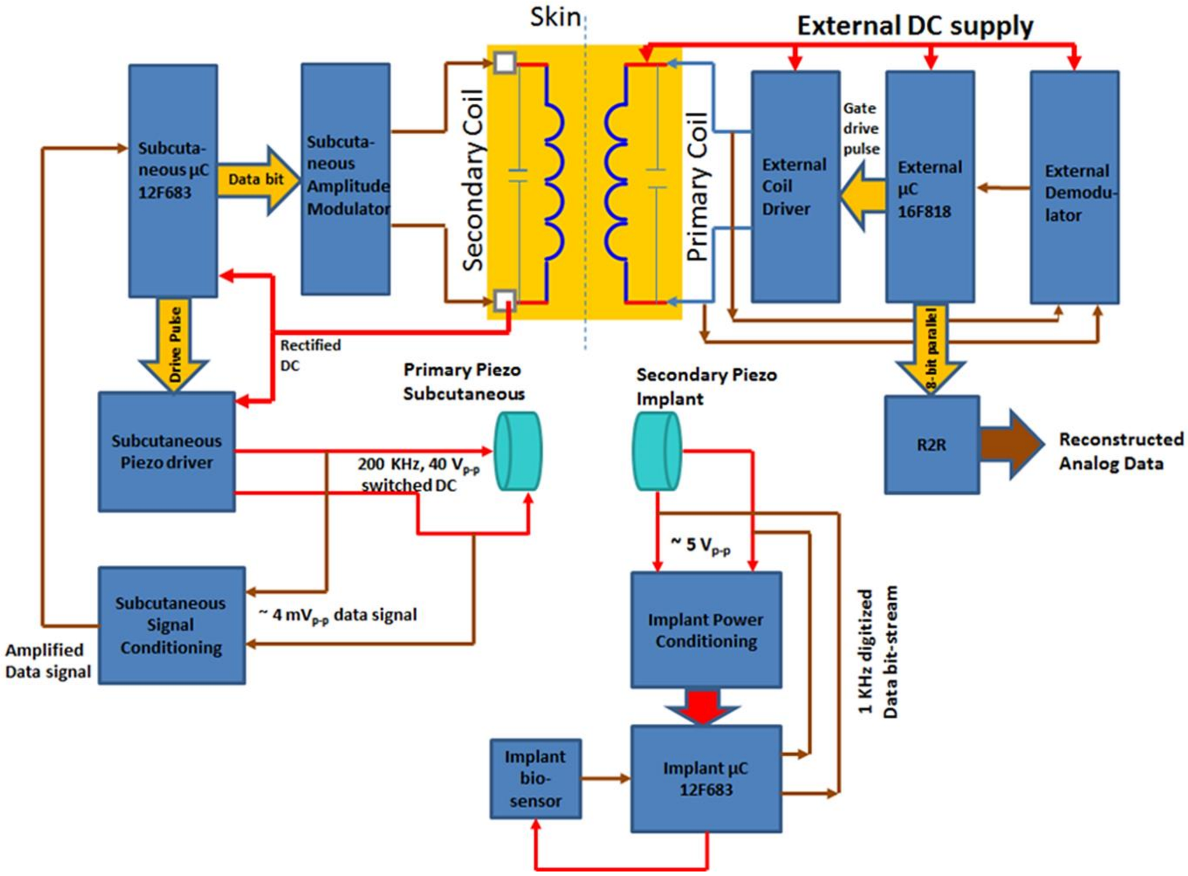

Figure 52: Block diagram of combined Inductive and Ultrasonic sub-systems [Red denotes power, brown analog data and yellow analog data]

Figure 52 is the block diagram of the combined Inductive Coupling and Ultrasonic sub-systems developed in Chapter 3. In Figure 52, red signifies power lines; brown indicates analog data signals; and yellow indicates µC generated digital signals. The external devices and circuitry are situated in the upper right hand side; the subcutaneous devices and circuitry are placed on the left hand side, while the implant devices and circuitry are situated in the bottom right hand side. The external DC supply drives the primary coil via the driver circuit. This power is transferred through the air-gap to the secondary coil via mutual inductance. The rectified induced AC voltage on the secondary coil powers both the subcutaneous µC and the subcutaneous piezo driver circuit driving the primary piezo disc. The driven primary piezo disc generates ultrasonic waves (via the indirect effect) which are sensed and converted by the secondary (implant) piezo disc. The low-amplitude ac voltage output from the secondary piezo disc is fed to the power conditioning circuit which powers the implant µC and then the implant bio-sensor. This is the power transfer phase. In the data transmission phase, the powered implant µC senses analog data from the implant bio-sensor and converts to digital using it's in built ADC. The generated digital bit stream is used to drive the implant piezo disc. Ultrasonic waves generated by the implant piezo disc are converted by the primary piezo disc (via the direct effect) to low amplitude ac voltage output which is passed through the signal conditioning circuit and the in-built comparator circuit of the subcutaneous µC to reconstruct the transmitted digital bit stream. The reconstructed digital bit stream is then amplitude modulated on the power carrier at the secondary coil. The induced modulated power carrier sensed at the primary coil is passed through the demodulator circuit and the in-built comparator circuit of the external µC to reconstruct the transmitted digital bit stream. The R2R digital to analog converter (DAC) reconstructs the transmitted analog data. The PCB fabricated implant circuit is shown in Figure 53.

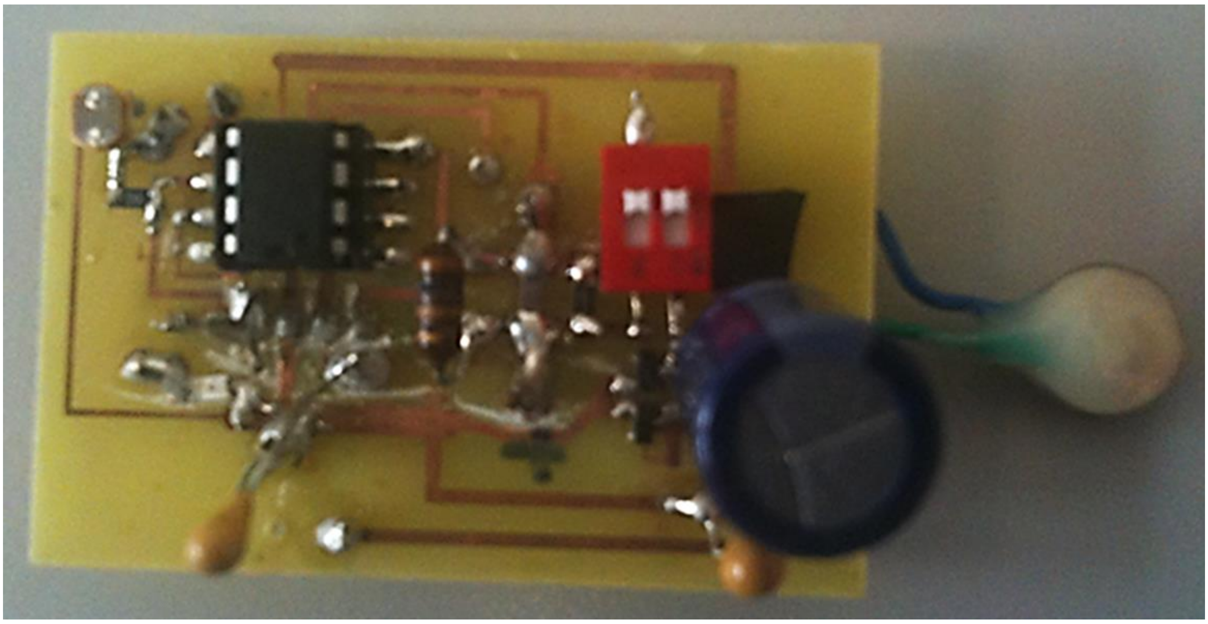

Figure 53: PCB fabricated implant circuit

The implant circuit in Figure 53 consists of the power conditioning circuit, the implant µC, the bio-sensor (in this case a light sensitive resistor), and the secondary piezo disc. Notice that the implant secondary piezo disc in Figure 53 is covered in glue. It was observed during tests that discs covered in glue suffered minimal degradation due to high DC voltage switching when immersed in liquid.

4.1. System test set-up

To verify the performance of the proposed multi-tier interface system, tests were conducted to measure power transfer (i.e. efficiency) as well as data transmission. The overall experimental system test setup is shown in Figure 54.

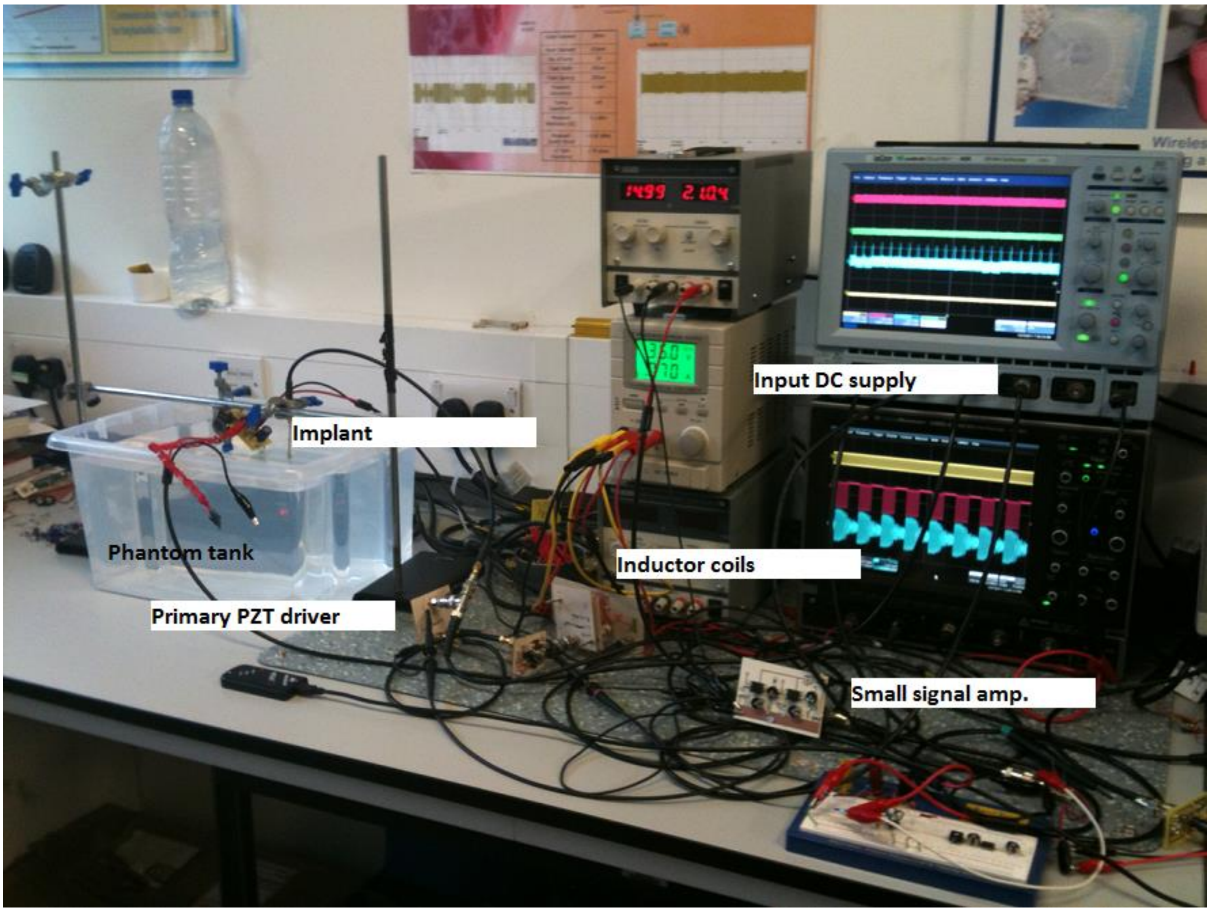

Figure 54: Experimental system test set-up

A CircuitSpecialists CS11200K 120 V, 1 A DC regulated Power Supply Unit (PSU) [390] is preset to supply 35 V DC. Using inductive coupling (via mutual inductance), this voltage is transferred using a single pair of parallel-tuned, circular, air-cored, planar printed spiral coils (PSC) placed 10 mm apart. Human skin is between 2 mm and 5 mm thick so an air-gap of 10 mm was used as a ‘worst case scenario’. Previous tests carried out using meat/pork/sausages showed that attenuation is equivalent to that of air.

Table 12: Specifications of test primary and secondary PSCs

Outer Diameter (mm)	39 (External Primary coil)	33 (Subcutaneous Secondary coil)
Inner diameter (mm)	13	11
Number of turns	29.9	25.4
Track width (µm)	250	250
Track spacing (µm)	200	200
Measured inductance (µH)	17.1	14.8
Tuning resonance capacitor (pF)	221	361
Measured DC resistance (Ω)	7.8	5.6
Measured Quality factor @ 2 MHz	17	13
LC tank impedance @ 2MHz (Ω)	204	170

The coils, specified in Table 12, were produced to the highest density allowable using the standard FR4 chemical 'wet' etching techniques detailed in Section 3.2.1.2. The Fluke PM 6303A RCL meter [391] was used to measure the inductance, DC resistance and quality factor of the PSCs.

The primary coil, driven by the prototype and power-efficient CMOS logic gate circuit (Section 3.2.2.2), produces upto 80 $V_{p\text{-}p}$ AC voltage across the secondary coil via mutual inductance. This is full wave rectified to provide 5 V DC for the subcutaneous µC and 40 V DC for the subcutaneous piezo driver – switching the 40 V DC across the primary piezo disc to excite it in its radial/planar mode. There is no additional power source of any kind under the skin. The Microchip PIC 12F683 µC was selected because of its inherent ability to be software configured to operate with an input supply as low as 2 V DC, a built-in comparator and ADC circuitry, and a software-selected operating frequency of as low as 31 KHz for ultra-low power consumption.

Table 13: Specifications of test primary and secondary piezo discs

Type	Pz21 Primary piezo disc	Pz26 Secondary piezo disc
Diameter (mm)	10	10
Thickness (mm)	1	1
Hardness	Soft relaxor	Hard
Relative Dielectric Constant, K_{33}^T	3800	1300
Coupling coefficient, k_p	0.6	0.57
Coupling coefficient, k_{31}	0.33	0.33
Piezoelectric charge coefficient, d_{31} (pC/N)	260	130
Mechanical Quality factor, $Q_{m,p}$	65	> 1000
Density, ρ (g/cm^3)	7.8	7.7
Piezoelectric voltage coefficient, g31 (Vm/N)	0.0074	0.0109
Measured Capacitance (F)	2.43n	850p
Measured Impedance (Ω)	1K	800

Primary and secondary piezo discs, specified in Table 13, are fixed 70 mm apart, face-to-face, and immersed in the prepared homogeneous phantom (see Section 3.1.4.1 for recipe details) contained in a tank measuring 38 x 27 x 20 cm (L x B x H). The combination pair of Pz21-Pz26 was chosen because of their experimentally-determined maximum power transfer (Section 3.1.5). The radially excited primary piezo disc generates ultrasonic energy pressure waves which are radially propagated through the phantom. By the direct piezoelectric effect, the secondary piezo disc on the implant circuit converts the received ultrasonic energy into low-amplitude AC voltage which is then boosted by the parallel LC resonator circuit in the power conditioner

(Section 3.1.9) to ensure that 0.3 V DC is supplied to the input of the Seiko start-up chip (Figure 30) after rectification. This turns on the start-up chip intermittently supplying the implant µC with 2.4 V DC each time its load capacitor is fully charged. The implant µC is programmed to turn on for an input supply voltage of 2 V DC. The energised implant µC powers the implant bio-sensor and samples its output analog sensed data converting it into a digital bit-stream using its built in ADC and transmits the converted digital sensed data bit-stream as a burst of ultrasonic pulses into the phantom at the moment when the power carrier is switched off, momentarily. The implant transmitted data bit-stream is recovered at the output of the subcutaneous signal conditioning circuit and amplitude modulated on the power carrier and reconstructed as described in Section 3.2.3.

In compliance with the 0.4 W/kg limit of exposure of humans to RF electromagnetic signals as well as limits to ultrasonic signals [392]-[400], power transfer through the skin, and thus through the body to the implant is intermittent. According to [73], [92] - [93], [401], and [402], a low active duty-cycle – achieved by operating the system intermittently - ensures that system power consumption is kept to a minimum.

Collated results will be discussed under the following headings: power transfer efficiency and transmission signals (comprising energy transfer signals, data transmission signals and timing signals).

4.2. Power transfer efficiency

The power transfer efficiency results will be discussed for both the inductive as well as the ultrasonic sub-system.

4.2.1. Inductive sub-system power transfer efficiency

The primary and secondary tuned (inductive) circuits (Figure 52) both form a parallel resonant LC tank. The equivalent circuit for parallel LC circuits considers two additional resistances: R_L – the series inductive resistance and R_C – the series capacitive resistance [403]. In this view, the total tuned impedance can be calculated using:

$$Z = \frac{(R_L + X_L)*(R_C - X_C)}{(R_L + R_C)+(X_L - X_C)} \tag{17}$$

Where:
R_L = series inductor resistance
R_C = series capacitor resistance
X_L = inductor coil impedance @ 2 MHz
X_C = tuning capacitor impedance @ 2 MHz

Primary coil
39 mm; L = 17.1 µH (measured), R_L = 7.8 Ω (measured); Tuning capacitor (@ 2 MHz) = 221 pF, R_C = 2.7 KΩ (measured); supply voltage, V = 35 V_{DC}
$X_L = 2\pi fL = 215\ \Omega$; $X_C = 1/2\pi fC = 360\ \Omega$
From (17), $Z_{Primary} = 204\ \Omega$
Power, $P = V^2/Z_{Primary} = 6$ W

Secondary coil
33 mm; L = 14.8 µH (measured);
R_L = 5.6 Ω (measured); R_C = 1.7 KΩ (measured);
Tuning capacitor (@ 2MHz) = 361 pF;
Voltage across secondary coil = 80 V_{p-p};
$V_{rms} = V_{peak}/\sqrt{2} = V_{p-p}/2\sqrt{2} = 28.3$ V
$X_L = 2\pi fL = 186\ \Omega$; $X_C = 1/2\pi fC = 220\ \Omega$
From (17), $Z_{Secondary} = 170\ \Omega$
Power, $P = V_{rms}^2/Z_{Secondary} = 5$ W

4.2.2. Ultrasonic sub-system power transfer efficiency

Using the ultrasonic piezo disc equivalent circuit in [404] and [405],

$$Z_{\text{Total}} = \frac{X_C * Z}{X_C + Z} \qquad (18)$$

Where: X_C = Piezo disc capacitive impedance @ 200 kHz
Z = Total parallel internal impedance

Primary piezo Pz21: C = 2.43 nF; Z = 1 KΩ (measured)
$X_C = 1/2\pi fC = 328$ @ 200 kHz
From (18), $Z_{\text{Total}} = 247\ \Omega$
Effective supply voltage, $V = V_{\text{rms}}$ x duty cycle
$= (V_{\text{p-p}}/2\surd 2) \times 0.5 = 14$ V
Power, $P_{\text{Primary}} = V^2/Z_{\text{Total}} = 0.8$ W

Secondary piezo Pz26: C=850 pF; Z = 800 Ω (measured)
$X_C = 1/2\pi fC = 936\ \Omega$ @ 200 kHz
From (18), $Z_{\text{Total}} = 431\ \Omega$
Effective supplied voltage, $V = V_{\text{p-p}}/2\surd 2 = 1.77$ V
Power, $P_{\text{Secondary}} = V^2/Z_{\text{Total}} = 8$ mW

4.2.3. Overall system power transfer efficiency

Power transfer efficiency across the entire prototype system is shown in the block diagram in Figure 55.

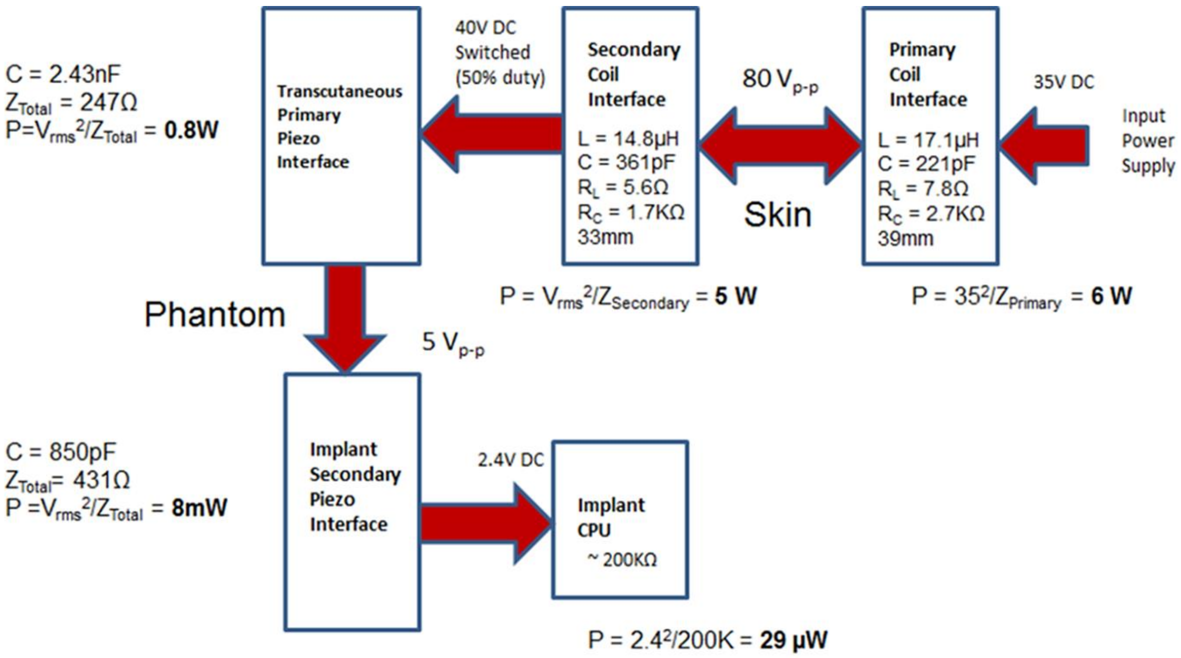

Figure 55: Power efficiency values across the prototype system

It can be noted from Figure 55 that a single 35 V DC external source supplies 29 µW to an implant immersed 70 mm deep inside a homogenous liquid phantom using a multi-tier interface combining inductive coupling and ultrasonics. Though this power supplied to the implant is small, it is sufficient to power a 200 KΩ implant circuit causing it to sample and send sensed data as an 8-bit digital bit-stream to the external receiver through the same multi-tier interface system.

An input supply of 35 V_{DC} across the primary coil (input power = 6 W) produces 80 V_{p-p} (which is below the FCC Maximum Permissible EM Exposure levels) across the subcutaneous secondary coil (transferred power = 5 W) via mutual inductance giving an inductive sub system transfer efficiency of 83%. The full wave rectified secondary coil voltage supplies 40 V_{DC} (which is below the FDA limits of I_{SPTA} = 720 mW/cm^2 and Mechanical Index (MI) = 1.9) which is switched across the subcutaneous primary piezo disc (power = 0.8 W). The 5 V_{p-p} output voltage across the implant secondary piezo disc (transferred power = 8 mW) supplies 2.4 V_{DC} to the implant circuitry giving an ultrasonic sub system efficiency of 1%.

Table 14: Summary of power transfer efficiency of prototype system

Circuit	**Power in (W)**	**Power out (W)**	**Efficiency (%)**
Inductive sub system	6	5	83
Ultrasonic sub system	0.8	0.008	~ 1

The summary of the power transfer efficiency for both the Inductive sub-system and the ultrasonic sub system is tabulated in Table 14. The power transfer efficiency of the ultrasonic sub system is low, yet it is corroborated by simulation results by Denisov [298].

Comparison of the prototype multi-tier interface system with single-tier interface systems is tabulated in Tables 15 and 16 for ultrasonic systems and inductive systems, respectively

Table 15: Comparison of ultrasonic interface systems

Ref	Disc specification	Excitation mode	Distance between discs (mm)	Power transfer efficiency (%)	Power consumption (mW)
[202]	Transmitter = 18mm, 3.15MHz. Receiver = 35mm, 4.2MHz Single pair of disc both immersed	Not included	70	0.3	229
[203]	Transmitter = 15mm, 673kHz. Receiver = 15mm, 673kHz 1.3mm graphite matching layer Single pair of disc, transmitter external	Thickness	40	27	260
[200]	Transmitter = 30mm, 840kHz. Receiver = 25mm, 840kHz Single pair of disc, transmitter external	Thickness	98	25	1000 (max)
[72] our paper	Transmitter = 10mm, 200kHz Receiver = 10mm, 200kHz Single pair of disc, both immersed	Radial	70	1	28

Table 16: Comparison of inductive interface systems

Ref	Device specifications	Drive scheme	Distance between coils (mm)	Power transfer efficiency (%)	Power consumption (W)
[157]	Primary=33cm, L=12µH, 2MHz. Secondary=square-angled 2cmX4cm, L=26µH, 2MHz. PCB printed coils	Class-E power amplifier	165	N/A	1000 (max)
[118]	Primary=45mm, L=26µH, 2MHz. Secondary=10mm, L=25µH, 2MHz. PCB printed coils	Class-E power amplifier	20 - 40	75	N/A
[158]	Primary=300mm, L=368.7µH, 260KHz. Secondary=10mm, L=451.2µH, 260KHz. Hand wound coils	Class-E power amplifier	60	1.3	30
[70] our paper	Primary=39mm, L=17.1µH, 2MHz. Secondary=33mm, L=14.8µH, 2MHz. PCB printed coils	CMOS logic gates-based	10	83	2.2

It can be noted from Table 15 that even though the transducer discs are similar in size, the power consumption for the high frequency, thickness excited discs in [200], [202], and [203] averages between 230 – 1000 mW compared to a power consumption of just 28 mW for the low frequency, radially excited discs of this work published in [70]. This highlights the fact that though the thickness mode is more efficient than the radial mode, it is achieved using much more drive and power consumption. In Table 16, though a greater effective transfer distance is achieved in [157] and [158], this is at the expense of a higher power consumption (> 30 W) compared with the prototype system's consumption of 2.2 W.

4.3. Transmission signals

In the experimental test set up of Figure 54, there are three transmission signals, namely power transfer, data transmission, and timing.

4.3.1. Power transfer transmission signals

The 35 V DC – driven external primary coil generates an 80 V_{p-p} 'inductively-coupled' sinusoidal AC voltage across the subcutaneous secondary coil (well below the FCC Maximum Permissible Exposure levels [406]). Figure 56 is the power transfer transmission signal traces across the prototype system.

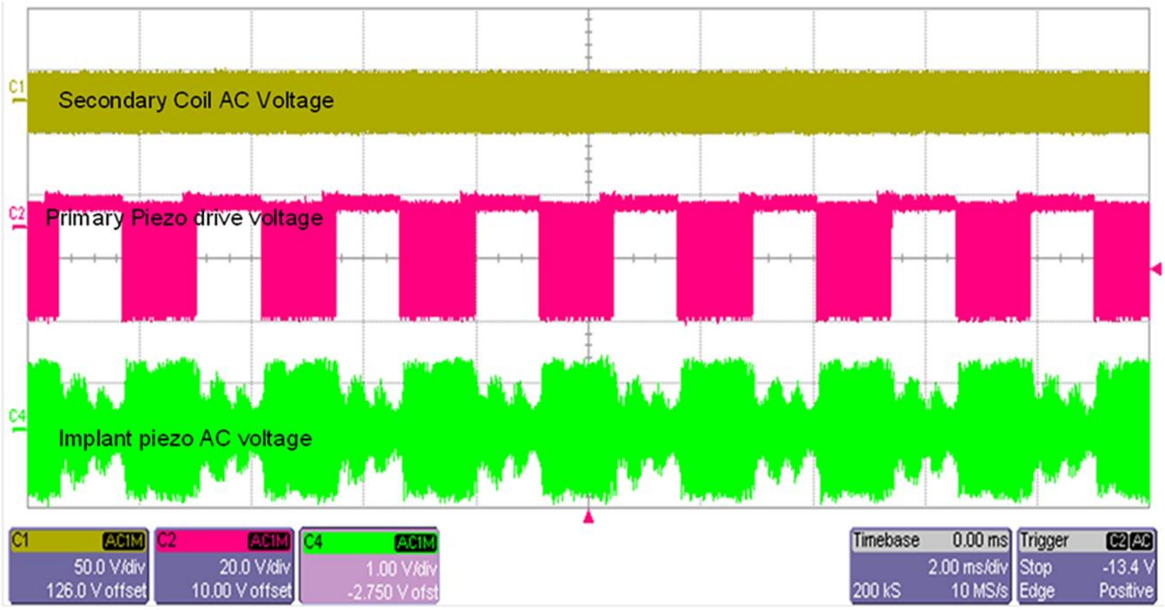

Figure 56: Power transfer transmission signal traces across the prototype

Figure 56 is the oscilloscope-generated trace of power transfer signals across the prototype system. In Figure 56, the horizontal axis denotes propagation delay while the vertical axis denotes voltage. Trace C1 (brown) in Figure 56 is the 80 V_{p-p} inductively-coupled AC signal across the transcutaneous secondary coil. Trace C2 (red) is the 40 V DC rectified voltage switched across the transcutaneous primary piezo disc Pz21 which is immersed in a homogenous liquid phantom. The energized Pz21 primary piezo disc is radially excited and generates ultrasonic waves which are propagated through the liquid phantom and received by the implant Pz26 piezo disc placed 70 mm away. By the direct piezoelectric effect, the Pz26 generates a 5 V_{p-p} sinusoidal AC voltage – Trace C4 (green). Processing the Pz26 output voltage through the implant power conditioning circuit, 2.4 V DC is intermittently supplied to the implant circuitry.

4.3.2. Data transmission signals

The implant μC is intermittently powered every 800 ms - the time it takes the Seiko startup chip to recharge its 10 μF load capacitor, C3 in Figure 30. This reduces to ~ 25 ms after the power carrier is interrupted by software-control. The value of 25 ms therefore represents the effective available time window to power the implant μC, power the implant analog bio-sensor, sample sensed analog data, convert to a digital bit stream, and then transmit the digital bit stream as a burst of ultrasonic pulses through the phantom.

Table 17: Effective data transmission size based on implant operating frequency

Implant µC operating frequency (kHz)	**Available implant supply window (ms)**	**Transmitted data size**
31	~ 24	2 bit
250	~ 20	2 bit
500	~18	4 bit
1000	~ 16	8 bit

The data transmission time window varies according to the effective µC load which is influenced by the software-selected operating frequency of the µC as shown in Table 17. It can be noted that a byte of data (8 bits) can only be transmitted when the implant µC is programmed to operate at 1 MHz which translates to a time window of 16 ms to sample data, condition it, and then transmit. On the other hand, operating the implant µC at 500 kHz would allow the transmission of just a nibble (4-bits) of data within 18 ms but will require two runs to transmit the entire byte of data.

On interrupting the power carrier, capacitor C2 in Figure 30 holds enough charge to power the Seiko startup chip and consequently power the implant µC between 800 ms and 1 s after power-down. This ensures that when data transmission commences from the implant, turbulence created within the tank by the power carrier has already died down. Figure 57 is the 4 bits (nibble) transmitted by a programmed 500 kHz implant µC. Tests carried out show that on power off, Capacitor C2 (2200 µC) holds sufficient charge to activate the Seiko startup chip three times thus ensuring that the entire byte can be transmitted from the implant before the recommencement of the power carrier.

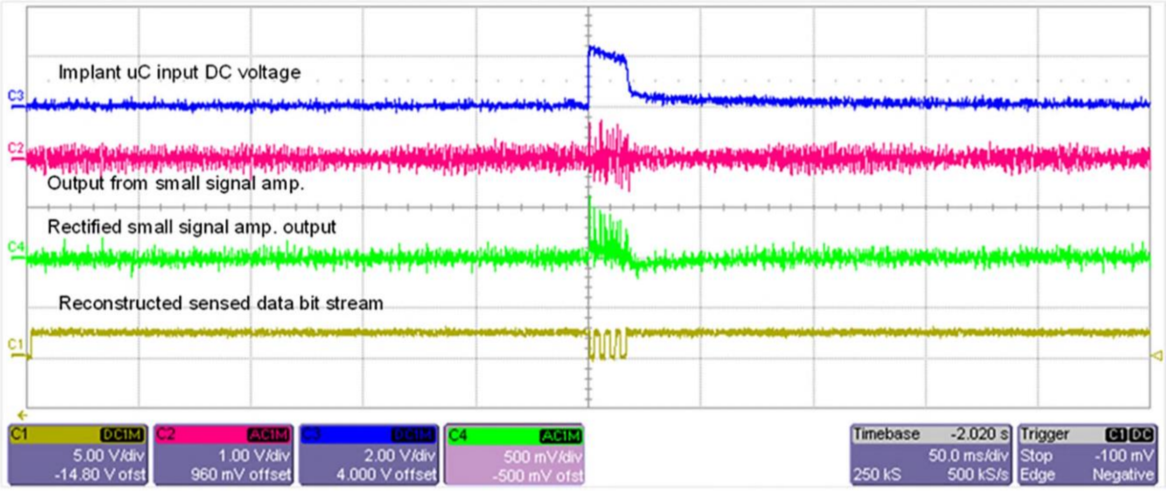

Figure 57: Traces of the prototype system data transmission signals

Figure 57 is the oscilloscope generated traces of data transmission signals across the prototype system. The horizontal axis in Figure 57 represents propagation delay while the vertical axis represents voltage. Trace C3 (blue) in Figure 57 is the 2.4 V DC powered implant µC which transmits the digitized data bit stream as a burst of ultrasonic pulses. The low amplitude sinusoidal AC output voltage across Pz21 (by direct piezoelectric effect) is processed by the subcutaneous signal conditioning circuit. Trace C2 (red) is the output of the signal conditioning circuit while trace C4 (green) is the rectified signal in trace C2 which is fed to the built in comparator circuit of the subcutaneous µC. Trace C1 (brown) in Figure 57 is the reconstructed data bit-stream at the output of the comparator. The remaining nibble (of the one byte of transmitted digital sensed data bit-stream) is transmitted at the next power phase of the implant. It can be noted that when the input supply to the implant µC in trace C3 (blue) reaches 2 V_{DC}, the implant µC switches off and data transmission stops.

4.3.3. Timing signals

The timing signals for the implant µC programmed to operate at an operating frequency of 500 kHz is as shown in Figure 58.

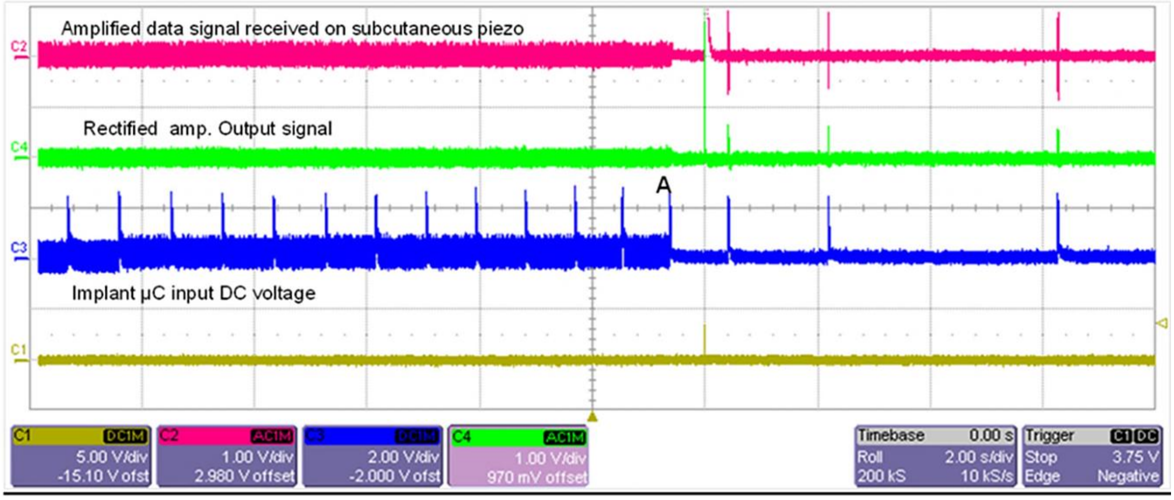

Figure 58: Traces of timing signals across prototype system

Figure 58 is the oscilloscope generated traces of timing signals across the prototype system. In Figure 58, the horizontal axis represents propagation delay while the vertical axis represents voltage. Trace C3 (blue) in Figure 58 shows that the implant µC is powered every 800 ms when the power carrier is on. It can be noted that when the power carrier is turned off, denoted by point A in Trace C3, the implant is powered by the Seiko startup chip for at least three times (signified by the three spikes to the right hand side of point A in Trace C3) covering a total time period of up to 7 s after power-off. From Trace C3 it can be noted that power to the implant from the startup chip after power off is not uniform. The implant is initially powered about 1 s after power off, then a further 2 s after that and then a further 4 s after. Because this timing is software-controlled it can be easily adjusted to suit varied application-specific transmission data sizes. One second after power off, the implant µC is turned on and it transmits the first nibble of sensed data signified by the first spike in Trace C2 (pink). In order for this signal to be suitable for the comparator in the implant µC to reconstruct the transmitted digital bit stream, it is first rectified (allowing only the positive half cycle) as shown in Trace C4 (green). To allow for the entire sensed data to be transmitted from the implant, the power carrier is programmed to be switched off for about 1 min.

4.4. System software flowchart

A simplified system software flowchart for the prototype multi-tier interface system discussed is offered for reference in Figure 59.

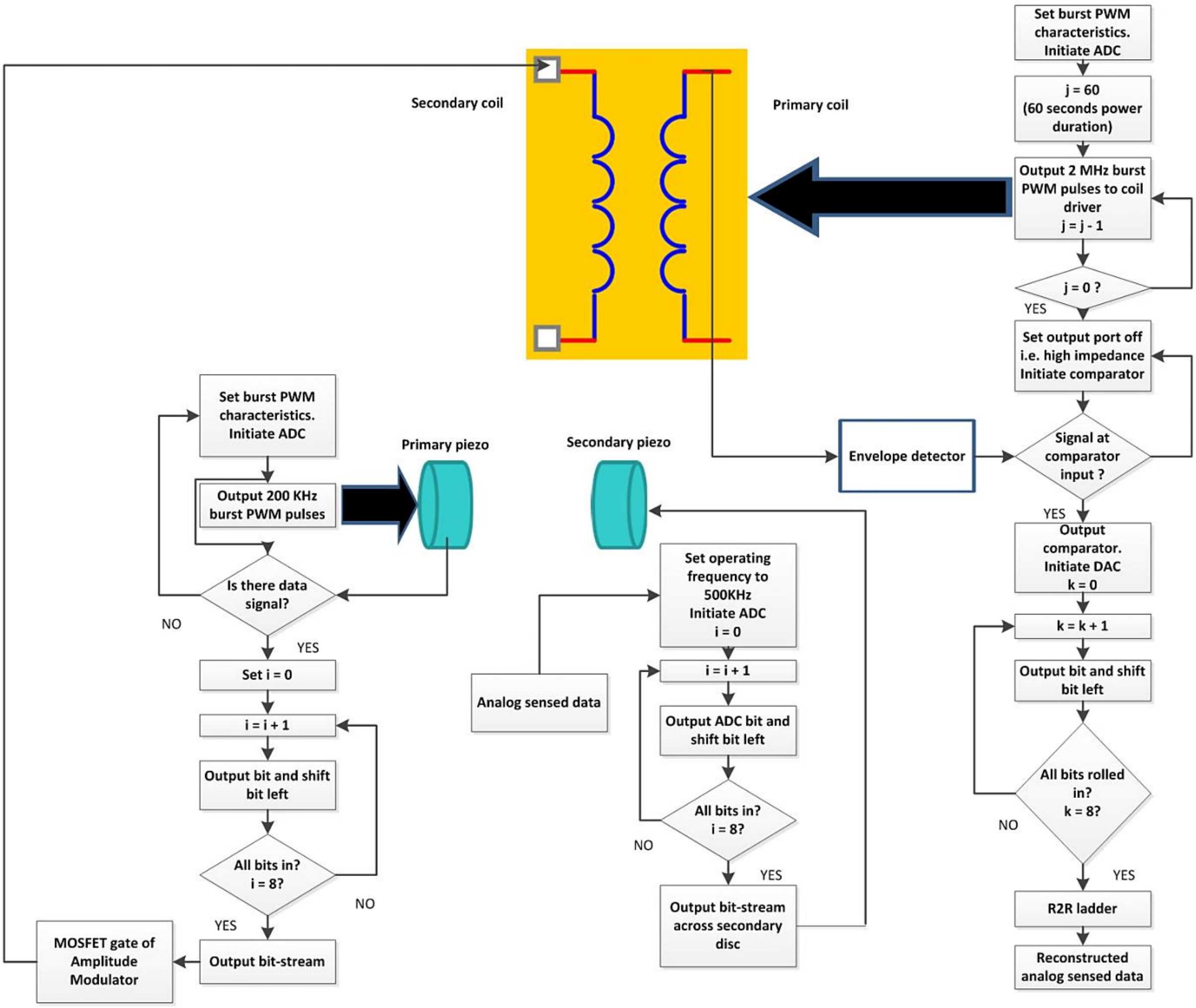

Figure 59: Prototype system software flow chart

In this chapter, the complete system, combining the inductive and ultrasonic sub systems, is set-up for testing in the laboratory. Measurements of both inductive sub system power transfer efficiency and ultrasonic sub system power transfer efficiency are collated and compared with single tier systems. Details of transmission signals within the prototype system – power transfer transmission signals, data transmission signals and timing signals – are also discussed. Results show that the inductive sub system has a power transfer efficiency of 83 % while the ultrasonic sub system has a power transfer efficiency of 1 %.

5. CONCLUSIONS

This work has addressed the urgent requirement for a reliable communications platform that is capable of continuously monitoring deeply implantable biomedical devices.

Traditional battery-powered IMDs are now becoming an expensive, risky and therefore uncomfortable option because of the required risky scheduled replacements over the lifetime of the patient. Low power alternatives currently been globally researched and published include RF, inductive coupling, ultrasonics, energy harvesting, magnetic resonance, volume conduction, witricity, permanent magnet, bone conduction, and microbial fuel cells to mention but a few. In conjunction with the global drive to create novel power and data communication platform alternatives for IMDs, this work offers a proof-of-concept, multi-tier interface system that is based on the publically accepted advantages of inductive coupling and 'human-friendly' ultrasonics. To reiterate, the research contributions from this work include the following:

- the design, fabrication on PCB, and evaluation of circular, planar printed spiral coils (PSCs) for power transfer and data communication – discussed in Chapter 3

- the demonstration and evaluation of the feasibility of PZT piezo transducer discs, driven in their low frequency, radial/planar excitation (-31) mode, to transfer power and transmit data within a homogenous liquid medium (phantom) – detailed in Chapter 3

- Demonstration and evaluation of a prototype CMOS logic gates based primary coil driver circuit, discussed in Chapter 3
- Evaluation, by experimental verification, of a novel, generic, low power, wireless multi-tier interface platform system for IMDs combining inductive coupling and ultrasonics – detailed in Chapter 4

The design, simulation, and fabrication (on PCB) of a multi-tier power transfer and data communication interface has been described in this work and published in [70]. The prototype platform uses a single 35 V DC external supply source that drives a 39 mm primary (PCB fabricated) PSC via the prototype CMOS logic gates based driver. This inductively couples 80 V_{p-p} across a 33 mm secondary (PCB fabricated) PSC placed 10 mm apart (air gap) with a measured power transfer efficiency of 83%. The mutually-induced ac voltage across the secondary coil is full - wave rectified to power the subcutaneous circuitry (as published in [71]), switching 40 V_{DC} across the subcutaneous primary Pz21 transducer disc immersed within a (homogenous) liquid phantom. This drives the Pz21 disc in its 200 kHz, radially - excited (- 31) mode instead of the more conventionally used thickness – excited (- 33) mode. By the reverse piezoelectric effect, the Pz21 produces (radial) ultrasonic waves which are propagated through the homogeneous home-made liquid phantom and received by the implant secondary Pz26 transducer disc, situated 70 mm deep within the phantom. By the direct piezoelectric effect, the Pz26 generates a 5 V_{p-p} sinusoidal ac voltage signal which is passed through an implant power conditioning circuit that intermittently supplys 2.4 V_{DC} to the implant circuitry. The powered implant Microchip 12F683µC powers the implant bio-sensor, samples its analog sensed data, converts the sensed data to digital using its built-in ADC, and then transmits the resulting digital bit-stream as a burst of ultrasonic pulses through the phantom. Measured power transfer efficiency for the ultrasonic sub-system is ~ 1%; which compares favourably to simulations published by Denisov [298].

The digitized bit-stream, transmitted as a burst of ultrasonic pulses from the implant, creates up to 4 mV_{p-p} ac voltage signal across the primary Pz21 disc via the direct piezoelectric effect. This low-amplitude data signal is then passed through the subcutaneous signal conditioning circuit, the output of which is applied to the built-in comparator of the subcutaneous Microchip 12F683 µC to reconstruct the transmitted sensed data bit-stream. The reconstructed data bit-stream is then amplitude modulated (ASK) onto the power carrier at the secondary coil. The modulated signal seen on the primary coil is passed through an envelope detection circuit, the output of which is applied to the built-in comparator of the external Microchip 16F818 µC where the transmitted digital data bit-stream is reconstructed. The comparator output is passed through the in-built DAC of the external Microchip 16818 µC to produce an 8-bit parallel output which when passed through an R2R network reconstructs the actual transmitted analog sensed data as published in [72].

5.1. Future work

Denser printed spiral coils could be produced using clean-room lithography technology which, as cited in literature, can produce minimum feature lengths of nano meters when fabricated on thin silicon wafers. These would result in a further degree of miniaturisation and will produce coils having quality factor and inductance figures that correlate with theory. Investigation into inductive driver circuits with high power transfer efficiency coupled with low power consumption would be crucial.

Investigations could be made to develop a more efficient driver circuit to ensure maximum propagation of ultrasonic waves through the phantom. Additionally, the design of application specific piezoelectric transducer discs in a clean room environment to meet the peculiar requirements of the prototype multi-tier interface platform system would be useful.

With additional funding; animal and then human trials can be carried out which will provide an avenue to determine the characteristics and properties of this prototype interface within real life biomedical applications.

Despite the biomedical background of this work, future work can cover the use of this prototype interface system in sonar, industrial, and NDT applications.

Finally, as ultra-low power consumption is a critical requirement for IMDs, it would be advantageous to look into developing application specific µCs that have only essential hardware functions for the purpose e.g. low power clock/oscillator, integrated ADC, comparator, PWM, and DAC.

List of Publications

Sanni, A.; Vilches, A. and Toumazou, C., "Inductive and Ultrasonic Multi-Tier Interface for Low-Power, Deeply Implantable Medical Devices," *IEEE Transactions on Biomedical Circuits and Systems,* vol.6, no.4, pp.297-308, Aug. 2012 [70]

Sole, M; Sanni, A.; Vilches, A.; Toumazou, C. and Constandinou, T., “A bio-implantable platform for inductive data and power transfer, with integrated battery charging,” *2011 IEEE International Symposium on Circuits and Systems (ISCAS)*, pp.2605-2608, 15-18 May 2011 [71]

Vilches, A.; Sanni, A. and Toumazou, C., “Single coil pair transcutaneous energy and data transceiver for low-power bio-implant use,” *Electronics Letters, IET*, vol.45, no.14, pp.727-728, July 2009 [72]

REFERENCES

1. Dare, F. and Macaulay, J., “The health of nations: perspectives from global leaders reveal untapped opportunity,” 2011 [Online access http://www.cisco.com/web/about/ac79/docs/hc/Health_of_Nations_ExecSumm.pdf]
2. Allan, R., “Medical devices get ready to make home calls,” 2010 [Online access http://electronicdesign.com/article/cover-story/medical_devices_get_ready_to_make_house_calls.aspx)]
3. Gross, A., “Updates on China’s medical device market,” 2010 [Online access http://www.pacificbridgemedical.com/publications/china/2011_updates_china.php]
4. “Destination 2025: focus on the future of the medical device industry,” 2009 [Accessed from http://biobusinessalliance.org/Files/531111_d2025_whitepaper_medical_device_smaller_secured.pdf]
5. Poon, C. and Zhang, Y., "Perspectives on High Technologies for Low-Cost Healthcare," *Engineering in Medicine and Biology Magazine, IEEE*, vol.27, no.5, pp.42-47, September-October 2008
6. Adams, J.; Bakalar, R.; Boroch, M.; Knecht, K.; Mounib, E. and Stuart, N., “Healthcare 2015 and care delivery: delivery models refined, competencies defined,” 2008 [Online access ftp://public.dhe.ibm.com/common/ssi/ecm/en/gbe03061usen/GBE03061USEN.PDF)
7. Reid, P.; Compton, W.; Grossman, and Fanjiang, G., “Building a better delivery system: a new engineering/health care partnership,” 2005 [Online access http://www.nationalacademies.org/onpi/030909643X.pdf]
8. Cleland, J.; Louis, A.; Rigby, A.; Janssens, U. and Balk, A., “Non-invasive home telemonitoring for patients with heart failure at high risk of recurrent admission and death: the Trans-European Network-Home-Care Management System (TEN-HMS) study,” *J. Am. Coll. Cardiol.*, vol.45, no. 10, pp.1654-64, May 2005
9. Werner, C., “Analyst reports medical device market flourishes,” 2003 [Online access http://findarticles.com/p/articles/mi_m0BPC/is_4_27/ai_100484234/]
10. Dean, S., “Current and future trends in medical electronics,” [Online access http://www.arrownac.com/services-tools/design/whitepapers/ti_trends_in_med_devices.pdf]

11. Gomez, J. and Sullivan, T., “Various “7 billionth” babies celebrated worldwide,” 2011 [Online access http://news.yahoo.com/various-7-billionth-babies-celebrated-worldwide-064439018.html]
12. Crary, D., “World population nears 7 billion: can we handle it?” 2011 [Online access http://www.msnbc.msn.com/id/44928812/ns/world_news/t/world-population-nears-billion-can-we-handle-it/#.Tti8uVbeKJo]
13. “World population prospects: the 2006 revision,” United Nations, 2007 [Online access http://www.un.org/esa/population/publications/wpp2006/WPP2006_Highlights_rev.pdf]
14. Bloom, D.; Canning, D. and Fink, G., “Implications of population aging for economic growth,” 2011 [Online access http://www.hsph.harvard.edu/pgda/WorkingPapers/2011/PGDA_WP_64.pdf]
15. Bloom, D.; Canning, D. and Fink, G., “Population aging and economic growth,” 2008 [Online access http://www.growthcommission.org/storage/cgdev/documents/gcwp032web.pdf]
16. “World population aging: 1950 – 2050,” United Nations, 2002 [Online access http://www.un.org/esa/population/publications/worldageing19502050/]
17. Riley, G., “Labour market – the ageing population,” 2006 [Online access http://tutor2u.net/economics/revision-notes/a2-micro-labour-market-ageing-population.html]
18. “Britain’s ageing population,” 2011 [Online access http://www.21stcenturychallenges.org/60-seconds/britains-ageing-population/]
19. “Global medical device industry outlook survey 2011-2012: industry dynamics, market trends and opportunities, marketing size and sales strategies,” 2011 [Online access http://www.infogrok.com/index.php/healthcare/global-medical-device-industry-outlook-survey-20112012-industry-dynamics-market-trends-and-opportunities-marketing-spend-and-sales-strategies.html]
20. “Medical devices industry outlook – April 2011,” [Online access http://money.gather.com/viewArticle.action?articleId=281474979191796]
21. “Emerging medical device markets and technologies,” 2008 [Online access http://www.cims.rit.edu/ne/Emerging_Medical_FINAL_PDF.pdf]
22. “Health care costs around the world,” 2006 [Online access http://www.creditloan.com/blog/2010/03/01/healthcare-costs-around-the-world/]

23. He, W.; Sengupta, M.; Velkoff, V. and DeBarrow, K., “65+ in the United States: 2005,” 2005 [Online access http://www.census.gov/prod/2006pubs/p23-209.pdf]
24. “Spending on health: a global overview,” World Health Organization, 2007 [Online access http://www.who.int/mediacentre/factsheets/fs319.pdf]
25. A global village, Imperial College Union, Issue 5, Autumn 2011
26. “TEN-HMS study demonstrates clinical and financial efficacy of home telemonitoring,” Phillips, 2003 [Online access http://www.alexianbrothershealth.org/pdf/telehealth_program.pdf]
27. Smith, J.M.; "The doctor will see you ALWAYS," *Spectrum, IEEE*, vol.48, no.10, pp.56-62, Oct. 2011
28. Vasanth, K.; "The future of medical electronics," *Bipolar/BiCMOS Circuits and Technology Meeting (BCTM), IEEE*, pp.184-187, 4-6 Oct. 2010
29. Kelleher, T., “Telehealth programme shows reduced hospital admissions and high patient satisfaction,” *British Journal of Cardiology*; vol.18, no.2, April 2011
30. “Implantable medical devices: 2014 & 2019 Forecasts,” The Freedonia Group, April 2010 [Online access http://www.freedoniagroup.com/brochure/25xx/2595smwe.pdf]
31. “2011 survey of health care consumers global report: key findings, strategic implications,” Deloitte, 2011 [Online access http://www.deloitte.com/assets/Dcom-UnitedStates/Local%20Assets/Documents/US_CHS_2011ConsumerSurveyGlobal_062111.pdf]
32. “The eleven most implanted medical devices in America,” 24/7 Wall St., 2011 [Online access http://247wallst.com/2011/07/18/the-eleven-most-implanted-medical-devices-in-america/]
33. “Global micro electromechanical (MEMS) device market to reach US$9.2 Billion by 2015,” Electronics.ca research network, 2011 [Online access http://www.electronics.ca/presscenter/articles/1400/1/Global-Micro-Electromechanical-Systems-MEMs-Devices-Market-to-Reach-US92-Billion-by-2015/Page1.html]
34. “The outlook for medical devices in western Europe,” ESPICOM Business Intelligence, 2011 [Online access http://www.espicom.com/Prodcat2.nsf/Product_ID_Lookup/00000934?OpenDocument]

35. Gerrish, P.; Herrmann, E.; Tyler, L. and Walsh, K., “Challenges and constraints in designing implantable medical ICs,” *Device and Materials Reliability, IEEE Transactions on,* vol.5, no.3, pp.435-44, Sept. 2005
36. Sun, M.; Hackworth, S.; Tang, Z.; Gilbert, G.; Cardin, S. and Sclabassi, R., "How to Pass Information and Deliver Energy to a Network of Implantable Devices within the Human Body," *Engineering in Medicine and Biology Society, EMBS 2007, 29th Annual International Conference of the IEEE*, pp.5286-89, 22-26 Aug. 2007
37. Townsend, K.; Haslett, J.; Tsang, T.; El-Gamal, M. and Iniewski, K., “Recent advances and future trends in low-power wireless systems for medical applications,” *System-on-chip for Real-Time Applications, Proceedings, 5th International Workshop on*, pp.476-81, 20-24 July 2005
38. Pfahl, R. and McElroy, J., "Emerging Markets and Emerging Technologies," *High Density packaging and Microsystem Integration, HDP '07, International Symposium on*, pp.1-5, 26-28 June 2007
39. Walker, G.; Ramsey, J.; Calvin, R.; Herr, D,; Merzbacher, C. and Zhirnov, V., “A framework for bioelectronics: delivery and innovation,” 2009 [Online access http://www.nist.gov/pml/div683/upload/bioelectronics_report.pdf]
40. Borenstein, J., “BioMEMS technologies for regenerative medicine,” 2009 [Online access http://medicaldesign.com/engineering-prototyping/research-development/biomems-evolution-advancement-20091201/]
41. WHO, “Medical devices: managing the mismatch: an outcome of the priority medical devices project,” 2010 [Online access http://whqlibdoc.who.int/publications/2010/9789241564045_eng.pdf]
42. Guler, N. and Ubeyil, E., “Theory and applications of biotelemetry,” *Journal of Medical Systems,* vol.26, no.2, pp.159-78, 2002
43. Fotiadis, D.; Glaros, C. and Likas, A., “Wearable medical devices,” *Wiley Encyclopedia of Biomedical Engineering,* April 2006 [Online access http://onlinelibrary.wiley.com/doi/10.1002/9780471740360.ebs1326/pdf]
44. Bradley, P., "Wireless medical implant technology — Recent advances and future developments," *ESSCIRC, 2011 Proceedings of the*, pp.37-41, 12-16 Sept. 2011

45. Rashvand, H.F.; Salcedo, V.T.; Sanchez, E.M. and Iliescu, D., "Ubiquitous wireless telemedicine," *Communications, IET*, vol.2, no.2, pp.237-254, February 2008
46. Saliterman, S., “Fundamentals of BioMEMS and medical microdevices,” Bellingham, Washington, SPIE, 2006
47. Grayson, A.; Shawgo, R.; Johnson, A.; Flynn, N.; Yawen, L.; Cima, M. and Langer, R., “A BioMEMS review: MEMS technology for physiologically integrated devices,” *Proceedings of the IEEE,* vol.92, no.1, pp.6-21, Jan. 2004
48. Tsai, T.; Lee, J.; Lee, S. and Lee, S., "Low-Power Analog Integrated Circuits for Wireless ECG Acquisition Systems," *Information Technology in Biomedicine, IEEE Transactions on*, 2012
49. Pen-Li Huang; Po-Hung Kuo; Yu-Jie Huang; Hsin-Hung Liao; Yang, Y.-J.J.; Tao Wang; Yao-Hung Wang and Shey-Shi Lu, "A Controlled-Release Drug Delivery System on a Chip Using Electrolysis," *Industrial Electronics, IEEE Transactions on*, vol.59, no.3, pp.1578-1587, March 2012
50. Sham, I.; Chow, C.; Lui, H.; Lam, P.; Yeung, J.; Jing, L. and Chen, S., "Challenges in developing cost-effective system-in-package (SiP) for tyre pressure monitoring system (TPMS)," *Electronic Packaging Technology and High Density Packaging (ICEPT-HDP), 12th International Conference on*, 1-6, 8-11 Aug. 2011
51. Chung, D.; Polcawich, R.; Pulskamp, J. and Papapolymerou, J., "Reduced-Size Low-Voltage RF MEMS X-Band Phase Shifter Integrated on Multilayer Organic Package," *Components, Packaging and Manufacturing Technology, IEEE Transactions on*, 2012
52. Chakrabarty, K., "Design, testing, and applications of digital microfluidics-based biochips," *VLSI Design, 18th International Conference on*, pp. 221- 226, 3-7 Jan. 2005
53. Wu, W.; Liang, C. and Huang, J., "MEMS-based flow cytometry: microfluidics-based cell identification system by fluorescent imaging," *Engineering in Medicine and Biology Society, IEMBS '04, 26th Annual International Conference of the IEEE*, pp.2579-2581, 1-5 Sept. 2004
54. Sawan, M., "Implantable Smart Medical Microsystems: Limits and Challenges," *Electronics, Circuits and Systems, ICECS '06, 13th IEEE International Conference on*, pp.522-524, 10-13 Dec. 2006

55. Panescu, D., "An imaging pill for gastrointestinal endoscopy," *Engineering in Medicine and Biology Magazine, IEEE*, vol.24, no.4, pp. 12- 14, July-Aug. 2005

56. Yawen Chan; Meng, M.Q.H. and Xiaona Wang, "A prototype design of wireless capsule endoscope," *Mechatronics and Automation, 2005 IEEE International Conference*, pp. 400- 403 Vol. 1, 29 July-1 Aug. 2005

57. Ciuti, G.; Menciassi, A. and Dario, P., "Capsule Endoscopy: From Current Achievements to Open Challenges," *Biomedical Engineering, IEEE Reviews in*, vol.4, no., pp.59-72, 2011

58. Toennies, J; Tortora, G.; Simi, M.; Valdastri, P. and Webster, R., “Swallowable medical devices for diagnosis and surgery: state of the art,” *Proceedings of the Institution of mechanical Engineers, Part C: Journal of Mechanical Engineering Science,* vol.224, no.7, pp.1397-414, July 2010

59. Oesterle, S.; Gerrish, P. and Peng, C., “New interfaces to the body through implantable-system integration,” *Solid-State Circuits Conference Digest of Technical Papers (ISSCC), IEEE International,* pp.9-14, 20-24 Feb. 2011

60. Wei, X. and Liu, J., “Power sources and electrical recharging strategies for implantable medical devices,” *Frontiers of Energy and Power Engineering in China,* vol.2, no.1, pp.1-13, 2008

61. Chandrakasan, A.; Verma, N. and Daly, D., “Ultralow-power electronics for biomedical applications, *Annual Reviews of Biomedical Engineering,* vol.10, pp.247-74, August 2008

62. Kannally, T., “Biocompatible materials drive the success of implantable medical devices,” 2010 [Online access http://www.ecnmag.com/Articles/2010/04/Biocompatible-Materials/]

63. Olivo, J.; Carrara, S. and De Micheli, G., “Energy harvesting and remote powering for implantable biosensors,” *Sensors Journal, IEEE,* no.9, pp.1-13, 2010

64. Khare, A.; Saxena, M. and Jain, H., “Next generation micro-power systems,” *International Journal of Engineering and Advanced Technology (IJEAT),* vol.1, no.1, pp.25-9, October 2011

65. Srinivasan, R., “Implantable devices: challenges and opportunities,” *Medical Device Technology,* vol.20, no.5, pp.32-34, 2009

66. “A layperson’s view of future technology and society” [Online access

http://www.futureforall.org/futureofmedicine/medical_technology.htm]

67. “Advances in medical technology: what does the future hold?” 2009 [Online access http://www.sciencedaily.com/releases/2009/06/090616080133.htm]

68. Wade, C. and Wade, J., “The impact of medical applications on the electronics industry,” [Online access http://www.techforecasters.com/whitepapers/wp_wade_impact_medical.pdf]

69. Wikipedia, “List of emerging technologies,” 2012 [Online access http://en.wikipedia.org/wiki/List_of_emerging_technologies]

70. Sanni, A.; Vilches, A. and Toumazou, C., "Inductive and Ultrasonic Multi-Tier Interface for Low-Power, Deeply Implantable Medical Devices," *Biomedical Circuits and Systems, IEEE Transactions on*, vol.6, no.4, pp.297-308, Aug. 2012

71. Sole, M; Sanni, A.; Vilches, A.; Toumazou, C. and Constandinou, T., “A bio-implantable platform for inductive data and power transfer , with integrated battery charging,” *Circuits and Systems (ISCAS), 2011 IEEE International Symposium on*, pp.2605-2608, 15-18 May 2011

72. Vilches, A.; Sanni, A. and Toumazou, C., “Single coil pair transcutaneous energy and data transceiver for low-power bio-implant use,” *Electronics Letters, IET*, vol.45, no.14, pp.727-728, July 2009

73. Xiao-Fei, T.; Yuan-Ting, Z.; Poon, C.C.Y. and Bonato, P., "Wearable Medical Systems for p-Health," *Biomedical Engineering, IEEE Reviews in*, vol.1, pp.62-74, 2008

74. Malasri, K. and Lan, W., "Securing wireless implantable devices for healthcare: Ideas and challenges," *Communications Magazine, IEEE*, vol.47, no.7, pp.74-80, July 2009

75. Romero, E.; Warrington, R.O. and Neuman, M.R., "Powering biomedical devices with body motion," *Engineering in Medicine and Biology Society (EMBC), 2010 Annual International Conference of the IEEE*, pp.3747-3750, Aug. 31 2010-Sept. 4 2010

76. Wu, P., "The perspective of biomedical electronics," *Sensors 2010 IEEE*, pp.1187, 1-4 Nov. 2010

77. Devaraj, S.J. and Ezra, K., "Current trends and future challenges in wireless telemedicine system," *Electronics Computer Technology (ICECT), 2011 3rd International Conference on*, vol.4, pp.417-421, 8-10 April 2011

78. Bashirullah, R., "Wireless Implants," *Microwave Magazine, IEEE,* vol.11, no.7, pp.S14-S23, Dec. 2010
79. Pantelopoulos, A. and Bourbakis, N.G., "A Survey on Wearable Sensor-Based Systems for Health Monitoring and Prognosis," *Systems, Man, and Cybernetics, Part C: Applications and Reviews, IEEE Transactions on*, vol.40, no.1, pp.1-12, Jan. 2010
80. Gatzoulis, L. and Iakovidis, I., "Wearable and Portable eHealth Systems," *Engineering in Medicine and Biology Magazine, IEEE*, vol.26, no.5, pp.51-56, Sept.-Oct. 2007
81. Greatbatch, W. and Holmes, C., "History of implantable devices," *Engineering in Medicine and Biology Magazine, IEEE,* vol.10, no.3, pp.38-41, Sept. 1991
82. Turicchia, L.; Do Valle, B.; Bohorquez, J.; Sanchez, W.; Misra, V.; Tavakoli, M. and Sarpeshkar, R., "Ultralow-power electronics for cardiac monitoring," *Circuits and Systems I: Regular Papers, IEEE Transactions on,* vol.57, no.9, pp.2279-90, Sept. 2010
83. Kiourti, A., "Biomedical Telemetry: communication between implanted devices and the external world," 2010 [Online access http://www.ucl.ac.uk/opticon1826/archive/issue8/articles/Kiourti_article.pdf]
84. Escayola, J.; Martinez, I.; Trigo, J.; Garcia, J.; Martinez-Espronceda, M.; led, S. and Serrano, L., "Recent innovative advances in biomedical engineering: standard-based design for ubiquitous p-health," *Computing in Global Information Technology, ICCGI'09, 4th International Multi-Conference on,* pp.109-17, 23-29 Aug. 2009
85. Mingui, S.; Hackworth, S.; Zhide, T.; Gilbert, G.; Cardin, S. and Sclabassi, R., "How to pass information and deliver energy to a network of implantable devices within the human body," *Engineering in Medicine and Biology Society, EMBS 2007, 29th Annual International Conference, IEEE,* pp.5286-89, 22-26 Aug. 2007
86. Asgarian, F. and Sodagar, A., "Wireless telemetry for implantable biomedical microsystems," 2010 [Online access http://www.intechopen.com/source/pdfs/12899/InTech-Wireless_telemetry_for_implantable_biomedical_microsystems.pdf]
87. Turricchia, L.; Mandal, S.; Tavakoli, M.; Fay, L.; Misra, V.; Bohorquez, J.; Sanchez, W. and Sarpeshkar, R., "Ultra-low power electronics for non-invasive medical monitoring," *Custom*

Integrated Circuits Conference, CICC'09, IEEE, pp.85-92, 13-16 Sept. 2009

88. Majerus, S. and Gaverick, S., "Telemetry platform for deeply implanted biomedical sensors," *Networked Sensing Systems, INSS 2008, 5th International Conference on,* pp.87-92, 17-19 June 2008
89. Dabiri, F.; Massey, T.; Noshadi, H.; Hagopian, H.; Lin, C.; Tan, R.; Schmidt, J. and Sarrafzadeh, M., "A telehealth architecture for networked embedded systems: a case study in vivo health monitoring," *Information Technology in Biomedicine, IEEE Transactions on,* vol.13, no.3, pp.351-59, May 2009
90. Eberle, W.; Mecheri, A.; Thi Kim Thoa, N.; Gielen, G.; Campagnolo, R., Burdett, A, Toumazou, C. and Volckaerts, B., "Health-care electronics: the market, the challenges, the progress," *Design, Automation & Test in Europe Conference and Exhibition, DATE'09,* pp.1030-34, 20-24 April 2009
91. Poon, A.; O'Driscoll, S. and Meng, T., "Optimal frequency for wireless power transmission into dispersive tissue," *Antennas and Propagation, IEEE Transactions on,* vol.58, no.5, pp.1739-50, May 2010
92. Sridhara, S., "Ultra-low power microcontrollers for portable, wearable, and implantable medical electronics," *Design Automation Conference (ASP-DAC), 2011 Asia and South Pacific,* pp.556-60, 25-28 Jan. 2011
93. Kailas, A. and Ingram, M., "Wireless aspects of telehealth," *Wireless Personal Communications,* vol.51, no.4, pp.673-86, 2009
94. Kyriacou, E.; Voskarides, S.; Pattichis, C.; Istepanian, R.; Pattichis, M. and Schizas, C., "Wireless telemedicine systems: a brief review," *Computer,* pp.1-8 [Online access http://www.citeulike.org/user/kilter/article/8917244]
95. American Telemedicine Association [Online access http://www.americantelemed.org/i4a/pages/index.cfm?pageID=3333]
96. Furse, C., "Biomedical telemetry: today's opportunities and challenges," *Antenna Technology, iWAT 2009, IEEE International Workshop on,* pp.1-4, 2-4 March 2009
97. Galarraga, M.; Serrano, L.; Martinez, I.; De Toledo, P. and Reynolds, M., "Telemonitoring systems interoperability challenge: an updated review of the applicability of ISO/IEEE 11073 standards for interoperability in telemonitoring,"

Engineering in Medicine and Biology Society, EMBS 2007, 29th Annual International Conference, IEEE, pp.6161-5, 22-26 Aug. 2007

98. Pattichis, C.; Kyriacou, E.; Voskarides, S.; Pattichis, M.; Istepanian, R. and Schizas, C., "Wireless telemedicine systems: an overview," *Antennas and Propagation Magazine, IEEE,* vol.44, no.2, pp.143-53, Apr. 2002
99. Sharma, V., "The future is wireless: advances in wireless diagnostic and therapeutic technologies in gastroenterology," *Gastroenterology,* vol.137, no.2, pp.434-65, 2009
100. Yeandle, S., "Telecare – a crucial opportunity to help save our health and social system," 2009 [Online access http://www.tunstall.co.uk/assets/Literature/Reports/bow_group_report.pdf]
101. Abouei, J.; Plataniotis, K. and Pasupathy, S., "Energy efficiency and reliability in wireless biomedical implant systems," *Information Technology in Biomedicine, IEEE Transactions on,* vol.15, no.3, pp.456-66, May 2011
102. Poon, C.; Wenbo, G. and Zhang, Y., "Health informatics for low-cost and high quality health care," *Engineering in Medicine and Biology Society (EMBC), 2010 Annual International Conference, IEEE,* pp.1755-58, 31 Aug. – 4 Sept. 2010
103. Zhou, B.; Hu, C.; Wang, H.; Guo, R. and Meng, M., "A wireless sensor network for pervasive medical supervision," Integration Technology, *Proceedings, 2007 IEEE International Conference on,* pp.740-4, 20-24 March 2007
104. Ohta, J.; Tokuda, T.; Sasagawa, K. and Noda, T., "Implantable CMOS biomedical devices," *Sensors,* vol.9, no.11, pp.9073-93, 2009
105. Mokwa, W., "Medical implants based on microsystems," *Measurement Science and Technology,* vol.18, no.5, pp.47-57, 2007
106. Panescu, D., "MEMS in medicine and biology," *Engineering in Medicine and Biology Magazine, IEEE,* vol.25, no.5, pp.19-28, 2006
107. ISO 13485 2003 [Online access http://www.praxiom.com/iso-13485-definitions.htm]
108. "Wireless telemetry system," 2006 [Online access http://www.electronics-manufacturers.com/info/data-acquisition/wireless-telemetry-system.html]

109. Tofighi, S., “Wireless medical implants,” 2006 [Online access http://www2.etown.edu/physics/news/SoheilTofighiIEEE_Oct2006.pdf]

110. Sagan, D., “RF integrated circuits for medical applications: meeting the challenge of ultra-low power communications,” 2007 [Online access http://stf.ucsd.edu]

111. Bradley, P., “RF integrated circuits for medical implants: meeting the challenges of ultra-low power communications,” *CMOS Emerging Technologies workshop,* 19-21 July 2006

112. “Top 30 global medical devices companies,” July/August 2006 [Online access http://www.mpo-mag.com/articles/2006/07/top-medical-device-companies-report]

113. Pharmalive, “Top 100 medical device companies,” June 2010 [Online access http://www.pharmalive.com/special_reports/sample.cfm?reportID=309]

114. “The eleven most implanted medical devices in America,” 2011 [Online access http://247wallst.com/2011/07/18/the-eleven-most-implanted-medical-devices-in-america/]

115. Heinila, H.; Riistama, J. Heino, P. and Lekkala, J., “Low cost miniaturization of an implantable prototype,” *Circuit World,* vol.35, no.1, pp.34-40, 2009

116. Farahi, R.; Ferrell, T.; Guiseppi-Elie, A. and Hansen, P., “Integrated electronics platforms for wireless implantable sensors,” Life Science Systems and Applications Workshop, LISA 2007, IEEE/NIH, pp.27-30, 8-9 Nov. 2007

117. Haider, M. and Islam, S., “Ultra-low power sensor signal processing unit for implantable biosensor applications,” Electrical and Computer Engineering (ICELCE), 2010 International Conference on, pp.302-5, 18-20 Dec. 2010

118. Loughlin, S. and Williams, J., “The top 10 medical device challenges,” Biomedical Instrumentation & Technology (BIT), vol.45, no.2, pp.98-104, March/April 2011

119. Xiali Hei and Xiaojiang Du, "Biometric-based two-level secure access control for Implantable Medical Devices during emergencies," INFOCOM, Proceedings IEEE , pp.346-350, 10-15 April 2011

120. Fei Hu; Qi Hao; Lukowiak, M.; Qingquan Sun; Wilhelm, K.; Radziszowski, S.; Yao Wu, "Trustworthy Data Collection From Implantable Medical Devices Via High-Speed Security

Implementation Based on IEEE 1363," Information Technology in Biomedicine, IEEE Transactions on, vol.14, no.6, pp.1397-1404, Nov. 2010

121. Huang Xiao-Hui and Guo Yuan-Bo; Liu Wei, "Design and implementation of a WLAN intrusion detection and DoS attack analyse system," Mechatronic Science, Electric Engineering and Computer (MEC), International Conference on, pp.1722-1725, 19-22 Aug. 2011
122. Seungjin Son; Kwangwoo Lee; Dongho Won; Seungjoo Kim, "U-healthcare system protecting privacy based on cloaker," Bioinformatics and Biomedicine Workshops (BIBMW), IEEE International Conference on, pp.417-423, 18-18 Dec. 2010
123. Xiali Hei; Xiaojiang Du; Jie Wu and Fei H., "Defending Resource Depletion Attacks on Implantable Medical Devices," GLOBECOM 2010, IEEE Global Telecommunications Conference, pp.1-5, 6-10 Dec. 2010
124. Fengyuan X.; Zhengrui Q.; Tan, C.; Baosheng W. and Qun L., "IMDGuard: Securing implantable medical devices with the external wearable guardian," INFOCOM, 2011 Proceedings IEEE, pp.1862-1870, 10-15 April 2011
125. Schuylenbergh, K. and Puers, R., Inductive powering: basic theory and application to biomedical systems. Verilag, NY: Springer, 2009
126. Potkay, J., “Long term implantable blood pressure monitoring systems,” *Biomedical Microdevices,* vol.10, no.3, pp.379-92, 2008
127. Goto, K.; Nakagawa, T.; Nakamura, O. and Kawata, S., “An implantable power supply with an optically rechargeable lithium battery,” *Biomedical Engineering, IEEE Transactions on,* vol.48, no.7, pp.830-3, 2001
128. Hamici, Z.; Itti, R. and Champier, J., “A high-efficiency power and data transmission system for biomedical implanted electronic devices,” *Meas. Sci. Technol.,* vol.7, pp.192-201, 1996
129. Yazdandoost, K. and Kohno, R., “Medical implant communication system,” *2006 IEEE p802.15 working group for wireless personal area networks* [Doc: IEEE 802.15-06-0342-00-0ban]
130. Chen, I.; Phee, S.; Luo, Z. and Lim, C., “Personalized biomedical devices & systems for healthcare applications,” *Front. Mech. Eng.,* vol.6, no.1, pp.1-12, 2010
131. Wang, Z.; Mai, S.; Zhang, C. and Chen, C., “Design practice of power-oriented integrated circuits for biomedical implant

systems,” *Electronics, Circuits and Systems, ICECS 2007, 14th IEEE International Conference on,* pp.11-14, 11-14 Dec. 2001

132. Budinger, T., “Biomonitoring with wireless communication,” *Annu. Rev. Biomed. Eng.,* vol.5, pp.383-412, 2003
133. Holmes, C. and Owens, B., “Batteries for implantable biomedical applications,” 2006 [Online access http://onlinelibrary.wiley.com/doi/10.1002/9780471740360.ebs1369/pdf]
134. Linford, R.; Latham, R. and Schlindwein, W., “Biomedical applications of batteries,” *Solid State Ionics*, vol.7, no.1-4, pp.7-11, August 2004
135. Soykan, O., “Power sources for implantable medical devices,” 2002 [Online access http://www.touchbriefings.com/pdf/753/mdev02_p_soykan.pdf]
136. Schmidt, C. and Skarstad, P., “The future of lithium and lithium-ion batteries in implantable medical devices,” *Journal of Power Sources*, vol.97-98, pp.742-6, July 2001
137. Heller, A., “Potentially implantable miniature batteries,” *Anal. Bioanal. Chem.*, vol.385, no.3, pp.469-73, 2006
138. Spillman, D.M.; Takeuchi, E.S., "Lithium ion batteries for medical devices," *Battery Conference on Applications and Advances, The Fourteenth Annual*, pp.203-208, 1999
139. Rubino, R.S.; Gan, H. and Takeuchi, E., "Implantable medical applications of lithium-ion technology," Battery Conference on Applications and Advances, The Seventeenth Annual, pp.123-127, 2002
140. Pandey, A.; Allos, F.; Hu, A.P. and Budgett, D., "Integration of supercapacitors into wirelessly charged biomedical sensors," *Industrial Electronics and Applications (ICIEA), 6th IEEE Conference on,* pp.56-61, 21-23 June 2011
141. Purushothaman, B., “Development of batteries for implantable applications,” 2006 PhD Thesis
142. Mallozzi, J., “Delivering on the promise of thin-film batteries,” R & D Magazine, April 2004 [Online access http://www.rdmag.com/Featured-Articles/2004/04/Delivering-on-the-Promise-of-Thin-Film-Batteries/]
143. Vincent, C., “Lithium batteries: a 50 year perspective, 1959-2009,” *Solid State Ionics,* vol.134, no.1-2, pp.159-67, Oct. 2000
144. Qing, X.; Chen, Z.; See, T.; Goh, C. and Chiam, T., "RF transmission characteristics in/through the human body," *Cybernetics and*

Intelligent Systems (CIS), IEEE Conference on, pp.20-23, 28-30 June 2010

145. Yang, W.; Sayrafian-Pour, K.; Hagedorn, J.; Terrill, J.; Yazdandoost, K.; Taparugssanagorn, A.; Hämäläinen, M. and Linatti, J., "Impact of an aortic valve implant on body surface UWB propagation: A preliminary study," *Medical Information & Communication Technology (ISMICT), 5th International Symposium on,* pp.84-88, 27-30 March 2011
146. Chow, E.Y.; Yang, C.; Ouyang, Y.; Chlebowski, A.; Irazoqui, P. and Chappell, W., "Wireless Powering and the Study of RF Propagation Through Ocular Tissue for Development of Implantable Sensors," *Antennas and Propagation, IEEE Transactions on,* vol.59, no.6, pp.2379-2387, June 2011
147. Chen, Z.; Liu, G. and See, T., "Transmission of RF Signals between MICS Loop Antennas in Free Space and Implanted in the Human Head," *Antennas and Propagation, IEEE Transactions on,* vol.57, no.6, pp.1850-1854, June 2009
148. Copani, T.; Min, S.; Shashidharan, S.; Chakraborty, S.; Stevens, M.; Kiaei, S. and Bakkaloglu, B., "A CMOS Low-Power Transceiver With Reconfigurable Antenna Interface for Medical Implant Applications," *Microwave Theory and Techniques, IEEE Transactions on,* vol.59, no.5, pp.1369-1378, May 2011
149. Soantornpipit, P.; Furse, C. and Chung, Y., “Design of implantable microstrip antenna for communication with medical implants,” *Microwave Theory and Technique, IEEE Transactions on,* vol.35, no.8, pp.1944-51, Aug. 2004
150. Burke, P. and Rutherghen, C., “Towards a single-chip implantable RFID system: is a single cell radio possible?” *Biomedical Microdevices,* vol.12, no.4, pp.589-96, 2010
151. Lin, Y.; Hung, T. and Lin, C., “A novel end-shorted printed open loop antenna for IEEE 802.15 2.4 GHz wireless sensor network platform applications,” *Wireless Personal Communications,* vol.59, no.1, pp.135-45, 2011
152. Yazdandoost, K.Y., "A 2.4 GHz antenna for medical implanted communications," *Microwave Conference, APMC 2009. Asia Pacific,* pp.1775-1778, 7-10 Dec. 2009
153. Mizuno, H.; Takahashi, M.; Saito, K.; Haga, N. and Ito, K., "Design of a helical folded dipole antenna for biomedical implants," *Antennas and Propagation (EUCAP), Proceedings of the 5th European Conference on,* pp.3484-3487, 11-15 April 2011

154. Gupta, B.; Sankaralingam, S. and Dhar, S., "Development of wearable and implantable antennas in the last decade: A review," *Microwave Symposium (MMS), 2010 Mediterranean,* pp.251-267, 25-27 Aug. 2010

155. Zengin, F.; Akkaya, E.; Turetken, B. and San, S., "Design and realization of ultra-wide band implant antenna for biotelemetry systems," *General Assembly and Scientific Symposium, XXXth URSI,* pp.1-4, 13-20 Aug. 2011

156. Kiourti, A.; Christopoulou, M. and Nikita, K., "Performance of a novel miniature antenna implanted in the human head for wireless biotelemetry," *Antennas and Propagation (APSURSI), IEEE International Symposium on,* pp.392-395, 3-8 July 2011

157. Merli, F.; Bolomey, L.; Zurcher, J.; Corradini, G.; Meurville, E. and Skrivervik, A., "Design, Realization and Measurements of a Miniature Antenna for Implantable Wireless Communication Systems," *Antennas and Propagation, IEEE Transactions on,* vol.59, no.10, pp.3544-3555, Oct. 2011

158. Qi, Z.; Xiaofei, K. and Nanjian, W., "An ultra-low power RF transceiver for WBAN in medical applications," *Journal of Semiconductors,* vol.32, no. 6, June 2011

159. Marcelli, E.; Scalambra, F.; Cercenelli, L. and Plicchi, G., "A new hermetic antenna for wireless transmission systems of implantable medical devices," *Medical Eng. & Phy.,* vol.29, no.1, pp.140-7, Jan. 2007

160. Chuang, C.; Chua, E.; Lai, Y. and Fang, W., "RF-powered Li-ion battery charger for biomedical applications," *Life Science Systems and Applications Workshop, LiSSA 2009, IEEE/NIH,* pp.187-9, 9-10 April 2009

161. Jones, I.; Ricciardi, L.; Hall, L.; Hansen, H.; Varadan, V.; Bertram, C.; Maddocks, S.; Enderling, S.; Saint, D.; Al-Sarawi, S. and Abbott, D., "Wireless RF communication in biomedical applications," *Smart Mater. Struct.,* vol.17, no.1, pp.1-10, February 2008

162. Valdastri, P.; Rossi, S.; Menciassi, A.; Lionetti, V.; Bernini, F.; Recchia, F. and Dario, P., "An implantable ZigBee-ready telemetric platform for in-vivo monitoring of physiological parameters," *Sensors and Actuators A: Physical,* vol.142, no.1, pp.369-78, March 2008

163. Bradley, P., "An ultra-low power, high performance Medical Implant Communications System (MICS) transceiver for

implantable devices," *Biomedical Circuits and Systems Conference BioCAS 2006, IEEE,* pp.158-161, 29 Nov. – 1 Dec. 2006

164. Sawan, M.; Hashemi, S.; Sehil, M.; Hajj-Hassan, M. and Khouas, A., "Multi-coils based inductive links dedicated to power-up implantable medical devices," *Biomed. Microdevices,* vol.11, no.2, pp.1059-70, 2009
165. Wu, Y.; Hu, A.; Budgett, D.; Malpas, S. and Dissanayake, T., "Efficient power transfer capability analysis of TET system using the equivalent small parameter method," *Biomedical Circuits and Systems, IEEE Transaction on,* no.99, pp.1-11, December 2010
166. Dissanayake, T.; Budgett, D.; Hu, P.; Bennet, L.; Pyner, S.; Booth, L.; Amirapu, S.; Wu, Y. and Malpas, S., "A novel low-temperature transcutaneous energy transfer system suitable for high power implantable medical devices," *Artificial Organs,* vol.34, no.5, pp.E160-7, May 2010
167. Givrad, T.; Maarek, J.; Moore, W. and Holschneider, D., "Powering an implantable minipump with a multi-layered printed circuit coil for drug transfusion applications in rodents," *Annals. of Biomedical Eng.,* vol.38, no.3, pp.707-13, March 2010
168. Guanying, M.; Guozheng, Y. and Xiu, H., "Power transmission for gastrointestinal microsystems using inductive coupling," *Physiol. Meas.,* vol.28, no.3, pp.N9-N18, 2007
169. Scholz, P.; Reinhold, C.; John, W. and Hilleringmann, U., "Analysis of energy transmission for inductive coupled RFID tags," *RFID, IEEE International Conference on,* pp.183-190, 26-28 March 2007
170. Ghovanloo, M. and Lazzi, G., "Transcutaneous magnetic coupling of power and data," 2006 [Online access http://onlinelibrary.wiley.com/doi/10.1002/9780471740360.ebs1372/pdf]
171. Huang, K.; Zhou, Y.; Wu, X.; Liu, W. and Yang, Z., "Design and optimization of inductive power link for biomedical applications," [Online link http://www.intechopen.com/source/pdfs/18023/InTech-Design_and_optimization_of_inductive_power_link_for_biomedical_applications.pdf]
172. Aubert, H., "RFID technology for human implant devices," *C. R. Physique,* vol.12, no.7, pp.675-83, 2011
173. Fang, W.; Liu, W.; Qian, J.; Tang, H. and Ye, P., "Modelling and Simulation of a Transcutaneous Energy Transmission System

Used in Artificial Organ Implants,” *Artificial Organs,* vol.33, no.12, pp.1069-74, 2009

174. Wu, J., “Inductive links with integrated receiving coils for MEMS and implantable applications” 2003 PhD Thesis [Online access http://etd.nd.edu/ETD-db/theses/available/etd-09302003-162720/unrestricted/WuJ092003.pdf]
175. Duan, Y. and Guo, Y., "Rectangular coils modelling for inductive links in implantable biomedical devices," *Antennas and Propagation (APSURSI), 2011 IEEE International Symposium on*, pp.388-391, 3-8 July 2011
176. Jungsuk, K.; Hyunchul, K. and Pedrotti, K., "Power-efficient inductive link optimization for implantable systems," *Radio and Wireless Symposium (RWS), 2011 IEEE*, pp.418-421, 16-19 Jan. 2011
177. Kiani, M.; Jow, U.-M. and Ghovanloo, M.; , "Design and Optimization of a 3-Coil Inductive Link for Efficient Wireless Power Transmission," *Biomedical Circuits and Systems, IEEE Transactions on*, vol.5, no.6, pp.579-591, Dec. 2011
178. Jow, U. and Ghovanloo, M., "Design and Optimization of Printed Spiral Coils for Efficient Transcutaneous Inductive Power Transmission," *Biomedical Circuits and Systems, IEEE Transactions on,* vol.1, no.3, pp.193-202, Sept. 2007
179. Silay, K.; Dehollain, C. and Declercq, M., "Inductive Power Link for a Wireless Cortical Implant With Two-Body Packaging," *Sensors Journal, IEEE,* vol.11, no.11, pp.2825-2833, Nov. 2011
180. Mounaim, F. and Sawan, M., "Integrated High-Voltage Inductive Power and Data-Recovery Front End Dedicated to Implantable Devices," *Biomedical Circuits and Systems, IEEE Transactions on,* vol.5, no.3, pp.283-291, June 2011
181. Suster, M. and Young, D., "Wireless recharging of battery over large distance for implantable bladder pressure chronic monitoring," *Solid-State Sensors, Actuators and Microsystems Conference (TRANSDUCERS), 16th International,* pp.1208-1211, 5-9 June 2011
182. Lee, S.; Hsieh, C. and Yang, C., "Wireless Front-End With Power Management for an Implantable Cardiac Microstimulator," *Biomedical Circuits and Systems, IEEE Transactions on,* 2012
183. Zou, L. and Larsen, T., "Dynamic power control circuit for implantable biomedical devices," *Circuits, Devices & Systems, IET,* vol.5, no.4, pp.297-302, July 2011

184. Wu, W. and Fang, Q., "Design and simulation of printed spiral coil used in wireless power transmission systems for implant medical devices," *Engineering in Medicine and Biology Society (EMBC) , Annual International Conference, IEEE,* pp.4018-4021, Aug. 30 2011-Sept. 3 2011

185. Lee, S.; Cheng, C. and Liang, M., "A Low-Power Bidirectional Telemetry Device With a Near-Field Charging Feature for a Cardiac Microstimulator," *Biomedical Circuits and Systems, IEEE Transactions on,* vol.5, no.4, pp.357-367, Aug. 2011

186. Mirbozorgi, S.; Nabovati, G. and Maymandi-Nejad, M., "Duty Cycle Shift Keying data transfer technique for bio-implantable devices," *Circuits and Systems (ISCAS), 2011 IEEE International Symposium on,* pp.917-920, 15-18 May 2011

187. Jow, U. and Ghovanloo, M., "Optimization of Data Coils in a Multiband Wireless Link for Neuroprosthetic Implantable Devices," *Biomedical Circuits and Systems, IEEE Transactions on,* vol.4, no.5, pp.301-310, Oct. 2010

188. Li, X.; Yin, L.; Wang, Z.; Yuan, Q.; Fang, D. and Zhang, H., "High efficiency coupling with stacked MEMS coils," *Nano/Micro Engineered and Molecular Systems (NEMS), 5th IEEE International Conference on,* pp.509-512, 20-23 Jan. 2010

189. Ma, Q.; Haider, M.R. and Islam, S., "A high efficiency inductive power link and backward telemetry for biomedical applications," *Sensors, 2010 IEEE,* pp.89-93, 1-4 Nov. 2010

190. Rush, A. and Troyk, R., "Electronic performance of a dual inductive link for a wireless neural recording implant," *Engineering in Medicine and Biology Society (EMBC), Annual International Conference,* IEEE, pp.6348-6351, Aug. 30 2011-Sept. 3 2011

191. Wang, G.; Liu, W.; Sivaprakasam, M. and Kendir, G., "Design and analysis of adaptive transcutaneous power telemetry for biomedical implants," *Circuits and Systems I: Regular Papers, IEEE Transactions on,* vol.52, no.10, pp. 2109- 2117, Oct. 2005

192. Lee, S.; Lee, H.; Kiani, M.; Uei-Ming J. and Ghovanloo, M., "An Inductively Powered Scalable 32-Channel Wireless Neural Recording System-on-a-Chip for Neuroscience Applications," *Biomedical Circuits and Systems, IEEE Transactions on,* vol.4, no.6, pp.360-371, Dec. 2010

193. Russell, D.; McCormick, D.; Taberner, A.; Nielsen, P.; Hu, P.; Budgett, D.; Lim, M. and Malpas, S., "Wireless power delivery

system for mouse telemeter," *Biomedical Circuits and Systems Conference, BioCAS 2009, IEEE,* pp.273-276, 26-28 Nov. 2009

194. Puers, R.; Carta, R. and Thone, J., “Wireless power and data transmission strategies for next generation capsule endoscopes,” *Journal of Micromechanics and Microengineering,* vol.21, no.5, pp.1-15, April 2011
195. Ma, Q.; Haider, M.; Yuan, S. and Islam, S., "Power-oscillator based high efficiency inductive power-link for transcutaneous power transmission," *Circuits and Systems (MWSCAS), 53rd IEEE International Midwest Symposium on,* pp.537-540, 1-4 Aug. 2010
196. Russell, D.; McCormick, D.; Taberner, A.; Malpas, S. and Budgett, D., "A high bandwidth fully implantable mouse telemetry system for chronic ECG measurement," *Engineering in Medicine and Biology Society (EMBC), Annual International Conference,* IEEE, pp.7666-7669, Aug. 30 2011-Sept. 3 2011
197. Ghovanloo, M., "An overview of the recent wideband transcutaneous wireless communication techniques," *Engineering in Medicine and Biology Society (EMBC), Annual International Conference of the IEEE,* pp.5864-5867, Aug. 30 2011-Sept. 3 2011
198. Leung, H.; Budgett, D. and Hu, A., "Minimizing Power Loss in Air-Cored Coils for TET Heart Pump Systems," *Emerging and Selected Topics in Circuits and Systems, IEEE Journal on,* vol.1, no.3, pp.412-419, Sept. 2011
199. Fotopoulou, K. and Flynn, B. , "Wireless Power Transfer in Loosely Coupled Links: Coil Misalignment Model," *Magnetics, IEEE Transactions on,* vol.47, no.2, pp.416-430, Feb. 2011
200. Low, Z.; Casanova, J.; Maier, P.; Taylor, J.; Chinga, R. and Lin, J., "Method of Load/Fault Detection for Loosely Coupled Planar Wireless Power Transfer System With Power Delivery Tracking," *Industrial Electronics, IEEE Transactions on,* vol.57, no.4, pp.1478-86, April 2010
201. Algora, C. and Pena, R., “Recharging the battery of implantable biomedical devices by light,” *Artificial Organs,* vol.33, no.10, pp.855-60, June 2009
202. Bin Dai, A. and Lodder, R., “Implantable sensor batteries. Prospects for implantable sensors powered by near infrared rechargeable batteries,” *NIR News,* vol.17, no.2, pp.8-9, 2006
203. Pagidmarry, N. and Konijeti, V., “A high efficiency optical transmitting system to a rechargeable lithium battery for all

implantable medical devices," 3^{rd} *Int. Conf. on Biomedical Engineering, IFMBE, Proceeding on,* vol.5, no.14, pp.533-7, 2006

204. Ayazian, S. and Hassibi, A., "Delivering optical power to subcutaneous implanted devices," *Engineering in Medicine and Biology Society (EMBC), Annual International Conference of the IEEE*, pp.2874-2877, Aug. 30 2011-Sept. 3 2011
205. Hwang, N.; Patterson, W.; Song, Y.; Atay, T. and Nurmikko, A., "Photovoltaic energy converter as a chipscale high efficiency power source for implanted active microelectronic devices," *Engineering in Medicine and Biology Society, IEMBS '04, 26th Annual International Conference of the IEEE*, vol.2, pp.4091-4092, 1-5 Sept. 2004
206. Ackermann, D.; Smith, B.; Wang, X.; Kilgore, K. and Hunter Peckham, P., "Designing the Optical Interface of a Transcutaneous Optical Telemetry Link," *Biomedical Engineering, IEEE Transactions on*, vol.55, no.4, pp.1365-1373, April 2008
207. Larson, B., "An optical telemetry system for wireless transmission of biomedical signals across the skin," 1999 PhD Thesis [Online access http://dspace.mit.edu/bitstream/handle/1721.1/16716/42648143.pdf?sequence=1]
208. Song, Y.; Stein, J.; Patterson, W.; Bull, C.; Davitt, K.; Serruga, M.; Zhang, J.; Nurmikko, A. and Donoghue, J., "A microscale photovoltaic neurostimulators for fibre optic delivery of functional electrical stimulation," *Journal of Neural Engineering,* vol.4, no.2, pp.213-8, April 2007
209. Yoon, Y.; Jung, E.; Kang, H.; Kim, M.; Song, B. and Cho, J., "Design of implantable wireless biomedical signals telemetry system," *Industrial Electronics Society, IECON 2004, 30th Annual Conference of IEEE*, vol.3, pp. 2982- 2986 Vol. 3, 2-6 Nov. 2004
210. Arra, S.; Leskinen, J.; Heikkila, J. and Vanhala, J., "Ultrasonic power and data link for wireless implantable applications," *Wireless Pervasive Computing, ISWPC'07,* 2^{nd} *Int. Symposium on,* 5-7 Feb. 2007
211. Shih, P. and Shih, W., "Design, fabrication and application of bio-implantable acoustic power transmission," *Microelectromechanical Systems, Journal of,* vol.19, no.3, pp.494-502, June 2010

212. Shigeta, Y.; Yamamoto, T,; Fujimori, K.; Sanagi, M.; Nogi, S. and Tsukagoshi, T., “Development of ultrasonic wireless power transmission system for implantable electronic devices,” *Wireless Tech. Conference, EuWIT 2009, European,* pp.49-52, 28-29 Sept. 2009

213. Ozeri, S. and Shmilovitz, D., “Ultrasonic transcutaneous energy transfer for powering implanted devices,” *Ultrasonics,* vol.50, no.6, pp.55-66, May 2010

214. Bardaweel, H.; Al Hattamleh, O.; Richards, R.; Bahr, D. and Richards, C., “Comparison of piezoelectric materials for MEMS power generation,” *6th Int. Workshop on Micro and Nanotechnology for power generation and energy conversion applications,* pp.207-10, 29 Nov. – 1 Dec. 2006

215. Sandoz, J. P., "3D-6 New Solution to Air-Data Transmission Using Low-Cost Narrow-Band Ultrasonic Transducers," *Ultrasonics Symposium, 2007. IEEE*, pp.162-165, 28-31 Oct. 2007

216. Sai Chun Tang; Jolesz, F.A.; Clement, G.T., "A wireless batteryless deep-seated implantable ultrasonic pulser-receiver powered by magnetic coupling," *Ultrasonics Symposium (IUS), 2010 IEEE*, pp.837-840, 11-14 Oct. 2010

217. Benditt, D.; Goldstein, M. and Belalcazar, A., “The leadless ultrasonic pacemaker: a sound idea?” *Heart Rhythm,* vol.6, no.6, pp.749-51, June 2009

218. The Ultrasponder project [Online access http://www.ultrasponder.org/project/project.html]

219. Cheng, X., “Minimally invasive capacitive micromachined ultrasonic transducers array for biomedical applications,” 2008 PhD thesis [Online access http://repository.unm.edu/handle/1928/6916]

220. Zhong Lin Wang; Xudong Wang; Jinhui Song; Jin Liu; Yifan Gao, "Piezoelectric Nanogenerators for Self-Powered Nanodevices," *Pervasive Computing, IEEE*, vol.7, no.1, pp.49-55, Jan.- March 2008

221. Sarvazyan, A.; Rudenko, O. and Nyborg, W., “Biomedical Applications of Radiation Force of Ultrasound: Historical Roots and Physical Basis,” *Ultrasound in Medicine and Biology,* vol.36, no.3, pp.1379-94, Sept. 2010

222. Lewis, George K.; Olbricht, William L., "Design and characterization of a high-power ultrasound driver with ultralow-

output impedance," *Review of Scientific Instruments*, vol.80, no.11, pp.114704-114704-8, Nov 2009

223. Kluge, M.; Becker, T.; Schalk, J.; Otterpohl, T., "Remote acoustic powering and data transmission for sensors inside of conductive envelopes," *Sensors, 2008 IEEE Conference*, pp.41-44, 26-29 Oct. 2008

224. Lee, K.; Echt, D. and Hood, M., "First human demonstration of cardiac stimulation with transcutaneous ultrasound energy delivery," *Journal of the American College of Cardiology,* vol.50, no.9, pp.877-83, Aug. 2007

225. Johansson, J. and Delsing, J., "Microelectronics mounted on a piezoelectric transducer: method, simulations, and measurements," *Ultrasonics,* vol.44, no.1, pp.1-11, Jan. 2006

226. Platt, S.R.; Farritor, S.; Garvin, K.; Haider, H., "The use of piezoelectric ceramics for electric power generation within orthopaedic implants," *Mechatronics, IEEE/ASME Transactions on*, vol.10, no.4, pp. 455- 461, Aug. 2005

227. Masys, A. J.; Ren, W.; Yang, G.; Mukherjee, B. K., "Piezoelectric strain in lead zirconate titante ceramics as a function of electric field, frequency, and dc bias," *Journal of Applied Physics*, vol.94, no.2, pp.1155-1162, Jul 2003

228. Johansson, J. and Delsing, J., "A compact ultrasonic transducer using the active piezoceramic material as electronics carrier," [Online access http://www.epotek.com/SSCDocs/whitepapers/Tech.Paper52.pdf]

229. Suzuki, S.; Katane, T. and Saito, O., "Fundamental study of an electric power transmission system for implanted medical devices using magnetic and ultrasonic energy," *Japanese Society for Artificial Organs,* vol.6, pp.145-8, 2003

230. Javel, E.; Grant, I. and kroll, K., "In vivo characterization of piezoelectric transducers for implantable hearing aids," *Otology & Neurology,* vol.24, no.5, pp.784-95, 2003

231. Suzuki, S.; Kimura, S.; Katane, T.; Saotome, H.; Saito, O. and Kobayashi, K., "Power and interactive information transmission to implanted medical device using ultrasound," *Jpn. J. Appl. Phys.,* vol.41, pp.3600-3, May 2002

232. Kawanabe, H.; Katane, T.; Saotome, H.; Saito, O. and Kobayashi, K., "Power and information transmission to implanted medical

devices using ultrasonic," *Jpn. J. Appl. Phys.* Vol.40, pp.3865-66, May 2001

233. Mukherjee, N.; Roseman, R. and Willging, J., "The piezoelectric cochlear implant: concept, feasibility, challenges, and issues," *Journal of Biomedical Materials Research,* vol.53, no.2, pp.181-7, March 2000
234. Towe, B.C.; Larson, P.J.; Gulick, D.W., "Wireless ultrasound-powered biotelemetry for implants," *Engineering in Medicine and Biology Society, EMBC 2009, Annual International Conference of the IEEE*, pp.5421-5424, 3-6 Sept. 2009
235. Nasiri, A.; Zabalawi, S. and Jeutter, D., "A linear permanent magnet generator for powering implanted electronic devices," *Power Electronics, IEEE Transactions on,* vol.26, no.1, pp.192-9, Jan. 2011
236. Ping, H.; Arof, H. and Wijono; , "Design of a Permanent Magnet Linear Generator," *Strategic Technology, The 1st International Forum on*, pp.231-234, 18-20 Oct. 2006
237. Sang-Yong, J.; Ho-Yong C.; Hyun-Kyo J.; Yang-Seung C. and Kyu-Man C., "Performance evaluation of permanent magnet linear generator for charging the battery of mobile apparatus," *Electric Machines and Drives Conference, IEMDC 2001, IEEE International*, pp.516-521, 2001
238. Kumar, A.; Mirabbasi, S. and Mu Chiao, "Resonance-based wireless power delivery for implantable devices," *Biomedical Circuits and Systems Conference, BioCAS 2009, IEEE*, pp.25-28, 26-28 Nov. 2009
239. RamRakhyani, A.; Mirabbasi, S. and Chiao, M., "Design and Optimization of Resonance-Based Efficient Wireless Power Delivery Systems for Biomedical Implants," *Biomedical Circuits and Systems, IEEE Transactions on*, vol.5, no.1, pp.48-63, Feb. 2011
240. Luo, X.; Niu, S.; Ho, S. and Fu, W., "A Design Method of Magnetically Resonanting Wireless Power Delivery Systems for Bio-Implantable Devices," *Magnetics, IEEE Transactions on*, vol.47, no.10, pp.3833-3836, Oct. 2011
241. Pan, G.; Xin, W.; Yen, G. and Chen, J., "A video wireless capsule endoscopy system powered wirelessly: design, analysis, and experiment," *Measurement Science and Technology,* vol.22, no.6, pp.1-9, March 2011

242. Xuelin Fang; Hao Liu; Guiyang Li; Qi Shao and Hongyi L, "Wireless power transfer system for capsule endoscopy based on strongly coupled magnetic resonance theory," *Mechatronics and Automation (ICMA), International Conference on*, pp.232-236, 7-10 Aug. 2011
243. Peng Hou; Meng-Jun Jia; Liang Feng; Yu Mao; Yu-Hua Cheng, "An Analysis of Wireless Power Transmission Based on Magnetic Resonance for Endoscopic Devices," *Bioinformatics and Biomedical Engineering, (iCBBE), 5th International Conference on*, pp.1-3, 10-12 May 2011
244. Chen, L.; Liu, S.; Zhou, Y.; Cui, T.; , "An Optimizable Circuit Structure for High-Efficiency Wireless Power Transfer," *Industrial Electronics, IEEE Transactions on*, Jan. 2012
245. Hackworth, S., “Design, optimization, and implementation of a volume conduction energy transfer platform for implantable devices” 2010 PhD Thesis [Online access http://etd.library.pitt.edu/ETD/available/etd-03152010-105250/unrestricted/HackworthSA_2010.pdf]
246. Hackworth, S.A.; Mingui Sun; Sclabassi, R.J., "Skin-electrode circuit model for use in optimizing energy transfer in volume conduction systems," *Engineering in Medicine and Biology Society, EMBC 2009, Annual International Conference of the IEEE*, pp.4508-4511, 3-6 Sept. 2009
247. Hackworth, S.A.; Mingui Sun; Sclabassi, R.J., "A prototype volume conduction platform for implantable devices," *Bioengineering Conference, NEBC '07, IEEE 33rd Annual Northeast*, pp.124-125, 10-11 March 2007
248. Yi Zhao; Zhide Tang; Lihua Huang; Yan Zhang; Di Xie; Xiaofeng Xu, "Research of the modal of volume conduction energy transfer," *Automation Congress, WAC 2008, World*, pp.1-4, Sept. 28 2008-Oct. 2 2008
249. Fei Zhang; Hackworth, S.A.; Xiaoyu Liu; Haiyan Chen; Sclabassi, R.J.; Mingui Sun, "Wireless energy transfer platform for medical sensors and implantable devices," *Engineering in Medicine and Biology Society, EMBC 2009, Annual International Conference of the IEEE*, pp.1045-1048, 3-6 Sept. 2009
250. Junhua Wang; Ho, S.L.; Fu, W.N.; Mingui Sun, "Analytical Design Study of a Novel Witricity Charger With Lateral and Angular Misalignments for Efficient Wireless Energy Transmission,"

Magnetics, IEEE Transactions on, vol.47, no.10, pp.2616-2619, Oct. 2011

251. Qingxin Yang; Guizhi Xu; Jianqiang Jin; Duyan Geng; Weinong Fu; Weili Yan; Mingui Sun, "Optimal design of energy transmission system for implantable device base on WiTricity," *Electromagnetic Field Computation (CEFC), 2010 14th Biennial IEEE Conference on*, pp.1, 9-12 May 2010
252. Ho, S.L.; Junhua Wang; Fu, W.N.; Mingui Sun, "A Comparative Study Between Novel Witricity and Traditional Inductive Magnetic Coupling in Wireless Charging," *Magnetics, IEEE Transactions on*, vol.47, no.5, pp.1522-1525, May 2011
253. Fei Zhang; Xiaoyu Liu; Hackworth, S.A.; Sclabassi, R.J.; Mingui Sun, "In vitro and in vivo studies on wireless powering of medical sensors and implantable devices," *Life Science Systems and Applications Workshop, LiSSA 2009. IEEE/NIH*, pp.84-87, 9-10 April 2009
254. Yang Li; Qingxin Yang; Haiyan Chen; Xian Zhang; Zhuo Yan, "Experimental System Design of Wireless Power Transfer Based on Witricity Technology," *Control, Automation and Systems Engineering (CASE), 2011 International Conference on*, pp.1-3, 30-31 July 2011
255. Gozalvez, J., "WiTricity-The Wireless Power Transfer [Mobile Radio]," *Vehicular Technology Magazine, IEEE*, vol.2, no.2, pp.38-44, June 2007
256. Fei Zhang; Xiaoyu Liu; Hackworth, S.A.; Sclabassi, R.J.; Mingui Sun, "Wireless energy delivery and data communication for biomedical sensors and implantable devices," *Bioengineering Conference, IEEE 35th Annual Northeast*, pp.1-2, 3-5 April 2009
257. Nakagawa, S., "Mechanisms of bone-conducted ultrasonic (BCU) perception assessed by electrophysiological measurements in humans," *Complex Medical Engineering (CME), 2011 IEEE/ICME International Conference on*, pp.312-316, 22-25 May 2011
258. Yishan Luo; Yuanyuan Wang; Weiqi Wang, "Simulation studies for comparison of Bone-conducted Ultrasound and Bone-conducted Audible Sound," *Complex Medical Engineering, CME 2007, IEEE/ICME International Conference on*, pp.1546-1549, 23-27 May 2007
259. Logan, B.; Hamelers, B.; Rozendal, R.; Schroder, U.; Keller, J.; Freguia, S.; Aelterman, P.; Verstraete, W. and Rabaey, K.,

”Microbial fuel cells: methodology and technology,” *Environ. Sci. Technol.,* vol.40, no.17, pp.5181-92, July 2006

260. Sherrit, S., “The physical acoustics of energy harvesting,” *Ultrasonics Symposium 2008, IUS 2008, IEEE,* pp.1046-1055, 2-5 Nov. 2008
261. Chao, P., “Energy harvesting electronics for vibratory devices in self-powered sensors,” *Sensors Journal, IEEE,* vol.11, no.12, pp.3106-21, Dec. 2011
262. Venkatasubramanian, R.; Watkins, C.; Stokes, D.; Posthill, J. and Caylor, C., “Energy harvesting for electronics with thermoelectric devices using nanoscale materials,” *Electron Devices Meeting, 2007, IEDM 2007, IEEE International,* pp.367-70, 10-12 Dec. 2007
263. Lebedev, G.; Gusarov, B.; Viala, B.; Delamare, J.; Cugat, O.; Lafont, T. and Zakharov, D., “Thermal energy harvesting using shape memory/piezoelectric composites,” *Solid-state Sensors, Actuators and Microsystems Conference (TRANSDUCERS), 2011 16th International,* pp.669-70, 5-9 June 2011
264. Xin, L. and Shuang-Hua, Y., “Thermal energy harvesting for WSNs,” *Systems Man and Cybernetics (SMC), 2010 IEEE International Conference on,* pp.3045-52, 10-13 Oct. 2010
265. Hoang, D.; Tan, Y.; Chng, H. and Panda, S., “Thermal energy harvesting from human warmth for wireless body area network in medical healthcare systems,” *Power Electronics and Drive Systems, 2009, PEDS 2009, International Conference on,* pp.1277-82, 2-5 Nov. 2009
266. Lay-Ekuakille, A.; Vendramin, G.; Trotta, A. and Mazzotta, G., "Thermoelectric generator design based on power from body heat for biomedical autonomous devices," *Medical Measurements and Applications, MeMeA, IEEE International Workshop on*, pp.1-4, 29-30 May 2009
267. Leonov, V.; Van Hoof, C. and Vullers, R., "Thermoelectric and Hybrid Generators in Wearable Devices and Clothes," *Wearable and Implantable Body Sensor Networks, BSN 2009, Sixth International Workshop on*, pp.195-200, 3-5 June 2009
268. Russer, P.; Fichtner, N.; Lugli, P.; Porod, W.; Russer, J. and Yordanov, H., “Nanoelectriconics-based integrate antennas,” *Microwave Magazine, IEEE,* vol.11, no.7, pp.58-71, Dec. 2010
269. Aminurrahim bin Othman, M., “Waste of radio frequency signal analysis for wireless energy harvester,” *Signal Processing and its*

Applications (CSPA), 2010 6th International Colloquium on, pp.1-3, 21-23 May 2010

270. Jabbar, H.; Song, Y. and Jeong, T., “RF energy harvesting systems and circuits for charging of mobile devices,” *Consumer Electronics, IEEE Transactions on,* vol.56, no.1, pp.247-53, February 2010
271. Heer, R.; Wissenwasser, J.; Milnera, M.; Farmer, L.; Hopfner, C. and Vellekoop, M., “Wireless powered electronic sensors for biological applications,” *Engineering in Medicine and Biology Society (EMBC), 2010 Annual International Conference, IEEE,* pp.700-3, 31 Aug. 2010
272. Kimball, J.; Kuhn, B. and Balog, R., “A system design approach for unattended solar energy harvesting supply,” *Power Electronics, IEEE Transactions on,* vol.24, no.4, pp.952-62, April 2009
273. Woojoo, L.; Younghyun, K.; Yanzhi, W.; Naehyuck, C.; Pedram, M. and Soohee, H., “Versatile high-fidelity photovoltaic module emulation system,” *Low Power Electronics and Design (ISLPED), 2011 International Symposium on,* pp.91-6, 1-3 Aug. 2011
274. Ayazian, S.; Soenen, E. and Hassibi, A., “A photovoltaic-driven and energy-autonomous CMOS implantable sensor,” *VLSI Circuits (VLSIC), 2011 Symposium on,* pp.148-9, 15-17 June 2011
275. Chung-Yang, S. and Nan-Chyuan, T., “Human-powered MEMS-based energy harvest devices,” *Applied Energy,* January 2012
276. Mitcheson, P.; Yeatman, E.; Rao, G.; Holmes, A. and Green, T., “Energy harvesting from human and machine motion for wireless electronic devices,” *Proceedings of the IEEE, vol.*96, no.9, pp.1457-86, Sept. 2008
277. Dayal, R.; Dwari, S. and Parsa, L., “A new design for vibration-based electromagnetic energy harvesting systems using coil inductance of microgenerator,” *Industry Applications, IEEE Transactions on,* vol.47, no.2, pp.820-30, March-April 2011
278. Rocha, J.; Goncalves, L.; Rocha, P.; Silva, M. and Lanceros-Mendez, S., “Energy harvesting from piezoelectric materials fully integrated in footwear,” *Industrial Electronics, IEEE Transactions on,* vol.57, no.3, pp.813-19, March 2010
279. Bo, R.; Siu, W.; Feifei, W.; Xiangyong, Z.; Haosu, L.; Xiaobing, L.; Qinhui, Z.; Wenning, D. and Yaoyao, Z., “Piezoelectric energy harvesting based on shear mode $0.71Pb(Mg_{1/3}Nb_{2/3})O_3$-$0.29PbTiO_3$ single crystals,” *Ultrasonics, Ferroelectrics and*

Frequency Control, IEEE Transactions on, vol.57, no.6, pp.1419-25, June 2010

280. Daue, T. and Kunzmann, J., “Energy harvesting systems using piezo-electric MFCs,” *Applications of Ferroelectrics, ISAF 2008, 17th IEEE International Symposium on the,* vol.1, pp.1, 23-28 Feb. 2008
281. Junrui, L. and Wei-Hsin, L., “improved design and analysis of self-powered synchronized switch interface circuit for piezoelectric energy harvesting systems,” *Industrial Electronics, IEEE Transactions on,* vol.59, no.4, pp.1950-60, April 2012
282. Dallago, E.; Danioni, A.; Marchesi, M.; Nucita, V. and Venchi, G., “A self-powered electronic interface for electromagnetic energy harvester,” *Power Electronics, IEEE Transactions on,* vol.26, no.11, pp.3174-82, Nov. 2011
283. Zhihua, W.; Bowen, W.; Minwei, W.; Huijuan, Z. and Weiping, H., “Model and experimental study of permanent magnet vibration-to-electrical power generator,” *Applied Superconductivity*, *IEEE Transactions on,* vol.20, no.3, pp.1110-13, June 2010
284. Florentino, H.; Freire, R., Raimund, C.; Sa, A.; Florentino, C. and Galayko, D., “Electrostatic vibration energy harvester with piezoelectric start-up generator,” *Circuits and Systems (ISCAS), 2011 IEEE International Symposium on,* pp.1343-46, 15-18 May 2011
285. Yuwei, Z.; Xueliang, H.; Linlin, T.; Yang, B. and Jianhua, Z., “Current research situation and developing tendency about wireless power transmission,” *Electrical and Control Engineering (ICECE), 2010 International Conference on,* pp.3507-11, 25-27 June 2010
286. Bradley, P., “Implantable ultra-low power radio chip facilitates in-body communications,” [Online access http://mobiledevdesign.com/hardware_news/implant-rf-transmission-chip-power-design-0607]
287. Puers, R.; Schuylenbergh, K.; Catrysse, M. and Hermans, B., “Wireless inductive transfer of power and data,” [Online access http://personnel.univ-reunion.fr/lanson/typosite/fileadmin/documents/pdf/TMO_M2/Biblio/WIRELESS_INDUCTIVE_TRANSFER_OF_POWER_AND_DATA.pdf]
288. Young, D.J., "Wireless powering and data telemetry for biomedical implants," *Engineering in Medicine and Biology*

Society, EMBC 2009, Annual International Conference of the IEEE, pp.3221-3224, 3-6 Sept. 2009

289. Adeeb, M.; Islam, B.; Haider, M.; Tulip, M.; Ericson, M. and Islam, S., “An inductive link based wireless power transfer system for biomedical applications,” 2011 [Online access http://downloads.mts.hindawi.com/MTS-Files/APEC/papers/regular/879294.v2.pdf?AWSAccessKeyId=0CX53QQSTHRYZZQRKA02&Expires=1335034348&Signature=Q1yjVAUnP89aXW2Pdrob%2FDp3PfA%3D]
290. Yazaki, T.; Morita, I. and Tanaka, H., "Demonstration of optical wireless USB 2.0 system with wireless power transfer," *Consumer Electronics (ICCE),IEEE International Conference on*, pp.11-12, 9-12 Jan. 2011
291. Hmida, G.; Ghariani, H. and Samet, M., “Design of wireless power and data transmission circuits for implantable biomicrosystem,” *Biotechnology,* vol.6, no.2, pp.153-164, 2007 [Online access http://scialert.net/qredirect.php?doi=biotech.2007.153.164&linkid=pdf]
292. Liang, C.; Young, G.; Chen, J. and Chen, C., “A microcontroller – based implantable neuromuscular stimulation system with wireless power and data transmission for animal experiments,” *Journal of the Chinese Institute of Engineers,* vol.26, no.4, pp.493-501, 2003 [Online access http://ir.lib.stut.edu.tw/bitstream/987654321/3719/2/Paper_A%252520micontroller-based%252520implantable.pdf]
293. Carta, R. and Puers, R., “Wireless power and data transmission for robotic capsule endoscopes,” *J. Micromech. Microeng.,* vol. 21, no.5, pp. 4008-13, 2011
294. Seydnejad, S. and Samani, M.M., "An implantable telemetry system for long-term bio-signal recording," *Instrumentation and Measurement Technology Conference (I2MTC), IEEE*, pp.867-870, 3-6 May 2010
295. Martinez-Flores, J.; Becerra-Garcia, J. and Herrera-Espinosa, J., “Design of a transcutaneous magnetic link to energize electronic devices implanted in a biological medium,” December 2010 [Online access http://jvr.freewebpage.org/TableOfContents/Volume5/Issue4/10_JFlores-Martinez_DesignOfATranscutaneousMagneticLinkToEnergizeElec

tronicDevicesImplantedInABiologicalMedium_092410B_92_98.pdf]

296. Shiba, K.; Nukaya, M.; Tsuji, T. and Koshiji, K., "Analysis of Current Density and Specific Absorption Rate in Biological Tissue Surrounding Transcutaneous Transformer for an Artificial Heart," *Biomedical Engineering, IEEE Transactions on*, vol.55, no.1, pp.205-213, Jan. 2008
297. Mazzilli, F.; Peisino, M.; Mitouassiwou, R.; Cotté, B.; Thoppay, P.; Lafon, C.; Favre, P.; Meurville, E. and Dehollain, C., "In-vitro platform to study ultrasound as source for wireless energy transfer and communication for implanted medical devices," *Engineering in Medicine and Biology Society (EMBC), 2010 Annual International Conference of the IEEE* , pp.3751-3754, Aug.31 2010-Sept. 4 2010
298. Denisov, A.; Yeatman, E., "Ultrasonic vs. Inductive Power Delivery for Miniature Biomedical Implants," *Body Sensor Networks (BSN), 2010 International Conference on*, pp.84-89, 7-9 June 2010
299. Cotté, B.; Lafon, C.; Chapelon, J. and Dehollain, C., "Suitable acoustic paths to transfer energy in depth using ultrasound," *Engineering in Medicine and Biology Society (EMBC), 2010 Annual International Conference of the IEEE*, pp.6694-6697, Aug.31 2010-Sept. 4 2010
300. Zhu, Y.; Moheimani, S. and Yuce, M.R., "A 2-DOF MEMS Ultrasonic Energy Harvester," *Sensors Journal, IEEE*, vol.11, no.1, pp.155-161, Jan. 2011
301. Rodig, T.; Schonecker, A. and Gerlach, G., “A survey on piezoelectric ceramics for generator applications,” *Journal of the American Ceramic Society,* vol.93, no.4, pp.901-12, April 2010
302. Davilis, Y.; Kalis, A. and Ifantis, A., “On the use of ultrasonic waves as a communications medium in biosensor networks,” *Information Technology in Biomedicine, IEEE Transactions on,* vol.14, no.3, pp.650-6, May 2010
303. Vilkomerson, D.; Chilipka, T.; Bogan, J.; Blebea, J.; Choudry, R.; Wang, J.; Salvatore, M.; Rotella, V. and Soundararajan, K., “Implantable ultrasound devices,” *Proceedings of the SPIE,* vol.6920, pp.69200C-69200C-11, 2008
304. Waters, B.H.; Sample, A.P.; Bonde, P. and Smith, J.R., "Powering a Ventricular Assist Device (VAD) With the Free-Range Resonant Electrical Energy Delivery (FREE-D) System," *Proceedings of the IEEE*, vol.100, no.1, pp.138-149, Jan. 2012

305. Spera, G., “The next wave in minimally invasive surgery,” 2008 [Online access http://www.mddionline.com/article/next-wave-minimally-invasive-surgery]
306. Mitragotri, S., “Healing sound: the use of ultrasound in drug delivery and other therapeutic applications,” *Nature Reviews Drug Discovery,* vol.4, pp.255-60, 2005
307. Yadav, K.; Kymissis, I. and Kinget, P.R., "A 4.4uW wake-up receiver using ultrasound data communications," *VLSI Circuits (VLSIC), 2011 Symposium on*, pp.212-213, 15-17 June 2011
308. Bhuyan, S.; Sivanand, K.; Panda, S.; Kumar, R. and Junhui, H., "Resonance-Based Wireless Energizing of Piezoelectric Components," *Magnetics Letters, IEEE*, vol.2, pp.6000204, 2011
309. Larson, P. and Towe, B., "Miniature ultrasonically powered wireless nerve cuff stimulator," *Neural Engineering (NER), 5th International IEEE/EMBS Conference on*, pp.265-268, April 27 2011-May 1 2011
310. Roundy, S.; Wight, P. and Rabaey, J., “Study of low-level vibrations as a power source for wireless sensor nodes,” *Comput. Commun.,* vol.26, pp.1131-44, 2003
311. Tressler, J.; Howarth, T. and Dehua, H., “A comparison of the underwater acoustic performance of single crystal vs. piezoelectric ceramic based cymbal projectors,” *OCEANS 2003 Proceedings,* vol.5, pp.2372-9, 22-26 Sept. 2003
312. Koyama, D. and Nakamura, K., “Electric power generation using a vibration of a polyuria piezoelectric thin film,” *Ultrasonics Symposium, IUS 2008, IEEE,* pp.938-41, 2-5 Nov. 2008
313. Sodano, H.; Magliula, E.; Park, G. and Inman, D., “Electric power generation using piezoelectric devices,” *13th International Conference on Adaptive Structures and Technologies,* pp.153-61, 2004
314. Platt, S.; Farritor, S. and Haider, H., “On low-frequency electric power generation with PZT ceramics,” *Mechatronics, IEEE/ASME Transactions on,* vol.10, pp.240-52, 2005
315. Lin, S., “Study on the radial composite piezoelectric ceramic transducer in radial vibration,” *Ultrasonics,* vol.46, pp.51-9, 2007
316. Shen, D.; Choe, S. and Kim, D., “Comparative study of piezoelectric transducers for power scavengers,” *Applications of Ferroelectrics, ISAF’06, 15th IEEE International Symposium on the,* pp.224-7, July 30 – Aug. 3, 2006

317. Boumchedda, K.; Ayadi, A.; Aouaroun, T. and Fantozzi, G., “Study of vibratory behaviour of interconnected porous PZT by impulse method,” *Journal of the European Ceramic Society,* vol.30, no.1, pp.101-5, Jan. 2010
318. Jeon, Y.; Sood, J.; Jeong, J. and Kim, S., “MEMS power generator with transverse-mode thin film PZT,” *Sensors and Actuators A: Physical,* vol.122, no.1, pp.16-22, July 2005
319. Ramsay, M. and Clark, W., “Piezoelectric energy harvesting for Bio-MEMS applications,” *Proc. SPIE 4332,* pp.429, 2001
320. Maleki, T.; Cao, N.; Song, S.; Kao, C.; Ko, S. and Ziaie, B., "An Ultrasonically Powered Implantable Micro-Oxygen Generator (IMOG)," *Biomedical Engineering, IEEE Transactions on*, vol.58, no.11, pp.3104-3111, Nov. 2011
321. Lach, M.; Platte, M. and Ries, A., “Piezoelectric materials for ultrasonic probes,” *NDTnet,* vol.1, no.9, pp.1-9, Sept. 1996
322. Gururaja, T.; Schulze, W.; Cross, L.; Newnham, R.; Auld, B. and Wang, Y., "Piezoelectric Composite Materials for Ultrasonic Transducer Applications. Part I: Resonant Modes of Vibration of PZT Rod-Polymer Composites," *Sonics and Ultrasonics, IEEE Transactions on*, vol.32, no.4, pp.481-498, July 1985
323. Shrout, T., "Innovations in piezoelectric materials for ultrasound transducers," *Applications of Ferroelectrics, ISAF 2008, 17th IEEE International Symposium on the*, vol.3, pp.1-4, 23-28 Feb. 2008
324. Seung-Eek P. and Shrout, T., "Characteristics of relaxor-based piezoelectric single crystals for ultrasonic transducers," *Ultrasonics, Ferroelectrics and Frequency Control, IEEE Transactions on*, vol.44, no.5, pp.1140-1147, Sept. 1997
325. Thompson, M., “On the material properties and constitutive equations of piezoelectric Poly Vinylidene Fluoride (PVDF),” PhD Thesis, Apr. 2002 [Online access http://dspace.library.drexel.edu/bitstream/1860/86/14/thompson_thesis.pdf]
326. http://www.ferroperm-piezo.com/
327. Wild, G. and Hinckley, S., "Wireless acoustic communications and power supply for in vivo biomedical devices," Jan. 2011. [Online access http://cdn.intechopen.com/pdfs/12904/InTech-Wireless_communications_and_power_supply_for_in_vivo_biomedical_devices_using_acoustic_transmissions.pdf]
328. Burelew, M.; Madsen, E.; Zagzebski, J.; Banjavic, R. and Sum, S., “A new ultrasound tissue equivalent material,” *Radiology*, vol. 134, pp.517-20, 1980

329. Kondo, T. and Kitatuji, M., “New tissue mimicking materials for ultrasound phantoms,” 2005, [Online access http://ieeexplore.ieee.org/stamp/stamp.jsp?arnumber=01603183]

330. Onishi, T. and Uebayashi, S., “Biological tissue-equivalent phantoms usable in broadband frequency range,” [Online access http://www.nttdocomo.co.jp/english/binary/pdf/corporate/technology/rd/technical_journal/bn/vol7_4/vol7_4_061en.pdf]

331. Takimoto, T.; Onishi, T.; Saito, K.; Takahashi, M.; Uebayashi, S. and Ito, K., “Characteristics of biological tissue-equivalent phantoms applied to UWB communications,” [Online access http://onlinelibrary.wiley.com/doi/10.1002/ecja.20300/pdf]

332. http://www.olympus-ims.com/data/File/panametrics/UT-technotes.en.pdf

333. Ontega, R.; Tellez, A.; Leiia, L. and Vera, A., “Measurement of ultrasonic properties of muscle and blood biological phantoms,” *Physics Procedia,* vol.3, pp.627-34, Jan. 2010

334. Treeby, B.; Zhang, E.; Thomas, A. and Cox, B., “Measurements of the ultrasound attenuation and dispersion in whole human blood and its components from 0 – 7 MHz,” *Ultrasound in Med. & Biol.,* vol.37, no.2, pp.289-300, Feb. 2011

335. Liu, Y.; Maruvada, S.; King, R.; Herman, B. and Wear, K., “Development and characterization of a blood mimicking fluid for high intensity focused ultrasound,” *J. Acoust. Soc. Am.,* vol.124, no.3, pp.1803-10, 2008

336. Oates, C., “Towards an ideal blood analogue for doppler ultrasound phantoms,” *Phys. Med. Biol.,* vol.36, no.11, pp.1433-442, 1991

337. http://www.reson.com/wp-content/uploads/2010/12/TC4034.pdf

338. http://www.seaconnectwiki.org/doku.php/reson_products:transducers_and_hydrophones:how_do_i_determine_signal_pressure_level_spl_or_energy_level_from_a_source_at_the_tip_of_a_hydrophone

339. Lingfang, S.; Guoliang, F. and Jia-qi, Y., "Design of Excitation Circuits in Ultrasonic Transducers for Fouling Detection," *Genetic and Evolutionary Computing (ICGEC), Fourth International Conference on*, pp.841-844, 13-15 Dec. 2010

340. Chebli, R. and Sawan, M., "A CMOS high-voltage DC-DC up converter dedicated for ultrasonic applications," *System-on-Chip for Real-Time Applications Proceedings, 4th IEEE International Workshop on*, pp. 119- 122, 19-21 July 2004

341. Borg, J. and Johansson, J., "An Ultrasonic Transducer Interface IC With Integrated Push-Pull 40 Vp-p, 400 mA Current Output, 8-bit

DAC and Integrated HV Multiplexer," *Solid-State Circuits, IEEE Journal of*, vol.46, no.2, pp.475-484, Feb. 2011

342. Schweitzer, P.; Tisserand, E.; Hamed, A.; Andrea, J. and Coutard, F., “Feedback sinewave driver design for ultrasonic transducer,” *Eur. Phys. J. Appl. Phys.,* vol.47, no.1, 12703, July 2009
343. Ishikawa, J.; Mizutani, Y.; Suzuki, T.; Ikeda, H. and Yoshida, H., "High-frequency drive-power and frequency control for ultrasonic transducer operating at 3 MHz," *Industry Applications Conference, Thirty-Second IAS Annual Meeting, IAS '97., Conference Record of the 1997 IEEE*, vol.2, pp.900-905 vol.2, 5-9 Oct 1997
344. http://www.fairchildsemi.com/ds/2N/2N7000.pdf
345. http://ww1.microchip.com/downloads/en/DeviceDoc/41211D_.pdf
346. http://datasheet.sii-ic.com/en/charge_pump_ic/S882Z_E.pdf
347. http://www.fairchildsemi.com/ds/BA/BAT54.pdf
348. http://www.ti.com/lit/ds/symlink/opa277.pdf
349. Jow, U. and Ghovanloo, M., "Modelling and Optimization of Printed Spiral Coils in Air, Saline, and Muscle Tissue Environments," *Biomedical Circuits and Systems, IEEE Transactions on*, vol.3, no.5, pp.339-347, Oct. 2009
350. Harrison, R., "Designing Efficient Inductive Power Links for Implantable Devices," *Circuits and Systems, ISCAS, IEEE International Symposium on*, pp.2080-2083, 27-30 May 2007
351. Zolog, M.; Pitica, D. and Pop, O., "Characterization of Spiral Planar Inductors Built on Printed Circuit Boards," *Electronics Technology, 30th International Spring Seminar on*, pp.308-313, 9-13 May 2007
352. Zheng, H., "Numerical modelling for planar spiral inductors in silicon-based radio-frequency integrated circuits," *Microwave Conference Proceedings, APMC 2005, Asia-Pacific Conference Proceedings*, vol.1, pp. 4 pp., 4-7 Dec. 2005
353. Shah, M.; Phillips, R. and Normann, R., "A study of printed spiral coils for neuroprosthetic transcranial telemetry applications," *Biomedical Engineering, IEEE Transactions on*, vol.45, no.7, pp.867-876, July 1998
354. Mohan, S.; Del Mar Hershenson, M.; Boyd, S. and Lee, T., "Simple accurate expressions for planar spiral inductances," *Solid-State Circuits, IEEE Journal of*, vol.34, no.10, pp.1419-1424, Oct 1999

355. Jenei, S.; Nauwelaers, B. and Decoutere, S., "Physics-based closed-form inductance expression for compact modelling of integrated spiral inductors," *Solid-State Circuits, IEEE Journal of*, vol.37, no.1, pp.77-80, Jan 2002
356. Zierhofer, C. and Hochmair, E.S., "Geometric approach for coupling enhancement of magnetically coupled coils," *Biomedical Engineering, IEEE Transactions on*, vol.43, no.7, pp.708-714, July 1996
357. Ghovanloo, M. and Atluri, S., "A Wide-Band Power-Efficient Inductive Wireless Link for Implantable Microelectronic Devices Using Multiple Carriers," *Circuits and Systems I: Regular Papers, IEEE Transactions on*, vol.54, no.10, pp.2211-2221, Oct. 2007
358. Chen, J., "*On-chip spiral inductor/transformer design and modelling for RF applications*," PhD thesis, University of Florida, Orlando, 2006
359. Grover, F., "*Inductance calculations: working formulas and tables*," Dover Publications, Inc., New York, 1946 + Thompson, M., "Inductance calculation techniques – Part II: Approximation and handbook methods," Dec. 1999 [Online access http://www.thompsonrd.com/induct2.pdf]
360. Yang, Z.; Wentai Liu, W. and Basham, E., "Inductor Modelling in Wireless Links for Implantable Electronics," *Magnetics, IEEE Transactions on*, vol.43, no.10, pp.3851-3860, Oct. 2007
361. Zhao, J., "A new calculation for designing multi-layer planar spiral inductors," *EDN,* July 2010 [Online access http://www.edn.com/file/25510-A_new_calculation_for_designing_multilayer_planar_spiral_inductors_PDF.pdf]
362. www.agilent.com
363. Burghartz, J. and Rejaei, B., "On the design of RF spiral inductors on silicon," *Electron Devices, IEEE Transactions on*, vol.50, no.3, pp. 718- 729, March 2003
364. http://www.megauk.com/artwork_films.php
365. http://www.megauk.com/uv_exposure_units.php
366. http://www.megauk.com/pcb_processing_tanks.php
367. http://h10010.www1.hp.com/wwpc/ca/en/sm/WF06b/12144670-12144918-12144920-12144920-12144986-12144996-29519525.html?dnr=1
368. http://www.lumenera.com/products/microscopy-cameras/infinity2-1.php
369. http://www.megauk.com/plotting_systems.php

370. http://www.megauk.com/datasheets/5140_Data_Sheet_FP8000&_FP8000XL_Photoplotter%28ver0109%29.pdf

371. http://www.wieweb.com/ns6/index.html

372. http://www.layouteditor.net/screenshots/index.php5

373. http://www.megauk.com/pcb_chemicals.php

374. http://en.wikipedia.org/wiki/LC_circuit

375. Gutmann, R., "Application of RF Circuit Design Principles to Distributed Power Converters," *Industrial Electronics and Control Instrumentation, IEEE Transactions on*, vol.IECI-27, no.3, pp.156-164, Aug. 1980

376. Schulenbergh, K. and Puers, R., “Inductive powering: basic theory and application to biomedical systems,” Springer Science + Business Media B. V., 2009

377. http://svn.clifford.at/metaparts/trunk/datasheets/DS_c484a2d577f40b67eb80b24e6ca00077.pdf

378. http://www.dimensionengineering.com/appnotes/Gmeter/PIC16F818.pdf

379. http://www.nxp.com/documents/data_sheet/74HC_HCT08.pdf

380. http://www.onsemi.com/pub_link/Collateral/74HC86.REV1.PDF

381. http://www.powersystems.com.uy/robotica/archivos/40106.pdf

382. http://pdf1.alldatasheet.com/datasheet-pdf/view/15021/PHILIPS/1N4148.html

383. http://www.new-wave-concepts.com/ed/wizard.html

384. http://www.microchip.com/stellent/idcplg?IdcService=SS_GET_PAGE&nodeId=1406&dDocName=en019469

385. http://ww1.microchip.com/downloads/en/DeviceDoc/MPLAB_User_Guide_51519c.pdf

386. http://www.ccsinfo.com/

387. http://www.microchip.com/stellent/idcplg?IdcService=SS_GET_PAGE&nodeId=1406&dDocName=en538340

388. http://ww1.microchip.com/downloads/en/DeviceDoc/PICkit_3_User_Guide_51795A.pdf

389. http://www.saleae.com/logic

390. http://www.circuitspecialists.com/benchtop-power-supply-csi12001x.html

391. http://www.artisan-scientific.com/info/Fluke_PM6303_Manual.pdf

392. International Commission on non-ionizing radiation protection (ICNIRP), “Guidelines for limiting exposure to time-varying electric, magnetic and electromagnetic fields (up to 300 GHz),” *Health Physics*, vol.74, no.4, pp.494-522, 1998 [Online access http://www.icnirp.de/documents/emfgdl.pdf
393. Friedl, K.; Schmautzer, E. and Fickert, L., "Effect of the new ICNIRP guidelines on exposure evaluation of electrical power systems," Energetics (IYCE), *Proceedings of the 3rd International Youth Conference on*, pp.1-5, 7-9 July 2011
394. Health Canada, “Limits of human exposure to radiofrequency electromagnetic energy in the frequency range from 3 KHz to 300 GHz (Safety Code 6),” 2009 [Online access http://www.rfsafetysolutions.com/PDF%20Files/Health%20Canada%20Safety%20Code%206%20Standard_2009.pdf
395. Guy, A.W., "Safety Level with Respect to Human Exposure to Radiofrequency Electromagnetic Fields (300 KHz-100 GHz)," *Microwave symposium Digest, IEEE MTT-S International*, pp.335-336, 28-30 May 1980
396. Bernardi, P.; Cavagnaro, M.; Pisa, S. and Piuzzi, E., "Specific absorption rate and temperature elevation in a subject exposed in the far-field of radio-frequency sources operating in the 10-900- MHz range," *Biomedical Engineering, IEEE Transactions on*, vol.50, no.3, pp.295-304, March 2003
397. National Radiological Protection Board (NRPB), “Advice on limiting exposure to electromagnetic fields (0 – 300 GHz),” vol.15, no.2, 2004 [Online access http://www.hpa.nhs.uk/webc/HPAwebFile/HPAweb_C/1194947415497]
398. Health Protection Agency (HPA), “Health effects of exposure to ultrasound and infrasound,” [Online access http://www.hpa.org.uk/webc/HPAwebFile/HPAweb_C/1265028759369]
399. Harris, G.R.; , "Medical ultrasound exposure measurements: update on devices, methods, and problems," *Ultrasonics Symposium, Proceedings, IEEE*, vol.2, pp.1341-1352 , 1999
400. Duck, F., “The measurement of exposure to ultrasound and its application to estimations of ultrasound ‘dose’,” *Phys. Med. Biol.*, vol.32, no.3, pp.303-25, 1987
401. Xu, Z. and Li, Y., “Energy constrained duty-cycle optimisation for wireless implanted communication devices,” *E-health Telecommunication Systems Networks (ETSN)*, vol.1, no.1, pp.6-11, 2011

402. Bradley, P., “The ultra-low-power wireless medical device revolution,” *Medical Electronic Design (MED)*, Apr. 2005 [Online access http://www.medicalelectronicsdesign.com/article/ultra-low-power-wireless-medical-device-revolution]
403. http://www.arachnoid.com/sage/tuned_circuits.html
404. Yaacob, M.; Arshad, M. and Manaf, A., "Theoretical characterization of square piezoelectric micro ultrasonic transducer for underwater applications," *Mechatronics and its Applications (ISMA), 7th International Symposium on*, pp.1-5, 20-22 April 2010
405. Ohki, M., “Estimation of piezoelectric equivalent circuit parameters using principle of least variance,” *Jpn. J. Appl. Phys.*, vol.47, no.5, pp.4029-33, 2008
406. http://www.rfcafe.com/references/electrical/fcc-maximum-permissible-exposure.htm